BRNO UNIVERSITY OF TECHNOLOGY

VYSOKÉ UČENÍ TECHNICKÉ V BRNĚ

FACULTY OF CHEMISTRY

FAKULTA CHEMICKÁ

INSTITUTE OF PHYSICAL AND APPLIED CHEMISTRY

ÚSTAV FYZIKÁLNÍ A SPOTŘEBNÍ CHEMIE

NOVEL DEVICES AND MATERIALS FOR BIOELECTRONICS

NOVÁ ZAŘÍZENÍ A MATERIÁLY PRO BIOELEKTRONIKU

DOCTORAL THESIS

DIZERTAČNÍ PRÁCE

AUTHOR — Ing. Jiří Ehlich

AUTOR PRÁCE

SUPERVISOR — doc. Ing. Ota Salyk, CSc.

ŠKOLITEL

BRNO 2022

BRNO UNIVERSITY OF TECHNOLOGY
FACULTY OF CHEMISTRY

Assignment Doctoral Thesis

Department:	Institute of Physical and Applied Chemistry	Academic year: 2022/23
Student:	**Ing. Jiří Ehlich**	
Study programme:	Chemistry, Technology and Properties of Materials	
Study field:	Chemistry, Technology and Properties of Materials	
Head of thesis:	**doc. Ing. Ota Salyk, CSc.**	

Title of Doctoral Thesis:

Novel Devices and Materials for Bioelectronics

Doctoral Thesis:

1. Develop a reliable, reproducible, and user–friendly platform composed of multiple Microbial Fuel Cells arranged in a standard 96 or 24 well–plate configuration for electrochemical characterization of electrogenic microorganisms.
2. Fabricate a platform for electrical stimulation of stem cells and apply the platform in biological experiements towards directed stem cell differentiation by electric stimulation.
3. Investigate whether and to what extent are irreversible oxygen reduction reactions happening on standard electrode materials under various DC conditions and AC stimulation protocols.

Deadline for Doctoral Thesis delivery: 11.9.2022:

Ing. Jiří Ehlich student	doc. Ing. Ota Salyk, CSc. Head of thesis	prof. Ing. Miloslav Pekař, CSc. Head of department

prof. Ing. Martin Weiter, Ph.D.
Dean

In Brno dated 1.9.2021

ABSTRACT

This dissertation represents a synthesis of projects I have been working on in the course of my Ph.D. studies. The projects evolve around a wide range of topics, which is the reason for the broad and general title. Projects described it the thesis involve the development of electronic tools which can be applied to several areas of bioelectronics: The first part of the thesis concerns platforms for the study of unique microorganisms capable of direct electron exchange with electronic devices. This involved design, fabrication, and application of such platforms. The second part of the thesis deals with electrical stimulation; its application to stem cells towards their directed differentiation, and fundamental studies of possibly harmful irreversible faradaic reactions happening in the course of broadly used electrical stimulation protocols applied in clinical practice.

All the projects share core, common, theoretical, and practical foundation originating in chemical engineering, electrochemistry, and materials science. A unifying feature playing a major factor and appearing throughout all the projects would be a family of oxygen reduction reactions. Oxygen reduction is a necessary half-cell reaction taking place in the developed device studying electroactive microorganisms. Oxygen reduction and subsequent generation of reactive oxygen species might arguably play a significant role in the direct electrical stimulation of stem cells towards their differentiation. Lastly, oxygen reduction reactions were the main irreversible faradaic reactions we have been observing during standard electrical stimulation protocols.

The thesis presents summarized theoretical background necessary to understand presented projects. Goals are defined. Results are introduced as a commented list of published scientific publications. Achieved outcomes are summarized and discussed. Also, a perspective into the future is given.

Main results can be summarized as follows. First goal was to develop a platform for electrochemical characterization of electroactive microorganisms. The platform was based on 24 or 96-well Microbial Fuel Cell array. After two design iterations a prototype fulfilling all the intended requirements was developed, tested, and proven to be reliably working.

Next, a multi-well platform of interdigitated electrodes was fabricated and used for electrical stimulation of stem cells. Unfortunately, the platform turned out to be unreliable and not working properly which resulted in the failed attempt to differentiate stem cells into a specific type of cells.

Lastly, we have examined oxygen reduction reactions (ORRs) on electrodes made of typical materials used for neural stimulation electrodes. Oxygen can be reduced either to water or hydrogen peroxide. Both reactions can significantly reduce the quantity of dissolved oxygen near the electrode, creating hypoxic conditions harmful to neurons. Peroxide, meanwhile, can induce toxic reactions or act as a signaling molecule. We have examined the amount of reduced oxygen and produced peroxide by various stimulation protocols using amperometric sensors and compared electro-catalytic activities of studied materials. Main finding is that typical protocols lead to irreversible ORRs. Some electrode materials induce highly hypoxic conditions, others additionally produce hydrogen peroxide into the mM range.

ABSTRAKT

Tato dizertace je syntézou hlavních projektů, kterým jsem se věnoval v průběhu mého doktorského studia. Projekty se rozvíjejí kolem širokého spektra témat, z toho důvodu byl zvolen široký a obecný název. Projekty popsané v této práci se zabývají vývojem elektronických zařízení s využitím v řadě bioelektronických aplikací. První část práce se věnuje vývoji, testování a aplikací platforem pro studium mikroorganismů schopných přímé výměny elektronů s elektronickými zařízeními. Druhá část práce se věnuje elektrické stimulaci kmenových buněk pro jejich řízenou diferenciaci. Dále se zabývá fundamentálním studiem potenciálně škodlivých faradaických reakcí, ke kterým dochází v průběhu stimulačních protokolů používaných v klinické praxi.

Všechny popsané projekty sdílí společné teoretické a praktické základy vycházející z chemického inženýrství, elektrochemie a materiálových věd. Sjednocující faktor hrající zásadní roli a objevující se napříč všemi projekty je skupina reakcí souvisejících s redukcí kyslíku. Redukce kyslíku je nezbytná reakce odehrávající se v katodovém poločlánku zařízení pro stadium elektroaktivních mikroorganismů. Redukce kyslíku a následná produkce reaktivních forem kyslíku může mít diskutabilně větší vliv na diferenciaci kmenových buněk pomocí elektrické stimulace než samotná elektrická stimulace. V neposlední řadě reakce související s redukcí kyslíku byly hlavními reakcemi, které jsme pozorovali při aplikaci standardních stimulačních protokolů.

Disertace prezentuje stručný teoretický úvod nezbytný pro pochopení prezentovaných projektů. Definuje cíle a prezentuje výsledky formou komentovaného seznamu vědeckých publikací. Rovněž nastiňuje budoucí směřování práce.

Hlavní dosažené výsledky mohou být shrnuty následujícím způsobem: Prvním cílem bylo vyvinout platformu založenou na poli mikrobiálních palivových článků pro elektrochemickou charakterizaci elektroaktivních mikroorganismů. Po sérii testovacích prototypů byla vyvinuta platforma splňující všechny předem určené parametry. Platforma se osvědčila jako dostatečně přesná a spolehlivá pro zamýšlené biologické experimenty.

Dalším cílem bylo vyrobit platformu pro řízenou diferenciaci kmenových buněk pomocí elektrické stimulace. Bohužel připravená platforma se ukázala jako nespolehlivá a nevhodná pro daný účel. To vedlo k neúspěšné snaze o diferenci kmenových buněk požadovaným směrem.

Nakonec jsme se zabývali reakcemi souvisejícími s redukcí kyslíku na elektrodách připravených z nejčastěji používaných materiálů pro neurální stimulaci. Kyslík může být redukovaný na vodu a na peroxid vodíku v závislosti na katalytické aktivitě daného materiálu a charakteru stimulačního protokolu. Změřili jsme množství redukovaného kyslíku a produkovaného peroxidu v blízkosti stimulačních elektrod při aplikaci standardních stimulačních protokolů. Následně jsme porovnali katalytickou aktivitu všech materiálů vzhledem k množství redukovaného kyslíku a produkovaného peroxidu vodíku. Hlavním zjištěním bylo, že všechny elektrodové materiály a všechny testované stimulační protokoly vedou k redukci kyslíku, v některých případech až k lokální hypoxii a všechny materiály generují peroxid vodíku, některé až v řádech jednotek mM. Tyto zjištění považujeme za velmi významné, jelikož ovlivnění koncentrace kyslíku a generace peroxidu vodíku mohou mít výrazný vliv na tkáň v okolí elektrod.

KEYWORDS

Bioelectronics, Microbial Fuel Cell, Electrical stimulation, Stem cell differentiation, Oxygen reduction, Hydrogen peroxide evolution

KLÍČOVÁ SLOVA

Bioeletronika, Mikrobiální palivový článek, Elektrická stimulace, Diferenciace kmenových buněk, Redukce kyslíku, Evoluce peroxide vodíku

BIBLIOGRAPHIC CITATION:

EHLICH, J. *Novel devices and materials for bioelectronics*. Brno, 2022. Dizertační práce. Vysoké učení technické v Brně, Fakulta chemická, Ústav fyzikální a spotřební chemie. Vedoucí práce doc. Ing. Ota Salyk, CSc...

DECLARATION:

I declare that the dissertation thesis has been worked out by myself and that all the references from the used literary sources are accurate and complete. The content of the dissertation thesis is the property of the Faculty of Chemistry of Brno University of Technology and all commercial uses are allowed only if approved by both the supervisor and the dean of the Faculty of Chemistry, BUT.

PROHLÁŠENÍ:

Prohlašuji, že jsem dizertační práci vypracoval samostatně a že všechny použité literární zdroje jsem správně a úplně citoval. Dizertační práce je z hlediska obsahu majetkem Fakulty chemické VUT v Brně a může být využita ke komerčním účelům jen se souhlasem vedoucího disertační práce a děkana FCH VUT.

Ing. Jiří Ehlich

ACKNOWLEDGEMENT

The path of my Ph.D. studies was not a simple and straight forward. Nevertheless, I had a lot of fun and created bunch of close friends on the way. I would like to thank all the friends and colleagues who helped me on that way:

My supervisor **Ota Salyk** for allowing me the full independence in my pursuits. The head of Organic Electronics group **Martin Weiter** for providing resources and support for some of my activities. To **Matouš Kratochvíl**, **Standa Stříteský** and **Michal Hrabal** for helping me when needed as well as for highly sophisticated discussions over coffee and beer. **Ivaylo Zhivkov** for being exceptionally helpful with many hardware projects and co-supervision of my students. **Eva Šafaříková** for having sometimes difficult collaboration with us and for organizing many sport and social activities at the Biophysics institute. My students **Vojta Florián** and **Nikola Runštuková** for the help needed to finish some of the projects.

To **Lukasz Szydlowski** for a very fruitful collaboration. Inside out Japanese experience and proper introduction to the Polish culture. Also, to other friends and colleagues from the Okinawa Institute of Science and Technology.

To my current friends and colleagues from the Bioelectronics Materials and Devices group at the CEITEC, especially to **Marie Jakešová** for being my Gin & Tonic partner in crime and to **Eric Glowacki** for being always helpful, supportive, and full of ideas.

Part of this work was done with the support of research infrastructure CzechNanoLab (ID LM2018110, MŠMT, 2020–2022), CEITEC Brno University of Technology.

TABLE OF CONTENTS

1 INTRODUCTION

Bioelectronics is a multidisciplinary field merging engineering disciplines with life sciences and medicine. It involves integration of electrical and biological systems on all possible levels from biomolecules, cells, organs to whole organisms in all life domains. The motivation lies in the ability to "read" biological signals, process them, understand them, and "write" to them if needed. All this is done using primarily electrical means of communication.

Bioelectronics is closely entangled with related disciplines like biosensor research, electrophysiology, neuroscience, neural engineering, organic electronics, and others. Altogether this discipline has generated many devices and methods used today in everyday life. Glucose monitors with insulin pumps, cochlear implants, cardiac pacemakers and defibrillators are among the examples with the largest impact at present. Many other exist and many more are under development with a strong promise to treat many health conditions and even enhancing our current abilities and creating capabilities our species never had.

This thesis focuses on the "writing" aspect. The ability to write, respectively trigger desired physiological response is in the bioelectronics field accomplished by direct electrical stimulation of targeted cells or tissues. This is contrary to application of chemical signals by pharmacology. Part of the thesis will be dealing with safety aspects of electrical stimulation. We will examine irreversible chemical reactions which might be occurring at the electrode surfaces when the standard "safe" stimulation protocols are being applied. We will also apply electrical stimulation to stem cells in order to control their differentiation.

Another part of the thesis will be focused on relatively niche topic related to the study of electroactive microorganisms, specifically development of novel tools for their research. The subject of electroactive microorganisms is currently more of a scientific curiosity because of the rare ability of specific microorganisms to conduct electric currents over long distances. Research of such phenomena has not led to broad industrial applications, but it brings a promise of new conductive bio-materials and a new generation of biosensors.

2 ELECTROCHEMICAL CHARACTERIZATION OF ELECTROACTIVE MICROORGANISMS

Microorganisms able to generate electric currents have been in the scientific interest since their discovery by Potter in 1911. [1] However, no practical advances were made because of the necessity of external chemical compounds (electron shuttles) to mediate transfer of electrons between microorganisms and electrodes, until the 1999 breakthrough when Kim et al. discovered mediators were not necessary. [2][3]

Since then, microorganisms capable of electron transfer with external electrodes lacking the necessity of artificially added electron shuttles became the cornerstones of Bioelectrochemical Systems (BESs) - a category of technologies which spreads from Microbial Fuel Cells (MFCs) for power generation to Microbial Electrolysis Cells (MECs) for hydrogen or methane production Microbial Electrosynthesis Cells (MESs) for production of biofuels and other valuable chemicals and Microbial Desalination Cells (MDCs) to various other technologies, for heavy metal remediation, biosensing and other applications. [4]

Electroactive microorganisms that are able to transfer electrons to the electrode are called electrogens whereas organisms capable of accepting electrons from the electrode are called electrotrophs. [5] Electromicrobiology studies such organisms, their properties, interactions within themselves and between microbes and electrodes, as well as fundamental mechanisms behind the charge transfer inside such systems. [6] Mechanisms behind the charge transfer within biofilms of electroactive microorganisms are not yet fully understood (2.2.1), however, conductive and semiconductive properties of such biofilms have been observed. [7]

Microbial Fuel Cells were the beginning of all the BESs and now this technology is the most understood. It became popular among scientists for its potential as a renewable energy source. Later on, it became obvious that MFCs would not become competitive enough and would be useful only for niche applications such as power sources for deep sea sensors. [5] Nevertheless, MFCs are still essential devices for studying electroactive microorganisms in order for them to be used more optimally in the above-mentioned applications.

The rest of the chapter focuses on MFCs, their working principles, architectures, used materials as well as electrogenic microorganisms and their unique charge transfer mechanisms. It presents sufficient theoretical background for the practical part of the thesis focused on the development and the implementation of the platform for high throughput screening and characterization of electrogenic microorganisms based on multi-well arrays of MFCs.

2.1 Microbial Fuel Cell

An MFC is a device in which electrogenic bacteria can, under specific conditions, respire electrons directly to the anode to close the respiratory chain when no terminal acceptor of electrons is present. Electrons then pass through the external circuit to the cathode where the reduction of the terminal acceptor of the electrons occurs. This flow of electrons generates electric power which can be used as work.

MFCs thus consist of an anode and a cathode. Both electrodes are placed inside anodic and cathodic chambers and are connected by a load resistor (Figure 1). Both chambers are usually separated by a membrane permeable to protons. In the anodic chamber, electrogenic bacteria are growing on the surface of the anode, forming a biofilm. Under anaerobic conditions, the

bacteria are oxidizing organic substrates such as glucose, producing CO_2, protons, and electrons. Protons are diffusing out of the microbes into the solution and further diffuse through the membrane to the cathode compartment. Electrons are transferred to the anode by mechanisms described later (2.2.1) and flow through the outer electrical circuit to the cathode. At the cathode, protons diffused from the anode chamber, electrons from the external circuit, and terminal acceptor of electrons - in this case oxygen - all combine while forming water. Designs of the MFCs could differ from the Figure 1 as well as terminal acceptor of the electrons can be different. (2.3)

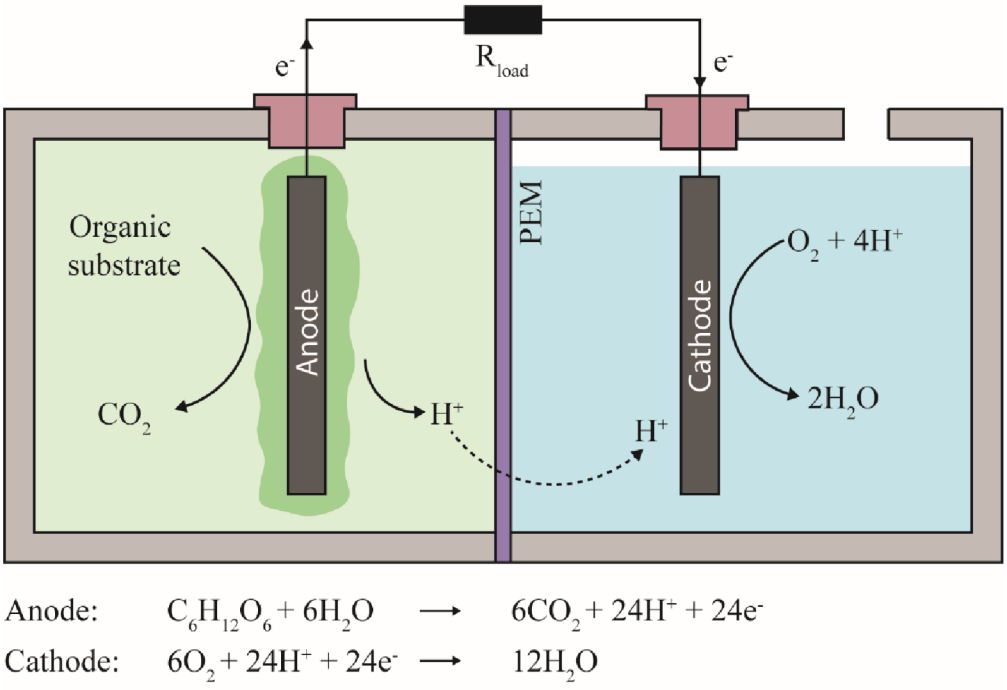

Figure 1: Schematic representation of a dual-chamber MFC. Electrogenic microorganisms in the anode chamber transfer electrons gained from oxidizing organic substrate to the anode by the mechanisms described in (2.2.1). During this process, carbon dioxide and protons are produced. Protons diffuse through the Proton Exchange Membrane (PEM) into the cathode chamber. Electrons flow from the anode through an external conductor and a load to the cathode where they combine with protons and oxygen forming water.

Maximum power produced by an MFC (P) is a function of the electric current (I) and voltage (U). (1)

$$P = U \cdot I \tag{1}$$

Electric current is related to the amount of substrate and bacteria in the anodic chamber and bacterial capability of transferring the charge to the anode known as **Coulombic efficiency** which is a ratio between theoretical number of coulombs stored in the organic substrate and the actual number of coulombs transferred to the anode. Coulombic efficiency decreases with the utilization of the alternative terminal electron acceptors present in the anodic chamber which could be part of the substrate or diffusing into the chamber. Other factor lowering coulombic efficiency is bacterial growth and other microorganisms in the anode consortia without electrogenic ability, which use the substrate for fermentation and(or) methanogenesis. [8] The

theory behind the voltage generated by MFCs is more complex and is described in the following chapter.

2.1.1 Voltage generation

In standard chemical fuel cells such as the hydrogen one, the maximum theoretical voltage is easily determined from a difference of standard redox potentials of the half-cell reactions (2)(3). Theoretical voltage for the hydrogen fuel cell is thus 1.23 V. [9]

Anode:	$H_2 \rightarrow 2H^+ + 2e^-$	$E^0_{an} = 0.00\ V\ (vs. SHE)$	(2)
Cathode:	$O_2 + 4e^- + 4H^+ \rightarrow 2H_2O$	$E^0_{cat} = 1.23\ V\ (vs. SHE)$	(3)

MFCs are, however, more complicated. In the anode compartment many substrates can be oxidized with various standard redox potentials. Similarly, in the cathode compartment several terminal electron acceptors could compete. Concentrations of both substrates and electron acceptors varies in time. On top of that the microorganisms in the cell could dynamically change their counts and composition which greatly influences half-cell potential. Because of these factors it is very difficult to correlate measured voltages with theoretical maximum cell voltage even when pure cultures and controlled substrates are used.

Nevertheless, thermodynamics sets limits to such systems and helps us understand what maximum voltages could be theoretically obtained in MFCs using known electron donors (substrates) and terminal electron acceptors (oxidizers). This knowledge helps us discover factors limiting actual cell voltage and improve cell performances.

MFCs can generate voltage only if the sum of all reactions is thermodynamically favorable. This is usually evaluated by the Gibbs free energy ΔG (J). In the case of MFCs it is preferable to use electromotive force E_{emf} (V) instead (4). [8]

$$E_{emf} = E^0_{emf} - \frac{RT}{nF} \ln (Q) \tag{4}$$

E^0_{emf} (V) is standard cell electromotive force, calculated for standard conditions (298.15 K, 1 M concentration for involved species and 1 bar pressure), R (8.314 J mol^{-1} K^{-1}) is the universal gas constant, T (K) is the temperature, n is the number of electrons involved, F ($9.649 \cdot 10^4$ C mol^{-1}) is Faraday's constant and Q (unitless) is the reaction quotient given by the activities of the products over activities of the reactants. For a positive E_{emf} value, the reaction is favorable and E_{emf} is equal to the maximum theoretical cell voltage.

Anode:	$2HCO_3^- + 8e^- + 9H^+ \rightarrow CH_3COO^- + 4H_2O$	$E^0_{an} = 0.19$ V	(5)
Cathode:	$O_2 + 4e^- + 4H^+ \rightarrow 2H_2O$	$E^0_{cat} = 1.23$ V	(6)

To determine the cell E_{emf} we need to know the half-cell reactions. Considering a simple system using acetate as substrate oxidized by bacteria (5) and oxygen as terminal acceptor of electrons (6). The standard redox potentials for such reactions and most other biological reactions could be found in the literature. [10] From the half-cell reactions and their standard redox potentials Standard Electrode Potentials could be calculated (7))(8).

Anode:

$$E_{an} = E^0_{an} - \frac{RT}{8F} \ln \left(\frac{[CH_3COO^-]}{[HCO_3^-]^2 [H^+]^9} \right) \tag{7}$$

Cathode:
$$E_{cat} = E^0_{cat} - \frac{RT}{8F} \ln\left(\frac{1}{pO_2[H^+]^4}\right) \quad (8)$$

Overall E_{emf} is given by equation (9). Which results in $E_{emf} = 0.805 + 0.296 = 1.101\,\text{V}$ ($HCO_3^- = 5\text{mM},\ pO_2 = 0.2,\ pH = 7$). [8]

$$E_{emf} = E_{cat} - E_{an} \quad (9)$$

Maximum theoretical voltage generated by an MFC with acetate and oxygen couple would thus be 1.1 V. This value can differ based on the substrates and electron acceptors present between 0 to 1.2 V. Such values should be measurable when the MFC is left at the open circuit potential (both electrodes are disconnected) until the equilibrium state is reached. This is called **Open Circuit Voltage (OCV)**. In an ideal state OCV should be equal to E_{emf} but in reality OCV never reaches values of E_{emf} due to internal loses (2.1.1.1). Typical OCV values for MFCs range between 0.2 to 0.6 V, in highly optimized systems, OCV can slightly exceed 0.8 V. [11]

2.1.1.1 Factors decreasing cell voltage

The first noticeable voltage drop occurs between theoretical E_{emf} and measured OCV (Figure2). Unlike in traditional chemical fuel cells, in MFC, bacteria act as a living catalyst for oxidation of organic substrates and as a living organism that needs its share of energy for metabolic functions. Electrons from a substrate must pass through a chain of respiratory enzymes inside the bacteria and only then can be transferred to the electrode. During this process a part of the energy is lost which results in the difference between E_{emf} and OCV. [12][13]

The next voltage drop occurs when a load is connected to a cell and current starts to flow. Three distinct regions are observed (Figure2). In the first region under high external resistance, currents are low, and voltage is dropping rapidly (I.). Overpotential and Activation losses are dominant in this region. The second region of linear voltage drop at intermediate currents is attributed to ohmic losses (II.). The third region of rapid voltage drop at high currents is due to the concentration loses (III.).

Overpotential and Activation losses arise due to the energy loss for kinetic initiation oxidation/reduction reactions and energy lost due to electron transfer from the terminal microbial enzyme to the electrode. These losses could be improved by higher electrode surface area, more effective catalysis at the cathode, and improved electron transport between bacteria and anode. [13] More about this topic can be found in the chapter dedicated to anode and cathode materials (2.3).

Ohmic losses are caused by the series resistance of all components in the MFC. The anode, the cathode, all the electrical interconnects, the proton exchange membrane (if present) and the electrolyte. These losses are most important to reduce for improving the MFC power efficiency (2.3.4). Ohmic losses could be reduced by using electrodes with low resistivity and good interconnects, by using a low resistivity membrane, by increasing the medium conductivity and decreasing the electrode spacing. [13]

Concentration losses have the most significant influence on the voltage drop at high currents. These losses are caused by insufficient diffusion of the substrate molecules to the electrode or conversely the products from the electrode.

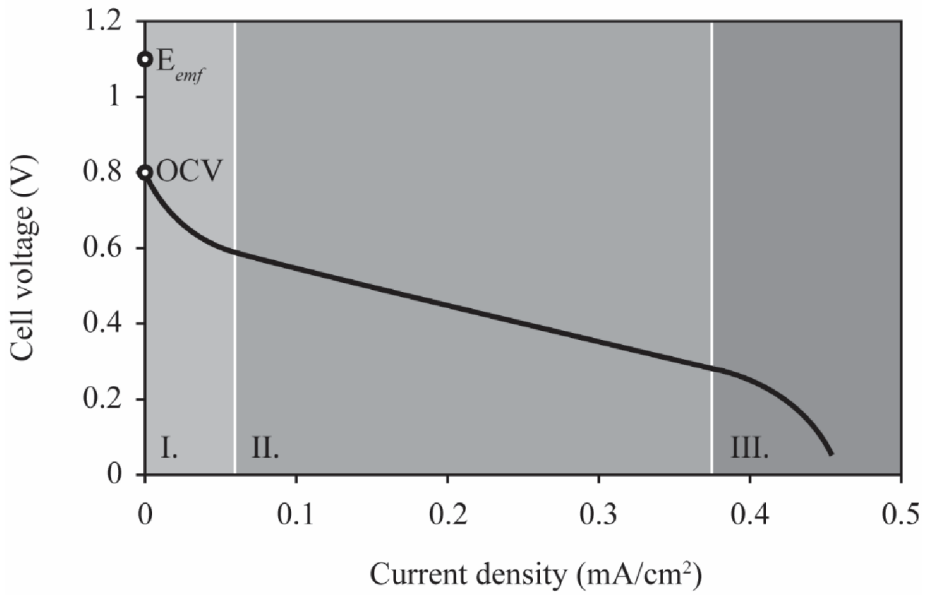

Figure2: Example of polarization curve representing cell voltage and cell current dependence and different types of losses negatively influencing output current.

A linear dependence between the voltage and the current in the middle part of the polarization curve is a typical feature of MFCs. This relationship is described by equation (10). OCV^* represents y-intercept of the extrapolated linear part of the polarization curve. IR_{int} represents sum of all internal losses in the cell which are directly proportional to the current (I) and **Internal resistance** (R_{int}). Internal resistance is an important parameter for the MFC characterization. MFCs which obey linear relationship (10) tend to achieve maximum power outputs when external load resistance (R_{ext}) is equal to R_{int}. [8]

$$E_{cell} = OCV^* - IR_{int} \tag{10}$$

2.1.2 Power generation

An MFC is primarily a device for generation of electric power. Electric power is thus the parameter most commonly used to assess MFCs performance. It is defined as:

$$P = I \cdot E_{cell} \tag{11}$$

MFCs are normally run under constant load, usually a fixed resistor (R_{ext}). Electric current is then calculated using Ohm's law as the voltage drops over the R_{ext}.
Equation (11) gives us a direct measure of electric power under constant load. This measure is not very practical for quantitative comparison of different MFC systems. Because of this, power output of an MFC is always presented as **Power Density** which is usually normalized to the anode surface area, as this is the most limiting factor for power production in the MFCs. In rare occasions, the cathode could be the limiting factor, power in such cases could be normalized to the cathode area. When MFCs are being scaled up for power generation applications, power is normalized to the entire reactor volume. Power density normalized to the anode surface area (P_{an}, $\mathrm{W \cdot m^{-2}}$) is defined by eq. (12). [8] Where A_{an} is surface area of the anode ($\mathrm{m^2}$).

$$P_{an} = \frac{E_{cell}^2}{A_{an} R_{ext}} \tag{12}$$

Similarly to the polarization curve, a **Power curve** is obtained to display the dependence between the cell output power and current or electric load. The power curve is directly calculated from polarization curve and is usually presented as a power density and current density relationship (Figure 3). Starting from the OCP, no current is flowing and no power is being generated. With decreasing load, current starts to flow and the power is rising up until it reaches the maximum. **Maximum power** (P_{max}) output of an MFC is important parameter and is reported when describing MFC performance. After this point, the power starts to decrease due to ohmic, polarization and concentration losses.

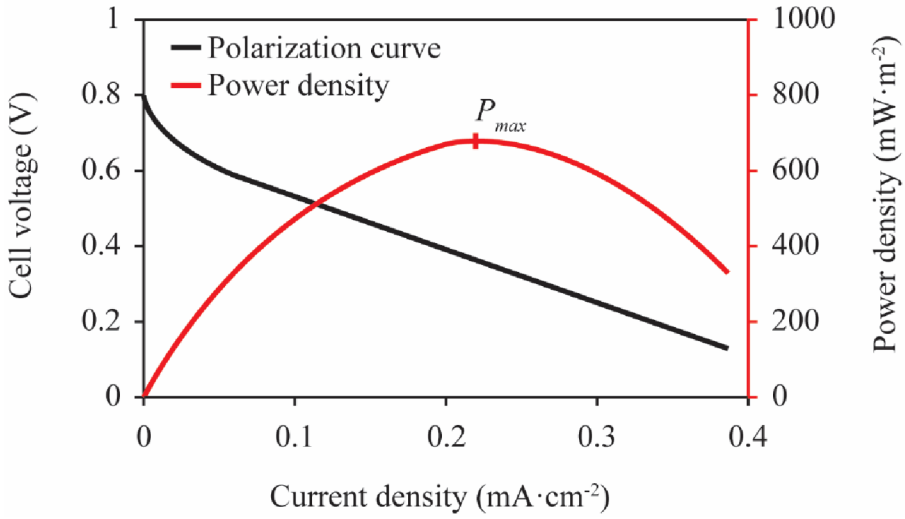

Figure 3: Typical MFC power curve derived from a polarization curve.

Maximum power could be described as a function of OCV, R_{ext} and R_{int} in eq. (13). [13] This equation tells us about the impact of internal resistance on maximum power. The MFC will be producing the maximum power when $R_{ext} = R_{int}$ and the lower the internal resistance, the higher the power produced. Lowering internal resistance should be an important factor taken into consideration when designing a new MFC reactor to optimize power output.

$$P_{max} = \frac{OCV^2 \cdot R_{ext}}{(R_{int} \cdot R_{ext})^2} \tag{13}$$

2.2 Electrogenic microorganisms

A vast number of microorganisms from all domains of life (Bacteria, Archea, Eukaryota) are under the right conditions able to exchange electrons with electrodes. Reasons why microorganisms developed the ability of exocellular and endocellular electron transfer could be described by at least three ways:

Cellular respiration is probably the main reason. In order to survive in anaerobic conditions deep inside the soil and sediment, microorganisms had to learn how to utilize different terminal

acceptors of electrons than oxygen. Electrogenic microorganisms thus developed the ability of reducing solid metal oxides such as Fe^{III} or Mn^{IV} by transferring electrons from terminal oxidase in the respiratory chain directly to the surface of these minerals.

Direct interspecies electron transfer would be another reason. Recently more evidence is being acquired about complex symbiotic and parasitic interactions involving direct electron transfer between microorganisms of the same or different kind. [5] These findings are quite profound because it has been believed that electron transfer between species was mostly intermediated by hydrogen, where electron-donating microorganisms were reducing protons to hydrogen and electron-accepting species were oxidizing hydrogen. [6]

Cell-cell communication is a possible but not yet proven possibility. It is well known that microbial communities are able to communicate through quorum sensing chemicals. This means that some microorganisms can release chemicals to signal environmental changes to other microorganisms. Communication using only electric signals within microbial communities would be highly interesting from a scientific as well as practical perspective. [5]

2.2.1 Mechanisms of electron transfer

As described earlier, many microorganisms including yeast can exchange electrons with BES due to the addition of artificial electron shuttles. Example of such mediators are neutral red, anthraquinone-2-6,disulfonate (AQDS), thionin, potassium ferricyanide, methyl viologen, and others. [13] These molecules can be periodically reduced in the cell cytoplasm and oxidized at the electrode surface. Application of such artificial shuttles is, however, highly impractical because of their often-toxic nature, added costs and their incompatibility with open systems.
Without the addition of artificial electron shuttles, microorganisms can transfer electrons to the anode in three ways (Figure 4): (a) electron transfer by soluble microbially produced or naturally occurring electron shuttles, (b) direct electron transport by specific protein molecules at the cell surface, (c) long range electron transport by conductive pili sometimes called nanowires.

Electron transfer by microbially produced or naturally occurring electron shuttles.
Some species can reduce solid Fe^{III} oxides without being in the direct contact with them by utilizing naturally occurring humic substances as electron shuttles [13] or by releasing its own shuttle molecules, namely pyocyanin and related compounds produced by *Pseudomonas aeruginosa* [16], or flavin molecules produced by *Shewanella* species [17].
The role of flavins was well described for *Shewanella oneidensis* by electrochemical studies. [18] This mostly planktonic species produces flavins, which can be reduced at the cell surface by c-type cytochrome MtrC, which is a part of a protein complex spanning from cytoplasm to the outer cell surface. This protein serves as flavin reductase and can directly transfer electrons to the anode when they are in direct contact, but the rates of electron transfer directly to the anode are an order of magnitude lower than in the case when flavins act as electron shuttles. [18]

Direct electron transport by specific protein molecules at the cell surface.

Direct electron transport has been observed and proved for several microorganisms, *Geobacter sulforreducens* being studied most extensively. [19] This species did not exhibit electron transport via shuttle molecules. Instead, *Geobacter* species produces a variety of c-type cytochromes. These proteins are often exposed on the outer surface of the cell membrane which allows them to be an electron-gate between electrodes and the cell cytoplasm when bacteria form a biofilm on an electrode surface. These proteins have been examined by many purification, electrochemical, and gene deletion methods which proved their ability of transferring electrons between themselves as well as between cytochromes and electrodes. [19] Recently, a detailed structure of cytochrome protein complex has been revealed. [20] The structure resembles naturally produced isolated molecular wire spanning from the cytoplasm through the lipid membrane to the exterior of the cell. The conductive path consists of closely spaced heme molecules forming a chain through the center of the protein complex and spanning out forming high surface area at the end exposed to the environment for more convenient electrical connection to the outside environment.

Long range electron transport by conductive pili.

Electrogenic microorganisms tend to produce pilus-like appendages in the electron-acceptor limited environments. It has been proved that these 3-5 nm thick, tens of microns long appendages are electrically conductive and provide an efficient path for electron transfer between microorganisms and their environment. Their conductivity was first confirmed in the z-plane using scanning tunneling microscopy (STM) [14] and later also along their length by two independent methods: By microfabricated electrodes deposited over the pili structures and by deposition of a microelectrode over pili structure, or by scanning the pili over their length using conductive probe atomic force microscope. From I-V curves obtained from both measurements, the resistivity of the pili was determined in the order of $1\,\Omega \cdot \mathrm{cm}$. [21] Later measurements determined electron transport rate of $9 \cdot 10^8$ electrons per second at 100 mV bias, enough to support respiratory rate of the cell. Resistivity of $0.23 - 0.70\ \Omega \cdot cm$ and carrier mobility of $3.2 \cdot 10^{-2}\ \mathrm{cm^2 V^{-1} s^{-1}}$. [22] Such values are in the order similar to the organic semiconductors. [23]

Interestingly, these studies [14][21] also revealed conductive pili in non-electrogenic species as photosynthetic cyanobacteria and fermentative bacteria, which suggests that microbial "nano wires" could be a common strategy of electron transfer and energy distribution between microorganisms.

Conductive microbial nanowires are composed of type IV pili a cluster of approximately 30 genes with embedded c-type cytochromes. [24] Cytochromes are believed to intermediate the electron transfer between the nanowire and outside environment, but they are probably not responsible for the conductivity along the wire due to their large spacing of 1-2 nm. However, they are necessary for sufficient electron transport. Mutants lacking cytochromes displayed poor conductivity. [14] Mechanism behind the conductivity along the pili length is attributed to the electron hoping between aromatic amino acids in the pili structure. [22] Mutants lacking aromatic amino acids in the core pili structure decreased their conductivity by 90 percent, but

they remained conductive. [25] This suggest more complex mechanism behind the conductivity of the pili structure which has not been fully understood yet.
Electrogenic microorganisms often form biofilms tens of micrometers thick at the electrode's surfaces. SEM images show dense networks of microbial nanowires connecting many of the bacteria. It has been shown that such biofilms are conductive ($5\,mS \cdot cm^{-1}$) due to the connection through microbial nanowires and can conduct current to centimeter-long distances. [26]

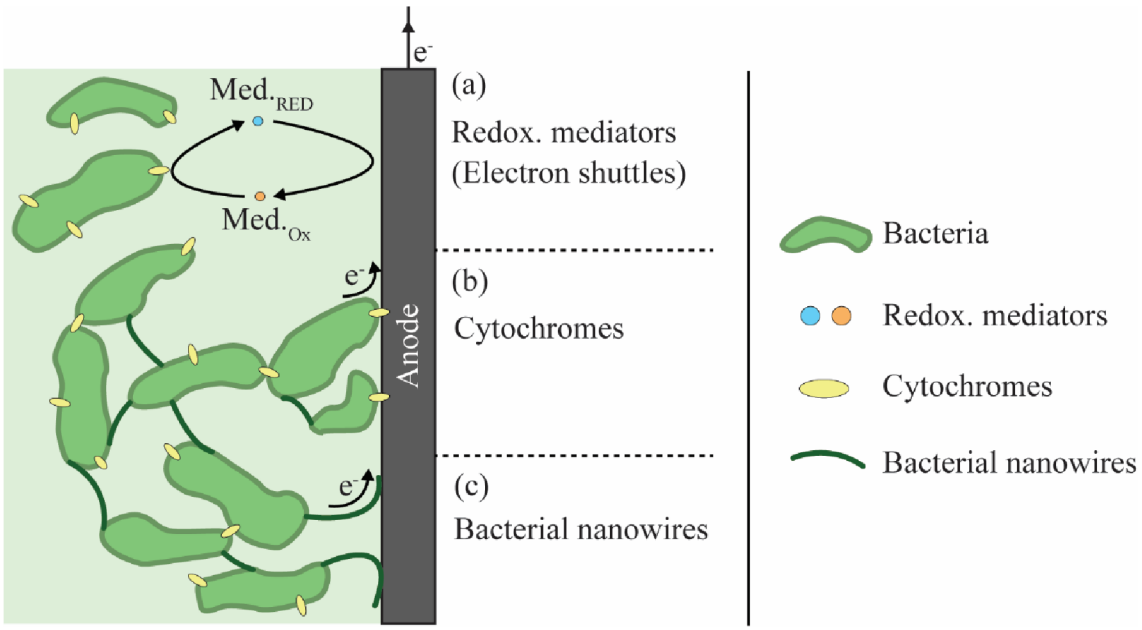

Figure 4: Illustration of three different electron transport mechanisms between electrogenic microorganisms and electrodes via: (a) electron shuttles, (b) cytochromes in the cytoplasmic membrane, (c) bacterial nanowires. [14]

MFCs can be inoculated by a pure culture of one microorganism species or with rich and diverse inoculum. The highest power densities are always achieved with mixed cultures rather than with isolates. [27] Considering, different species prefer different electron transfer mechanisms, MFCs with mixed cultures will be exchanging electrons by multiple mechanisms described earlier.

2.3 Materials and architectures

As mentioned previously, MFCs consist of three key components: an anode, a cathode, and a membrane. Each of the components has specific requirements for its function which can be fulfilled by various materials.
The Anode, the cathode, and the membrane are then arranged in a way to form a functional MFC. The arrangement can differ based on the application and nature of organic substrate and terminal acceptor of electrons. Most used materials and architectures will be described in the following sections.

2.3.1 Anodes

Key requirements for the anode materials are high conductivity, high porosity (specific surface area), corrosion resistance, biocompatibility, and antifouling properties. This sum of

requirements rules out many materials. The remaining applicable ones can be divided into two groups: carbon and non-carbon materials.

Non-carbon materials did not receive much appreciation within the BES community and are used in the minority of applications probably due to their higher cost, more difficult processing, biocompatibility, and corrosion resistance issues. Suitable materials from this category are gold, silver, copper, nickel, cobalt, titanium, and stainless steel.

Some of these materials were benchmarked against graphite standard with maximum average current density ($984\ \mu A \cdot cm^{-2}$). This value was exceeded by copper ($1515\ \mu A \cdot cm^{-2}$) followed by gold ($1175\ \mu A \cdot cm^{-2}$) and silver ($1119\ \mu A \cdot cm^{-2}$). Stainless steel ($674\ \mu A \cdot cm^{-2}$) and nickel ($384\ \mu A \cdot cm^{-2}$) performed worse. [28]

Copper and silver may be surprising anode materials for BES applications. They are believed to have antimicrobial properties. However, it has been demonstrated that electrogenic microorganisms can form viable biofilms on their surfaces. [28]

Carbon based materials are generally preferred as anodes in BES. Carbon is highly versatile material which can be used in many forms. Graphite can be used as plates, rods, or granules with defined surface area, good conductivity, excellent biocompatibility, and corrosion resistance. Carbon is also used in various other fiber forms such as cloth, felt, paper, foams, or brushes. These forms of carbon have higher surface area, which is proportional to the resulting current densities. Highest current densities are achieved with carbon felt followed by carbon foam, carbon paper, and unmodified graphite. [29]

The above-mentioned carbon materials can be successfully used in their original form, or they can be modified to achieve higher current densities. Many strategies have been tried [8]. Most efficient being pretreatment of the carbon cloth with ammonia gas leading to an increase of power production by 48% and reduction of the start-up time by 50%. [30] Modern strategies focus on utilization of conductive polymers and nanomaterials such as various forms of carbon nanotubes or graphene. [31][32]

2.3.2 Cathodes

Choice of the cathode material depends highly on the main terminal acceptor of the electrons and the architecture of the MFC. Generally, most of the above-mentioned anode materials can also be used as cathode materials.

Least number of requirements on the cathode material is demanded when aqueous catholytes containing ferricyanide, hexacyanoferrate, or permanganate are used. These chemicals are often used as terminal acceptors of electrons due to their low overpotentials at the carbon-based cathodes. The main disadvantages of these chemicals are the necessity of periodic replacement with fresh unreduced catholyte and their toxic nature. [8]

Due to these disadvantages, oxygen is the most preferred terminal acceptor of electrons in MFCs.

Oxygen is freely available in the air and can be delivered to the cathode by aeration of the catholytes or by using a so-called air cathode (Figure 5). Oxygen can by directly reduced at the carbon-based cathodes. The rate of oxygen reduction on the plain carbon cathodes is often not sufficient, so cathodes are modified with platinum catalyst to increase the reduction rate by factor of 10 approximately. [13]

Air cathodes are facing catholytes with one side and air with the other. These cathodes do not require aeration or periodic exchange of the catholyte. Because of this, air cathodes are the most popular. However, engineering of such cathodes is not a trivial task. Electrons in the electrode (solid phase), protons in the catholyte (liquid phase), and oxygen in the air (gas phase) must all meet at the catalyst in this three-phase reaction. The catalyst must be supported by a conductive material which must be both exposed to air and water, prevent leakage of catholyte out of reactor, and excessive diffusion of oxygen into the reactor. Materials meeting such requirements are carbon cloth, paper, or fine metal mesh. Most used material is the carbon paper, which can be purchased preloaded with platinum catalyst and treated with Teflon coating preventing catholyte leakage.
A long-term effort among the scientists working on the cathode optimization is replacement of the platinum with a cheaper catalyst. Main research centers around boron nitride, molybdenum disulfide, and various forms of doped or modified graphene. [31][32]

2.3.3 Membranes

The membrane in MFCs separates anodic and cathodic parts. It prevents terminal acceptor of electrons getting in the proximity of microorganisms which would lead to the decrease of coulombic efficiency and allow transport of protons from anodic part to the cathode. This selective transport of protons is achieved using Proton Exchange Membranes (PEM), or Cation Exchange Membranes (CEM). Most commonly used PEM is commercially available membrane Nafion (Dupont Co. USA). Nafion can be purchased in the form of solid polymer foils or in a liquid form which can be coated to desired surfaces. Nafion is sulfonated polytetrafluoroethylene (sulfonated PTFE, known also as Teflon, Dupont Co. USA). Sulfonyl groups attached to the PTFE backbone allow the polymer to be solvated in the aqueous environment and conduct protons in highly selective manner. Nafion conducts protons with high efficacy and thus does not add much to the internal resistance of the MFC. Nafion also acts as a good barrier preventing terminal acceptors of electrons such as ferricyanide to diffuse in the anode chamber. It does not limit the diffusion of oxygen entirely but well enough to be most widespread PEM in MFCs as well as standard fuel cells.
Although Nafion is a favorite material, it is also expensive (up to $1400\ \$ \cdot \mathrm{m}^{-2}$) [13]. Due to high cost of Nafion, cheaper alternatives based on different sulfonated polymers and other strategies exist or are being explored by various researchers. [32]

2.3.4 Architectures

The majority of MFC designs are based on two simple architectures: **two-chamber** (Figure 1) and **single chamber with air-cathode** (Figure 5). Resulting MFC designs differ based on the application, spanning from small batch reactors for basic material, and biological research in laboratories to large flow reactors for wastewater treatment. [8][13]
Two-chamber MFCs are logically composed of two chambers (anodic and cathodic) separated by the PEM. It is a simple design often used in research laboratories because a standard H-Cell can be used instead of the more complex custom designs. H-Cells allow simple exchange of membrane and electrode materials, which are highly useful features in basic materials research. Many different terminal acceptors of electrons could be used in the cathodic chamber such as ferricyanide, hexacynoferrate, permanganate, or simply purging the cathode chamber with air

for oxygen delivery. Two chamber design usually displays high internal resistance due to the large electrode spacing which limits the resulting current densities. This can be partially compensated by using electron acceptors with low overpotential like ferricyanide, however, as mentioned earlier, such electron acceptor has to be periodically replaced or electrochemically regenerated which is not very practical. MFCs with double chamber design using dissolved oxygen in the cathodic chamber generally does not produce high current densities.
Higher current densities using oxygen as terminal electron acceptor are achieved using single chamber air-cathode architecture. These designs are composed of a single chamber with anode and anolyte. Cathode forms a part of reactor where one side of the cathode faces the interior of the reactor and other side faces the exterior of the reactor. Oxygen then meets the exterior part of the cathode. Such an architecture has a great advantage due to the unlimited availability of the oxygen in the air. No other chemicals than substrate must be added to the MFC to generate electric current. PEM in this architecture also acts as a barrier to prevent anolyte leakage out of the cell, because cathode has to be porous to allow a three-phase reaction and without a membrane, the anolyte would sieve through the cathode over time. Single chamber air-cathode MFC also displays low internal resistance because cathode and anode can be closely spaced. However, the PEM usually does not entirely prevent oxygen diffusion into the anolyte which results in lower coulombic efficiency when electrodes are too close.

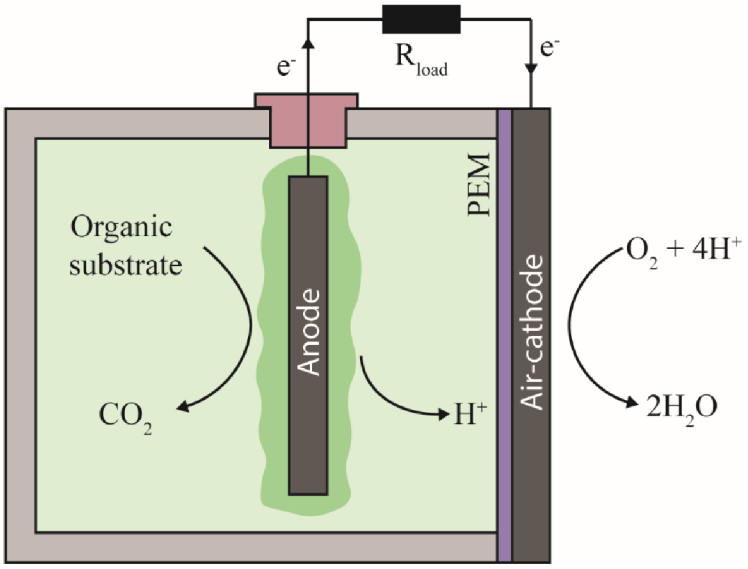

Figure 5: Single chamber air-cathode MFC. Air-cathode forms one or more sides of the reactor which supports oxygen from the atmosphere to be used as the terminal acceptor of electrons.

Poised potential reactors are special types of reactors designed for fundamental studies of electrogenic microorganisms. Instead of generating power, poised potential reactors are using a potentiostat as an outside power source [27]. Potentiostatic control allows to operate the reactor under chronoamperometric conditions. The anode is set to a constant potential, allowing efficient electron transfer between microorganisms and anode while on the cathode hydrogen is evolved. This type of reactor requires a reference electrode in the anode chamber. Architecture of such reactors is usually simple two-chamber (h-cell). Electrode materials are

usually similar to other standard MFCs. The main advantage of such reactors is the precise control of the anode potential which allows to test electrogenic microorganisms at conditions which are not well defined or possible in standard MFCs. Microorganisms at such conditions can achieve current densities which are not limited by the reactor limiting factors, such as R_{int}. On the other hand, each reactor requires its own potentiostat which adds the cost up significantly and limits the number of parallel experiments.

2.4 Electrical and electrochemical characterization methods

As mentioned earlier, when characterizing MFCs from electrical/electrochemical point of view, there are several variables which can be measured to provide important insight into the performance and properties of the reactor and electrogenic microorganisms.

OCV can be obtained directly by measuring the voltage difference between the electrodes at open circuit conditions. **Electrode potentials** can be measured against a reference electrode. [8]

Electric current is usually obtained by measuring voltage drop over the load resistor and calculated from Ohm's law. The **Polarization curve** and subsequently the **Power curve** can be measured by linear sweep voltammetry using a potentiostat by slowly sweeping the potential ($1\ mV \cdot s^{-1}$) between the end values while measuring current [34]. When a potentiostat is not available, a series of load resistors could be inserted ranging from high (megaohms) to low (ohms). Current is again calculated from Ohm's law. **Maximum power** (P_{max}) can be directly taken as a maximum of the Power curve. [8][13]

Internal resistance (R_{int}) could be determined by several ways [34][35]. It could be read as the resistance at P_{max}. It could be derived from the slope of the linear part of the polarization curve. More precisely it can be obtained from the current interrupt method [36] or Electrochemical Impedance Spectroscopy (EIS) which is a powerful but complex technique for MFC characterization. [37]

Coulombic efficiency can be calculated as a ratio between theoretical number of coulombs stored in the organic substrate and actual number of coulombs transferred to the anode obtained by integrating the current passed over the given batch cycle. [8][13]

Presence and nature of the microbially produced electron shuttles can be precisely studied by **Cyclic Voltammetry** [38]. Cultivation under chronoamperometric conditions in **Poised potential reactors** can be used to determine maximum achievable performance of studied microorganisms. [29]

2.5 High throughput screening and analysis of electrogenic microorganisms

Up to this date, there is no single unified and standardized MFC design. All groups in the field rely on custom made reactors which significantly vary in design and used materials. Power produced by electrogenic microorganisms differs based on the electrode materials, spacing, PEM type, reactor design and many other variables. Therefore, it is almost impossible to compare electrogenic microorganisms based on the produced power unless they are benchmarked in the same reactor architecture.

Benchmarking in the same type of reactor is possible but the nature of biological experiments requires many replications for the same experiment to be done which greatly increases the number of reactors needed. On top of that custom-made reactors can range from milliliter to many liter scales thus requiring substantial amount of space.
Another issue is the measuring apparatus for electrical and electrochemical characterization. There are commercially available and affordable multichannel dataloggers which can be used for continuous current recordings from many reactors. However, when more advanced electrochemical analysis is required, or cultivation under the poised potentials, most commercial potentiostats do not offer sufficient amount of channels or the price of such systems stems to tens of thousands euro.
Research in the field of electrogenic microorganisms is thus limited by the lack of adequate instrumentation. This is greatly apparent in the field of genetic engineering and synthetic biology which is trying to enhance the mechanisms of electrogenic species and utilize them for number of useful applications. For this field to thrive a standardized high-throughput system able to perform many experiments in parallel is a must.
Because of lack of such standardized systems, there is an effort among scientists and engineers to develop it. The first reported high throughput screening platform for growth monitoring of electrogenic bacteria was developed by Biffinger. [39] Platform was based on two-chamber architecture with nine 500 µl anodic chambers sharing single common cathode and cathodic chamber filled with ferricyanide catholyte. Due to the shared cathode, device displayed low variability in OCP (8%) but the R_{int} was quite high 2.8 kΩ.
Hou [40] developed a platform of 24 two-chamber MFCs with anolyte volume of 600 µl, ferricyanide catholyte and variability in produced power between all the individual cells of 8%. Internal resistance was not reported but based on high load resistor (1 MΩ) used, we can assume similar internal resistance. Later the platform was modified to 24 single-chamber air-cathode architecture. [41] Original two-chamber platform was upgraded with fluidic channels for catholyte and anolyte replenishment. [42]
A lot of subsequent work on MFC arrays has been done by S. Choi's group. First an array of six 1.5 µl two-chamber MFCs was developed. [43] This array displayed very low variability in the OCP of just 1.4%, however, high internal resistance (10 kΩ). Slightly modified version was used to study the effects of light on electrogenic bacteria. [44] Then group's focus moved towards platforms for rapid characterization of electrogenic microorganism from small liquid volumes and rapid characterization times in the order of minutes. Platforms were based on paper reservoirs patterned with wax layers to create hydrophobic and hydrophilic areas preventing mixing of the samples. First platform of this type [45] had 48 wells, two chamber architecture with ferricyanide as catholyte, low variability in OCV between the cells (2.5%). Printed circuit boards (PCBs) were for the first time used in such MFC array to accommodate all electrical connections. Next design [46] used air-cathode architecture with 8 individual cells. Anodic paper reservoir was treated with conductive polymer PEDOT:PSS to lower internal resistance down to 200 kΩ which is still quite high. The variability in OCP was within 1.7% range, however, the OCP itself displayed low values of approximately 100 mV due to the large oxygen diffusion to the anodic compartment. Next design [47] of 96-well platform used solid state electron acceptor Ag_2O on cathodes and again PEDOT:PSS treated paper anode. This device

displayed variability in OCP of 2.8% and issue with oxygen diffusion through air-cathode was eliminated by using Ag_2O solid electron acceptor. This platform was also accompanied with an automated station for polarization curves acquisition based on variable load resistor switchbox controlled by Arduino microcontroller. Previous platforms relied only on voltage measurements. Currents were calculated using Ohms' law knowing the voltage drop over the load resistor.

Absence of available and affordable hardware able to continuously measure currents produced by such multi-well platforms as well as to perform basic electrochemical procedures was partially tackled by Molderez [48][49] who developed a 128-channel potentiostat connected to an electrode array. This setup was able to poise potentials at working electrodes and monitor currents produced by biofilms growing on top of them. Similar approach was pursued by Frank [50] and Kuchenbuch [51] who also developed a platform consisting of 96 electrochemical cells accompanied with 96-channel potentiostat to cultivate microorganisms at chronoamperometric conditions.

3 ELECTRICAL STIMULATION OF CELLS AND TISSUES

Famous experiments using electricity to cause contraction of frog muscles performed by Galvani in 1771 revealed that exogenous electric signals have physiological effects on organisms. [52]. More discoveries followed and unveiled that electricity plays a significant role in our physiological development and bodily functions. Endogenous electric fields and currents are present in subcellular, cellular, tissue, organ, and organism levels and all together are termed as Bioelectricity.

Endogenous electric fields and currents are the result of unique cell membrane properties. The cell membrane acts as a dielectric with embedded ion pumps and selective ion channels. Ion pumps actively move charged ions between extracellular and intracellular environment creating charge imbalance, which results in an electrical potential difference over the cell membrane as well as concentration gradients. Ion channels can be opened when needed giving rise to ionic currents flowing down the potential or concentration gradient. All mature cells develop a potential difference over their membranes and are thus polarized. Cells have a negative polarization relative to the extracellular space and polarization of a cell membrane differs based on the cell type and can vary between negative few millivolts up to negative 100 mV. [53]

Cells aggregate together forming tissues with dedicated functions. Epithelium for example serves as a barrier tissue. Cells in the epithelium are closely packed together and connected by gap junctions. Epithelial cells create trans-epithelial electric fields spanning up to a few hundred $\mathrm{mV} \cdot \mathrm{mm}^{-1}$. It is known that these spatiotemporal electric fields and currents play a critical role during embryogenesis, growth of the organism, tissue repair, and wound healing. [54]

These electric fields are stable or slowly changing in time. Another types of cells produce rapidly changing electric fields. Such cells are called excitable cells and include neurons, myocytes, and some endocrine cells. Excitable cells can rapidly depolarize and repolarize their cell membrane in a process known as action potential (AP). Action potentials can propagate from cell to cell and are the basis of muscle contraction and fast long-range communication within our nervous system.

The electric nature of physiological structures encourages scientists and engineers to develop electronic devices which can tap into such modalities to sense electrical signals, modulate, or initiate them. Bioelectronics is a multidisciplinary field which involves development of such electronic devices and basic research around them. The purpose lies within repairing, restoring, or even enhancing our bodily functions.

Over the decades of research and development many bioelectronic devices found their way out of research laboratories and are routinely used in clinical practice. Great examples are cochlear implants restoring hearing, cardiac pacemakers and defibrillators restoring proper heart functions, deep brain stimulators alleviating symptoms of Parkinson's disease, spinal cord, and peripheral nerve stimulators reducing chronic pain. Many more devices are in the development such as retinal implants to restore vision or brain-machine interfaces allowing bidirectional communication between the person and computer to control robotic limbs.

This chapter will focus on electrical stimulation of both excitable and non-excitable cells. The basis of action potential triggering by safe electrical stimulation as well as the motivation and approaches for non-excitable cell stimulation will be given. Materials used for stimulation electrodes will be listed and electrochemical methods for stimulation electrodes

characterization will be described. All these information should provide sufficient theoretical background for the experimental part of the thesis.

3.1 Direct electrical stimulation of excitable cells

Among the applications of electrical stimulation, excitable cells are the most frequent target. This applies to neurons inside the brain, nerves in the peripheral system, muscles of the heart or cells grown on top of a chip during basic research. All these cells require some kind of stimulus to initiate their action potentials. There are several means of triggering AP like using chemical signals or by application of distant electric or magnetic fields. Focus of this thesis will be only to direct electrical stimulation by charge injection from the stimulation electrode to the cells in close proximity of the stimulation electrode. Before the mechanisms and considerations behind the direct stimulation are revealed, membrane potential and action potential have to be explained in the first place.

3.1.1 Membrane potential

The cell membrane is a centerpiece of cell electrical activity. It is built up of a phospholipid bilayer restricting exchange of the charged particles between both sides of the membrane thus acting as a dielectric (Figure 6). Special protein complexes are embedded into the membrane spanning from the cytoplasm to the cell exterior. These protein complexes have specific functions.

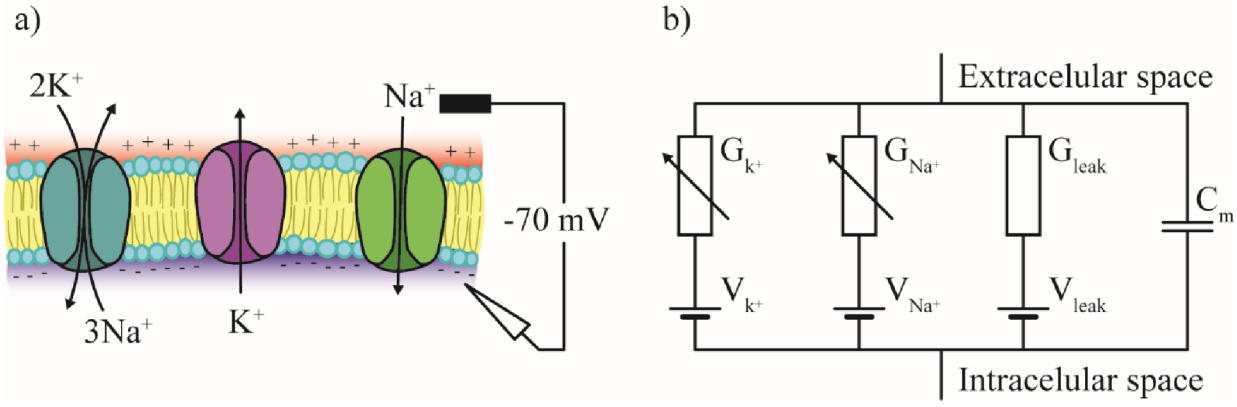

Figure 6: a) Schematic description of the cell membrane consisting of lipid double-layer with embedded sodium-potassium pump, potassium and sodium channels. Charge separation and resting membrane potential are depicted too. b) Equivalent circuit diagram of a cell membrane displaying cell membrane capacitance in parallel with voltage-gated ion channels and leak potassium channel.

One of the complexes, the sodium-potassium pump is an active transport molecular machine responsible for maintaining constant cell polarization. The sodium-potassium pump literally pumps sodium ions from the cell and potassium ions into the cell in exchange for energy in the form of ATP. It does so in a 3:2 ratio against the concentration gradients. More positive charge is pumped out of the cell than it is pumped into the cell. The result is a net negative charge accumulation inside the cell.

Separation of the charges across the membrane reaches an equilibrium state at which the electrochemical gradient is formed. The membrane potential at the equilibrium can be

calculated using a modified Nernst equation known as the Godman-Hodgkin-Katz equation (14). [55]

$$V_m = \frac{RT}{F} ln \frac{p_K[K^+]_o + p_{Na}[Na^+]_o + p_{Cl}[Cl^-]_i}{p_K[K^+]_i + p_{Na}[Na^+]_i + p_{Cl}[Cl^-]_o} \quad (14)$$

V_m is the membrane potential, R, T and F have been already defined for equation (4), p_x is relative permeability of a specific ion and $[ion]_{o/i}$ are concentrations of specific ions outside and inside of the membrane.

The resulting membrane potential is a function of individual ion equilibrium potentials and their different permeability. Table 1 lists the inner and outer membrane concentration for the most significant ions involved in the equilibrium potential and their individual equilibrium potentials derived from the Nernst equation.

The resulting membrane potential lies typically around -75 mV for neurons. It is a membrane potential of the cell at rest, thus also called **Resting membrane potential**.

Table 1: Concentrations of ions responsible for membrane potential inside the cell membrane and outside. Equilibrium membrane potentials for individual ions are listed also. These potentials are calculated from Nernst equation and apply to the condition when only the given ion is present. [55]

Ion	c_i (mM)	c_o (mM)	E_{eq} (mV)
K^+	140	4	-95
Na^+	18	145	+56
Cl^-	7	120	-76

3.1.2 Action Potential

Action potential is a rapid reversible change of the membrane potential. Action potential is initiated by external stimuli in the form of chemical, electrical or other sensory signal like heat or pressure. The membrane potential rapidly shifts from its polarized resting state to the depolarized state and back to the slightly hyperpolarized state from which it is slowly returning to its standard resting state.

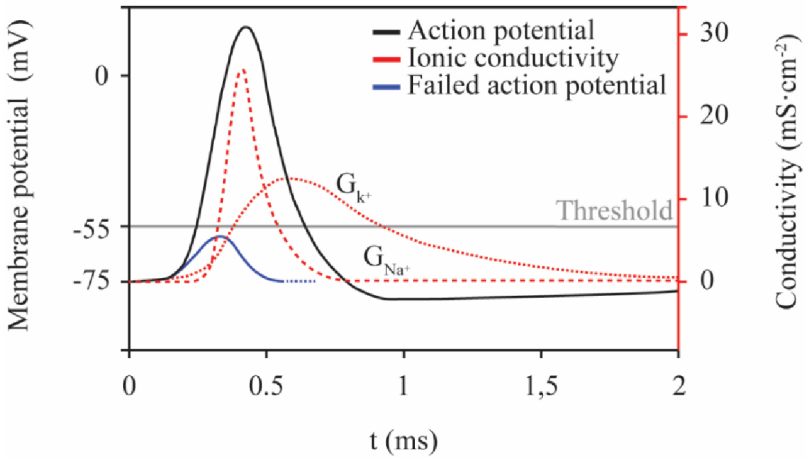

Figure 7: Action potential time dependency with overlapping changes in sodium and potassium channels. Threshold potential and failed action potential due to weak sub-threshold stimuli are also depicted.

The exact mechanism was described by Hodgkin, Huxley, and Katz. [55][56][57][58][59] Action potential is all or nothing event (Figure 7). Initial stimuli must depolarize the membrane to the point the threshold potential is reached. At this point selective K^+ and Na^+ channels open (change their conductivity). Conductivity of the Na^+ channels in the beginning of the AP rapidly increases allowing sodium ions follow along their concentration gradient and rush into the cell. Rapid increase of Na^+ ions inside the cell causes the cell potential to depolarize and moves it into the positive potential values. Sodium channels at this point close and potassium channels open. Outflow of the K^+ ions cause membrane to repolarize until it reaches slightly overpolarized potentials (overshoot). At this point sodium-potassium pump and leak channels slowly restore resting membrane potential.

3.1.3 Action potential initiation

The mechanism behind electrical excitation of excitable cells with an extracellular electrode has been described by Schoen & Fromherz. [60] During the standard stimulation procedure a stimulation electrode is placed in the vicinity of the excitable tissue. Electric charge is injected by a cathodic current pulse. Resulting current passes through the tissue of interest to a distant counter electrode. The electric field generated by the passing current will interact with the cell membrane (Figure 8) which will lead to the charge redistribution inside the cell. The part of the cell membrane distant from the electrode will slightly hyperpolarize meanwhile the cell membrane in the proximity of the electrode will depolarize. If the depolarization reaches the threshold potential, voltage-gated sodium channels open and AP will continue to propagate spontaneously.

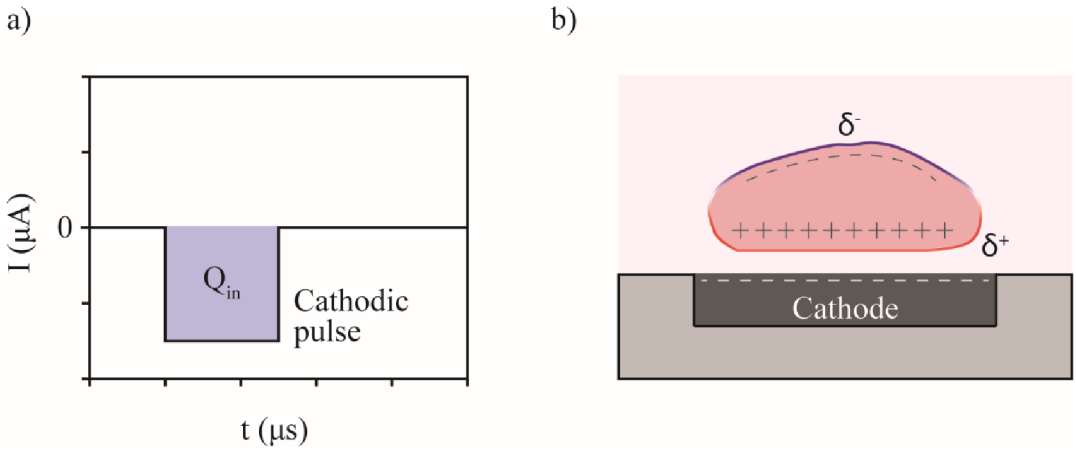

Figure 8: Action potential initiation. a) Charge is being injected through the stimulation electrode by a cathodic (negative) current pulse. c) Illustration of the cell in the proximity of the electrode during the cathodic charge injection. The cell membrane is being partially hyperpolarized at the distant part from the electrode and depolarized in the proximity of the electrode. Partial depolarization will cause the AP by causing opening of voltage-gated sodium channels in this region and allowing sodium cations into the cell.

Anodic current pulse could also trigger AP. However, it will depolarize the distant part of the cell where the strength of the resulting electric field strongly diminishes. Anodic stimulation thus requires higher charge densities which makes it up to one order of magnitude less effective than the cathodic stimulation. [61]

3.1.4 Charge injection for efficient stimulation

During electrical stimulation charge has to be injected from the stimulation electrode to the tissue, pass through the tissue and enter the counter electrode to close the electric circuit (Figure 9). Current is conducted by the electrons in the electrode and charged ions in the tissue. At the electrode-tissue interface charge transfer between the solid and liquid phases takes place. We distinguish two main charge transfer mechanisms: **Capacitive** and **Faradaic**. A capacitive mechanism results from the formation of the double layer at the electrode-electrolyte interface. The electrons (holes) accumulate at the electrode surface and their charge is compensated by the oppositely charged ions in the electrolyte. No electrons cross over the electrode/electrolyte interface.

In parallel with the capacitive charge transfer, charge can be transferred in faradaic reactions. During faradaic charge transfer the electrons are transferred between the electrodes and chemical species in the fluid surrounding the tissue (electrolyte). This means that discrete redox reactions take place at the electrode interface.

The ratio between capacitive and faradic charge transfer is a function of multiple variables. Electrode capacitance is a function of electrode active surface area and voltage. Faradaic charge transfer is a function of electrode material catalytic properties towards specific faradaic reactions, medium composition, and applied overpotential. When a current pulse is applied, the electrode potential starts to move from its standard electrode potential to higher potentials Figure 11.

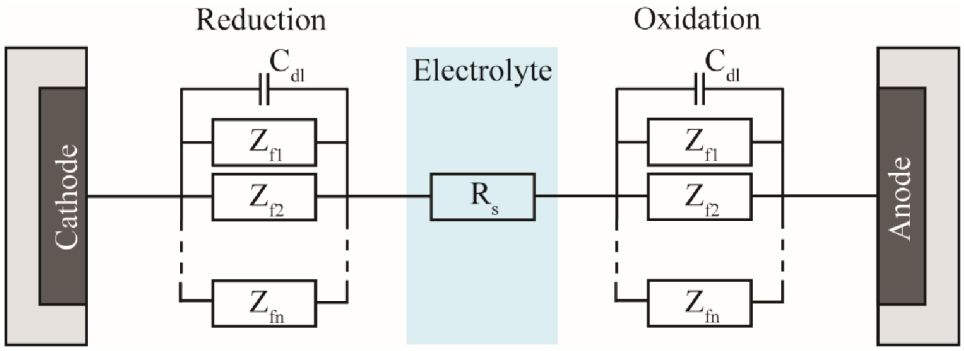

Figure 9: Charge injection diagram of the electrode-tissue interface. The charge is injected from the cathode. It is injected by capacitive and faradaic routes in parallel. Charged species pass through the conductive medium (electrolyte) in the tissue to the anode where they are collected to close the electric circuit. The current path is completed by capacitive charge coupling and/or by complementary redox (faradaic) reactions.

In the beginning of the current pulse, the double layer starts to form. The potential of the electrode rises as the double layer capacitance charges (Figure 9). At some point, the potential reaches a threshold upon which a specific faradaic reaction starts to happen (overpotential) described as Z_f in the Figure 9. This faradaic reaction starts to consume injected charge, but the amount of that charge is limited by the amount of available substrate and its transfer rate towards the electrode. Electrode potential rises more and reaches an overpotential for another faradaic reaction. This process goes on until the overpotential for water splitting is reached. At this point water is always at the surface of the electrode, thus the reaction is not transport limited

and can consume most of the remaining charge. This is evident from the sharp peaks for the hydrogen and oxygen evolution in the Figure 10a.
Based on the main charge transfer mechanism of a given electrode material we distinguish three main material classes. A faradaic, capacitive, and pseudo-capacitive (pseudo-faradaic).
As their names suggests, faradaic materials will mainly support faradaic charge transfer, capacitive will support capacitive charge transfer and pseudo-capacitive (pseudo-faradaic) will support special highly reversible faradaic process inside the bulk of the electrode material.

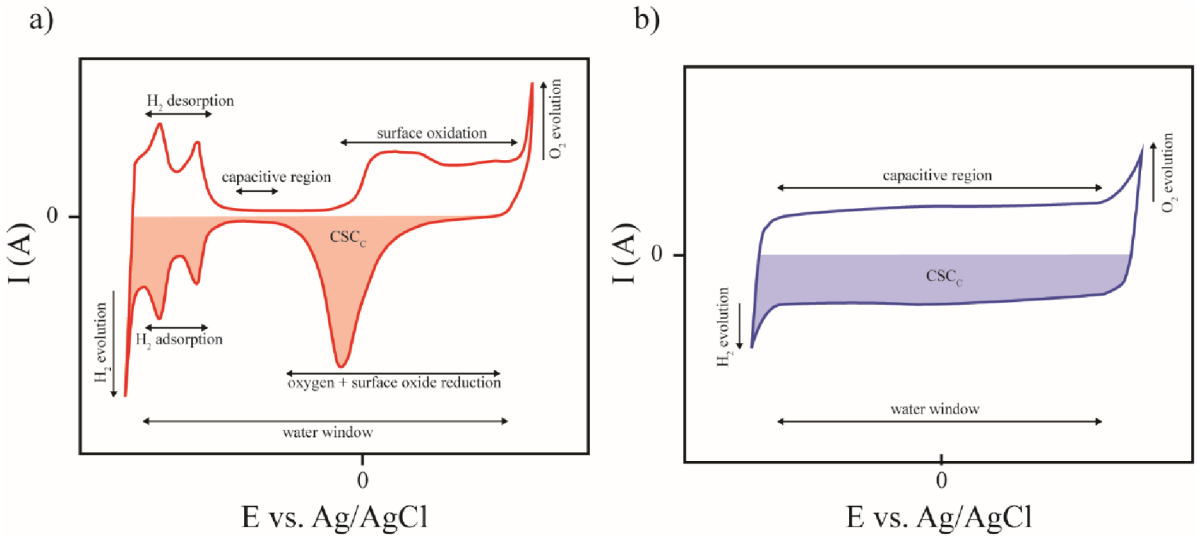

Figure 10: Cyclic voltammogram of platinum, a typical example of a faradaic electrode a) and CV of a typical capacitive electrode. In this case TiN b). Colored areas represent cathodic Charge Storage Capacity (CSC_C)

The Figure 10 shows cyclic voltammograms (CVs) of a typical faradaic electrode (a) in this case platinum and a typical capacitive electrode (b) represented by titanium nitride. CVs of a faradaic materials typically have multiple oxidation and reduction peaks representing electron transfer from the electrode to chemical species (reduction) and opposite (oxidation). Faradaic materials also usually have a capacitive region where only the charging and discharging of the capacitive double layer occurs. Capacitive materials on the other hand typically have minimal redox peaks. Instead, they do have a rectangular capacitive region within a relatively wide potential range.

Reduction:	$2H_2O + 2e^- \rightarrow H_2 + 2OH^-$	(Hydrogen evolution)	(15)
Reduction:	$Pt + H^+ + e^- \leftrightarrow Pt - H$	(Hydrogen atom de/plating)	(16)
	$PtO + 2H^+ + 2e^- \leftrightarrow Pt + H_2O$	(Oxidation and reduction of Pt)	(17)
Oxidation:	$2H_2O \rightarrow O_2 + 4H^+ + 4e^-$	(Oxygen evolution)	(18)
Oxidation:	$Pt + 4Cl^- \rightarrow [PtCl_4]^{2-} + 2e^-$	(Corrosion)	(19)
Oxidation:	$2Cl^- \rightarrow Cl_2 + 2e^-$	(Chlorine evolution)	(20)

Both faradaic and capacitive materials will eventually start to break down the water molecules once the potential of the electrode reaches the high enough overpotential. This will result in

evolution of hydrogen and oxygen gas. The range of electrical potential before water splitting occurs is called the **water window**. Electrode potentials during the electrical stimulation are usually kept within the water window because harmful radicals and pH changes accompany this process which could damage the surrounding tissue and electrodes themselves.
Capacitive charge injection is in principle the most desirable mechanism because no faradaic species are produced or consumed during the stimulation pulse. However, double-layer capacitance of purely capacitive materials is often not sufficient in delivering charge densities necessary to trigger APs. Faradaic or pseudo-faradaic materials must be used instead.
Some possible faradaic reactions occurring at the platinum electrodes are listed in the equations (15)-(20). Some of these reactions are highly reversible and harmless (16)(17), but other reactions will lead to pH changes (15)(18), corrosion of the electrode material (19), and even accumulation of toxic faradaic products. To prevent net accumulation of faradaic products in the tissue caused by electric stimulation **charge balanced bi-phasic stimulation** protocols are typically applied (Figure 11). [61][62][65]

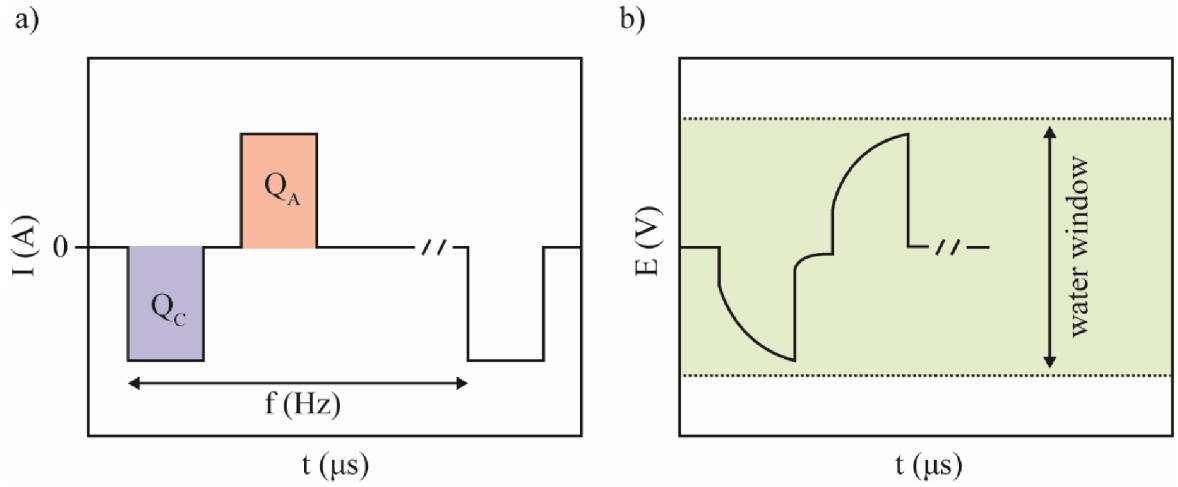

Figure 11: a) Example of charge balanced bi-phasic stimulation protocol. b) Transient voltage accompanying the current pulses. In ideal conditions the voltage should not protrude outside the water window.

During charge balanced bi-phasic stimulation protocol the cathodic current pulse is applied first. Cathodic pulse triggers the action potential while subsequent opposite anodic pulse of the equal charge is supposed to reverse all the faradaic reactions which happened during the first cathodic pulse. In theory such protocols are charge balanced, meaning there is no accumulation of charge in the tissue and there is no net accumulation of the faradaic products.
In reality, complete reversal of the faradaic reactions is rarely achieved. [63] The kinetics of some reactions are slow and require high overpotential. Before the electrode is polarized to opposite direction enough to reverse such reaction, the reaction product could have diffused outside of the electrode-electrolyte interface. Many variations of charge balanced bi-phasic protocols are used to minimize this issue. [64] The protocols vary in waveforms, being DC biased, electrodes are shorted between the pulses or coupled with capacitors. [65]
Despite all the efforts some amount of electric charge is lost due to the irreversible faradaic reactions. Up to this date the reactions and process involved in the charge dissipation have not been fully uncovered. Most of the research is focused on the electrode corrosion [66] or

protrusion outside of the water window. However, there can be many more faradaic reactions happening. The fluid surrounding the tissue is a complex electrolyte containing species which could possibly undergo redox reactions. Another possible family of reactions are the oxygen reduction reactions which have been proposed as one of the possible causes of charge dissipation. [67][68][69][70] Such reactions have not been studied in detail up to this date, thus their research has become one of the goals of this thesis.

3.2 Stimulation electrodes, architectures, and materials

Stimulation devices have electrodes of various shapes, sizes, and number of active electrode sites. Final design depends on the device application. For *in-vitro* work, Micro Electrode Arrays (MEAs) are the golden standard. They are arrays of electrodes prepared usually on rigid substrates like silicon or transparent glass which makes them compatible with inverse microscopes for simultaneous optical and electrical monitoring. MEAs contain few individual electrodes up to hundreds of electrodes and are used in basic research for both recording and stimulation. [71]

For *in-vivo* applications the diversity greatly increases due to target specific requirements. Some applications require surface electrodes like electrocorticography (ECoG) electrode arrays which are placed on the surface of the brain for both recording and stimulation. [72] When the target neurons lie beneath the brain surface, penetrating electrodes have to be applied like Michigan type electrodes [73], Utah arrays [74], new generation of flexible electrode probes [75] or Deep Brain Stimulation (DBS) electrodes. [76]

Special types of electrodes are used in cochlear implants [77], retinal implants [78] or a special Stentrode electrode array operating from the inside of the vessel where it is delivered by a catheter. [79] Spinal cord and peripheral nerves can be stimulated by the surface mount electrodes, cuff electrodes, or by penetrating electrodes. [80]

Materials used for stimulation electrodes must fulfill strict requirements. Electrode material must be biocompatible. Thus, it cannot induce toxic or strong immune response. The material must have adequate mechanical properties for a given application. Material has to be able to deliver sufficient charge to stimulate the tissue of interest while delivering the charge safely without harming the tissue and accumulation of toxic faradaic products. The material should not corrode significantly over its designated lifetime and should also preserve its electrical properties over the device lifetime.

All these requirements restrict the selection to few acceptable materials. They can be broken down to three categories based on the main charge injection mechanism.

3.2.1 Capacitive electrodes

Titanium nitride (TiN) is a typical capacitive material as was demonstrated in the Figure 10. It is known for great mechanical and chemical stability. TiN is usually deposited by reactive sputtering. Such electrodes have high intrinsic capacitance which can be greatly enhanced by tuning the deposition parameters to produce highly porous layers with electrochemical surface area greatly exceeds the geometrical surface area. This leads to maximum reported charge injection capacity of 900 $\mu C \cdot cm^{-2}$. [65]

Even though TiN is considered a capacitive material, it is capacitive only in the relatively narrow potential range. When the overpotential becomes too high, faradaic reactions start to

take place. One of the strategies to create ideally capacitive electrode is to cover the electrode with thin layer of high-κ dielectric. Good examples are valve metals like Ta or Ti which can be anodized to form passivation oxide layers of Ta_2O_5 or TiO_2. But despite the effort, such electrodes are not widely used due to their low charge injection capacity and high driving voltages necessary for charge injection. [82] More promising strategy is to use ferroelectric passivation layer. Layer of ferroelectric material can greatly enhance the charge injection capacity by utilizing ferroelectric polarization current. [83] One of the promising ferroelectric materials is HfO_2 which was also used by Fromherz to unveil the mechanism of capacitive electrical stimulation. [60]

3.2.2 Faradaic electrodes

Noble metals such as Pt, Au, Ir, Pd, and Rh are most often used as faradaic stimulation electrodes due to their presumed inertness. But even these noble metals can corrode in the physiological environment when stressed by passing electric currents. Dissolution of these electrodes can result in toxic effects for the tissue. [63]

From the family of faradaic materials platinum is used predominantly. It has safe charge injection capacity up to 100 $\mu C \cdot cm^{-2}$. [84] Pt is too soft material for some of the implantable electrodes. To increase platinum stiffness, it is alloyed with 10-30 % iridium. PtIr electrodes are the most commonly used electrodes in clinical practice, they are employed in DBS, cochlear implants, cardiac pacemakers, and other stimulation devices.

Among other faradic materials, Ti, W, various forms of carbon, such as carbon fibers, nickel-chromium alloy, or stainless steel are occasionally used. [63]

3.2.3 Pseudo-faradaic or pseudo-capacitive electrodes

Pseudo-faradaic (pseudo-capacitive) materials have an ability of fast, highly reversible transition between two or more redox states within the bulk of the material. This ability greatly increases the charge injection capacity of a given material.

Iridium oxide (IrOx) is typical material from this category. IrOx can be reversibly oxidized or reduced between multiple redox states. [89] This process can store large amount of charge and is proportional to the thickness of the oxide layer. IrOx charge injection capacity can thus reach up to 5 $mC \cdot cm^{-2}$. [65]

Iridium oxide can be made by electrochemical activation of the iridium metal by periodic anodization. [85] It can be sputtered from an iridium target in reactive oxygen plasma, [86] it can be prepared by thermal decomposition of iridium salt on the metal electrode, [87] and it can be electrodeposited. [88]

Second material which quickly became the center of attention for many researchers is poly(3,4-ethylenedioxythiophene) shortly (PEDOT). This material is also a mixed conductor able to conduct both ions and electrons (holes) especially in its doped state. Most often PEDOT is doped with polystyrene sulfonate (PSS) resulting in polymer complex PEDOT:PSS. Other dopants are possible too. PEDOT can similarly to IrOx transition between two redox states benzoid and quinoid. This transition can again store a lot of charge in addition to the porous, high surface area, gel-like structure with high double layer capacitance.

PEDOT:(dopant) can be deposited to the electrode surface from solution by printing, electrodeposition, or in-situ polymerization. Charge injection capacity of PEDOT can reach up to 15 $mC \cdot cm^{-2}$. [65]

3.2.4 Future perspectives

Many of the above-mentioned materials fulfill the basic criteria to be used in the implantable stimulation devices and such devices are chronically used by millions of patients. There is a large room for improvements, though.

Most of the used materials corrode and generate faradaic side products. This might be an issue when designing a device lasting a patient lifetime. More effort has to be given to the understanding the nature of these processes, their influence on the surrounding tissue and finding ways how to eliminate or control them.

Stimulation devices are not just the stimulation electrodes, but also substrates and encapsulants providing mechanical support and electrical isolation of conductive leads. Interconnects, power sources, and means of the communication with the external world. All these components must face the issues of long-term stability, reliability, and compatibility with each other. If one of the components fails, the whole device can become dysfunctional.

The mechanical mismatch between the implantable devices and tissue also presents a problem which must be addressed for the implantable devices to be viable for long time periods. Although the used materials are biocompatible, their dry, hard, and static nature makes them foreign in the wet, soft, and dynamic tissue environment. This leads to the reactive tissue response. Immediately after device implantation acute response follows. Implantation will cause inflammation that will lead to necrosis of the surrounding tissue and release of reactive oxygen species by inflammatory cells in the effort to destroy the foreign body object. Shortly after the acute response, chronic response follows. More reactive oxygen species and enzymes are released to destroy the implant and what is left gets encapsulated by glial scar. A glial scar will create a barrier between the cells of target and the electrode. Such barrier can be tens to few hundred micrometers thick resulting in higher charge densities that are needed for efficient stimulation and of course more faradaic products generated. Future efforts will tackle these issues by developing electrode materials and coatings more similar to the tissue environment in order to avoid the foreign body response.

3.3 Electrochemical characterization of stimulation electrodes

A stimulation electrode must be able to safely inject sufficient charge to elicit the desired outcome. With large area electrodes it is relatively easy, but many applications require microelectrodes for precise targeting of small tissue regions or even single cells. When the electrode size is decreasing, the required charge densities are increasing, and it is becoming more difficult to inject charge in a safe way because less charge is passed through the desired capacitive route. An ideal stimulation electrode thus should have large capacitance or pseudo capacitance to support charge delivery through these mechanisms.

Electrode impedance is also an important factor. Electrode impedance is getting larger with decreasing electrode size resulting in the higher applied voltages needed to drive the currents over the electrode tissue interface. The higher the voltages, the higher chances of irreversible faradaic reactions. One should thus strive for high capacitance, low impedance electrodes.

When designing a stimulation electrode system, one must take into account the charge injection densities needed for the effective stimulation of the target tissue. Such charge densities differ based on the target tissue and some are listed in the literature. [68] It is thus necessary to design the system using a suitable electrode material, stimulation protocol, and test if the system can deliver the desired amount of charge in a safe and sustainable way.
When characterizing the stimulation electrode, the safe stimulation region (water window), capacitance, and impedance have to be determined. Then maximum amount of injectable charge within the safety limits is obtained for a given stimulation procedure. Finally, electrode long term stability when exposed to the harsh biological environment and electrochemical stressing is tested.
Standard electrochemical techniques for stimulation electrodes characterization are cyclic voltammetry, voltage transient measures upon application of a stimulation current pulses, and electrochemical impedance spectroscopy.

3.3.1 Cyclic voltammetry

CV is a powerful technique to identify presence of electrochemical reactions, their magnitude, and reversibility at the electrode surface. It can determine which charge transfer mechanism is predominating based on the mechanisms described in (3.2).
CVs are used to determine theoretical cathodic Charge Storage Capacity (CSC_C) of an electrode (Figure 10). CSC is the total amount of charge obtained by integrating the cathodic part of a CV. This charge is theoretically available for the charge injection during the cathodic stimulation pulse, however, in practice the available charge is smaller, mainly because of two factors:
Theoretical CSC_C is obtained during slow potential sweeps. When a highly porous electrode is used, the deep pores have high access resistance which impedes the double layer formation and faradaic charge transfer. The electrode area inside deep pores is effectively utilized only during the slow sweeps when higher sweep-rates (close to the actual stimulation frequency) are used, the surface area inside the deep pores cannot be effectively utilized. CSC_C is thus sweep-rate (frequency) dependent. [68][89]
Another factor is the standard electrode potential. As we can see in the Figure 10, Pt has standard electrode potential positioned in a very convenient way. The majority of the CSC_C area is below $0\,mV$ which makes most of the charge to be accessible during the cathodic pulse. Other materials may not be so convenient (Figure 10b) and a DC offset is needed during AC stimulation for the CSC_C to be maximally accessible. A typical example of such material is IrOx. [68]
Cyclic voltammetry is also a good method to determine electrode double layer capacitance (C_{dl}). C_{dl} can be obtained by measuring the CV in a purely capacitive region and calculated from the equation (21).

$$C_{dl} = \frac{\int I \cdot V dV}{2 \cdot \mu \cdot \Delta V \cdot A} \tag{21}$$

Where $\int I \cdot V dV$ is the integral area of the CV, μ is the scanrate ($V \cdot s^{-1}$), ΔV is the potential window within the CV is obtained and A is the electrode geometrical surface area (m).
Caution must be paid to the way the voltage is swept during the CV. Modern potentiostats use Analog-to-digital convertor (ADC) to sweep the voltage in discrete digital steps. Unfortunately,

this will lead to lower CV resolution (some electrochemical peaks might not be visible) and underestimation of the electrode capacitance. A potentiostat with current averaging method or better "true linear scan" module has to be used for accurate capacitance estimation. [90]
Finally, cyclic voltammetry is a good tool to examine electrode stability. Thousands of CV scans can be applied to the electrode to see how the electrode surface is changing upon this stress and CVs can be periodically measured when electrode material is exposed to harsh testing environment and electrical stresses (3.3.4).

3.3.2 Voltage transient measurements

Voltage transient measurements are typically used to determine maximum Charge Injection Capacity (CIC_{max}). Maximum charge injection capacity is the maximum amount of charge which can be delivered with a given stimulation protocol before the water window is breached by the transient voltage (Figure 11).
Voltage transients are typically measured *in-vitro* in a three-electrode setup. The current pulses are being applied to the stimulation and counter electrode by dedicated current stimulator while voltage transients are being recorded by oscilloscope between the stimulation electrode and a close reference electrode.
The voltage transient method could also provide a little information about the ongoing irreversible reactions. If such reactions are taking place, the standard electrode potential will start to shift towards one direction where it will eventually stabilize, and the electrode becomes polarized. Such behavior is a direct effect of irreversible faradaic reactions, called ratcheting. [63] More detailed analysis can provide a deeper insight into such reactions. [91]

3.3.3 Electrochemical Impedance Spectroscopy

EIS is key method for characterization of the recording electrodes. Typically, it is reported as absolute impedance value at 1kHz, because most of the neural activity lies around this frequency. The lower the impedance of a recording electrode at 1kHz, the better is the recorded signal. It has higher signal to noise ratio.

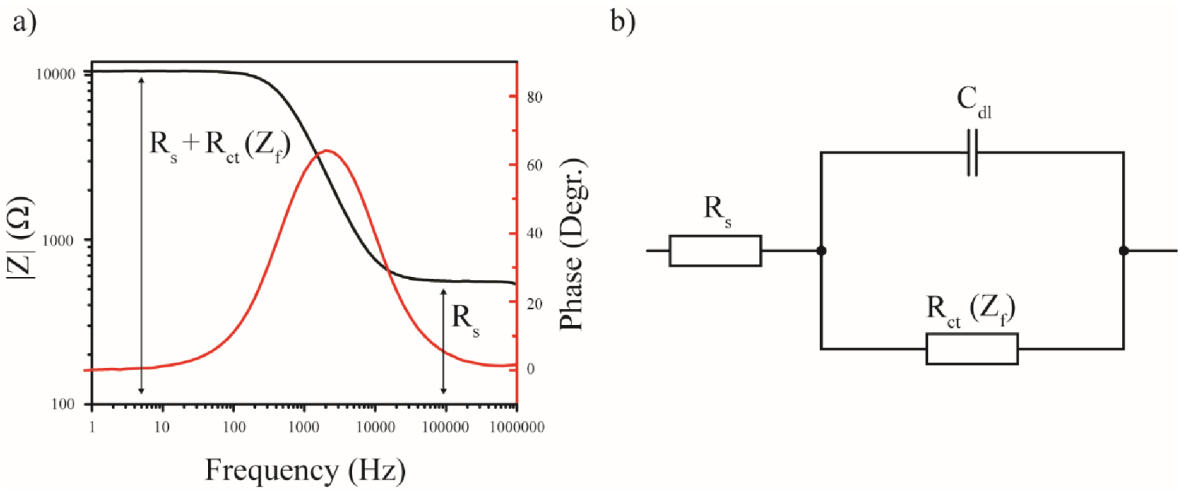

Figure 12: a) Illustrative Electrochemical Impedance Spectra of a stimulation electrode in the form of a Bode plot. b) Basic equivalent circuit diagram of an electrode (Randles circuit). Spectra shown in (a) are constructed by fitting this circuit diagram ($R_s = 560\Omega;\ R_{ct} = 10k\Omega;\ C_{dl} = 33nF$).

As it was mentioned earlier, low impedance is also important for stimulation electrodes. Further, it can provide more insight into the electrode characteristics. When the EIS is fitted with an equivalent circuit diagram correctly representing the system under the investigation, useful parameters can be extracted. The Figure 12 shows simple EIS spectra of an electrode with its equivalent circuit diagram. When the spectrum is fitted with a model of such diagram, parameters like electrolyte resistivity (R_s), charge transfer resistivity (R_{ct}), or as we called it previously faradaic impedance (Z_f) can be extracted. Double layer capacitance (C_{dl}) can be extracted also. In reality, more sophisticated models have to be used to accurately represent the non-idealities of the real electrode.

Electrochemical impedance spectroscopy is also a great method for assessing electrode fitness over the time. Due to the low applied voltage amplitude during the measurement, EIS can be performed *in-vivo* without any side effects. Usually upon the implantation of the electrode, impedance is rising due to the protein adsorption (biofouling) and it can vary over time due to the many factors, like glial scar formation or gradual loss of lead conductivity due to the mechanical stresses.

3.3.4 Long term stability testing

High capacitance, low impedance electrodes are useless unless they can maintain their properties over the intended lifetime. With designed lifespan of stimulation devices ranging from years to decades it is obvious that stability tests cannot be performed under the real conditions. Instead, accelerated aging tests are performed to test device lifespan under harsher conditions than the device would experience under the standard conditions and approximate device real lifespan.

Common protocols for testing the device long term stability are using exposure to electrolytes with elevated temperatures, exposure to reactive oxygen species, and electrochemical stressing. Standardized electrode performance tests have been suggested. [89] Such tests recommend stressing the device in the electrolytes elevated to 60 °C and in electrolytes containing up to 30 mM hydrogen peroxide. The devices should also be stressed by high amount of charge balanced biphasic pulses (10^6-10^9) with about 80% of the maximum charge injection capacity. The device performance should be assessed by CV and EIS multiple times over the test period.

3.4 Electrical stimulation of non-excitable cells

Electrical stimulation of non-excitable cells is interesting, but as of yet a poorly understood discipline. As it was mentioned in the chapter introduction, DC fields and currents are present within living systems. DC fields are observed in subcellular, cellular, tissue, organ, and organism levels. They are caused by active ion transport over the cell membranes. Cells aggregate together and selectively exchange ions by the gap junctions. Electronic signals can thus propagate through neighboring cells. Selective ion transport in some tissues can lead to the development of electric fields and ionic currents over the tissue scale distances.

Interestingly, varying electric current densities were first measured near epithelial layers during embryogenesis. An ultrasensitive, self-calibrating vibrating probe was used to perform such measurements. [92] Embryonic epithelial layers displayed different outward current densities. Later on, areas with high current densities became the centers of large anatomical changes like limb or eye formation. Increased current densities in such places preceded more than a week

before the anatomical changes appeared. Whether the observed currents were the cause or the consequence of such change is not clear, but when the epithelium is artificially ruptured leading to short circuit and increased current density (Figure 13), the limbs can be formed at places they do not belong. [93]

Subsequently, with the development of fluorescent voltage probes it became clear, that endogenous electric fields are widely present and are guiding cell shape, orientation, migration, proliferation, and tissue regeneration. [53] They affect limb formation and eye formation, polarity of body anatomical axes and craniofacial patterning. [94]

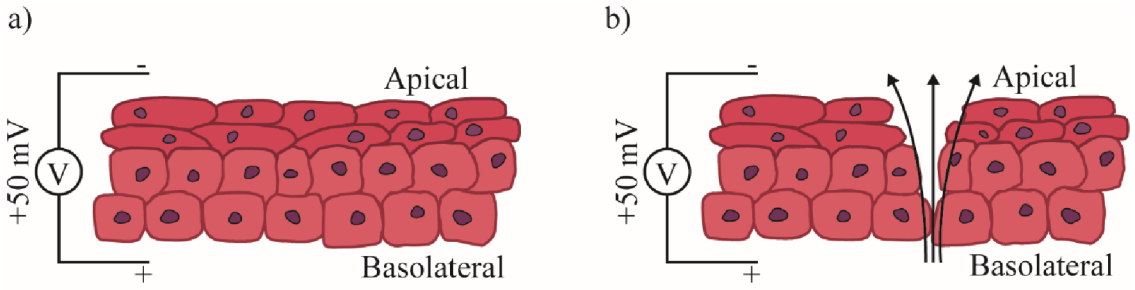

Figure 13: (a) Trans Epithelial Potential measured over its Basolateral and Apical side typically ranges in $40 - 200\ mV \cdot cm^{-1}$. *(b) Injury current caused by the rupture (short-circuit) of the epithelium layer. Resulting DC current densities are usually between* $1 - 300\ \mu A \cdot cm^{-2}$. *[95]*

With all the above-mentioned discoveries, obvious question emerges: Can exogenous electric field be used to our benefit? Many researchers are trying to find the answer by focusing towards understanding the intricate mechanisms of interaction between the living cells and electric fields. The idea is to apply electric fields to form, heal, or regenerate tissue.

One of the strategies used by regenerative medicine and tissue engineering is the recruitment of stem cells. Stem cells are undifferentiated cells which can become any cell type under the right conditions. There are many factors affecting the stem cell differentiation. Most understood are biological and chemical factors. However, physical factors like mechanical stress and electrical stimulation could be important too.

As it was mentioned before, all the cells are polarized. Stem cells are polarized the least. As stem cells differentiate and mature, they are more negatively polarized with a specific membrane potential for each cell type [53]. One could ask: Could exogenous electric field be applied to a stem cell culture to artificially modulate their membrane potential and guide their differentiation to the desired direction? Many people tried and some experienced partial success. Stem cells were successfully differentiated into muscle, bone and neural cells using electrical stimulation. [96][97][98][99]

Exogenous electric fields thus can direct stem cells differentiation and they also influence their orientation, movement, proliferation, and speed up maturation. However, the mechanisms behind such effects go beyond simple membrane depolarization. It is largely agreed that exogenous electric fields influence cellular response by multiple transduction pathways. Most influential pathways are cytoskeletal reorganization, actin and surface receptor redistribution, regulation of cytoplasmic calcium ion concentrations, ATP synthesis, heat shock protein activation, and Reactive Oxygen Species (ROS) evolution. [54]

ROS evolution during the electrical stimulation and its physiological effects to the cells is an important factor in the scope of this thesis. Most of the above-mentioned transduction pathways are based on the specific interactions between electric fields and charged ions or molecules which can move or orient themselves in a specific way. ROS evolution on the other hand assumes chemical changes in the system. As it was described in (3.1), ROS can be generated during direct electrical stimulation. ROS generated on the electrode surface have direct influence on the fate of the stem cells. [100] Reactive oxygen species are also generated intracellularly as a consequence of electric stimulation. [101] There is growing evidence showing that modest intracellular ROS generation induces stem cell differentiation by itself or in the combination with other factors. [102][103][104][105][106] This makes sense because ROS and hydrogen peroxide especially are highly influential signaling molecules involved in many biochemical pathways. [107][108]

3.4.1 Materials, stimulation setups and methods

Electrical stimulation targeting non-excitable cells is still mostly a subject of primary research. Thus, the majority of the experiments are taking place *in-vitro*. Materials used for stimulation electrodes follow similar requirements as materials used for the stimulation of excitable cells (3.2). The nature of *in-vitro* experiments does not require usage of rare and expensive materials like iridium. Most of the experiments are performed using platinum electrodes, other precious metals, stainless steel, and carbon-based electrodes.

Many different stimulation protocols are applied. From various AC protocols differing in the waveform, frequency, and amplitude to DC protocols under constant applied voltage or current over the time periods ranging from seconds to days.

Mostly scientists are trying to mimic electric fields or ionic currents cells experience in the native environment. They are applying voltages to the electrodes with the presumption that similar electric fields will be created. Scientists coming from biological background usually do not fully consider the physics and electrochemistry of such processes (3.2 & 3.3). Because of that, non-negligible number of studies is poorly designed and executed from the electrochemical point of view. Many more variables than electric fields and currents can be involved. Namely, redox reactions in the complex cell medium, ROS evolution, oxygen, and pH gradients. All these effects can cumulatively exert greater effect than electric fields and currents alone.

The simplest and most frequent experiments are performed in the cell culture with directly integrated electrode system (Figure 14a). Electrodes can be inserted to the medium in the form of wires, plates, or patterned at the bottom of the reactor. More sophisticated reactors separate the electrodes form the cell medium to prevent above mentioned undesired side effects. One of the strategies takes the electrodes from the medium entirely (Figure 14b). The cell culture is placed between two plates and electric field is applied. No actual electric field will exist in solution unless AC field is applied. There are published studies that ignore this simple physical fact. Such approach does not really belong to the category of direct electrical stimulation but it is worth mentioning. Similar purely physical approach can also utilize magnetic fields. [97][110]

Another strategy separates the cell culture from the anodic and cathodic faradic reactions by salt bridges (Figure 14b). This design can support continues DC ionic current without exposing

the cells to any harmful faradaic products. [54][99] The trick is in the application of silver electrodes coated with a silver-chloride layer. Such electrodes are typical example of ideally non-polarizable electrodes. When electric potential is applied, silver ions from silver-chloride will get reduced on the cathode while silver anode will oxidize forming silver-chloride. This redox process will result in the DC flow of chloride ions between the electrodes until the silver-chloride layer on the cathode is depleted. Then, the polarity can be simply reversed and the process starts again with current flowing opposite direction.

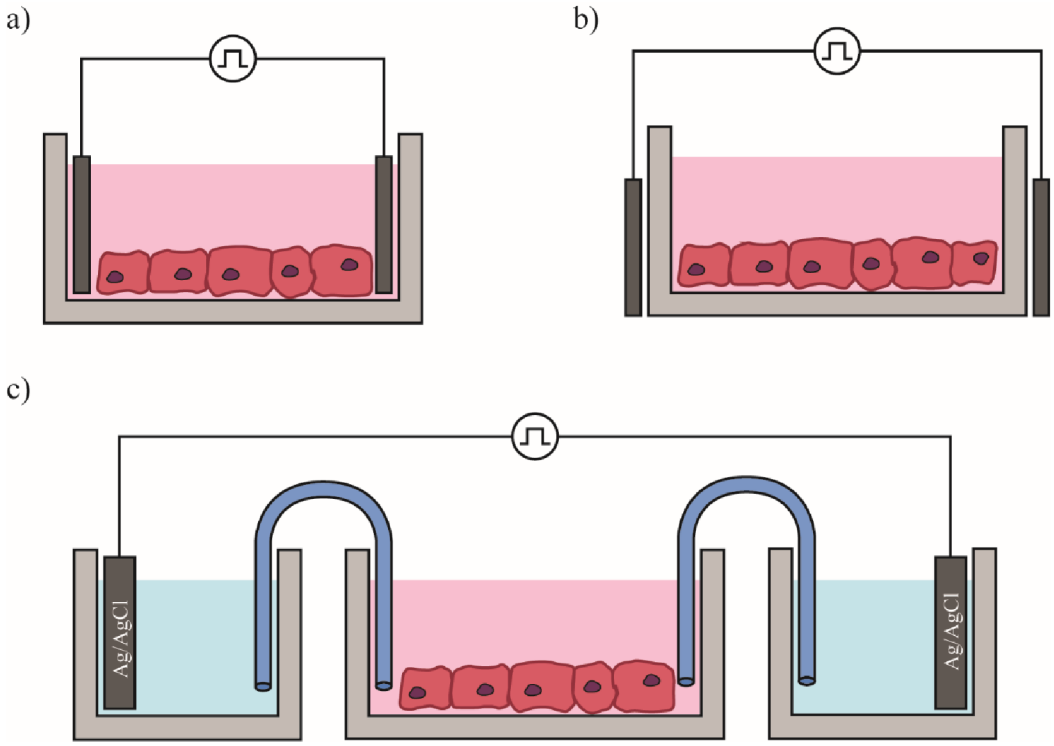

Figure 14: Basic experimental in-vitro stimulation setups. (a) Direct electrical stimulation with electrode system in the cell media. (b) Indirect stimulation setup by the electrodes outside of the tissue media. Also called capacitive, (c) Direct electrical stimulation by the electrodes placed in the separate reactors from the cell media connected by the salt bridges. Such setup allows only ionic currents to flow over the cell culture and protect it from faradic side-products.

4 GOALS OF THE WORK

This work is headed towards two main directions: The first is the development of Microbial Fuel Cell array for high throughput screening and characterization of electrogenic microorganisms. The second direction is heading towards electrical stimulation of cells and tissues. Focusing on guided differentiation of stem cells using electric fields and fundamental study of oxygen reduction reactions occurring at the electrodes during electrical stimulation.

The first goal of the thesis was to develop a reliable, reproducible, and user-friendly platform composed of multiple Microbial Fuel Cells arranged in a standard 96 or 24 well-plate configuration.

The second goal was to fabricate a platform for electrical stimulation of stem cells. Such a platform was supposed to be based on 24 well plate equipped with transparent bottom plate with system of interdigitated electrodes compatible with inverted microscope. This platform is intended for biological experiments aimed at directed differentiation of stem cells towards cardiomyocytes or neurons.

The third goal was to investigate whether and to what extent are irreversible oxygen reduction reactions happening on standard electrode materials under various DC conditions and AC stimulation protocols.

5 RESULTS AND DISCUSSION

5.1 Methodology

5.1.1 Fabrication

MFC arrays were based on two PCB layers containing conductive traces as well as contacts for the electrodes. PCBs were designed using Eagle PCB software and manufactured by an external manufacturer from provided Gerber files. Electrodes were made from carbon paper which was patterned using a CO_2 laser or a plotter. Wells were 3D printed using stereolithographic 3D printer or laser cut from acrylic sheets which were than welded together using dichloromethane. All models for 3D printing and CAD visualization models were constructed using Solidworks software. All parts were assembled using guiding screws and glued together using epoxy and PDMS. Electrodes were glued by conductive silver epoxy or carbon-based screen printing paste which were deposited to the exact locations by stencil printing. Nafion PEM was spray coated using an airbrush gun. Connectors were soldered to the PCBs by hand.

24-well stimulation platforms were made of commercial bottomless well plates. Conductive traces were thermally evaporated on a PEN (polyethylene naphthalate) substrate. First, the adhesive layer of NiCr and then Au were deposited using shadow masking. Some traces were coated by PEDOT:PSS deposited by screen printing. Substrate and well plate were subsequently glued together by PDMS and secured by screws.

Samples for oxygen reduction investigations were vacuum deposited utilizing three different methods: Thermal e-beam evaporation, magnetron sputtering, or by a dual source ion-beam sputtering system. The electrochemical cell for the measurements was constructed from laser cut acrylic sheets which were welded together using dichloromethane. Ag/AgCl pseudo reference electrode was made by anodizing a silver wire.

5.1.2 Characterization

MFC arrays were electrochemically characterized using a potentiostat. Cyclic voltammograms, polarization curves and electrochemical impedance spectra were acquired. Data logger was used to measure electric current generated by individual MFCs by measuring voltage drop over a known resistor. Visual biofilm observation and elemental analysis were performed by the SEM system with integrated EDX module. Sequencing was concluded by dedicated sequencing facility at Okinawa Institute of Science and Technology (Japan).

Characterization of 24-well stimulation platform was realized by a potentiostat. Chronoamperometry and electrochemical impedance spectroscopy were measured. Visual inspection was done using an optical microscope.

Oxygen reduction reactions were characterized by oxygen and hydrogen peroxide sensitive amperometric sensors. Samples were also characterized by cyclic voltammetry.

5.2 Published results

5.2.1 Scientific papers comprising the main experimental part of the thesis

[P1] Szydlowski, L., **Ehlich, J.**, Szczerbiak, P., Shibata, N., & Goryanin, I. Functional annotation and taxonomy profiling of electrogenic, Cu-tolerant microbial communities derived from a single inoculum and enriched in a 96well plate microbial fuel cell (MFC). *Frontiers in Microbiology* (Accepted).

[P2] Szydlowski, L., **Ehlich, J.**, Goryanin, I., & Pasternak, G. (2022). High-throughput 96-well bioelectrochemical platform for screening of electroactive microbial consortia. *Chemical Engineering Journal*, *427*. https://doi.org/10.1016/j.cej.2021.131692.

[P3] Šafaříková, E., **Ehlich, J.**, Stříteský, S., Vala, M., Weiter, M., Pacherník, J., Kubala, L., & Víteček, J. (2022). Conductive Polymer PEDOT: PSS-Based Platform for Embryonic Stem-Cell Differentiation. *International Journal of Molecular Sciences*, *23*(3). https://doi.org/10.3390/ijms23031107.

[P4] **Ehlich, J.**, Migliaccio, L., Sahalianov, I., Nikić, M., Brodský, J., Gablech, I., Vu, X. T., Ingebrandt, S., & Głowacki, E. D. (2022). Direct measurement of oxygen reduction reactions at neurostimulation electrodes. *Journal of Neural Engineering*, 19(3). https://doi.org/10.1088/1741-2552/ac77c0.

5.2.2 Other scientific papers

[P5] L. Szydlowski, **J. Ehlich**, N. Shibata, I. Goryanin, (2021). High-throughput screening and selection of PCB-bioelectrocholeaching, electrogenic microbial communities using single chamber microbial fuel cells based on 96-well plate array. *BioRxiv. 447729*. https://doi.org/10.1101/2021.06.09.447729.

[P6] **Ehlich, J.**, Zhivkov, I., Yordanov, R., Salyk, O., & Weiter, M. (2020). Optimized Impedance Measurement with AD5933. *2020 43rd International Spring Seminar on Electronics Technology (ISSE)*, *427*, 1-6. https://doi.org/10.1109/ISSE49702.2020.9121159.

[P7] Zhivkov, I., Vasicek, Z., Slavikova, Z., Yordanov, R., & **Ehlich, J.** (2020). Detection of the Yogurt Incubation Kinetics by Portable Impedance Converter. *2020 XXIX International Scientific Conference Electronics (ET)*, *427*, 1-4. https://doi.org/10.1109/ET50336.2020.9238319.

5.2.3 Supervised theses

[T1] Runštuková, N. Elektrochemická charakterizace bioelektronických systémů. Brno, 2021. Dostupné také z: https://www.vutbr.cz/studenti/zav-prace/detail/131468. Bakalářská práce. Vysoké učení technické v Brně, Fakulta chemická, Ústav chemie potravin a biotechnologií. Vedoucí práce: **Ehlich, J**.

[T2] Florian, V. Příprava a charakterizace mikro-referenčních elektrod pro bioelektronické systémy. Brno, 2022. Dostupné z: https://www.vutbr.cz/studenti/zav-

prace/detail/139042. Bakalářská práce. Vysoké učení technické v Brně, Fakulta chemická, Ústav chemie materiálů. Vedoucí práce: **Ehlich, J**.

5.2.4 Chronologically ordered conference contributions

[C1] **Ehlich, J.**; Salyk, O.; Stříteský, S.; Šafaříková, E.; Weiter, M. *Bioelectrical device for electrostimulation of stem cells.* Brno, Czech Republic: 7th Meeting on Chemistry and Life, 2018.

[C2] **Ehlich, J.** *Integration of engineered microorganisms with bioelectronics*. Siena, Italy: 5th International Synthetic & Systems Biology Summer School (SSBSS), 2018.

[C3] **Ehlich, J.**; Salyk, O.; Stříteský, S.; Šafaříková, E.; Weiter, M. *Bioelectrical device for electrostimulation of stem cells based on 24-well plate array of interdigitated electrodes coated with organic semiconductors.* Hasselt, Belgium: 15th International Conference on Organic Electronics (ICOE), 2019.

[C4] **Ehlich, J.**; Szydlowski, L. *High throughput platform for identification and characterization of electrogenic bacteria.* Okinawa, Japan: 7th International Society for Microbial Electrochemistry and Technology Conference (ISMET 7), 2019.

[C5] **Ehlich J.**, Szydlowski L. *High Throughput Platform for Identification And Characterization Of Electrogenic Bacteria.* Brno, Czech Republic: Chemistry and Life, 2020.

[C6] **Ehlich, J.**; Szydlowski, L. *High throughput platform for identification and characterization of electrogenic bacteria.* Thessaloniki, Greece: International symposium on flexible organic electronics, 2021.

[C7] **Ehlich, J.**; Szydlowski, L. *High throughput platform for identification and characterization of electrogenic bacteria.* Brno, Czech Republic: XXI. Workshop of Biophysical Chemists and Electrochemists, 2021.

[C8] **Ehlich, J.**; Migliaccio, L.; Nikić, M.; Brodský, J.; Gablech, I.; Glowacki, E. D. *Oxygen Reduction Reactions at Neurostimulation Electrodes*. Brno, Czech Republic: Chemistry and Life, 2021.

[C9] **Ehlich, J.**; Migliaccio, L.; Nikić, M.; Brodský, J.; Gablech, I.; Glowacki, E. D. *Oxygen Reduction Reactions at Neurostimulation Electrodes.* Zagreb, Croatia: Croatian Neuroelectronics Symposium / Zagreb Bioelectronics Workshop, 2021.

[C10] **Ehlich, J.**, Migliaccio, L., Sahalianov, I., Nikić, M., Brodský, J., Gablech, I., Vu, X. T., Ingebrandt, S., & Głowacki, E. D. *Direct measurement of oxygen reduction reactions at neurostimulation electrodes*. Kirchberg in Tirol, Austria: International Winterschool on Bioelectronics (BIOEL), 2022

[C11] **Ehlich, J.**, Migliaccio, L., Sahalianov, I., Nikić, M., Brodský, J., Gablech, I., Vu, X. T., Ingebrandt, S., & Głowacki, E. D. *Direct measurement of oxygen reduction reactions at neurostimulation electrodes*. Tübingen, Germany: 13th international Meeting on Substrate-integrated Microelectrode Arrays (MEA Meeting), 2022

[C12] **Ehlich, J.**, Migliaccio, L., Sahalianov, I., Nikić, M., Brodský, J., Gablech, I., Vu, X. T., Ingebrandt, S., & Głowacki, E. D. *Direct measurement of oxygen reduction reactions at neurostimulation electrodes*. Cambridge, United Kingdom: Whitaker Neuroengineering, 2022

5.3 Comments to the enclosed manuscripts

5.3.1 [P1]: Functional annotation and taxonomy profiling of electrogenic, Cu-tolerant microbial communities derived from a single inoculum and enriched in a 96well plate microbial fuel cell (MFC)

This publication is a result of the pilot experiments with the first developed prototype of the 96-well MFC platform (V_1.0). First prototype proved to be able to generate electric currents after the inoculation. However, it possessed many flaws. Sandwich style of the reactor did not prove to be user-friendly. Periodical openings due to the need of medium exchange led to the formation of short circuits caused by medium leakage to the adjacent wells over the custom made PDMS seal. This also led to cross-contamination of the adjacent wells, so full capacity of the well plate was not accessible. Opening the reactor to exchange the medium also often led to formation of bubbles underneath the air-cathode which dramatically increased internal resistance.

Printed circuit boards used as anodes, interconnects and structural parts proved to be not sufficiently chemically inert. Over the time of the MFC operation, anode started to oxidize producing blue/green precipitates which contaminated the MFCs. Later analysis determined copper from the PCBs to be the source of the contamination. Interestingly, some microbes were still able to thrive under high copper ion concentration and generate electric currents. This finding has become a cornerstone of the paper which became a metagenomic study of the selectively enriched microbial community in MFC with high copper content.

Evaluation of personal contribution:

Author designed and built the MFC array used during this experiment. Author participated during the experiments, the data processing with construction of the graphs and figures, then writing and reviewing the manuscript.

5.3.2 [P2]: High-throughput 96-well bioelectrochemical platform for screening of electroactive microbial consortia

In this sequel of [P1] an improved version of the V_1.0 MFC platform was used (V_2.0). Improved version had square wells to allow higher medium volume, thus support growth of microorganisms for longer time periods without a need of medium exchange. Platform was equipped with modified commercial silicone rubber sealing mat used for sealing up standard well plates. Commercial sealing was meant to prevent medium leakage, short circuiting and cross contamination issues caused by custom made seal. PCBs were in V_2.0 electroplated by gold. Electroplating is more expensive process than standard electroless plating but leads to a more homogeneous and robust gold layer preventing anode oxidation and contamination of the medium with copper ions.

Electroplated gold surface finish led to elimination of copper contamination. Commercial seal partially solved the problems of custom-made seal but the problems of medium leakage, short circuits and cross contamination remained. These problems were more of the architecture issue than a seal issue. Based on these findings a V_3.0 with different architecture was conceived.
Idea behind this publication was to follow up on the electrogenic microorganisms capable of withstanding high copper ion concentrations and causing its precipitation which could be useful for bioremediation. We have used the high throughput capabilities of V_2.0 platform to selectively screen for electrogenic microorganisms derived from metal contaminated sources and selectively enrich those that were able to withstand and thrive under high copper concentrations.

Evaluation of personal contribution:
Author designed and built the MFC array used during this experiment. Author participated in the writing and reviewing the manuscript and construction of the graphs and figures.

5.3.3 [P3]: Conductive Polymer PEDOT: PSS-Based Platform for Embryonic Stem-Cell Differentiation

The aim of this work was to apply electrical stimulation to direct stem cells differentiation towards neurons or cardiomyocytes. This work presents results of our first experiments in this field which we have entered without any prior experience in 2018. Looking back with current knowledge, we did not design and perform the experiments in the best way.
Issues started from the sub-optimal design of the stimulation platform which was not properly electrochemically characterized before it was provided for the experiments. Recently, after the proper characterization by EIS, we have discovered the prepared platforms had a low yield. Only about 75% of the wells in the well plate were functioning and the variability in R_s, R_{ct} and C_{dl} in the functioning wells warried over ± 100 %. The cause of this was a plastic substrate which was not compatible with thin film gold traces. The plastic substrate had micro cracks on the surface. The deposited 100 nm layer of gold was unable to provide electrical connection over some of these cracks. This was unfortunately not visible under the optical microscope and became only apparent after the EIS measurements long after the experiments have finished.
We have applied a stimulation protocol from the literature without having sufficient understanding what would be happening in our system and what effects should we expect from the different electrode materials.
The result is a study showing some not significant effects of electrical stimulation by two different electrode materials towards stem cell differentiation. Found effects have probably no significance because of the unreliable stimulation platform as well as the unknown effects of the faradaic process occurring during the stimulation.

Evaluation of personal contribution:
Author fabricated and tested stimulation platforms used in the experiments. Author participated in the experiments, writing and reviewing the manuscript, and construction of the graphs and figures.

5.3.4 [P4]: Direct measurement of oxygen reduction reactions at neurostimulation electrodes

In this study we have focused on irreversible electrochemical reactions happening within the water window during biphasic charge balanced stimulation. We have studied the family of oxygen reduction reactions. It has been suggested by multiple publications that oxygen can be irreversibly reduced to water and other reactive oxygen species. However no study before has directly proved it and quantified it.

We have proved that charge balance biphasic stimulation protocols lead to irreversible reduction of oxygen and generation of hydrogen peroxide. Such reactions are taking place on all commonly used electrode materials, even on the materials which are considered highly capacitive.

During prolonged stimulation, hypoxic environment can be induced in the electrode proximity and hydrogen peroxide can be locally accumulated up to mM concentration. Induced hypoxic conditions can have negative consequences to the exposed cells as well as hydrogen peroxide which can act as a signaling molecule in low (nM) concentrations and be toxic in the higher (μM) concentrations. Hydrogen peroxide presence can also have negative consequences to the electrode longevity.

This paper is a direct proof of oxygen reduction reactions and everyone applying direct electrical stimulation to the living systems should be aware of possible side effects induced by lower oxygen concentration and evolved hydrogen peroxide.

Evaluation of personal contribution:

Author designed and built the measurement setup. Author supervised the measurements and participated in the data acquisition, processing, and data analysis. Author constructed the main figures and participated in the writing and reviewing of the manuscript.

5.3.5 [P5]: High-throughput screening and selection of PCB-bioelectrocholeaching, electrogenic microbial communities using single chamber microbial fuel cells based on 96-well plate array

This paper is a preprint version of the [P1] lacking metagenomic data analysis using advanced bioinformatics methods.

Evaluation of personal contribution:

Author designed and built the MFC array used during this experiment. Author participated in the experiments, the data processing with construction of the graphs and figures, then writing and reviewing the manuscript.

5.3.6 [P6]: Optimized Impedance Measurement with AD5933

High throughput capabilities of MFC platforms developed in [P1] and [P2] cannot be fully utilized without appropriate measuring apparatus. Potentiostats are usually used to perform all the electrochemical tests needed for complete characterization of an MFC under the test (2.4). Commercial potentiostats usually do not offer multichannel versions able to monitor 24/96 channels. Potentiostats are also quite expensive and combining many single/multi-channel ones

to operate the platforms presented in [P1] and [P2] would be out of the reach for most researchers.
To solve this issue, in parallel with the MFC platforms we have also started to develop a multichannel potentiostat capable of performing all the necessary tests described in (2.4) including impedance measurements.
Impedance is a powerful tool for characterization of MFCs. Impedance meters and analyzers are as expensive as potentiostats. The lack of multichannel impedance analyzers is also a problem towards characterization of MFC arrays.
This paper covers part of our efforts to develop simple inexpensive hardware that would perform impedance measurements. It mainly focuses on the development of the analog front-end that is able to extend and simplify the impedance measurements with a commercially available Integrated Circuit (IC) AD5933. The best impedance measurement based on the improved analog-front-end unit agreed well with results obtained by expensive stand-alone single-channel impedance analyzer used in this work as a reference instrument. This is the first step towards designing a multichannel single chip impedance meter for MFC impedance measurements.

Evaluation of personal contribution:
Author participated in the analog front-end design. Constructed electronic circuits. Participated in the impedance measurements, the data processing, and construction of the figures. The author also partook in the writing and reviewing of the manuscript.

5.3.7 [P7]: Detection of Yogurt Incubation Kinetics by Portable Impedance Converter

This publication is a follow-up to the previous one [P6]. It is a result of our continuous effort to develop custom potentiostat with impedance measurement capability. Compared to previous publication we have moved to a more advanced version of the IC AD5940 which offers potentiostatic and impedance measurements, combined and miniaturized in a single chip.
For the purpose of this publication a development board containing AD5940 IC was used to test ICs capability to measure impedance of a system of microbiological objects during the yogurt incubation. This simple experiment proved the IC suitability for our type of electro-microbiological experiments and will be used in our future prototypes.

Evaluation of personal contribution:
Author participated in the experiment design and set-up. Author provided electrode system. Author partook in writing and reviewing the manuscript.

6 CONCLUSION

The first goal of the thesis, a development of Microbial Fuel Cell array for high throughput screening and characterization of electrogenic microorganisms was accomplished by the production of three generation of devices V_1.0, V_2.0 and V_3.x. The V_1.0 described in [P1] and [P5] had many flaws (5.3.1). These were partially removed in the subsequent V_2.0 version (5.3.2) and resulted in the publication [P2].

Both versions proved to be working but for practical applications many improvements were needed. After learning from previous successes and failures a third version (V_3.x) was designed (Figure 15). This version used the same construction materials and methods but the architecture changed. The cathode was placed at the bottom of the reactor, while the anode was inside the reactor and the top of the reactor remained opened. Such architecture resembled a standard well-plate way closer and allowed very similar handling. Anaerobic conditions were attained by using airtight lid (not depicted), the lid did not meet the liquid, thus V_3.x solved all the previous issues with medium leakage, short circuiting, and cross contamination. On top of that, the device was equipped with integrated pseudo-reference Ag/AgCl electrodes. Due to that, individual MFCs in V_3.x could be fully electrochemically characterized and run in chronoamperometric regime.

The V_3.x has not been documented in any peer-reviewed study yet, however, V_3.0 was well-described, tested, and characterized in a bachelor's thesis supervised by the author [T1]. V_3.0 proved to be reliable and user friendly. The full electrochemical characterization and inoculation with electrogenic microorganisms was performed. The variability between the individual MFCs was determined. R_{int} variability was 25%, OCV 15% and P_{max} 35%. Such variability is satisfactory considering it was the first hand-made prototype and all measurements were done well by well using a single channel potentiostat which resulted in large time difference between the first and last measurement.

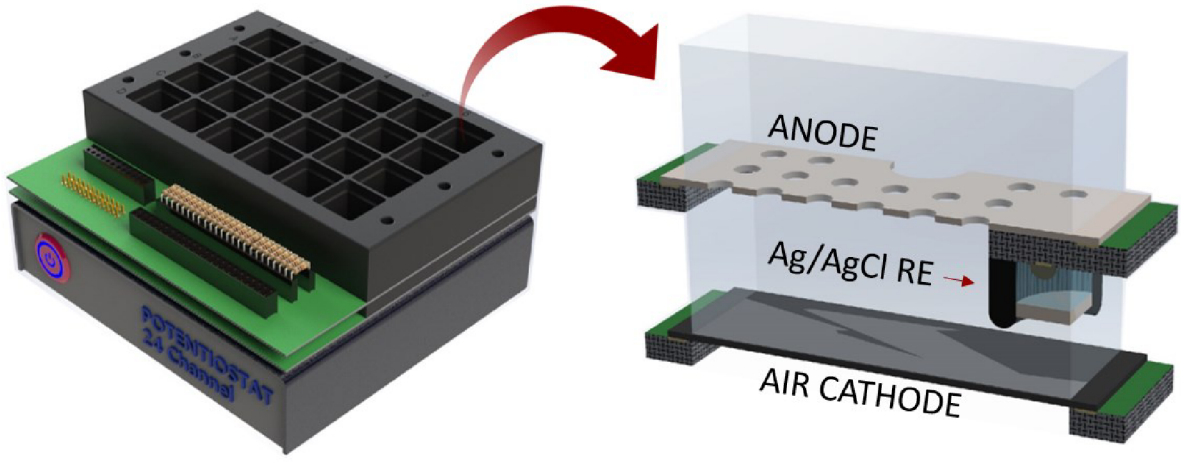

Figure 15: Conceptual description of the 24-well MFC array V_3.x design with integrated 24 channel potentiostat (left) and cross-section view of the singe MFC chamber (right).

Small pseudo-reference Ag/AgCl electrodes were also developed and tested in another bachelor's thesis supervised by the author [T2]. Electrodes based on anodized silver wire or titanium wire dipped in an Ag/AgCl screen printing paste proved to be stable within $\pm$ 5 mV

for the duration of one month in an electrolyte containing constant concentration of chloride ions.
The current V_3.1 version with integrated small pseudo-reference Ag/AgCl electrodes could be considered final working prototype which satisfied all the requirements we had put together in the beginning of this project. For this device to be used as a standard research tool in the laboratories focusing on electromicrobiology a multichannel potentiostat has to be finished and standardized fabrication and assembly process has to be brought to action to supply low-variability, high-quality, reliable devices.

The second goal of the thesis, fabrication of the stimulation platform and electrical stimulation of stem cells towards their directed differentiation was not fully achieved. [P3] The reason lies in the insufficient understanding of the physics behind the electrical stimulation and no prior experience with electrochemical methods required for device characterization and experiment execution (5.3.3). This could be justified by our no previous experience in the field since this project was executed first from all the projects covered in the thesis. Nevertheless, we have learned a lot of things the hard way and the lesson we have taken is highly valuable for our current and upcoming projects.

The third goal of the thesis focused on the study of oxygen reduction reactions during the neurostimulation resulted in the publication [P4]. The main finding is: Oxygen reduction is taking place on all materials and under all direct current and biphasic charge balanced stimulation protocols we have tested!
Oxygen reduction reactions are thus not fully reversible, leading to depletion of oxygen at the electrode surface. Oxygen can be reduced almost entirely leading to hypoxic conditions. On top of that, hydrogen peroxide is generated during this process (Figure 16). The amount of reduced oxygen and produced hydrogen peroxide is highly dependent on the material catalytic activity towards these reactions. This is an important finding and everyone performing a direct electrical stimulation should consider the effects of local hypoxia and generation of hydrogen peroxide.

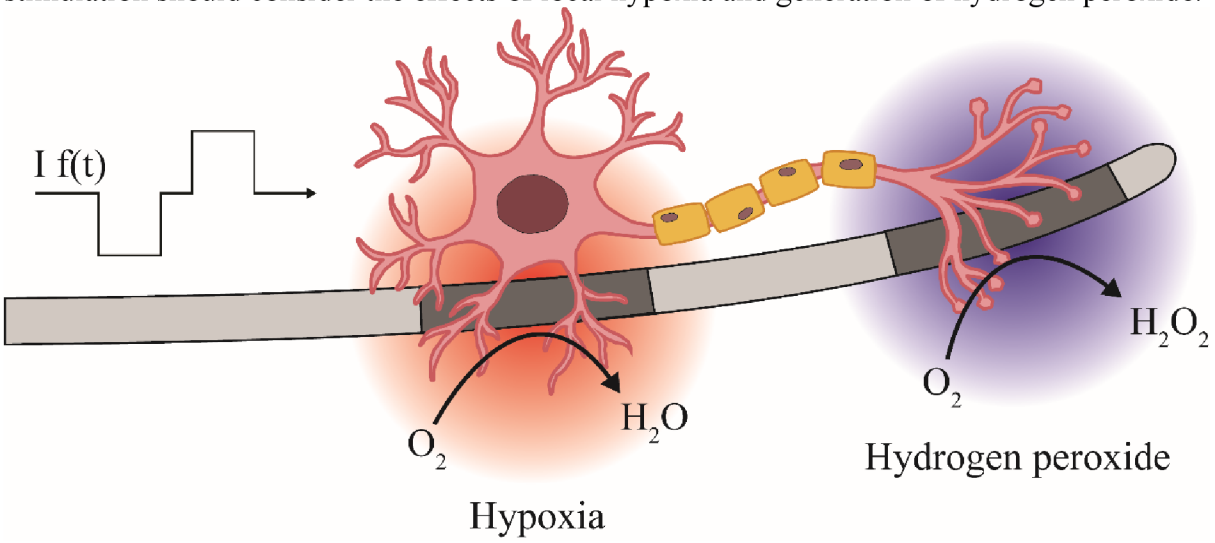

Figure 16: Illustrative demonstration of the oxygen reduction reactions taking place at DBS electrode interfaces.

7 FUTURE PERSPECTIVES

Development of the MFC platform does not end with the publication of this thesis. We have an advanced working prototype which is going to be used, tested, and further improved in collaboration with our partners. Hopefully, it might become trustful and reliable tool used for investigation of electrogenic microorganisms in the future.

Process of developing our own custom hardware, electronics and software showed us a demand for specific devices without suitable equivalent on the market. Our efforts continue towards development of small, affordable, wireless single/multi-channel potentiostats due to the clear demand for such devices way beyond MFC array applications. Also, we have spread our focus to other devices such as highly specific electric current and optical stimulators.

When we have taken look into the water window we have seen more than just oxygen reduction reactions. Water window is not as inert and innocent as it is generally perceived. Our current and future efforts will be directed towards revealing processes happening inside the water window, their possible physiological effects and means of preventing them from happening or using them to our advantage.

We have used a similar approach that we applied to oxygen reduction reactions. We have partially quantified some of the reactions but there is plenty of work to be done. One of the main points to tackle is to quantify hydrogen peroxide evolution by other method than the amperometric sensors due to the cross sensitivity of hydrogen peroxide and hydrogen. Therefore, the amperometric technique can result in overestimation of peroxide values. Next, we would like to explore means to minimize the irreversible faradaic reactions or even to entirely eliminate them by purely capacitive ways of stimulation.

Currently, we are starting to explore possibilities of exploiting the ORRs to our advantage. We see many applications for controlled and local hypoxia, both in research and industrial applications. The same applies for the hydrogen peroxide evolution.

8 REFERENCES

[1] Potter, M. C. (1911). Electrical effects accompanying the decomposition of organic compounds. *Proceedings of the Royal Society of London. Series B, Containing Papers of a Biological Character*, *84*(571), 260-276. https://doi.org/10.1098/rspb.1911.0073

[2] Kim, B. H., Kim, H. J., Hyun, M. S., & Park, D. H. (1999). Direct electrode reaction of Fe (III)-reducing bacterium, Shewanella putrefaciens. *Journal of microbiology and biotechnology*, *1999*, 127-131.

[3] Kim, B. H., Park, D. H., Shin, P. K., Chang, I. S., & Kim, H. J. Mediator-less biofuel cell - US Patent 5,976,719, 1999.

[4] Wang, H., & Ren, Z. J. (2013). A comprehensive review of microbial electrochemical systems as a platform technology. *Biotechnology Advances*, *31*(8), 1796-1807. https://doi.org/10.1016/j.biotechadv.2013.10.001

[5] Logan, B. E., Rossi, R., Ragab, A. 'a, & Saikaly, P. E. (2019). Electroactive microorganisms in bioelectrochemical systems. *Nature Reviews Microbiology*, *17*(5), 307-319. https://doi.org/10.1038/s41579-019-0173-x

[6] Lovley, D. R. (2012). Electromicrobiology. *Annual Review of Microbiology*, *66*(1), 391-409. https://doi.org/10.1146/annurev-micro-092611-150104

[7] Malvankar, N. S., Vargas, M., Nevin, K. P., Franks, A. E., Leang, C., Kim, B. -C., Inoue, K., Mester, T., Covalla, S. F., Johnson, J. P., Rotello, V. M., Tuominen, M. T., & Lovley, D. R. (2011). Tunable metallic-like conductivity in microbial nanowire networks. *Nature Nanotechnology*, *6*(9), 573-579. https://doi.org/10.1038/nnano.2011.119

[8] Logan, B. E., Hamelers, B., Rozendal, R., Schröder, U., Keller, J., Freguia, S., Aelterman, P., Verstraete, W., & Rabaey, K. (2006). Microbial Fuel Cells: Methodology and Technology, *40*(17), 5181-5192. https://doi.org/10.1021/es0605016

[9] Scott, K., & Yu, E. H. (2016). *Microbial Electrochemical and Fuel Cells: Fundamentals and Applications*. Woodhead Publishing.

[10] Alberty, R. A. (2003). *Thermodynamics of Biochemical Reactions*. Wiley Interscience.

[11] Cheng, S., & Logan, B. E. (2007). Ammonia treatment of carbon cloth anodes to enhance power generation of microbial fuel cells. *Electrochemistry Communications*, *9*(3), 492-496. https://doi.org/10.1016/j.elecom.2006.10.023

[12] Logan, B. E., & Regan, J. M. (2006). Microbial Fuel Cells—Challenges and Applications, *40*(17), 5172-5180. https://doi.org/10.1021/es0627592

[13] Logan, B. E. (2008). *Microbial Fuel Cells*. Wiley Interscience.

[14] Gorby, Y. A., Yanina, S., McLean, J. S., Rosso, K. M., Moyles, D., Dohnalkova, A., Beveridge, T. J., Chang, I. S., Kim, B. H., Kim, K. S., Culley, D. E., Reed, S. B., Romine, M. F., Saffarini, D. A., Hill, E. A., Shi, L., Elias, D. A., Kennedy, D. W., Pinchuk, G., et al. (2006). Electrically conductive bacterial nanowires produced by Shewanella oneidensis

strain MR-1 and other microorganisms. *Proceedings of the National Academy of Sciences*, *103*(30), 11358-11363. https://doi.org/10.1073/pnas.0604517103

[15] El-Naggar, M. Y., & Finkel, S. E. (2013). Live wires. *The Scientist*, *2013*(5), 38-44.

[16] Rabaey, K., Boon, N., Höfte, M., & Verstraete, W. (2005). Microbial Phenazine Production Enhances Electron Transfer in Biofuel Cells, *39*(9), 3401-3408. https://doi.org/10.1021/es048563o

[17] von Canstein, H., Ogawa, J., Shimizu, S., & Lloyd, J. R. (2008). Secretion of Flavins by Shewanella Species and Their Role in Extracellular Electron Transfer. *Applied and Environmental Microbiology*, *74*(3), 615-623. https://doi.org/10.1128/AEM.01387-07

[18] Baron, D., LaBelle, E., Coursolle, D., Gralnick, J. A., & Bond, D. R. (2009). Electrochemical Measurement of Electron Transfer Kinetics by Shewanella oneidensis MR-1. *Journal of Biological Chemistry*, *284*(42), 28865-28873. https://doi.org/10.1074/jbc.M109.043455

[19] Lovley, D. R. (2012). Electromicrobiology. *Annual Review of Microbiology*, *66*(1), 391-409. https://doi.org/10.1146/annurev-micro-092611-150104

[20] Edwards, M. J., White, G. F., Butt, J. N., Richardson, D. J., & Clarke, T. A. (2020). The Crystal Structure of a Biological Insulated Transmembrane Molecular Wire. *Cell*, *181*(3), 665-673.e10. https://doi.org/10.1016/j.cell.2020.03.032

[21] El-Naggar, M. Y., Wanger, G., Leung, K. M., Yuzvinsky, T. D., Southam, G., Yang, J., Lau, W. M., Nealson, K. H., & Gorby, Y. A. (2010). Electrical transport along bacterial nanowires from Shewanella oneidensis MR-1. *Proceedings of the National Academy of Sciences*, *107*(42), 18127-18131. https://doi.org/10.1073/pnas.1004880107

[22] Lampa-Pastirk, S., Veazey, J. P., Walsh, K. A., Feliciano, G. T., Steidl, R. J., Tessmer, S. H., & Reguera, G. (2016). Thermally activated charge transport in microbial protein nanowires. Scientific Reports, 6(1). https://doi.org/10.1038/srep23517

[23] Coropceanu, V., Cornil, J., da Silva Filho, D. A., Olivier, Y., Silbey, R., & Brédas, J. -L. (2007). Charge Transport in Organic Semiconductors. *Chemical Reviews*, *107*(4), 926-952. https://doi.org/10.1021/cr050140x

[24] Thapa, B. S., Kim, T., Pandit, S., Song, Y. E., Afsharian, Y. P., Rahimnejad, M., Kim, J. R., & Oh, S. -E. (2021). Overview of electroactive microorganisms and electron transfer mechanisms in microbial electrochemistry. *Bioresource Technology*. https://doi.org/10.1016/j.biortech.2021.126579

[25] Vargas, M., Malvankar, N. S., Tremblay, P. -L., Leang, C., Smith, J. A., Patel, P., Synoeyenbos-West, O., Nevin, K. P., Lovley, D. R., & Giovannoni, S. J. (2013). Aromatic Amino Acids Required for Pili Conductivity and Long-Range Extracellular Electron Transport in Geobacter sulfurreducens. *MBio*, *4*(2). https://doi.org/10.1128/mBio.00105-13

[26] Malvankar, N. S., Vargas, M., Nevin, K. P., Franks, A. E., Leang, C., Kim, B. -C., Inoue, K., Mester, T., Covalla, S. F., Johnson, J. P., Rotello, V. M., Tuominen, M. T., & Lovley,

D. R. (2011). Tunable metallic-like conductivity in microbial nanowire networks. *Nature Nanotechnology*, *6*(9), 573-579. https://doi.org/10.1038/nnano.2011.119

[27] Logan, B. E. (2009). Exoelectrogenic bacteria that power microbial fuel cells. Nature Reviews Microbiology, 7(5), 375-381. https://doi.org/10.1038/nrmicro2113

[28] Baudler, A., Schmidt, I., Langner, M., Greiner, A., & Schröder, U. (2015). Does it have to be carbon? Metal anodes in microbial fuel cells and related bioelectrochemical systems, *8*(7), 2048-2055. https://doi.org/10.1039/C5EE00866B

[29] Chaudhuri, S. K., & Lovley, D. R. (2003). Electricity generation by direct oxidation of glucose in mediatorless microbial fuel cells. *Nature Biotechnology*, *21*(10), 1229-1232. https://doi.org/10.1038/nbt867

[30] Cheng, S., & Logan, B. E. (2007). Ammonia treatment of carbon cloth anodes to enhance power generation of microbial fuel cells. *Electrochemistry Communications*, *9*(3), 492-496. https://doi.org/10.1016/j.elecom.2006.10.023

[31] Slate, A. J., Whitehead, K. A., Brownson, D. A. C., & Banks, C. E. (2019). Microbial fuel cells: An overview of current technology. *Renewable and Sustainable Energy Reviews*, *101*, 60-81. https://doi.org/10.1016/j.rser.2018.09.044

[32] Palanisamy, G., Jung, H. -Y., Sadhasivam, T., Kurkuri, M. D., Kim, S. C., & Roh, S. -H. (2019). A comprehensive review on microbial fuel cell technologies: Processes, utilization, and advanced developments in electrodes and membranes. *Journal of Cleaner Production*, *221*, 598-621. https://doi.org/10.1016/j.jclepro.2019.02.172

[33] Ren, H., Tian, H., Gardner, C. L., Ren, T. -L., & Chae, J. (2016). A miniaturized microbial fuel cell with three-dimensional graphene macroporous scaffold anode demonstrating a record power density of over 10 000 W m −3 . *Nanoscale*, *8*(6), 3539-3547. https://doi.org/10.1039/C5NR07267K

[34] Fan, Y., Sharbrough, E., & Liu, H. (2008). Quantification of the Internal Resistance Distribution of Microbial Fuel Cells, *42*(21), 8101-8107. https://doi.org/10.1021/es801229j

[35] Manohar, A. K., Mansfeld, F., & Liu, H. (2009). The internal resistance of a microbial fuel cell and its dependence on cell design and operating conditions. *Electrochimica Acta*, *54*(6), 1664-1670. https://doi.org/10.1016/j.electacta.2008.06.047

[36] Hoogers, G. (2004). *Fuel Cell Technology Handbook* (Seventh Edition). CRC Press, 2002.

[37] He, Z., Wagner, N., Minteer, S. D., & Angenent, L. T. (2006). An Upflow Microbial Fuel Cell with an Interior Cathode: Assessment of the Internal Resistance by Impedance Spectroscopy. *Electrochimica Acta*, *40*(17), 5212-5217. https://doi.org/10.1021/es060394f

[38] Rabaey, K., Boon, N., Siciliano, S. D., Verhaege, M., & Verstraete, W. (2004). Biofuel Cells Select for Microbial Consortia That Self-Mediate Electron Transfer. *Applied and Environmental Microbiology*, *70*(9), 5373-5382. https://doi.org/10.1128/AEM.70.9.5373-5382.2004

[39] Biffinger, J., Ribbens, M., Ringeisen, B., Pietron, J., Finkel, S., & Nealson, K. (2009). Characterization of electrochemically active bacteria utilizing a high-throughput voltage-based screening assay. *Biotechnology and Bioengineering*, *102*(2), 436-444. https://doi.org/10.1002/bit.22072

[40] Hou, H., Li, L., Cho, Y., de Figueiredo, P., Han, A., & Fox, D. (2009). Microfabricated Microbial Fuel Cell Arrays Reveal Electrochemically Active Microbes. *PLoS ONE*, *4*(8). https://doi.org/10.1371/journal.pone.0006570

[41] Hou, H., Li, L., de Figueiredo, P., & Han, A. (2011). Air-cathode microbial fuel cell array: A device for identifying and characterizing electrochemically active microbes. *Biosensors and Bioelectronics*, *26*(5), 2680-2684. https://doi.org/10.1016/j.bios.2010.06.037

[42] Hou, H., Li, L., Ceylan, C. Ü., Haynes, A., Cope, J., Wilkinson, H. H., Erbay, C., Figueiredo, P. de, & Han, A. (2012). A microfluidic microbial fuel cell array that supports long-term multiplexed analyses of electricigens. *Lab on a Chip*, *12*(20). https://doi.org/10.1039/c2lc40405b

[43] Mukherjee, S., Su, S., Panmanee, W., Irvin, R. T., Hassett, D. J., & Choi, S. (2013). A microliter-scale microbial fuel cell array for bacterial electrogenic screening. *Sensors and Actuators A: Physical*, *201*, 532-537. https://doi.org/10.1016/j.sna.2012.10.025

[44] Fraiwan, A., Hassett, D. J., & Choi, S. (2014). Effects of light on the performance of electricity-producing bacteria in a miniaturized microbial fuel cell array. *Journal of Renewable and Sustainable Energy*, *6*(6). https://doi.org/10.1063/1.4902094

[45] Choi, G., Hassett, D. J., & Choi, S. (2015). A paper-based microbial fuel cell array for rapid and high-throughput screening of electricity-producing bacteria. *The Analyst*, *140*(12), 4277-4283. https://doi.org/10.1039/C5AN00492F

[46] Gao, Y., Hassett, D. J., & Choi, S. (2017). Rapid Characterization of Bacterial Electrogenicity Using a Single-Sheet Paper-Based Electrofluidic Array. *Frontiers in Bioengineering and Biotechnology*, *5*. https://doi.org/10.3389/fbioe.2017.00044

[47] Tahernia, M., Mohammadifar, M., Gao, Y., Panmanee, W., Hassett, D. J., & Choi, S. (2020). A 96-well high-throughput, rapid-screening platform of extracellular electron transfer in microbial fuel cells. *Biosensors and Bioelectronics*, *162*. https://doi.org/10.1016/j.bios.2020.112259

[48] Molderez, T. R., Prévoteau, A., Ceyssens, F., Verhelst, M., & Rabaey, K. (2021). A chip-based 128-channel potentiostat for high-throughput studies of bioelectrochemical systems: Optimal electrode potentials for anodic biofilms. *Biosensors and Bioelectronics*, *174*. https://doi.org/10.1016/j.bios.2020.112813

[49] Molderez, T. R., Rabaey, K., & Verhelst, M. (2021). A Scalable 128-Channel, Time-Multiplexed Potentiostat for Parallel Electrochemical Experiments. *IEEE Transactions on Circuits and Systems I: Regular Papers*, *68*(3), 1068-1079. https://doi.org/10.1109/TCSI.2020.3048740

[50] Frank, R., Prönnecke, C., Azendorf, R., Jahnke, H. -G., Beck-Sickinger, A. G., & Robitzki, A. A. (2020). Advanced 96-microtiter plate based bioelectrochemical platform reveals molecular short cut of electron flow in cytochrome P450 enzyme. *Lab on a Chip*, *20*(8), 1449-1460. https://doi.org/10.1039/C9LC01220

[51] Kuchenbuch, A., Frank, R., Ramos, J. V., Jahnke, H. -G., & Harnisch, F. (2022). Electrochemical Microwell Plate to Study Electroactive Microorganisms in Parallel and Real-Time. *Frontiers in Bioengineering and Biotechnology*, *9*. https://doi.org/10.3389/fbioe.2021.821734

[52] Galvani, Luigi. (1791). Aloysii Galvani De viribus electricitatis in motu musculari commentarius. https://doi.org/10.5479/sil.324681.39088000932442.

[53] Levin, M. (2012). Molecular bioelectricity in developmental biology: New tools and recent discoveries. *BioEssays*, *34*(3), 205-217. https://doi.org/10.1002/bies.201100136

[54] Thrivikraman, G., Boda, S. K., & Basu, B. (2018). Unraveling the mechanistic effects of electric field stimulation towards directing stem cell fate and function: A tissue engineering perspective. *Biomaterials*, *150*, 60-86. https://doi.org/10.1016/j.biomaterials.2017.10.003

[55] Hodgkin, A. L., & Huxley, A. F. (1952). Currents carried by sodium and potassium ions through the membrane of the giant axon of Loligo. *The Journal of Physiology*, *116*(4), 449-472. https://doi.org/10.1113/jphysiol.1952.sp004717

[56] Hodgkin, A. L., Huxley, A. F., & Katz, B. (1952). Measurement of current-voltage relations in the membrane of the giant axon of Loligo. *The Journal of Physiology*, *116*(4), 424-448. https://doi.org/10.1113/jphysiol.1952.sp004716

[57] Hodgkin, A. L., Huxley, A. F., & Katz, B. (1952). The components of membrane conductance in the giant axon of Loligo. *The Journal of Physiology*, *116*(4), 473-496. https://doi.org/10.1113/jphysiol.1952.sp004718

[58] Hodgkin, A. L., Huxley, A. F., & Katz, B. (1952). The dual effect of membrane potential on sodium conductance in the giant axon of Loligo. *The Journal of Physiology*, *116*(4), 497-506. https://doi.org/10.1113/jphysiol.1952.sp004719

[59] Hodgkin, A. L., Huxley, A. F., & Katz, B. (1952). A quantitative description of membrane current and its application to conduction and excitation in nerve. *The Journal of Physiology*, *117*(4), 500-544. https://doi.org/10.1113/jphysiol.1952.sp004764

[60] Schoen, I., & Fromherz, P. (2007). The Mechanism of Extracellular Stimulation of Nerve Cells on an Electrolyte-Oxide-Semiconductor Capacitor. *Biophysical Journal*, *92*(3), 1096-1111. https://doi.org/10.1529/biophysj.106.094763

[61] Merrill, D. R. (2010). The Electrochemistry of Charge Injection at the Electrode/Tissue Interface. *Implantable Neural Prostheses 2*, *92*(3), 85-138. https://doi.org/10.1007/978-0-387-98120-8_4

[62] Brummer, S. B., & Turner, M. J. (1977). Electrochemical Considerations for Safe Electrical Stimulation of the Nervous System with Platinum Electrodes. IEEE

Transactions on Biomedical Engineering, BME-24(1), 59-63. https://doi.org/10.1109/TBME.1977.326218

[63] Merrill, D. R., Bikson, M., & Jefferys, J. G. R. (2005). Electrical stimulation of excitable tissue: design of efficacious and safe protocols. Journal of Neuroscience Methods, 141(2), 171-198. https://doi.org/10.1016/j.jneumeth.2004.10.020

[64] Günter, C., Delbeke, J., & Ortiz-Catalan, M. (2019). Safety of long-term electrical peripheral nerve stimulation: review of the state of the art. Journal of NeuroEngineering and Rehabilitation, 16(1), 171-198. https://doi.org/10.1186/s12984-018-0474-8

[65] Cogan, S. F. (2008). Neural Stimulation and Recording Electrodes. *Annual Review of Biomedical Engineering*, *10*(1), 275-309. https://doi.org/10.1146/annurev.bioeng.10.061807.160518

[66] Shepherd, R. K., Carter, P. M., Dalrymple, A. N., Enke, Y. L., Wise, A. K., Nguyen, T., Firth, J., Thompson, A., & Fallon, J. B. (2021). Platinum dissolution and tissue response following long-term electrical stimulation at high charge densities: review of the state of the art. *Journal of Neural Engineering*, *18*(3), 171-198. https://doi.org/10.1088/1741-2552/abe5ba

[67] Morton, S. L., Daroux, M. L., Mortimer, J. T., Enke, Y. L., Wise, A. K., Nguyen, T., Firth, J., Thompson, A., & Fallon, J. B. (1994). The Role of Oxygen Reduction in Electrical Stimulation of Neural Tissue: review of the state of the art. Journal of The Electrochemical Society, 141(1), 122-130. https://doi.org/10.1149/1.2054671

[68] Cogan, S. F., Ehrlich, J., Plante, T. D., Gingerich, M. D., Shire, D. B., Nguyen, T., Firth, J., Thompson, A., & Fallon, J. B. (2010). Contribution of Oxygen Reduction to Charge Injection on Platinum and Sputtered Iridium Oxide Neural Stimulation Electrodes: review of the state of the art. *IEEE Transactions on Biomedical Engineering*, *57*(9), 2313-2321. https://doi.org/10.1109/TBME.2010.2050690

[69] Musa, S., Rand, D. R., Bartic, C., Eberle, W., Nuttin, B., Borghs, G., Firth, J., Thompson, A., & Fallon, J. B. (2011). Coulometric Detection of Irreversible Electrochemical Reactions Occurring at Pt Microelectrodes Used for Neural Stimulation: review of the state of the art. Analytical Chemistry, 83(11), 4012-4022. https://doi.org/10.1021/ac103037u

[70] Dijk, G., Ruigrok, H. J., O'Connor, R. P., Eberle, W., Nuttin, B., Borghs, G., Firth, J., Thompson, A., & Fallon, J. B. (2021). PEDOT: PSS-Coated Stimulation Electrodes Attenuate Irreversible Electrochemical Events and Reduce Cell Electropermeabilization. *Advanced Materials Interfaces*, *8*(19), 4012-4022. https://doi.org/10.1002/admi.202100214

[71] Wheeler, B. C., & Nam, Y. (2011). In Vitro Microelectrode Array Technology and Neural Recordings. *Critical Reviews™ in Biomedical Engineering*, *39*(1), 45-61. https://doi.org/10.1615/CritRevBiomedEng.v39.i1.40

[72] Miller, K. J., Hermes, D., & Staff, N. P. (2020). The current state of electrocorticography-based brain–computer interfaces. *Neurosurgical Focus*, *49*(1), 45-61. https://doi.org/10.3171/2020.4.FOCUS20185

[73] Qing Bai, K. J., Wise, K. D., & Staff, N. P. (2020). Single-unit neural recording with active microelectrode arrays. *IEEE Transactions on Biomedical Engineering*, *48*(8), 911-920. https://doi.org/10.1109/10.936367

[74] Rousche, P. J., Normann, R. A., & Staff, N. P. (1998). Chronic recording capability of the Utah Intracortical Electrode Array in cat sensory cortex. *Journal of Neuroscience Methods*, *82*(1), 1-15. https://doi.org/10.1016/S0165-0270(98)00031-4

[75] Hanson, T., Diaz-Botia, C., Kharazia, V., Maharbiz, M., & Sabes, P. The "sewing machine" for minimally invasive neural recording. *BioRxiv*. https://doi.org/https://doi.org/10.1101/578542

[76] Krauss, J. K., Lipsman, N., Aziz, T., Boutet, A., Brown, P., Chang, J. W., Davidson, B., Grill, W. M., Hariz, M. I., Horn, A., Schulder, M., Mammis, A., Tass, P. A., Volkmann, J., & Lozano, A. M. (2021). Technology of deep brain stimulation: current status and future directions. *Nature Reviews Neurology*, *17*(2), 75-87. https://doi.org/10.1038/s41582-020-00426-z

[77] Fan-Gang Zeng, J. K., Rebscher, S., Harrison, W., Xiaoan Sun, A., Haihong Feng, P., Chang, J. W., Davidson, B., Grill, W. M., Hariz, M. I., Horn, A., Schulder, M., Mammis, A., Tass, P. A., Volkmann, J., & Lozano, A. M. (2008). Cochlear Implants: System Design, Integration, and Evaluation. *IEEE Reviews in Biomedical Engineering*, *1*(2), 115-142. https://doi.org/10.1109/RBME.2008.2008250

[78] Mills, J. O., Jalil, A., Stanga, P. E., Xiaoan Sun, A., Haihong Feng, P., Chang, J. W., Davidson, B., Grill, W. M., Hariz, M. I., Horn, A., Schulder, M., Mammis, A., Tass, P. A., Volkmann, J., & Lozano, A. M. (2017). Electronic retinal implants and artificial vision: journey and present. *Eye*, *31*(10), 1383-1398. https://doi.org/10.1038/eye.2017.65

[79] Oxley, T. J., Opie, N. L., John, S. E., Rind, G. S., Ronayne, S. M., Wheeler, T. L., Judy, J. W., McDonald, A. J., Dornom, A., Lovell, T. J. H., Steward, C., Garrett, D. J., Moffat, B. A., Lui, E. H., Yassi, N., Campbell, B. C. V., Wong, Y. T., Fox, K. E., Nurse, E. S., et al. (2016). Minimally invasive endovascular stent-electrode array for high-fidelity, chronic recordings of cortical neural activity: journey and present. *Nature Biotechnology*, *34*(3), 320-327. https://doi.org/10.1038/nbt.3428

[80] Navarro, X., Krueger, T. B., Lago, N., Micera, S., Stieglitz, T., Dario, P. (2005). A critical review of interfaces with the peripheral nervous system for the control of neuroprostheses and hybrid bionic systems: journey and present. *Journal of the Peripheral Nervous System*, *10*(3), 229-258. https://doi.org/10.1111/j.1085-9489.2005.10303.x

[81] Weiland, J. D., Anderson, D. J., Humayun, M. S. (2002). In vitro electrical properties for iridium oxide versus titanium nitride stimulating electrodes: journey and present. *IEEE Transactions on Biomedical Engineering*, *49*(12), 1574-1579. https://doi.org/10.1109/TBME.2002.805487

[82] Schmidt, E. M., Hambrecht, F. T., McIntosh, J. S. (1982). Intracortical capacitor electrodes: preliminary evaluation. *Journal of Neuroscience Methods*, *5*(1-2), 33-39. https://doi.org/10.1016/0165-0270(82)90048-6

[83] Becker, M. T. (2021). Charge injection capacity of ferroelectric microelectrodes for bioelectronic applications: preliminary evaluation. *AIP Advances*, *11*(6), 33-39. https://doi.org/10.1063/5.0049202

[84] Rose, T. L., Robblee, L. S. (2021). Electrical stimulation with Pt electrodes. VIII. Electrochemically safe charge injection limits with 0.2 ms pulses (neuronal application): preliminary evaluation. *IEEE Transactions on Biomedical Engineering*, *37*(11), 1118-1120. https://doi.org/10.1109/10.61038

[85] Robblee, L. S., Lefko, J. L., Brummer, S. B. (1983). Activated Ir: An Electrode Suitable for Reversible Charge Injection in Saline Solution. *Journal of The Electrochemical Society*, *130*(3), 731-733. https://doi.org/10.1149/1.2119793

[86] Klein, J. D., Clauson, S. L., Cogan, S. F. (1989). Morphology and charge capacity of sputtered iridium oxide films: An Electrode Suitable for Reversible Charge Injection in Saline Solution. *Journal of The Electrochemical Society*, *7*(5), 3043-3047. https://doi.org/10.1116/1.576313

[87] Robblee, L. S., Mangaudis, M. J., Lasinsky, E. D., Kimball, A. G., Brummer, S. B. (1985). Charge Injection Properties of Thermally-Prepared Iridium Oxide Films: An Electrode Suitable for Reversible Charge Injection in Saline Solution. *MRS Proceedings*, *55*(5), 3043-3047. https://doi.org/10.1557/PROC-55-303

[88] Meyer, R. D., Cogan, S. F., Nguyen, T. H., Rauh, R. D. (2001). Electrodeposited iridium oxide for neural stimulation and recording electrodes: An Electrode Suitable for Reversible Charge Injection in Saline Solution. *IEEE Transactions on Neural Systems and Rehabilitation Engineering*, *9*(1), 2-11. https://doi.org/10.1109/7333.918271

[89] Boehler, C., Carli, S., Fadiga, L., Stieglitz, T., & Asplund, M. (2020). Tutorial: guidelines for standardized performance tests for electrodes intended for neural interfaces and bioelectronics. *Nature Protocols*, *15*(11), 3557-3578. https://doi.org/10.1038/s41596-020-0389-2

[90] Weltin, A., & Kieninger, J. (2021). Electrochemical methods for neural interface electrodes. *Journal of Neural Engineering*, *18*(5). https://doi.org/10.1088/1741-2552/ac28d5

[91] Musa, S., Rand, D. R., Bartic, C., Eberle, W., Nuttin, B., & Borghs, G. (2011). Coulometric Detection of Irreversible Electrochemical Reactions Occurring at Pt Microelectrodes Used for Neural Stimulation. *Analytical Chemistry*, *83*(11), 4012-4022. https://doi.org/10.1021/ac103037u

[92] Jaffe, L. F., & Nuccitelli, R. (1974). AN ULTRASENSITIVE VIBRATING PROBE FOR MEASURING STEADY EXTRACELLULAR CURRENTS. *Journal of Cell Biology*, *63*(2), 614-628. https://doi.org/10.1083/jcb.63.2.614

[93] Nuccitelli, R. (1992). Endogenous ionic currents and DC electric fields in multicellular animal tissues. *Bioelectromagnetics*, *13*(S1), 147-157. https://doi.org/10.1002/bem.2250130714

[94] Levin, M., & Bement, W. (2014). Molecular bioelectricity: how endogenous voltage potentials control cell behavior and instruct pattern regulation in vivo. *Molecular Biology of the Cell*, *25*(24), 3835-3850. https://doi.org/10.1091/mbc.e13-12-0708

[95] Messerli, M. A., & Graham, D. M. (2011). Extracellular Electrical Fields Direct Wound Healing and Regeneration. *The Biological Bulletin*, *221*(1), 79-92. https://doi.org/10.1086/BBLv221n1p79

[96] Heng, B. C., Cao, T., Stanton, L. W., Robson, P., & Olsen, B. (2004). Strategies for Directing the Differentiation of Stem Cells Into the Osteogenic Lineage In Vitro. *Journal of Bone and Mineral Research*, *19*(9), 1379-1394. https://doi.org/10.1359/JBMR.040714

[97] Chen, C., Bai, X., Ding, Y., & Lee, I. -S. (2019). Electrical stimulation as a novel tool for regulating cell behavior in tissue engineering. *Biomaterials Research*, *23*(1). https://doi.org/10.1186/s40824-019-0176-8

[98] Yamada, M., Tanemura, K., Okada, S., Iwanami, A., Nakamura, M., Mizuno, H., Ozawa, M., Ohyama-Goto, R., Kitamura, N., Kawano, M., Tan-Takeuchi, K., Ohtsuka, C., Miyawaki, A., Takashima, A., Ogawa, M., Toyama, Y., Okano, H., & Kondo, T. (2007). Electrical Stimulation Modulates Fate Determination of Differentiating Embryonic Stem Cells. *Stem Cells*, *25*(3). https://doi.org/10.1634/stemcells.2006-0011

[99] McCaig, C. D., Rajnicek, A. M., Song, B., & Zhao, M. (2005). Controlling Cell Behavior Electrically: Current Views and Future Potential. *Physiological Reviews*, *85*(3), 943-978. https://doi.org/10.1152/physrev.00020.2004

[100] Serena, E., Figallo, E., Tandon, N., Cannizzaro, C., Gerecht, S., Elvassore, N., & Vunjak-Novakovic, G. (2009). Electrical stimulation of human embryonic stem cells: Cardiac differentiation and the generation of reactive oxygen species. *Experimental Cell Research*, *315*(20), 3611-3619. https://doi.org/10.1016/j.yexcr.2009.08.015

[101] Díaz-Vegas, A., Campos, C. A., Contreras-Ferrat, A., Casas, M., Buvinic, S., Jaimovich, E., Espinosa, A., & Csernoch, L. (2015). ROS Production via P2Y1-PKC-NOX2 Is Triggered by Extracellular ATP after Electrical Stimulation of Skeletal Muscle Cells. *PLOS ONE*, *10*(6). https://doi.org/10.1371/journal.pone.0129882

[102] Owusu-Ansah, E., & Banerjee, U. (2009). Reactive oxygen species prime Drosophila haematopoietic progenitors for differentiation. *Nature*, *461*(7263), 537-541. https://doi.org/10.1038/nature08313

[103] Schmelter, M., Ateghang, B., Helmig, S., Wartenberg, M., Sauer, H., Schmelter, M., Ateghang, B., Helmig, S., Wartenberg, M., & Sauer, H. (2006). Embryonic stem cells utilize reactive oxygen species as transducers of mechanical strain-induced cardiovascular differentiation. *The FASEB Journal*, *20*(8), 1182-1184. https://doi.org/10.1096/fj.05-4723fje

[104] Sart, S., Song, L., & Li, Y. (2015). Controlling Redox Status for Stem Cell Survival, Expansion, and Differentiation. *Oxidative Medicine and Cellular Longevity*, *2015*, 1-14. https://doi.org/10.1155/2015/105135

[105] Liu, H., Zhang, H., Iles, K. E., Rinna, A., Merrill, G., Yodoi, J., Torres, M., & Forman, H. J. (2009). The Adp-stimulated Nadph Oxidase Activates The Ask-1/mkk4/jnk Pathway In Alveolar Macrophages. *Free Radical Research*, *40*(8), 865-874. https://doi.org/10.1080/10715760600758514

[106] Wolf-Goldberg, T., Barbul, A., Ben-Dov, N., & Korenstein, R. (2013). Low electric fields induce ligand-independent activation of EGF receptor and ERK via electrochemical elevation of H and ROS concentrations. *Biochimica et Biophysica Acta (BBA) - Molecular Cell Research*, *1833*(6), 1396-1408. https://doi.org/10.1016/j.bbamcr.2013.02.011

[107] Sies, H. (2017). Hydrogen peroxide as a central redox signaling molecule in physiological oxidative stress: Oxidative eustress. *Redox Biology*, *11*, 613-619. https://doi.org/10.1016/j.redox.2016.12.035

[108] Antunes, F., & Brito, P. M. (2017). Quantitative biology of hydrogen peroxide signaling. *Redox Biology*, *13*, 1-7. https://doi.org/10.1016/j.redox.2017.04.039

[109] Tandon, N., Cannizzaro, C., Chao, P. -H. G., Maidhof, R., Marsano, A., Au, H. T. H., Radisic, M., & Vunjak-Novakovic, G. (2009). Electrical stimulation systems for cardiac tissue engineering. *Nature Protocols*, *4*(2), 155-173. https://doi.org/10.1038/nprot.2008.183

[110] Balint, R., Cassidy, N. J., & Cartmell, S. H. (2013). Electrical Stimulation: A Novel Tool for Tissue Engineering. *Tissue Engineering Part B: Reviews*, *19*(1), 48-57. https://doi.org/10.1089/ten.teb.2012.0183

9 ABBREAVIATIONS AND SYMBOLS LIST

BES	Bioelectrochemical System
MFC	Microbial Fuel Cell
PEM	Proton Exchange Membrane
CEM	Cation Exchange Membrane
PCB	Printed Circuit Board
IC	Integrated Circuit
P	Electric power
I	Electric current
U	Voltage
SHE	Standard Hydrogen Electrode
E_{emf}	Electromotive force
R	Universal gas constant
ΔG	Gibbs free energy
T	Temperature
n	number of electrons involved
F	Faraday's constant
Q	reaction quotient
OCV	Open Circuit Voltage
R_{int}	Internal resistance
P_{max}	Maximum power
SEM	Scanning electron Microscopy
EIS	Electrochemical Impedance Spectroscopy
CV	Cyclic Voltammetry
AP	Action Potential
ATP	Adenosine triphosphate
V_m	Membrane potential
PDMS	Polydimethylsiloxane
PEN	Polyethylene naphthalate
PEDOT:PSS	poly(3,4-ethylenedioxythiophene) polystyrene sulfonate
SW	Software
CAD	Computer Aid Design
RE	Reference electrode
CSC	Charge Storage Capacity
C_{dl}	double layer capacitance
ADC	Analog-to-digital convertor
CIC_{max}	maximum Charge Injection Capacity
(R_s)	solution resistivity
(R_{ct})	charge transfer resistivity
(Z_f)	faradaic impedance
ROS	Reactive Oxygen Species

10 CURRICULUM VITAE

Education

2017 – present
Brno University of Technology
Faculty of Chemistry

- Degree: PhD
- Programme: Materials Science
- Specialization: Materials for bioelectronics

2015 – 2017
Brno University of Technology
Faculty of Chemistry

- Degree: MSc.
- Programme: Applied Chemistry
- Specialization: Organic electronics; biosensors.
- Graduated with honors

2012 – 2015
Brno University of Technology
Faculty of Chemistry

- Degree: B.Sc.
- Programme: Applied Chemistry
- Specialization: Organic electronics; biosensors.

Internships

November 2018 – January 2019
September 2019 – November 2019
Okinawa Institute of Science and Technology (OIST)
Gorianin unit
Junior researcher

- Development of a platform for high throughput screening and characterization of electrogenic microorganisms.

Professional experience

2015 – present
Science & Technology Club
Nonprofit organization
Co-founder

- Popularization of science

October 2014 – March 2016
Opifer Ltd.
Early stage Venture capital company
Project manager

- Participation in the founding and development of 5 startup companies.
- Evaluation of new investment opportunities.

January 2021 – present
Central European Institute of Technology (CEITEC)
Bioelectronics Materials and Devices – Eric D. Glowacki
Researcher

- Electrochemical characterization of neural interfaces.

11 SELECTED PUBLICATIONS

Scientific papers comprising the main experimental part of the thesis.

frontiers | Frontiers in Microbiology

TYPE Original Research
PUBLISHED xx xx 2022
DOI 10.3389/fmicb.2022.951044

OPEN ACCESS

EDITED BY
Moupriya Nag,
University of Engineering and Management, India

REVIEWED BY
Liyuan Ma,
China University of Geosciences Wuhan, China
Chirayu Desai,
Gujarat Biotechnology University (GBU), India

*CORRESPONDENCE
Lukasz Szydlowski
lmszydlowski@gmail.com

SPECIALTY SECTION
This article was submitted to Microbiotechnology, a section of the journal Frontiers in Microbiology

RECEIVED 23 May 2022
ACCEPTED 17 August 2022
PUBLISHED xx xx 2022

CITATION
Szydlowski L, Ehlich J, Szczerbiak P, Shibata N and Goryanin I (2022) Novel species identification and deep functional annotation of electrogenic biofilms, selectively enriched in a microbial fuel cell array.
Front. Microbiol. 13:951044.
doi: 10.3389/fmicb.2022.951044

Novel species identification and deep functional annotation of electrogenic biofilms, selectively enriched in a microbial fuel cell array

Lukasz Szydlowski[1,2]*, Jiri Ehlich[3], Pawel Szczerbiak[2], Noriko Shibata[1] and Igor Goryanin[1,4,5]

[1]Biological Systems Unit, Okinawa Institute of Science and Technology, Onna, Japan, [2]Malopolska Centre of Biotechnology, Jagiellonian University, Krakow, Poland, [3]Faculty of Chemistry, Brno University of Technology, Brno, Czechia, [4]School of Informatics, University of Edinburgh, Edinburgh, United Kingdom, [5]Tianjin Institute for Industrial Biotechnology, Tianjin, China

In this study, electrogenic microbial communities originating from a single source were multiplied using our custom-made, 96-well-plate-based microbial fuel cell (MFC) array. Developed communities operated under different pH conditions and produced currents up to 19.4 A/m3 (0.6 A/m2) within 2 days ofinoculation. Microscopic observations [combined scanning electron microscopy (SEM) and energy dispersive spectroscopy (EDS)] revealed that some species present in the anodic biofilm adsorbed copper on their surface because of the bioleaching of the printed circuit board (PCB), yielding Cu2 + ions up to 600 mg/L. Beta- diversity indicates taxonomic divergence among all communities, but functional clustering is based on reactor pH. Annotated metagenomes showed the high presence of multicopper oxidases and Cu-resistance genes, as well as genes encoding aliphatic and aromatic hydrocarbon-degrading enzymes, corresponding to PCB bioleaching. Metagenome analysis revealed a high abundance of **Dietzia** spp., previously characterized in MFCs, which did not grow at pH 4. Binning metagenomes allowed us to identify novel species, one belonging to **Actinotalea** , not yet associated with electrogenicity and enriched only in the pH 7 anode. Furthermore, we identified 854 unique protein-coding genes in **Actinotalea** that lacked sequence homology with other metagenomes. The function of some genes was predicted with high accuracy through deep functional residue identification (DeepFRI), with several of these genes potentially related to electrogenic capacity. Our results demonstrate the feasibility of using MFC arrays for the enrichment offunctional electrogenic microbial consortia and data mining for the comparative analysis of either consortia or their members.

KEYWORDS

microbial fuel cell, metagenome, function prediction, copper, printed circuit board—PCB, bioleaching

Introduction

Microbial fuel cells (MFCs) are a type of chemical fuel cell in which the anodic reaction is catalyzed by various microorganisms that oxidize organic matter. When coupled with the cathodic reduction of oxygen, this system yields energy in the form of electricity. Given the exponential growth of studies focused on MFCs and electrogenic bacteria in general (Santoro et al., 2017), numerous reactor designs have been developed. However, the singularities ofthese systems render the reproducibility of experiments extremely difficult. Prior focus on unifying reactor conditions to study extracellular electron transfer (EET) has been on manufacturing multiple stand-alone microbial reactors, such as those based on small glass vials (Call and Logan, 2011a,b). The reactor design, materials used, dimensions, and electrochemical properties (e.g., internal resistance) have differed between research groups. Hou et al. (2009, 2011, 2012) demonstrated the use of 24-well plate arrays comprising microfabricated gold electrodes with ferricyanide (Hou et al., 2009), air-cathodes (Hou et al., 2011), or microfluidic channels with continuous anolyte and catholyte replenishment (Hou et al., 2012), which increased the power output by a factor ofthree. These reactors were used to screen previously selected electrochemically active environmental isolates.

Another example of a well plate array implementation was demonstrated by Yuan et al. (2011), in which EET was coupled to the color change ofthe probe. Recently, Molderez et al. (2021) constructed a 128-channel potentiostat connected to a printed circuit board (PCB) microarray. The entire microarray was immersed in an anolyte solution and supplied with a reference electrode to perform a high-throughput investigation pertaining to the effect ofthe anodic potential on electroactive biofilm growth. Zhou et al. (2015) proposed a well-plate-based, high-throughput colorimetric assay for microbial electrochemical respiration to indicate EET. Alternatively, a 48-well plate with a hydrophobic wax layer separating electrodes was developed by Choi et al. (2015), followed by a single-sheet paper-based electrofluidic array (eight cells) developed by Gao et al. (2017). Tahernia et al. (2019) developed paper-based, disposable 64-well arrays yielding power densities of up to 23 $\mu W/cm^2$. The device has been successfully used to characterize the electrochemical properties of various *Shewanella oneidensis* and *Pseudomonas aeruginosa* strains. They later developed, a 96-well electrofluidic array using the same fabrication method (Tahernia et al., 2020). Recently, another 96-microwell device (four 24-well modules) was demonstrated, with three electrodes and gas outlets to maintain anaerobic environment (Kuchenbuch et al., 2022). These newly developed MFC platforms allow higher precision in comparative studies of electrogenic biofilms. Metagenomes derived from electrogenic communities encode many unique genes that help with EET. Moreover, metabolic pathways within electrogenic communities can specialize in the degradation oftoxic compounds and precipitation ofheavy metals, thereby offering energetically favorable alternatives to existing bioprocesses.

Metagenomic assembly and annotation have become increasingly informative with the constant growth of databases. For example, the number of reference human gut bacterial genomes increased from 194 in 2010 to 204938 in 2021 (Almeida et al., 2021). Advances in sequencing technology now allow single genomes to be assembled directly from the metagenome, creating metagenome- assembled genomes (MAGs)(Tyson et al., 2004). Despite being more abundant than human microbiomes, environmental metagenomes are less resolved, with only 52,515 MAGs (Nayfach et al., 2021). MAGs have allowed for the discovery of novel metabolic pathways, such as commamox (Daims et al., 2015).

However, as the majority of MAGs are uncultured organisms, it is not surprising that a substantial proportion of genes lacks functional annotation. To make a comparative analyses of metagenomes easier, several tools for *de novo* annotation have been developed (Chen et al., 2020; Almeida et al., 2021; Beghini et al., 2021; Nayfach et al., 2021).

In this study, we present a 30-day enrichment of electrogenic consortia derived from a single inoculum [air-conditioning (AC) outflow] fed with an identical substrate. We applied different pH conditions to those consortia within identical reactors to compare their electrochemical performance in relation to changes in microbial community structure. We sampled anodic biofilms from all tested groups and visualized them under an electron microscope. Furthermore, we performed metagenomic sequencing and subsequent genome assembly and annotation from different compartments ofthe MFCs [anodes, cathodes, and open circuit potential (OCP) controls], which allowed for the identification of new species from the MAG isolates. Unannotated, unique genes present in novel electrogenic MAGs were further investigated using *in silico* analysis tools such as DeepFRI (Gligorijevic et al., 2021) and AlphaFold (Jumper et al., 2021).

Materials and methods

Microbial fuel cells construction and operation

Each well was built as an individual MFC with a membraneless design (**Figure 1**), as described previously (Szydlowski et al., 2022), with the following modifications: the base anode plate was built from a standard PCB comprising a thin copper sheet (17 μm) with electroless nickel plating and covered with a thin layer ofimmersion gold (ENIG—RoHS by JLCPCB, China). The seal was manufactured from polydimethylsiloxane (Sylgard 184; Sigma Aldrich) using a custom-made mold. The volume of each well was 0.577 cm^3

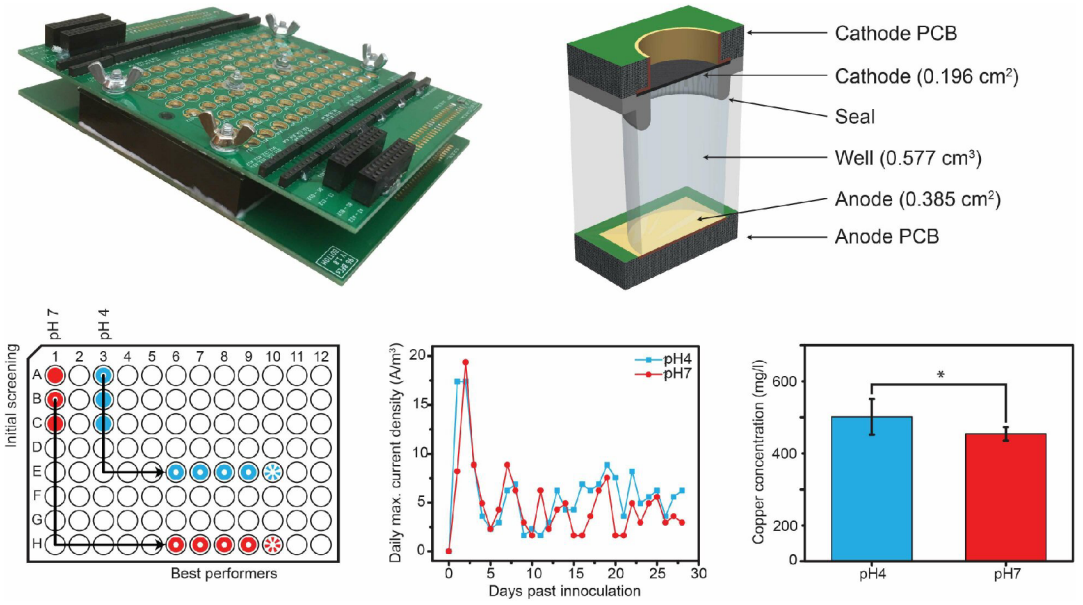

FIGURE 1
(A) Overview. **(B)** Cross-section of the used array. **(C)** Experimental setup, with the wells marked red being the pH 4 group, wells marked blue being the pH 7 group and wells with rays being the open circuit potential (OCP) controls. **(D)** Daily maximal current densities measured post inoculation. **(E)** Cu concentrations measured from the effluent samples of each well. Statistical significance was tested using ONE-way ANOVA (p-value < 0.05).

and the spacing between the electrodes was 1 cm. Samples from an AC unit outflow in Ishikawa, Japan (26.43°N, 127.84°E) were mixed (1:3) with basal medium containing 200 mg/L $CaCl22H_2O$, 250 mg/L $MgCl26H_2O$, 500 mg/L NH_4Cl, trace elements, and vitamin solution (medium 141; DSMZ) containing 1 g/L acetate and 2 g/L lactate as the carbon source. The pH ofthe medium was adjusted to either 4 or 7 prior to sample addition and samples were incubated overnight at 25°C. To inoculate the 96-well plate, 15 carbon veil (7 g Elite Motoring; United States) disks (0.385 cm^2 each) were immersed in each solution overnight and transferred to a 96-well plate (in stacks of five) as follows: disks incubated at pH7 were placed into wells A1-C1, and disks incubated at pH4 were placed into wells A4-C4. External resistors (R_{ext} = 330 Ω) were connected to the aforementioned wells, as determined by electrochemical impedance spectroscopy (EIS). The potential between the electrodes with attached external resistors was measured for 72 h, and the current was derived using Ohm's law. The best-performing wells from each pH regime were then selected (**Figure 1A**) and multiplied as follows: disks from A4 were placed into wells E6-E10 (pH4), and disks from B1 were placed into wells H6-H10 (pH7). Wells E10 and H10 served as OCP controls for the pH4 and pH7 group, respectively.

External resistors of 330 Ω were attached to wells E6-E9 and H6-H9. An additional four disks were added to each well to allow for biofilm growth. The same medium was used throughout the experiment, and the 96-well plate was incubated on a bench at 25°C. The medium was replaced with the same volume offresh medium (577 µl) daily by opening the top PCB. The samples were then subjected to volatile fatty acid (VFA) analysis using ion chromatography (IC). The top carbon sponges on the cathodes were washed daily with Milli-Q water. The potentials between electrodes with external resistors attached were measured for 4 weeks using PalmSens3, and the current was derived using Ohm's law. The current density (j) was normalized to the volume of each well (0.577 cm^3) or anode surface area (0.385 cm^2).

Electrochemical and chemical assays

Cyclic voltammetry (CV) and linear sweep voltammetry (LSV) measurements were performed using a PalmSens3. EIS was performed using a Gamry Interface 1,000 instrument. A two-electrode setup was used for measurements after 30 min left at the OCP, with anodes serving as the working electrodes and cathodes as the counter and reference electrodes. For CV measurements, the potential (E) range was from 0.4 V to −0.7 V and scan rate was 0.1 mV/s. For LSV measurements, the E range was from 0 mV vs. OCP to 0 mV vs. reference electrode, scan rate was 0.1 mV/s and ste was 0.2 mV. For EIS, the

frequency range was between 1 and 50 MHz, with 7 mV steps. The copper concentration in the liquid samples was determined using inductively coupled plasma mass spectrometry (ICP-MS). Samples were diluted 100,000 × with Milli-Q water and treated overnight with 5% HNO3 to remove residual organic matter. Each sample was measured in triplicate, and analysis of variance (ANOVA) was performed for all samples.

Scanning electron microscopy and energy dispersive spectroscopy analysis

Anodes were fixed by soaking in 2.5% glutaraldehyde for 12 h at 4°C. They were then washed three times with 0.1 M phosphate buffer of pH 7 at 4°C, dehydrated with a series of ethanol solutions (50, 70, 80, 90, 95, and three times in 100%). Next, the anodes were soaked in pure hexamethyldisilazane twice for 30 s, as previously described (Araujo et al., 2003). After drying for 10 min, the samples were sputter-coated with gold. The samples were observed by scanning electron microscopy (SEM) (JSM-7900F JEOL). Additionally, EDS scans were conducted to detect the presence of Cu in the biofilms.

Metagenomic sequencing and analysis

DNA was extracted from the AC outflow, as well as from the carbon veil disks, from each well (E6-10, H6-10) using the Maxwell RSC kit and automated station and subjected to Illumina NovaSeq sequencing at the Okinawa Institute of Science and Technology (OIST) DNA sequencing facility. DNA samples derived from wells E6-9 and H6-9 were pooled prior to sequencing. The metagenomic sequences were processed using the KBase platform (Arkin et al., 2018). First, paired-end reads were subjected to quality control and filtering using FastQC v0.11.5. For phylogenetic analysis ofthe metagenomes, paired-end libraries were subjected to the Kaiju pipeline (Menzel and Krogh, 2016), and beta-diversity was computed using QIIME2 (Caporaso et al., 2010) and PALADIN (Westbrook et al., 2017) (with the Swiss-Prot reference database) using taxonomic and functional features, respectively and the Principal coordinate analysis (PCoA) was performed, using Bray-Curtis dissimilarity on a relative abundance matrix. Subsequently, metagenomic reads were assembled using metaSPAdes v3.13.0 (Nurk et al., 2017). For functional analysis, contigs were binned using MaxBin2 v2.2.4 (Wu et al., 2016), and the quality ofthe extracted genomes was assessed using CheckM v1.0.18 (Parks et al., 2015). Multiple assemblies were annotated using RASTtk (Brettin et al., 2015) and multiple domain annotation tools and subjected to comparative studies. Binned contigs were subjected to average nucleotide identity (ANI) analysis (Ciufo et al., 2018) and a phylogenetic tree was constructed using FastTree2 (Price et al., 2010). For all binned contigs from each metagenome set, sequence similarity analysis was performed using a search command with default parameters in the MMseqs2 package (Steinegger and Soding, 2017). Two compared sequences were annotated as being similar ifthey were simultaneously evaluated with an E-value $\leq 10^{-5}$ and a bit score ≥ 50. Sequence-based functional annotations were generated by DeepFRI using CPU models (Gligorijevic et al., 2021).

Results

Microbial fuel cells operation and electrochemical measurements

Our AC outflow consortium was inoculated into a matrix of wells, with pH and circuit being the two variables (**Figure 1A**). The initial screening revealed that two wells from each group maintained stable potentials, equivalent to current densities of 9 and 1.2 A/m^3 in the pH 4 and pH 7 groups, respectively (**Supplementary Figure 1A**). Disks from these wells were used to inoculate new sets of wells. In the first 2 days post multiplication, current densities reached a maximum of 17.4 and 19.4 A/m^3 in the pH 4 (well E6) and pH 7 (well H8) samples, respectively. Then, the currents decreased and kept oscillating between 1.6 and 8.8 A/m^3 in the following days, with the pH4 wells showing slightly higher values than pH 7 (**Figure 1B**). In terms of power, our MFCs produced up to 30.1 and 80.2 nW (which is equivalent to 0.8 and 2.1 μW/m^2 or 52.2 and 139 mW/m^3) in wells E6 (pH 4) and H8 (pH 7), respectively (**Supplementary Figure 2**). Based on the IC analysis, the total chemical oxygen demand (COD) removal was 1996 ± 127 mg COD/L/d and 1806 ± 137 mg COD/L/d for the pH 4 and pH 7 samples, respectively (**Supplementary Figure 1B**). The pH increased from 4 to 7 in wells E6-E9 and from 7 to 10 in wells H6-H9 after 24 h.

CV scans in the pH 4 blank reveals a smooth curve non-Faradaic current of 30 μA and a small reduction peak at 0.55 V. Two weeks post inoculation, an oxidative peak was seen at 0.13 V, with an oxidative wave at 180 μA and a reductive peak at −0.44 V with a reductive wave below −200 μA (**Supplementary Figure 2A**). In the pH 7 samples, the non-Faradaic currents were below 30 μA, with no redox peaks. Two weeks after inoculation, the oxidative peak was approximately 0 V, with an oxidative wave at 80 μA and a reductive peak was −0.25 V with a reductive wave at −170 μA observed (**Supplementary Figure 2B**). Thus, the capacitance increase was over 12-fold and eightfold in the pH 4 and pH 7 MFCs, respectively, indicating the presence of a biofilm on our electrodes.

Copper presence and inductively coupled plasma mass spectrometry measurements

Two days after inoculation, we identified copper ions in the anolyte outflow ofthe pH 4 samples, potentially derived from PCB. We subjected outflow samples to ICP-MS and determined the average concentration of copper to be 510 ± 63 and 450 ± 24 mg/L for the pH 4 and pH 7 samples, respectively (**Figure 1E**), whereas the Cu^{2+} concentration in the prepared media was below the quantification limit (3 µg/L). ANOVA revealed a statistical difference in the Cu^{2+} concentration between the different pH groups.

Scanning electron microscopy and energy dispersive spectroscopy analyses

SEM images ofthe anodic biofilms clearly indicated that the particles were adsorbed on the cell surfaces. When further analysis was performed using an EDS detector, a strong signal was obtained from copper (**Figure 2**, right panel). Moreover, in some parts ofthe biofilm, Cu^{2+} was present only on some specimens, as the Cu signals from the arbon fibers and other parts ofbiofilm were much weaker (**Supplementary Figure 3**), suggesting that the community comprised members that actively sequestered Cu ions from the solution.

Metagenomic analysis

Taxonomy analysis and beta-diversity

Taxonomy profiles of our metagenomes revealed that *Dietzia* spp. was the most dominant anodic genus in both the pH 4 and 7 reactors (**Figure 3A**). Other abundant genera detected in the samples were *Bacillus*, *Glycocaulis*, and *Microbacterium* spp., which were also abundant in the OCP controls. In the pH 4 and pH 7 OCP controls, the most abundant genera were *Bacillus* and *Dietzia/Glycocaulis*, respectively, whereas the cathodes comprised mostly of *Bacillus* in both pH groups. In the AC outflow, *Geobacter* spp. was the most abundant genus, with 4% abundance. *Dietzia* comprised only 0.04% ofthe inoculum. PCoA was performed using the taxonomy (**Figure 3B**) and functional features (**Figure 3C**) of enriched metagenomes. In terms oftaxonomy, divergence was observed across all samples. However, when functional annotations were compared, clusters based on pH were observed, with the pH 4 anode and cathode being closer than their corresponding pH 7 metagenomes. The OCP controls from each ofthe groups diverged from the other samples, indicating that the electric circuits influenced biofilm metabolism.

Metagenome assembly and annotation

All metagenomes were then assembled using MetaSPAdes (Nurk et al., 2017), and the resulting contigs were annotated using Prokka (Seemann, 2014) and RAST (Brettin et al., 2015). A comparative analysis ofthe annotated contigs was performed, and the set intersections were aggregated, as shown in **Supplementary Figure 4**. The highest number of common annotations was found in all metagenomes except the pH 4 cathode (2419), whereas all metagenomes shared 709 common annotations. The entire pH 4 group (anode, cathode and OCP) had 959 common annotations, whereas the entire pH 7 group had 436 annotations. For the pH 4 and pH 7 anodes and cathodes, the number of common annotations was below 10, and control anodes (O) had only 10 common annotations. The highest number of unique annotations present in a single metagenome was in the pH 7 OCP sample. In contrast, the pH 4 OCP had the lowest number of unique annotations (35). The anodes showed 72 and 69 unique annotations in the pH 4 and pH 7 groups, respectively, whereas the cathodes showed 43 and 657 unique annotations in these groups. All annotation data are presented in **Supplementary Table 1**. As expected, all metagenomes also contained various Cu-related genes (**Table 1**), such as multicopper- and heme-copper oxidoreductases, metallochelatins, ATP-dependent heavy metal translocases, genes indicating Cu resistance (e.g., cupredoxins, *cop*- and *cut*-family resistance genes), copper-sensing two-component system response regulator *cpx*R, and the *cso*R repressor ofthe *cop*ZA operon. All metagenomes shared similar numbers ofthese genes (52–74), except for the pH 4 cathode, where only seven Cu-related annotations were found. Moreover, all contigs contained genes involved in electron transfer pathways, with two to three times more genes in the pH 7 anode community than the pH 4 counterparts. Notably, genes encoding the nitrogenase FixABCX protein complex were found in all metagenomes, but six *rnf* genes were found exclusively in the pH 7 OCP metagenome. In agreement with PCB bioleaching, as indicated by the presence

of dissolved Cu, genes involved in the degradation of various hydrocarbons (both aromatic and aliphatic) were also found, with higher gene counts observed in the pH 7 group.

Binned contigs from pH 7 anode that revealed high quality (> 95% completeness and < 2% contamination) MAGs were annotated as *Microbacterium* (Bin.1), *Maricaulaceae* (Bin.3), *Actinotalea* (Bin.4), *Bacillus* (Bin.5) and *Dietzia* spp. (Bin.6; **Figure 4A**). Among these MAGs, all bins except Bin.5 were identified as novel species, according to the phylogenetic analysis and ANI check (**Supplementary Table 2**). However, the aforementioned MAGs were found in both pH4 and pH7 anodes and OCP controls, except for Bin.4, which was found exclusively in the pH 7 anode, and its abundance in the initial inoculum was less than 0.002%. All binned MAGs were subjected to domain annotation using Prokka and RAST (**Supplementary Table 3**). All pH7 bins had 500 common annotations, whereas MAG-unique annotations varied from 305 to 1,393 in Bin.1 and Bin.5, respectively (**Figure 4B**), which corresponds to their genome sizes (3,137 and 4,744 genes in Bins 1 and 5, respectively). Within the shared group, several TRX-like ferredoxin, Ni-Fe and Fe-only hydrogenases, and Fe ion transporters were

10.3389/fmicb.2022.951044

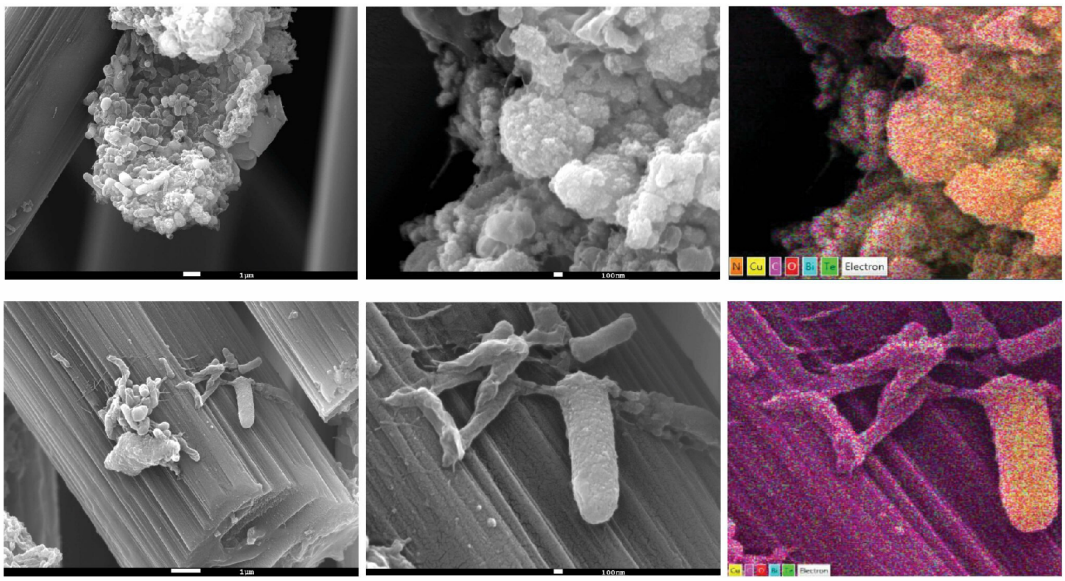

FIGURE 2
Scanning electron microscopy (SEM) and energy-dispersive spectroscopy (EDS) elemental mapping of anodic biofilms from the **(A)** pH 4 **(B)** and pH 7 electrodes.

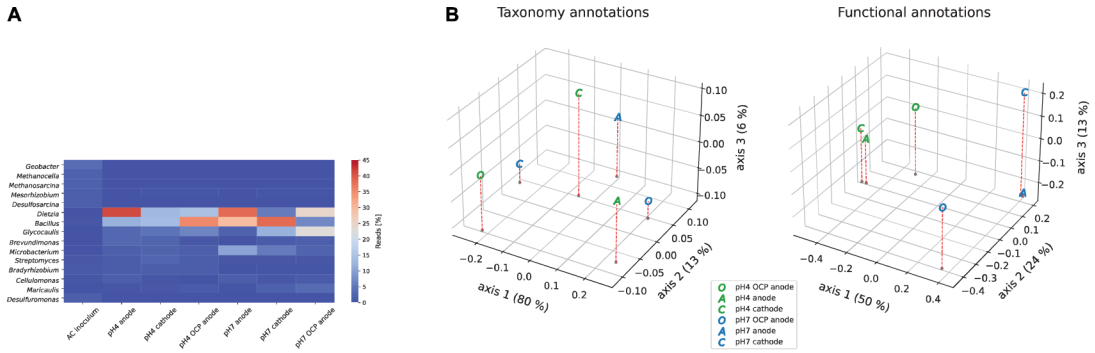

FIGURE 3
(A) Taxonomy analysis of the top 15 genera across all metagenomes. **(B)** Principal coordinate analysis (PCoA) based on taxonomy (genus level) and functional features of the metagenomes using Bray-Curtis dissimilarity on a relative abundance matrix.

TABLE 1 Gene count and abundance for the three pathways in all metagenomes.

Genes	pH4 A	pH4 OCP	pH4 C	pH7 A	pH7 OCP	pH7 C
Cu-related	65	68	7	74	74	52
Cu-related abundance	1.35%	1.22%	0.36%	1.33%	1.14%	0.99%
Electron transfer	10	11	4	21	34	11
Electron transfer abundance	0.21%	0.20%	0.21%	0.38%	0.52%	0.21%
Hydrocarbon degradation	2	2	1	4	8	4
Hydrocarbon degradation abundance	0.04%	0.04%	0.05%	0.07%	0.12%	0.08%

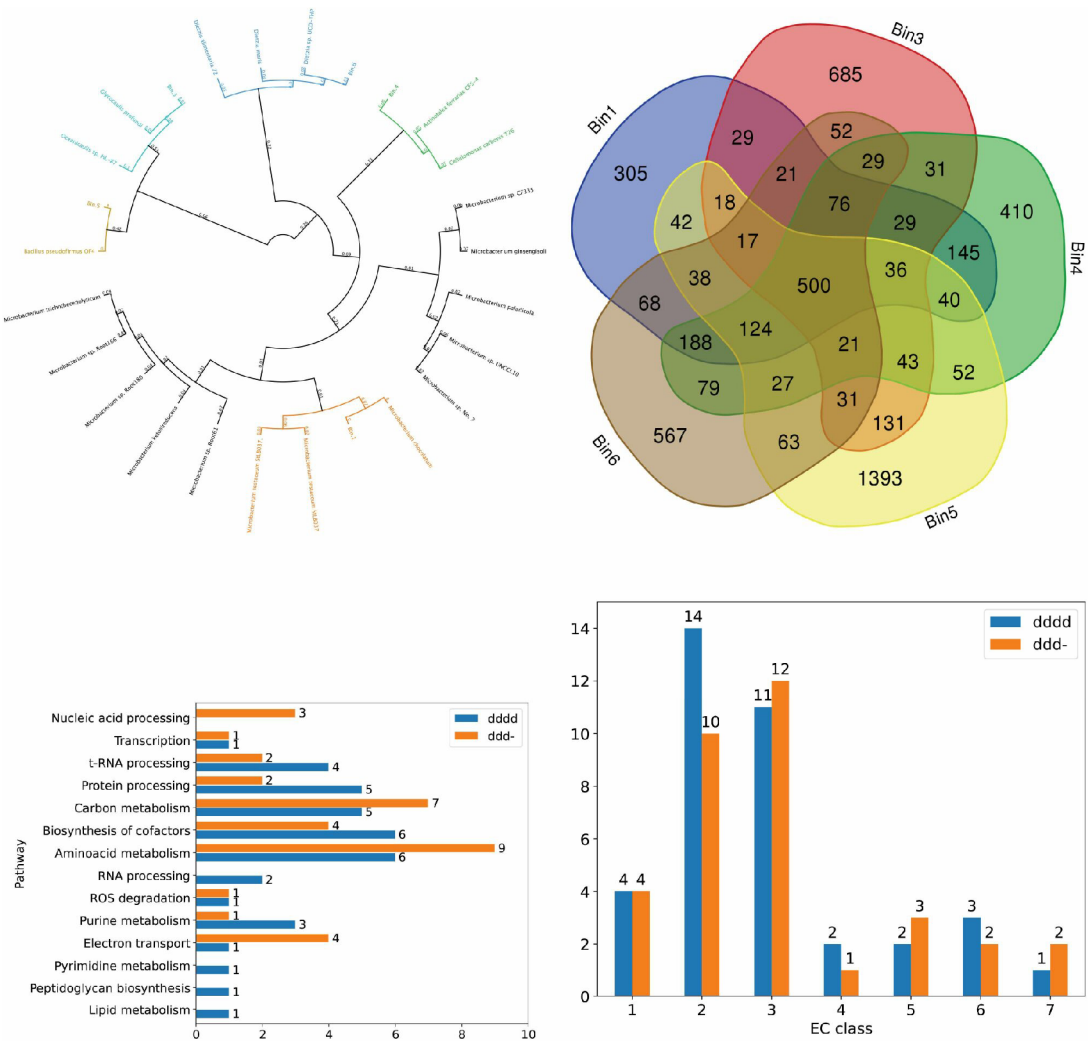

FIGURE 4
(A) Phylogenetic tree of bins from the pH7 anodes (numbers indicate substitutions per site). **(B)** Venn diagram showing common annotations. **(C)** The number of Bin.4-unique genes in different metabolic pathways. **(D)** The number of Bin.4-unique genes across EC classes for two deepest levels of EC classifications (dddd and ddd- respectively).

identified. All binned contigs shared genes encoding enzymes for degradation of various hydrocarbons (both aromatic and aliphatic) and steroids. All contigs also contained various Cu-related genes, such as multi- and heme-copper oxidoreductases and ATP-dependent heavy metal translocases, whereas genes indicating Cu resistance (e.g., cupredoxins, copper-resistance genes *copA/C/Z* or metallochelatins were not found in all MAGs, indicating community interactions and complementarity. Apart from the genes with known annotations, our focus was also on the unknown genes that contributed to a large portion of all MAGs and metagenomes. Given that the *Actinotalea* MAG was found exclusively in the pH 7 anode community, we performed a comparative analysis of MAGs within the pH 7 anode and identified 854 unique (showing e-value > 10^{-5} and bitscore < 50) open reading frames (ORFs) when aligned against other metagenomic sequences, which was the highest value for either annotated or unannotated ORFs. Next, we analyzed the potential functions ofthese unique genes using DeepFRI. Using the enzyme commission (EC) classification, we identified genes encoding enzymes present in each EC class with the highest DeepFRI score assigned (Figure 4D) and divided them into metabolic pathways (Figure 4C). The number of unique genes reflects the redundancy of a specific EC class, with an EC2 (transferases), and EC3 (hydrolases) being the most numerous

in Bin.4. These EC classes are generally the most abundant in all living organisms. In the case oftransferases, we identified genes encoding virus-specific RNA-directed RNA polymerase (EC 2.7.7.48), indicating the presence of prophage elements.

We especially focused on pathways that may play a key roles in the MFC environment: electron transfer (reductase, EC 7.2.1.-), reactive oxygen species (ROS) degradation (superoxide dismutase, EC 1.15.1.1), and cofactor biosynthesis (EC 2.5.1.78 involved in the flavin pathway and EC 4.2.1.96 involved in the quinone pathway). We processed ale these sequences using the trRosetta and AlphaFold algorithms to predict their structure, however, only one EC 7.2.1.- modeled with sufficient confidence (pTM score; **Figure 5**) In total, four Bin.4-unique genes encoding reductases (EC 7.2.1.-) were identified within the electron transfer pathway. This class contains three groups of enzymes: NAD + :ubiquinone (7.2.1.1), ferredoxin-NAD + (7.2.1.2) and ascorbate ferrireductase (7.2.1.3), which are all involved in the electron transfer pathway.

Discussion

Our analysis identified the novel electrogenic bacterium *Actinotalea* sp. nov. has been identified in the anodic community of our MFC. *Actinotalea* is a high GC, gram-positive, facultative anaerobic genus derived from *Cellulomonas*; the main taxonomic difference is the major respiratory quinone menaquinone, with MK-10(H4) in the former and MK-9(H3) in the latter (Yi et al., 2007; Jin et al., 2017). *Actinotalea* can survive across a wide pH spectrum (4–11), although the most optimal conditions for its growth was pH 7 in our test. Other species from this genus have been found in soil (Suman et al., 2014; Yan et al., 2018), iron mine (Li et al., 2013), and biofilm reactors (Jin et al., 2017). The presence of numerous sequences related to electron transfer in its genome, e.g., the type IV pilus biosynthesis gene *pilB*, confirmed that this organism can respire through anodes, just like the well-studied electrogen *Geobacter* (McCallum et al., 2017). It would be interesting to compare the expression levels ofthe *Actinotalea*'s unique genes while grown in the MFC wrt OCP. Moreover, the presence of novel and unique enzymes, such as NADH translocases, could provide resilience to high Cu content. Many ofthe unannotated sequences obtained from the *Actinotalea* MAG received medium DeepFRI prediction scores, which may indicate the presence of a novel homologue; however, this must be experimentally validated.

Overall, the metagenomes analyzed in this study contained many genes encoding pathways related to anaerobic respiration. The inoculum derived from the AC outflow also consisted of marine bacterial species originating from the deep sea. Abrevaya et al. (2015) previously found *Dietzia* to be enriched in MFCs, although it is mostly found in oil-contaminated marine environments (Yumoto et al., 2002). Interestingly, despite its alleged alkalinity, we found the abundance of *Dietzia* to be similar in both pH 4 and pH 7 anodic samples (**Figure 3**), and binned contigs from both samples revealed 99.9% sequence similarity between the MAGs. This suggests that *Dietzia* can withstand periods oflower pH, since the pH increased from 4 to 7 in our pH 4 group. Moreover, its abundance in anodic biofilms may be explained by its ability to degrade numerous hydrocarbons (Yumoto et al., 2002). Owing to bioleaching of the PCB, Cu together with the organic epoxy coating become oxidized, thus creating compounds toxic to many bacteria. Since *Dietzia* can degrade these compounds, its abundance in anodic consortia is not surprising. The high abundance of EET-related and hydrocarbon degrading genes in pH 7 OCP, as seen in **Table 1**, as well as the total number of unique annotations may reflect higher metabolic diversity ofthis community due to the lack of external electron circuit. Indeed previous studies comparing MFC communities (Ishii et al., 2018; Kouzuma et al., 2018; Szydlowski et al., 2020) reveal higher functional diversity in communities grown at OCP, whereas the presence of external circuit applies selective pressure on the microbial metabolism.

Despite our efforts to separate the PCB from electrogenic bacteria, our results revealed that chemically deposited Au on the electrodes did not provide a sufficient barrier for the PCB and ultimately led to its corrosion. Such problems could be avoided by using PCBs with the so-called hard gold finish (electrochemically plated gold) or by covering the PCB anode with other conductive materials, such as stainless steel sheets, thus protecting the underlying Cu from being oxidized. Indeed, the electrochemical plating ofthe PCB successfully prevented Cu leakage in our modified well plate (Szydlowski et al., 2022). Owing to this unexpected leakage of Cu ions, we successfully enriched the Cu-resistant communities using our 96-well platform. Through SEM analysis, we observed that the anodic biofilm comprised species that concentrated Cu on their surfaces, leaving other parts ofthe biofilm relatively Cu-free. Therefore, it is tempting to suggest that this mechanism can be mediated by direct interspecies EET or electron bifurcation using Cu ions, as in the FixABCX (Ledbetter et al., 2017) or Rnf (Kuhns et al., 2020) complexes. Especially Rnf-encoding genes may be particularly interesting since unique genes were identified in the *Actinotalea* MAG that are putative members ofthe *rnf* family (**Figure 5**). Rnf enable difficult reductions (reviewed in Buckel and Thauer, 2018), which may indicate the ongoing degradation ofthe PCBs' organic compounds, such as epoxy resins. Based on the studies describing Cu-bioleaching from PCB waste (Yang et al., 2009; Pant et al., 2012; Wu Y. et al., 2018), it can be concluded that Cu mobilization from its zero-valent state may be due to the bioelectrochemical cycle, which is also depicted in the model proposed by Becci et al. (2021). Copper can be usually oxidized by the simultaneous reduction of Fe^{3+} to Fe^{2+} and its efficiency depends on the reoxidation of iron back to Fe^{3+}. Iron oxidation may be catalyzed by bacteria in

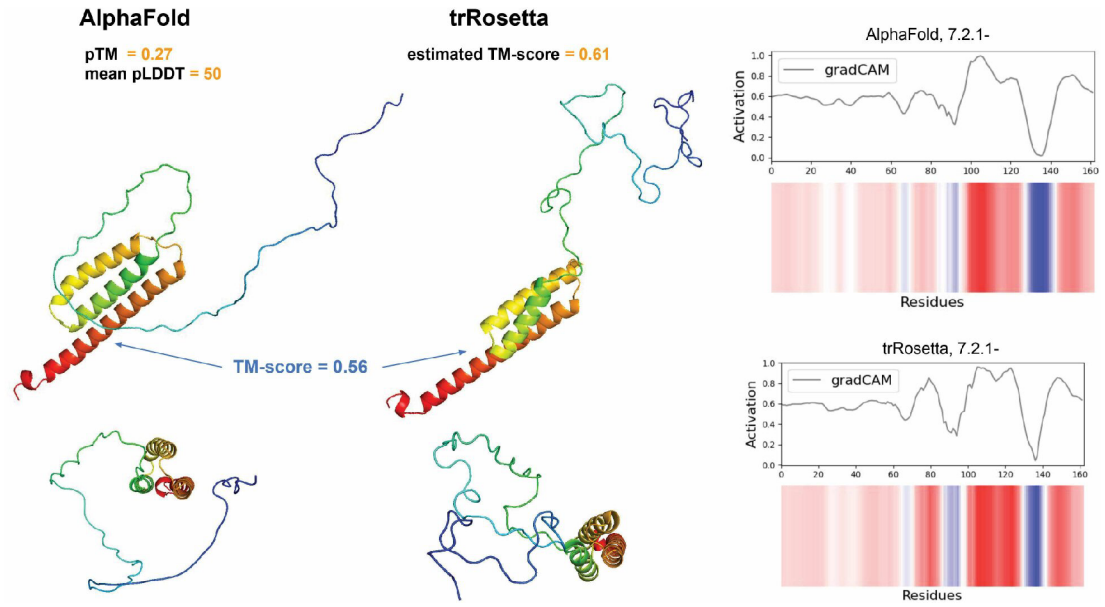

FIGURE 5
Alphafold (left) and trRosetta models (middle) of our putative reductase gene (EC 7.2.1.-). Each structure is shown from two different perspectives (lower and upper panels). The TM-score between both structures (excluding disordered tails) is depicted in blue. For both the AlphaFold and trRosetta predictions, the model quality measures are shown (see Yang et al., 2020; Jumper et al., 2021 for details). On the right panel, the DeepFRI activation map across residues is shown.

the presence of oxygen, as well as alternative electron acceptors, such as electrodes, which in turn may explain the high current densities observed in our reactors. Moreover, simultaneous proton consumption that accompanies Fe reoxidation (Becci et al., 2021), can explain the pH shift observed in our study, as well as the differences in Cu content (**Figure 1E**). Wu W. et al. (2018) demonstrated a bacterial-free supernatant derived from Fe/S-oxidizing bacteria, also known for their electrogenic activity, resulting in complete Cu recovery from wasted PCBs. Other studies on the metallurgic, Cu-removing MFCs demonstrated that electrogenic consortia can reduce Cu from aqueous solutions and precipitate it on electrodes. The efficiency ofthis process depends on various factors, such as the use of pH separators (membranes), presence/absence of oxygen, and initial copper concentration (Heijne et al., 2010; Tao et al., 2011a,b; Motos et al., 2015; Miran et al., 2017). Given that Cu was cycling from solid state (PCB) to the solution and precipitated back to the anodic biofilm, the microbial communities enriched in our well plate exhibit a combination of oxidative and reductive bioleaching (Brar et al., 2021), which may also indicate the fluctuations in the current densities (**Figure 1D**).

Our results illustrate the extent of selective enrichment of our MFC array, which yielded electrogenic microbial communities capable of adapting to different physical conditions, such as pH and electric circuits, and resulted in bioleaching ofthe PCB. Through a combination of phylogenetic analysis and metagenome binning with *in silico* functional assays, we were able to identify, characterize and compare the microbial communities and link their features to the electrochemical performance that was measured in unified array conditions. This platform is a rapid, high-throughput system that offers parallelization for the screening of electrochemical microorganisms, as well as comparative analysis offunctional metagenomes.

Data availability statement

The datasets presented in this study can be found in online repositories. The names ofthe repository/repositories and accession number(s) can be found below: https://narrative.kbase.us/narrative/62324, 62324/1/362/.

Author contributions

LS conceived the experiment(s). LS, JE, and NS conducted the experiment(s). LS and PS analyzed the results. All authors reviewed the manuscript and contributed to the article and approved the submitted version.

Funding

This work was funded by the Okinawa Institute of Science and Technology (OIST) Proof-of-concept (POC) Tier 2 programme and supported in part by PLGrid Infrastructure.

Acknowledgments

We would like to thank Toshio Sasaki (OIST Imaging Analysis Section) for help with SEM and EDS imaging, Yoshiteru Iinuma (OIST Instrumental Analysis Section) for chemical analysis, and Mayumi Kawamitsu (OIST Sequencing Section) for their help with metagenome sequencing.

Conflict ofinterest

The authors declare that the research was conducted in the absence of any commercial or financial relationships that could be construed as a potential conflict ofinterest.

Publisher's note

All claims expressed in this article are solely those ofthe authors and do not necessarily represent those oftheir affiliated organizations, or those ofthe publisher, the editors and the reviewers. Any product that may be evaluated in this article, or claim that may be made by its manufacturer, is not guaranteed or endorsed by the publisher.

Supplementary material

The Supplementary Material for this article can be found online at: https://www.frontiersin.org/articles/10.3389/fmicb.2022.951044/full#supplementary-material

References

Abrevaya, X. C., Sacco, N. J., Bonetto, M. C., Hilding-Ohlsson, A., and Cortdn, E. (2015). Analytical applications of microbial fuel cells. Part II: Toxicity, microbial activity and quantification, single analyte detection and other uses. *Biosens. Bioelectron.* 63, 591–601. doi: 10.1016/j.bios.2014.04.053

Almeida, A., Nayfach, S., Boland, M., Strozzi, F., Beracochea, M., Shi, Z. J., et al. (2021). A unified catalog of 204,938 reference genomes from the human gut microbiome. *Nat. Biotechnol.* 39, 105–114. doi: 10.1038/s41587-020-0603-3

Araujo, J. C., Téran, F. C., Oliveira, R. A., Nour, E. A. A., Montenegro, M. A. P., Campos, J. R., et al. (2003). Comparison ofhexamethyldisilazane and critical point drying treatments for SEM analysis of anaerobic biofilms and granular sludge. *J. Electron Microsc.* 52, 429–433. doi: 10.1093/jmicro/52.4.429

Arkin, A. P., Cottingham, R. W., Henry, C. S., Harris, N. L., Stevens, R. L., Maslov, S., et al. (2018). KBase: The United States department of energy systems biology knowledgebase. *Nat. Biotechnol.* 36, 566–569. doi: 10.1038/nbt.4163

Becci, A., Amato, A., Rodriguez-Maroto, J. M., and Beolchini, F. (2021). Bioleaching of end-of-life printed circuit boards: Mathematical modeling and kinetic analysis. *Ind. Eng. Chem. Res.* 60, 4261–4268. doi: 10.1021/acs.iecr.0c05566

Beghini, F., McIver, L. J., Blanco- Míguez, A., Dubois, L., Asnicar, F., Maharjan, S., et al. (2021). Integrating taxonomic, functional, and strain-level profiling of diverse microbial communities with biobakery 3. *Elife* 10, 1–42. doi: 10.7554/eLife.65088

Brar, K. K., Magdouli, S., Etteieb, S., Zolfaghari, M., Fathollahzadeh, H., Calugaru, L., et al. (2021). Integrated bioleaching-electrometallurgy for copper recovery–A critical review. *J. Clean. Prod.* 291:125257. doi: 10.1016/j.jclepro.2020.125257

Brettin, T., Davis, J. J., Disz, T., Edwards, R. A., Gerdes, S., Olsen, G. J., et al. (2015). RASTtk: A modular and extensible implementation ofthe RAST algorithm for building custom annotation pipelines and annotating batches of genomes. *Sci. Rep.* 5:8365. doi: 10.1038/srep08365

Buckel, W., and Thauer, R. K. (2018). Flavin-based electron bifurcation, a new mechanism ofbiological energy coupling. *Chem. Rev.* 118, 3862–3886. doi: 10.1021/acs.chemrev.7b00707

Call, D. F., and Logan, B. E. (2011a). A method for high throughput bioelectrochemical research based on small scale microbial electrolysis cells. *Biosens. Bioelectron.* 26, 4526–4531. doi: 10.1016/j.bios.2011.05.014

Call, D. F., and Logan, B. E. (2011b). Lactate oxidation coupled to iron or electrode reduction by *Geobacter sulfurreducens* PCA. *Appl. Environ. Microbiol.* 77, 8791–8794. doi: 10.1128/AEM.06434-11

Caporaso, J. G., Kuczynski, J., Stombaugh, J., Bittinger, K., Bushman, F. D., Costello, E. K., et al. (2010). Correspondence QIIME allows analysis ofhigh-throughput community sequencing data Intensity normalization improves color calling in SOLiD sequencing. *Nat. Publ. Group* 7, 335–336. doi: 10.1038/nmeth.f.303

Chen, L. X., Anantharaman, K., Shaiber, A., Eren, A. M., and Banfield, J. F. (2020). Accurate and complete genomes from metagenomes. *Genome Res.* 30, 315–333. doi: 10.1101/gr.258640.119

Choi, G., Hassett, D. J., and Choi, S. (2015). A paper-based microbial fuel cell array for rapid and high-throughput screening of electricity-producing bacteria. *Analyst* 140, 4277–4283. doi: 10.1039/C5AN00492F

Ciufo, S., Kannan, S., Sharma, S., Badretdin, A., Clark, K., Turner, S., et al. (2018). Using average nucleotide identity to improve taxonomic assignments in prokaryotic genomes at the NCBI. *Int. J. Syst. Evol. Microbiol.* 68, 2386–2392. doi: 10.1099/ijsem.0.002809

Daims, H., Lebedeva, E. V., Pjevac, P., Han, P., Herbold, C., Albertsen, M., et al. (2015). Complete nitrification by *Nitrospira* bacteria. *Nature* 528, 504–509. doi: 10.1038/nature16461

Gao, Y., Hassett, D. J., and Choi, S. (2017). Rapid characterization ofbacterial electrogenicity using a single-sheet paper-based electrofluidic array. *Front. Bioeng. Biotechnol.* 5:44. doi: 10.3389/fbioe.2017.00044

Gligorijevic, V., Renfrew, P. D., Kosciolek, T., Leman, J. K., Berenberg, D., Vatanen, T., et al. (2021). Structure-based protein function prediction using graph convolutional networks. *Nat. Commun.* 12:3168. doi: 10.1038/s41467-021-23303-9

Heijne, A. T., Liu, F., Van Der Weijden, R., Weijma, J., Buisman, C. J. N., and Hamelers, H. V. M. (2010). Copper recovery combined with electricity production in a microbial fuel cell. *Environ. Sci. Technol.* 44, 4376–4381. doi: 10.1021/es100526g

Hou, H., Li, L., Ceylan, C. U., Haynes, A., Cope, J., Wilkinson, H. H., et al. (2012). A microfluidic microbial fuel cell array that supports long-term multiplexed analyses of electricigens. *Lab Chip* 12, 4151–4159. doi: 10.1039/c2lc40405b

Hou, H., Li, L., Cho, Y., de Figueiredo, P., and Han, A. (2009). Microfabricated microbial fuel cell arrays reveal electrochemically active microbes. *PLoS One* 4:e6570. doi: 10.1371/journal.pone.0006570

Hou, H., Li, L., de Figueiredo, P., and Han, A. (2011). Air-cathode microbial fuel cell array: A device for identifying and characterizing electrochemically active microbes. *Biosens. Bioelectron.* 26, 2680–2684. doi: 10.1016/j.bios.2010.06.037

Ishii, S., Suzuki, S., Tenney, A., Nealson, K. H., and Bretschger, O. (2018). Comparative metatranscrip- tomics reveals extracellular electron transfer pathways conferring microbial adaptivity to surface redox potential changes. *ISME J.* 12, 2844–2863. doi: 10.1038/s41396-018-0238-2

Jin, L., Ko, S. R., Lee, C. S., Ahn, C. Y., Lee, J. S., Lee, K. C., et al. (2017). *Actinotalea caeni* sp. nov., isolated from a sludge sample ofa biofilm reactor. *Int. J. Syst. Evol. Microbiol.* 67, 1595–1599. doi: 10.1099/ijsem.0.001769

Jumper, J., Evans, R., Pritzel, A., Green, T., Figurnov, M., Ronneberger, O., et al. (2021). Highly accurate protein structure prediction with AlphaFold. *Nature* 596, 583–589. doi: 10.1038/s41586-021-03819-2

Kouzuma, A., Ishii, S., and Watanabe, K. (2018). Metagenomic insights into the ecology and physiology of microbes in bioelectrochemical systems. *Bioresour. Technol.* 255, 302–307. doi: 10.1016/j.biortech.2018.01.125

Kuchenbuch, A., Frank, R., Ramos, J. V., Jahnke, H. G., and Harnisch, F. (2022). Electrochemical microwell plate to study electroactive microorganisms in parallel and real-time. *Front. Bioeng. Biotechnol.* 9:821734. doi: 10.3389/fbioe.2021.821734

Kuhns, M., Trifunovic, D., Huber, H., and Muller, V. (2020). The Rnf complex is a Na+ coupled respiratory enzyme in a fermenting bacterium, *Thermotoga maritima*. *Commun. Biol.* 3, 1–10. doi: 10.1038/s42003-020-01158-y

Ledbetter, R. N., Garcia Costas, A. M., Lubner, C. E., Mulder, D. W., Tokmina-Lukaszewska, M., Artz, J. H., et al. (2017). The electron bifurcating FixABCX protein complex from *Azotobacter vinelandii*: Generation oflow-potential reducing equivalents for nitrogenase catalysis. *Biochemistry* 56, 4177–4190. doi: 10.1021/acs.biochem.7b00389

Li, Y., Chen, F., Dong, K., and Wang, G. (2013). *Actinotalea ferrariae* sp. nov., isolated from an iron mine, and emended description ofthe genus *Actinotalea*. *Int. J. Syst. Evol. Microbiol.* 63(PART9), 3398–3403. doi: 10.1099/ijs.0.048512-0

McCallum, M., Tammam, S., Khan, A., Burrows, L. L., and Howell, P. L. (2017). The molecular mechanism ofthe type IVa pilus motors. *Nat. Commun.* 8, 1–10. doi: 10.1038/ncomms15091

Menzel, P., and Krogh, A. (2016). Kaiju : Fast and sensitive taxonomic classification for metagenomics. *Nat. Commun.* 7, 1–9. doi: 10.1038/ncomms11257

Miran, W., Jang, J., Nawaz, M., Shahzad, A., Jeong, S. E., Jeon, C. O., et al. (2017). Mixed sulfate-reducing bacteria-enriched microbial fuel cells for the treatment of wastewater containing copper. *Chemosphere* 189, 134–142. doi: 10.1016/j.chemosphere.2017.09.048

Molderez, T. R., Prevoteau, A., Ceyssens, F., Verhelst, M., and Rabaey, K. (2021). A chip-based 128-channel potentiostat for high-throughput studies of bioelectrochemical systems: Optimal electrode potentials for anodic biofilms. *Biosens. Bioelectron.* 174:112813. doi: 10.1016/j.bios.2020.112813

Motos, P. R., Weijden, R. V., Heijne, A. T., Saakes, M., Buisman, C. J., and Sleutels, T. H. (2015). High rate copper and energy recovery in microbial fuel cells. *Front. Microbiol.* 6:527. doi: 10.3389/fmicb.2015.00527

Nayfach, S., Roux, S., Seshadri, R., Udwary, D., Varghese, N., Schulz, F., et al. (2021). A genomic catalog of Earth's microbiomes. *Nat. Biotechnol.* 39, 499–509. doi: 10.1038/s41587-020-0718-6

Nurk, S., Meleshko, D., Korobeynikov, A., and Pevzner, P. A. (2017). MetaSPAdes: A new versatile metagenomic assembler. *Genome Res.* 27, 824–834. doi: 10.1101/gr.213959.116

Pant, D., Joshi, D., Upreti, M. K., and Kotnala, R. K. (2012). Chemical and biological extraction of metals present in E waste: A hybrid technology. *Waste Manage.* 32, 979–990. doi: 10.1016/j.wasman.2011.12.002

Parks, D. H., Imelfort, M., Skennerton, C. T., Hugenholtz, P., and Tyson, G. W. (2015). CheckM: Assessing the quality of microbial genomes recovered from isolates, single cells, and metagenomes. *Genome Res.* 25, 1043–1055. doi: 10.1101/gr.186072.114

Price, M. N., Dehal, P. S., and Arkin, A. P. (2010). FastTree 2–Approximately maximum-likelihood trees for large alignments. *PLoS One* 5:e9490. doi: 10.1371/journal.pone.0009490

Qin, J., Li, R., Raes, J., Arumugam, M., Burgdorf, K. S., Manichanh, C., et al. (2010). A human gut microbial gene catalogue established by metagenomic sequencing. *Nature* 464, 59–65. doi: 10.1038/nature08821

Santoro, C., Arbizzani, C., Erable, B., and Ieropoulos, I. (2017). Microbial fuel cells: From fundamentals to applications. A review. *J. Power Sources* 356, 225–244. doi: 10.1016/j.jpowsour.2017.03.109

Seemann, T. (2014). Prokka: Rapid prokaryotic genome annotation. *Bioinformatics* 30, 2068–2069. doi: 10.1093/bioinformatics/btu153

Steinegger, M., and Soding, J. (2017). MMseqs2 enables sensitive protein sequence searching for the analysis of massive data sets. *Nat. Biotechnol.* 35, 1026–1028. doi: 10.1038/nbt.3988

Suman, J., Neeraj, S., Rahul, J., and Sushila, K. (2014). Microbial synthesis of silver nanoparticles by *Actinotalea* sp. MTCC 10637. *Am. J. Phytomed. Clin. Ther.* 2, 1016–1023.

Szydlowski, L., Ehlich, J., Goryanin, I., and Pasternak, G. (2022). High-throughput 96-well bioelectrochemical platform for screening of electroactive microbial consortia. *Chem. Eng. J.* 427:131692. doi: 10.1016/j.cej.2021.131692

Szydlowski, L., Sorokin, A., Vasieva, O., Boerner, S., Fedorovich, V., and Goryanin, I. (2020). Evolu-tionary dynamics of microbial communities in bioelectrochemical systems. *J. Comput. Sci. Syst. Biol.* 13, 0–8. doi: 10.1101/725580

Tahernia, M., Mohammadifar, M., Gao, Y., Panmanee, W., Hassett, D. J., and Choi, S. (2020). A 96-well high-throughput, rapid-screening platform of extracellular electron transfer in microbial fuel cells. *Biosens. Bioelectron.* 162:112259. doi: 10.1016/j.bios.2020.112259

Tahernia, M., Mohammadifar, M., Hassett, D. J., and Choi, S. (2019). A fully disposable 64-well papertronic sensing array for screening electroactive microorganisms. *Nano Energy* 65:104026. doi: 10.1016/j.nanoen.2019.104026

Tao, H. C., Li, W., Liang, M., Xu, N., Ni, J. R., and Wu, W. M. (2011a). A membrane-free baffled microbial fuel cell for cathodic reduction of Cu(II) with electricity generation. *Bioresour. Technol.* 102, 4774–4778. doi: 10.1016/j.biortech.2011.01.057

Tao, H. C., Liang, M., Li, W., Zhang, L. J., Ni, J. R., and Wu, W. M. (2011b). Removal of copper from aqueous solution by electrodeposition in cathode chamber of microbial fuel cell. *J. Hazard. Mater.* 189, 186–192. doi: 10.1016/j.jhazmat.2011.02.018

Tyson, G. W., Chapman, J., Hugenholtz, P., Allen, E. E., Ram, R. J., Richardson, P. M., et al. (2004). Community structure and metabolism through reconstruction of microbial genomes from the environment. *Nature* 428, 37–43. doi: 10.1038/nature02340

Westbrook, A., Ramsdell, J., Schuelke, T., Normington, L., Bergeron, R. D., Thomas, W. K., et al. (2017). PALADIN: Protein alignment for functional profiling whole metagenome shotgun data. *Bioinformatics* 33, 1473–1478. doi: 10.1093/bioinformatics/btx021

Wu, W., Liu, X., Zhang, X., Zhu, M., and Tan, W. (2018). Bioleaching of copper from waste printed circuit boards by bacteria-free cultural supernatant ofiron-sulfur-oxidizing bacteria. *Bioresour. Bioprocess.* 5:10. doi: 10.1186/s40643-018-0196-6

Wu, Y. W., Simmons, B. A., and Singer, S. W. (2016). MaxBin 2.0: An automated binning algorithm to recover genomes from multiple metagenomic datasets. *Bioinformatics* 32, 605–607. doi: 10.1093/bioinformatics/btv638

Wu, Y., Zhao, X., Jin, M., Li, Y., Li, S., Kong, F., et al. (2018). Copper removal and microbial community analysis in single-chamber microbial fuel cell. *Bioresour. Technol.* 253, 372–377. doi: 10.1016/j.biortech.2018.01.046

Yan, Z. F., Lin, P., Li, C. T., Kook, M., and Yi, T. H. (2018). *Actinotalea solisilvae* sp. Nov., isolated from forest soil and emended description ofthe genus *Actinotalea*. *Int. J. Syst. Evol. Microbiol.* 68, 788–794. doi: 10.1099/ijsem.0.002584

Yang, J., Anishchenko, I., Park, H., Peng, Z., Ovchinnikov, S., and Baker, D. (2020). Improved protein structure prediction using predicted interresidue orientations. *Proc. Natl. Acad. Sci. U.S.A.* 117, 1496–1503. doi: 10.1073/pnas.1914677117

Yang, T., Xu, Z., Wen, J., and Yang, L. (2009). Factors influencing bioleaching copper from waste printed circuit boards by *Acidithiobacillus ferrooxidans*. *Hydrometallurgy* 97, 29–32. doi: 10.1016/j.hydromet.2008.12.011

Yi, H., Schumann, P., and Chun, J. (2007). *Demequina aestuarii* gen. nov., sp. nov., a novel actinomycete ofthe suborder Micrococcineae, and reclassification of *Cellulomonas fermentans* Bagnara et al. 1985 as *Actinotalea fermentans* gen. nov., comb. nov. *Int. J. Syst. Evol. Microbiol.* 57, 151–156. doi: 10.1099/ijs.0.64525-0

Yuan, Y., Zhao, B., Zhou, S., Zhong, S., and Zhuang, L. (2011). Electrocatalytic activity of anodic biofilm responses to pH changes in microbial fuel cells. *Bioresour. Technol.* 102, 6887–6891. doi: 10.1016/j.biortech.2011.04.008

Yumoto, I., Nakamura, A., Iwata, H., Kojima, K., Kusumoto, K., Nodasaka, Y., et al. (2002). *Dietzia psychralcaliphila* sp. nov., a novel, facultatively psychrophilic alkaliphile that grows on hydrocarbons. *Int. J. Syst. Evol. Microbiol.* 52, 85–90. doi: 10.1099/00207713-52-1-85

Zhou, S., Wen, J., Chen, J., and Lu, Q. (2015). Rapid measurement of microbial extracellular respiration ability using a high-throughput colorimetric assay. *Environ. Sci. Technol. Lett.* 2, 26–30. doi: 10.1021/ez500405t

Chemical Engineering Journal 427 (2022) 131692

Contents lists available at ScienceDirect

Chemical Engineering Journal

journal homepage: www.elsevier.com/locate/cej

High-throughput 96-well bioelectrochemical platform for screening of electroactive microbial consortia

L. Szydlowski [a], J. Ehlich [b], I. Goryanin [a,c,d], G. Pasternak [e,*]

[a] Biological Systems Unit, Okinawa Institute of Science and Technology, Japan
[b] Faculty of Chemistry, Brno University of Technology, Czechia
[c] School of Informatics, University of Edinburgh, United Kingdom
[d] Tianjin Institute of Biotechnology, China
[e] Laboratory of Microbial Electrochemical Systems, Faculty of Chemistry, Wroclaw University of Science and Technology, 50-370 Wroclaw, Poland

ARTICLE INFO

Keywords:
Microbial fuel cells
Multi well array
Bioelectrochemistry
Dissimilatory metal reduction
Bioremediation
Wastewater treatment

ABSTRACT

The development of bioelectrochemical systems reinforces the necessity for the identification and engineering of electroactive bacteria with improved performance and novel biochemical properties. In this study, using a newly designed 96-well-plate array of microbial fuel cells (MFCs), we compared the electroactive capabilities of microbial communities derived from four mine drainages. The maximum power density of individual wells after two weeks of inoculation was 102 mW/m^3, whereas the maximum current density was 1.6 A/m^3. Transferring communities from individual wells into larger MFCs comprising low (20 mg/L) and high (200 mg/L) concentrations of Cu yielded maximum power densities of 445 and 58 mW/m^3, respectively, with up to a 3.7 fold decrease in Cu^{2+} ions within 24 h. Electrochemical data analysis revealed that microbial consortia can be distinguished based on their electrochemical profiles. Our results showed that a 96-well MFC array is a suitable platform for high-throughput screening, selection, and subsequent source of enriched electroactive consortia. The quantitative and comparative analysis followed by principal component analysis indicated that the initial environmental conditions, as well as physical and chemical parameters of the lakes were crucial to develop an efficient electroactive community. Further applications of the proposed platform include genetic engineering, phenotype screening, and mutagenesis studies of both microbial communities and single cultures. This is the first time that a high-throughput MFC platform is used to evaluate the performance of multiple electroactive consortia towards Cu removal.

1. Introduction

Microbial fuel cells (MFCs) are devices in which anodic microorganisms oxidize organic matter and produce electric current as a byproduct of their metabolism. The most typically investigated applications are water and wastewater treatments [1–4]. Nevertheless, MFCs and other types of bioelectrochemical systems (BESs) have been applied in biosensors [5,6], nutrient and metal recovery [7–9], remediation technology [10,11], the biosynthesis of organic compounds [12,13], biogas production [14].

The extensive studies conducted on MFCs worldwide have resulted in numerous reactor designs [15]. The most critical components of MFC design comprise several groups of separators [16,17], electrode materials, and catalysts [18,19]. Such diversity renders comparative studies extremely difficult, as a significant portion of electroactive bacteria activity is determined and limited by the reactor design, materials used, etc. Some researchers [20,21] have manufactured miniaturized MFCs from unified materials, such as serum vials, which allowed the comparative analysis of buffers and their effects on pure and mixed cultures of electrogens, as well as the Coulombic efficiencies of various electroactive strains fed with identical substrates. Hou *et al.* [22–24] developed multiwell arrays to further miniaturize and unify reactors by depositing Ti/Au on glass to fabricate anodes with ferricyanide [22], air-cathodes [23] or microfluidic channels with continuous anolyte and catholyte replenishment [24] which increased the power output by a factor of three. These reactors were used to screen previously selected electrochemically active environmental isolates. Another example of well-plate array implementation was demonstrated by Yuan *et al.*,

* Corresponding author.
E-mail address: grzegorz.pasternak@pwr.edu.pl (G. Pasternak).

https://doi.org/10.1016/j.cej.2021.131692
Received 12 April 2021; Received in revised form 30 July 2021; Accepted 3 August 2021
Available online 10 August 2021

([25]), where extracellular electron transfer was coupled to the color change of the probe. Recently, Molderez *et al.* [26] constructed a 128-channel potentiostat connected to a printed circuit board (PCB) microarray. The entire microarray was immersed in an anolyte solution and supplied with a reference electrode to perform a high-throughput investigation pertaining to the effect of the anodic potential on electroactive biofilm growth. Zhou *et al.* [27] proposed a well-plate-based, high-throughput colorimetric assay for microbial electrochemical respiration, which would indicate extracellular electron transfer. As an alternative approach, Choi *et al.* [28–31] developed a single sheet, paper-based electrofluidic array comprising six [28], eight [29], sixty four [30] and ninety six wells [31] using a novel wax printing fabrication method. The resulting microliter reactors allowed the rapid screening of various *P. aeruginosa* strains and mutants. The aforementioned designs successfully eliminated some of the problems of miniaturized devices, e.g., high internal resistance, complex manufacturing, and low sample accessibility. Our recently developed reactor [32] based on a 96-well plate exhibits the abovementioned features as well. Furthermore, it offers long-term operation capacity and reusability, thereby allowing the selective enrichment of electroactive consortia. Moreover, our design provides high endurance; therefore, it can be utilized in fieldwork, allowing high-throughput *in situ* operations. The electrical connections embedded in our design enable the well plate to be connected to the potentiostat, similar to the case described by Mohamed *et al.* [33].

In addition to the critical design components of MFCs, the most important component is the biocatalyst. Pure microbial cultures, as well as their synthetic or natural consortia, are fundamental for the operation and performance of MFCs as well as for the acquisition of certain products from their metabolism, e.g., electricity or particular metabolic pathways [34,35]. Similarly, the high-throughput approach for investigating the effects of electrode potential and external loads to control microbial metabolism is crucial for understanding MFC operation and community development [36,37]. Nevertheless, the number of high-throughput tools available for studies related to electroactive bacterial species and communities is limited.

High-throughput MFCs may be utilized as a platform for the robust screening and enrichment of electroactive microbial consortia derived from various environments. Because the most typical application of MFCs is wastewater treatment [15], such consortia may be conditioned for specific waste streams and removal of particular contaminants, such as heavy metals. One such application may be Cu removal from industrial waste streams. Cu is a micronutrient that serves as a co-factor for many enzymes, and its concentration up to 20 mg/L is not considered toxic for microorganisms [38], although higher concentrations pose an inhibitory effect on yeast and may affect the yield of fermentative processes. Moreover, Cu is accumulated by plants and hence poses a threat to agriculture [39]. However, Cu is a valuable element whose recovery from wastewater is economically attractive and can be a promising alternative for reducing the environmental effect of mining. In our previous study [32], we successfully enriched a microbial community resistant to up to 450 mg/L of Cu ions. Other studies [40,41] demonstrated that electroactive microbial communities can tolerate Cu concentrations of up to 6400 mg/L. The copper in such systems is being precipitated and deposited in the chamber. Subsequently it can be removed from the system. Although to the best of our knowledge this technology has not yet been demonstrated in pilot scale studies, the combination of electricity production with simultaneous Cu precipitation offers a great advantage over traditional methods of copper recycling in terms of electrical energy requirements to carry out the process. In order to scale-up the MFC technology towards copper precipitation, one must demonstrate the effective and stable transition of such preconditioned microbial consortia to larger-scale reactors.

Therefore, in this study, we demonstrated the application of a 96-well MFC platform for the high-throughput selection of the best-performing electrogenic consortia as an initial step toward the upscaling of these consortia to reduce the transition time while retaining the desired microbial activity. Using a novel 96-well array, we attempted to selectively enrich electroactive microbial communities from mineral (Cu, Zn, S) mine drainages and subsequently investigated their tolerance to Cu. We identified four sites of former Cu mine drainages in a Cu-rich area, that are geographically proximal but separated, thereby allowing the development of distinct communities. Deposits in this area, called Rudawy Janowickie, located in south-west Poland (Fig. 1), were formed by hydrothermal veins and mined from Middle ages up to the 20th century. It was identified as rich in Cu but poor in Pb, Ag, As, and Fe [42]. Using our platform, we continuously monitored the electrochemical performance of the environmental samples and sequenced the anodic biofilms from each group. Subsequently, we transferred two of the best-performing biofilms to larger reactors maintained under low and high Cu concentrations and then monitored their electrochemical performance, as well as the removal of Cu ions. When coupled with principal component analysis, by using 96-array, we were capable to select the best combination of environmental and physical–chemical parameters of the lakes desired for enriching the most efficient bacterial communities.

2. Materials and Methods

2.1. Sample collection

Environmental samples were obtained from four colorful lakelets in Rudawy Janowickie (50.8°N; 15.9°E, Fig. 1), which contained mine (Cu, Fe, S) drainages. The sampling session was conducted in January of 2020. Physical and chemical parameters such as temperature, pH, conductivity, and oxidation/reduction potential (ORP) were measured *in situ* using a CX-601 m (Elmetron, Poland). Samples from each lake were analysed for Cu concentration measurements (Copper TNTplus Vial Test, Hach), which were performed according to the manufacturer's instructions.

2.2. Well-plate design and operation

Each well was constructed as an individual MFC with a membraneless design. The base anode plate was a standard PCB with a thin Cu sheet (17 μm) that was electrolessly plated with nickel and shielded with a 2 μm layer of electroplated gold (PCBWAY, China). This component was exposed to an anolyte solution inside the reactor. The base cathode material was carbon paper (090, Toray, Japan) treated with polytetrafluoroethylene to prevent water leakage. Carbon paper was glued to the gold connective pads on the PCB using 8331S conductive epoxy (MG Chemicals, Japan), which provided robust mechanical and electrical connections. An additional layer of porous sponge-based material was placed on the air side of the cathode to prevent the cathode from drying out. The well-plate body was 3-D printed using an Objet 500 Connex 3 three-dimensional printer (Stratasys, USA), where compatible Vero resins were applied. The seal was adapted using a 96-well sealing mat (Thermofisher, USA) that was glued to the inner side of the cathode PCB. The design of the 96-well MFC is shown in Fig. 1ab.

The MFC array was inoculated with either water (concentrated) and sediment samples, as described in Table S1. To enable the analysis of microbial communities, six disks of carbon veil (CV, 3 mm in diameter) were placed on the bottom of the selected wells. Additionally, square rings were laser-cut and inserted into each inoculated well to press the CV disks and their biofilms onto the bottom of the electrode, which served as a current collector. Each well (1 cm^3 in volume) was fed with mineral salt medium (MSM) prepared as follows (per liter): NH_4Cl (1.5 g), Na_2HPO_4 (0.6 g), KCl (0.1 g), $NaHCO_3$ (2.5 g), and 10 mL/L of a trace element containing 1 g/L acetate as the carbon source. The MSM was changed daily by replacing 50% of its volume with fresh medium. During the operation, samples were obtained for Cu analysis (Copper TNTplus Vial Test, Hach), performed according to the manufacturer's

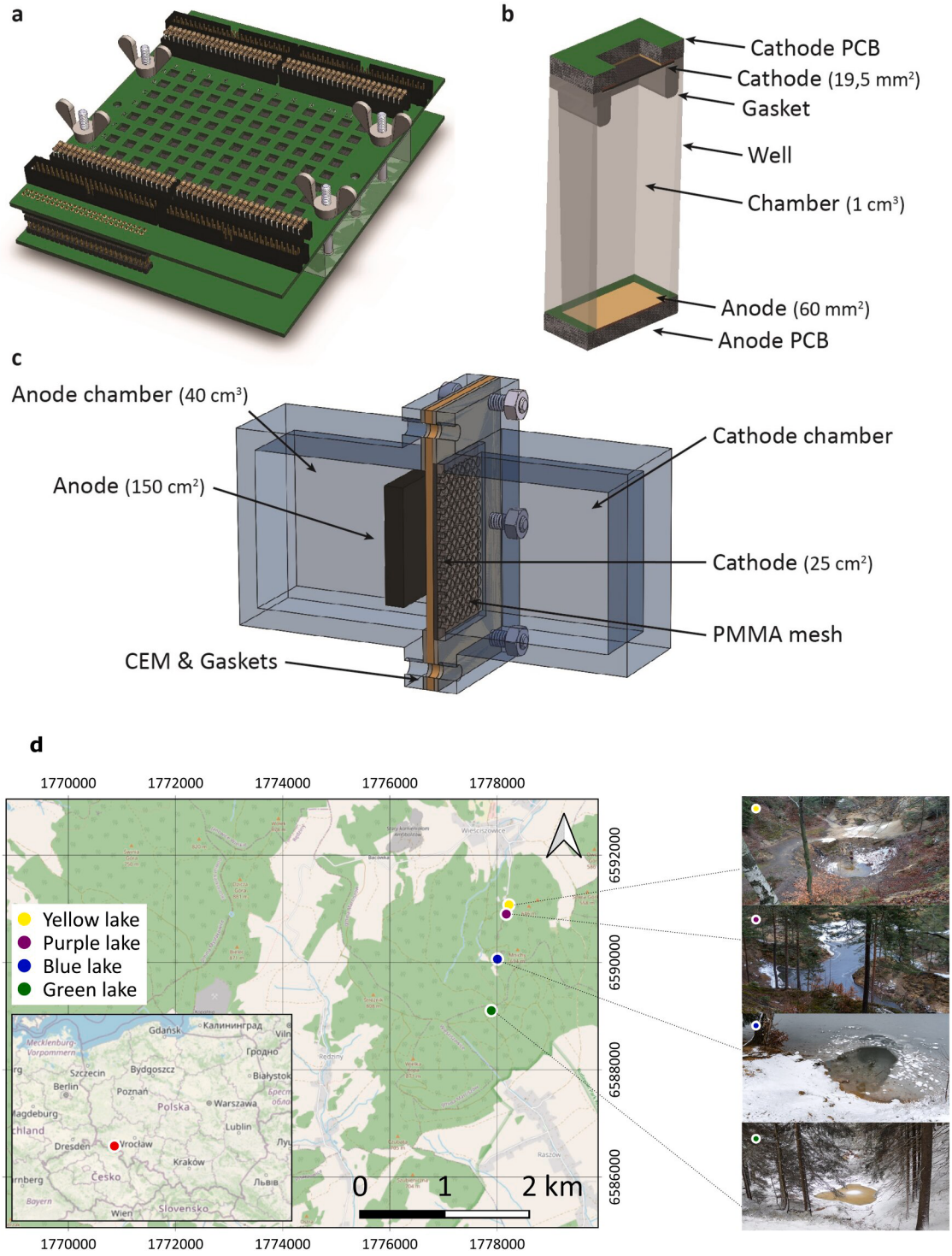

Fig. 1. Three-dimensional view of 96-well MFC design: **a)** whole plate view; **b)** cross-section of individual well; c) schematic view of large-scale MFC; d) location and photographs of sampling sites.

instructions.

2.3. *Large MFC design and biofilm transfer*

A larger (40 mL), air–cathode MFCs (Fig. 1c), were manufactured by using laser-cut poly(methyl methacrylate) sheets. The anodic and cathodic compartments were separated using a commercial cation exchange membrane (CMI-7000, Membranes International, USA). The anode electrode (projected surface area of 150 cm^2) comprised a 30 g/m^2 CV (PRF Composite Materials, Dorset, UK), whereas the cathode electrode (25 cm^2) was made of Vulcan carbon paper with 0.5 mg/cm^2 of 60% platinum (Fuel Cell Store, USA). A cathode chamber was used to maintain the hydration of the cathode. Both electrodes were connected by a Ni-Cr wire (Ø 0.66 mm, ALBu, Poland) to the external load. The displacement volumes of the anodic compartment were 40 and 62.2 cm^3 without the electrode.

After 4 weeks, two electrode disks derived from individual wells of the 96-well-plate BES, which comprised the best-performing consortia

(D7 and H1), were transferred into larger (40 mL) MFC reactors in duplicate. One set of these MFCs contained 20 mg/L of Cu (labeled as D7L and H1L), whereas the second set contained 200 mg/L of Cu (labeled as D7H and H1H) in MSM, which was replaced every 48 h. An external resistance (R_{ext}) of 4 kΩ was applied to each reactor, and its potential was monitored in real time using an ADC24 (Pico Technology, UK). After performing polarization experiments, R_{ext} was decreased to 2 and 1 kΩ after 3 and 4 weeks, respectively, for the D7L reactor.

2.4. Electrochemical measurements

Upon inoculation, linear sweep voltammetry (LSV) and electrochemical impedance spectroscopy (EIS) measurements were performed under the following conditions and parameters: two-electrode setup, where the reference electrode was connected to the counter electrode and the anode was the working operating electrode; for LSV, the potential range was from 0 mV vs. open circuit potential (OCP) to 0 mV vs. reference electrode, 0.1 mV/s scan rate, and 0.2 mV step. For EIS, the frequency range was between 1 MHz and 50 mHz, with 7 mV steps. EIS data (Table S2) were used to determine the internal resistance of the MFCs. The LSV measurements were performed repeatedly every week to conform to the growth dynamics of the electroactive communities. Upon transfer to the larger MFCs, the measurements were performed each week for 21 days.

2.5. Data analysis

All data derived from the experiments were preprocessed using Microsoft Excel 2016. Subsequently, the data were processed and analyzed using the RGUI environment v 3.6.1 [43]. Pearson's correlation coefficient was calculated and hierarchical clustering was performed to analyze the similarity in microbial growth dynamics in each of the communities derived from the same and from different lakelets in a manner similar to that described previously [36].

2.6. Scanning electron microscopy (SEM) and energy-dispersive x-ray spectroscopy (EDS)

Once the biofilm had matured in the 96-well MFC array, selected CV electrode disks (1 from each group), as well as electrode fragments from large-scale reactors, were collected. Subsequently, the biofilm was prepared as follows: samples were fixed in 2.5% glutaraldehyde (Sigma) in 0.1 M phosphate buffer (pH 7.3) for 12 h at 4 °C and then washed three times for 10 min each in 0.1 M phosphate buffer at 4 °C. Subsequently, the samples were dehydrated for 10 min each in 50%, 60%, 70%, 80%, 90%, 95%, and 100% ethanol, and a 100% wash was repeated three times. Next, the samples were immersed in pure HMDS (Sigma), followed by 10 min of air drying. Analyses were then performed using Xe-PFIB FEI (Helios PFIB), which was provided by Nanores (Wroclaw, Poland).

2.7. DNA extraction and 16S sequencing

Selected electrodes with biofilms of the best-performing well-plate MFCs (from each lakelet) were subjected to DNA extraction (two CV disks) using a soil extraction kit (A&A Biotechnology, Poland) followed by the DNA clean-up kit (A&A Biotechnology, Poland), performed according to the manufacturer's instructions. Subsequently, they were resuspended in equal volumes (50 μL) of TE buffer. The DNA concentration was measured using a UV–Vis spectrometer (Nanodrop) and the total DNA amount was normalized to the electrode surface area (0.283 cm^2) to estimate the biomass of the electrode communities, as shown in Figure S1. For 16S sequencing, 10 ng of genomic DNA was obtained from each sample, and the volume was adjusted to 10 μL with nuclease-free H_2O and subjected to PCR with 16S barcoded primers based on the manufacturer's instructions (16S barcoding kit, Oxford Nanopore). After the PCR, the concentration was measured using a Qubit fluorometer (Thermo Fisher) and further purified using AMPure XP magnetic beads (Beckman Coulter). The quality of the obtained amplicons was assayed using a BioAnalyzer (Agilent 2100), and peaks from the libraries are presented in Figure S2. The pooled barcoded 16S library was prepared and the sequencing of the four communities and their taxonomy analysis were performed using Oxford Nanopore Technology (Oxford Nanopore, UK) [44]. The sequences were analyzed, and a species richness table was generated using Geneious software (Biomatters, New Zealand). As a metric for biodiversity, the Shannon index was calculated for each sample.

3. Results and Discussion

3.1. MFC operation

The assembled well plate and its overview are shown in Fig. 1. After assembly, EIS was performed on each well prior to inoculation using a sterile medium as an electrolyte (Table S2). The results show that the average internal resistance was 646 ± 38 Ω for the entire plate. We inoculated wells from rows B, D, F, and H of the blue, purple, green, and Yellow Lakes, respectively. The physicochemical parameters of each lake are summarized in Table 1. The ORPs were measured to identify conditions that favor the presence of electroactive bacteria. Our results show that the purple sediment recorded the highest ORP and conductivity, i.e., 542 mV and 6.7 mS/cm, respectively. Similar findings were obtained for the Yellow Lake, although its ORP was higher in the water fraction (525 and 497 mV), whereas its conductivity was higher in the sediment fraction (4.7 mS/cm w.r.t. 3.15 mS/cm). The Green Lake exhibited the lowest values for the abovementioned parameters. Moreover, the Yellow Lake contained the highest amount of Cu (5.21 mg/L), whereas the purple, green, and Blue Lakes indicated 1.19, 0.16, and 0.15 mg/L of Cu, respectively. Samples originating from the water fraction were placed in wells B/D/F/H 1–5, whereas sediments were inserted in wells B/D/F/H 7–10 and 12. Wells 5 and 12 were used as OCP control. For the 40 wells used in our study, the average R_{int} was 637 ± 20 Ω. The experimental setup of the well-plate MFC is summarized in Table S1.

Real-time data monitoring is presented in the form of weekly maximum current densities (Fig. 2). A maximum current density of 1.6 A/m^3 (0.82 A/m^2) was observed in cell H1 in the third week of operation (15 d after inoculation). In the first week, cell H1 exhibited a maximum current density of 0.38 A/m^3, with 1.1 A/m^3 recorded in weeks 2 and 4. By contrast, the worst-performing cell, B8, yielded current densities not exceeding 0.1 A/m^3 in week 1, with a decrease to 0.02 A/m^3 in week 2 and a further decrease in the following weeks to less than the resolution of the datalogger. Cell H1 originated from the water fraction of the Yellow Lake. An initial analysis of all lakes (Table 1) indicates that conditions in the Yellow Lake may have facilitated the growth of electroactive bacteria, such as high ORP and conductivity. Other cells from this group, except H3 and H4, yielded current densities exceeding 1 A/m^3, and the peak performance was recorded in weeks 2–3. Consortia derived from the Green Lake, which indicated the lowest ORP and conductivity, demonstrated the worst performance in the MFCs. Cells F1–10 did not exceed 0.9 A/m^3, and their maximum values were recorded in weeks 2–3.

Meanwhile, hierarchical clustering (Fig. 2b) shows the aggregation of MFCs with similar electrochemical profiles that correspond to their inoculum sources. This pattern was adequate for either the best-performing (Yellow Lake) or worst-performing (Green Lake) community, where a more dispersed pattern was observed in the purple- and blue-lake-derived consortia. Therefore, the different microbial communities derived from different environments can be distinguished based solely on their electrochemical behavior reflected in the high-throughput system. In previous studies, Pasternak *et al.* [36,45] demonstrated that the physiological and electrochemical behaviors of

Table 1
Physical and chemical characteristics of the inocula measured *in situ* at sample collection site. ORP – oxidation/reduction potential.

Lake color/component		Well	Temp [°C]	pH	Conductivity [mS/cm]	ORP [mV]	Cu, mg/L Average ± SD
Blue	Water	B1-5	2.1	6.70	0.4	197	0
———	Sediment	B7-12	3.4	6.07	0.46	258	0.15 ± 0.01
Purple	Water	D1-5	1.76	3.51	1.8	465	0.16 ± 0.03
	Sediment	D7-12	3.86	3.11	6.3	542	1.19 ± 0.15
Green	Water	F1-5	2.21	7.75	0.17	234	0
	Sediment	F7-12	3.3	6.30	0.19	−6.2	1.05 ± 0.02
Yellow	Water	H1-5	1.74	3.36	3.15	525.1	0.26 ± 0.04
	Sediment	H7-12	3.73	3.18	4.7	497	5.21 ± 0.07

microorganisms are extremely stable and highly dependent on the adaptation conditions. In our study, these profiles were solely dependent on the environment type, as adaptation was performed in the same manner for each inoculate.

By monitoring the power density from LSV measurements, we observed that cell H1 (Fig. 2c) recorded the highest value of 102 mW/m^3 in week 2, whereas cell B4 recorded the lowest value of less than 20 mW/m^3 in the first week of operation, and the value further decreased throughout the operation. The Yellow Lake showed the highest power density, which increased continuously throughout the experiment. The Blue Lake exhibited the lowest average power density, and the Green Lake demonstrated the worst performance by the end of the experiment. The correlation coefficients calculated for each group indicated the highest value (0.82) for cells H1–5 derived from the Yellow Lake (water fraction). In all other groups, the correlation did not exceed 0.26. Similarly, the Yellow Lake demonstrated the lowest discrepancy in correlation, which is attributable to its abundance in electroactive microorganisms. Additionally, the result indicates the difficulties in maturing reproducible electroactive biofilms derived from weakly originating communities. Molderez *et al.* discussed the technical challenges in establishing MFC systems based on selecting only 77 among 128 electrodes to ensure the highest reproducibility [26].

Similar to other micro MFC arrays [22–24,29,30], current production was observed starting from the first day of inoculation in this study. Because we used plain carbon paper on our cathodes, the power densities were lower than those reported by Tahernia *et al.* [30,31]. The experiment conducted in this study shows that the electroactive consortia reached their peak performance 2–3 weeks after well-plate inoculation. This duration may indicate the optimal time for biofilm enrichment in the 96-well-plate setup, as a similar duration was reported previously in our study involving a 96-well-plate MFC [32]. Increasing the anode surface by adding more carbon disks might prolong this duration and result in better peak performances. In fact, recovered Cu might serve as a cathode catalyst, as previously described [46].

Statistical and data mining approaches for current and power densities, as presented in Figs. 2 and 3, respectively, identified two consortia that demonstrated the best electrochemical performance, stability, and reproducibility over time, suggesting the strongest and most promising microbial communities. Therefore, these consortia were sampled from H1 (derived from yellow water) and D7 (derived from purple sediment) cells. In addition, these two communities were derived from environmental samples and indicated the highest ORP, conductivity, and Cu content (Table 1). These findings suggest that these parameters can initially indicate the abundance of electroactive microorganisms. The changes in their electrochemical behavior and biofilm development, monitored through polarization experiments, are shown in Fig. 3 (a). In terms of power, communities D7 and H1 achieved 41 and 102 nW, respectively, which correspond to 2 and 5 mW/m^2 or 41 and 102 mW/m^3, respectively.

The analysis of Cu concentration revealed that the inoculates contained Cu^{2+} ions exceeding 1 mg/L, and that the well-plate BES maintained a Cu^{2+} ion concentration of 1.38 ± 0.38 mg/L. The Cu within the individual wells originated from environmental inoculates, as the MSM medium showed no traces of Cu, and the well plates tested for possible Cu leaching from the electrodes prior to inoculation indicated a concentration of less than 2 μg/L, which was the detection limit. To verify the tolerance of the consortia to Cu^{2+} ions, the electroactive biofilms from D7 and H1 were transferred into larger reactors, supplied with either 20 mg/L of Cu^{2+} (D7L, H1L) or 200 mg/L of Cu^{2+} (D7H, H1H). After the biofilm transfer, a rapid increase in power density was observed after 3 weeks. These results indicate that scaling-up (40x increase in reactor volume) and the corresponding expansion of pre-grown biofilm can be realized using the high-throughput approach presented herein. After 3 weeks of operation, the reactors inoculated with D7 achieved power densities of 191 and 57 mW/m^3 when grown with 20 and 200 mg/L of Cu, respectively (Fig. 3bc), whereas the reactors inoculated with H1 achieved 445 and 58 mW/m^3 when grown with 20 and 200 mg/L of Cu, respectively (Fig. 3bc). The results indicate that both communities can tolerate Cu content of up to 20 mg/L, which is known to be non-toxic for the majority of microorganisms [38]. Similarly, for both communities, a higher Cu^{2+} content resulted in decreased power densities.

3.2. Sequencing and biofilm investigation

Taxonomy analysis revealed that the best-performing community in well H1 (from Yellow Lakelet) exhibited the least diversity compared with the other reactors (Fig. 4), with a Shannon index of 1.62 and a Gammaproteobacteria class comprising 78.8% of the entire community. By contrast, well B8, which originated from the Blue Lake and was the worst-performing community in this study, showed the highest diversity (Shannon index 1.91), with a Gammaproteobacteria class comprising only 62.8% of all organisms identified. In wells D7 (from Purple Lake) and F8 (from Green Lake), the corresponding values were 1.68/64.9% and 1.81/63.8%, respectively. When estimating the biomass, the H1 sample (Yellow Lake water) yielded the highest value of DNA per electrode surface area – 189.7 ng/cm^2, which was more than two times higher than that of B8 (Blue Lake sediment, 80.1 ng/cm^2). The DNA amounts obtained from D7 (Purple Lake sediment) and F8 (Green Lake sediment) were of 145.8 and 106.2 ng/cm^2, respectively. The most abundant order in H1 was *Pseudomonadales*, which constituted 19.5% of the biofilm, whereas those in F8, D7, and B8, were 13.8%, 11.3%, and 5.1%, respectively. Moreover, in the B8 community, the most abundant family was *Xanthomonadaceae* (14%), whereas the most abundant genus was *Stentotrophomonas* (0.2%), which was five times more abundant than that in H1 (0.004%). The hierarchical clustering shown in Fig. 2 indicates that samples H1 and D7 were clustered more closely to each other compared with samples B8 and F8.

The electrochemical results from inocula screening indicated that the most electroactive consortia were obtained from the lakes that indicated the highest Cu content, ORP, and conductivity (yellow and purple, Table 1), which is consistent with previous studies pertaining to the effect of set potential on electrogenic biofilm growth [33,47–51]. Colorful lakelets contained various Cu and Zn oxyminerals, and hence expected to be a relevant source of electroactive bacteria [42,52–54]. Moreover, the cell with the best performance (H1) showed the least

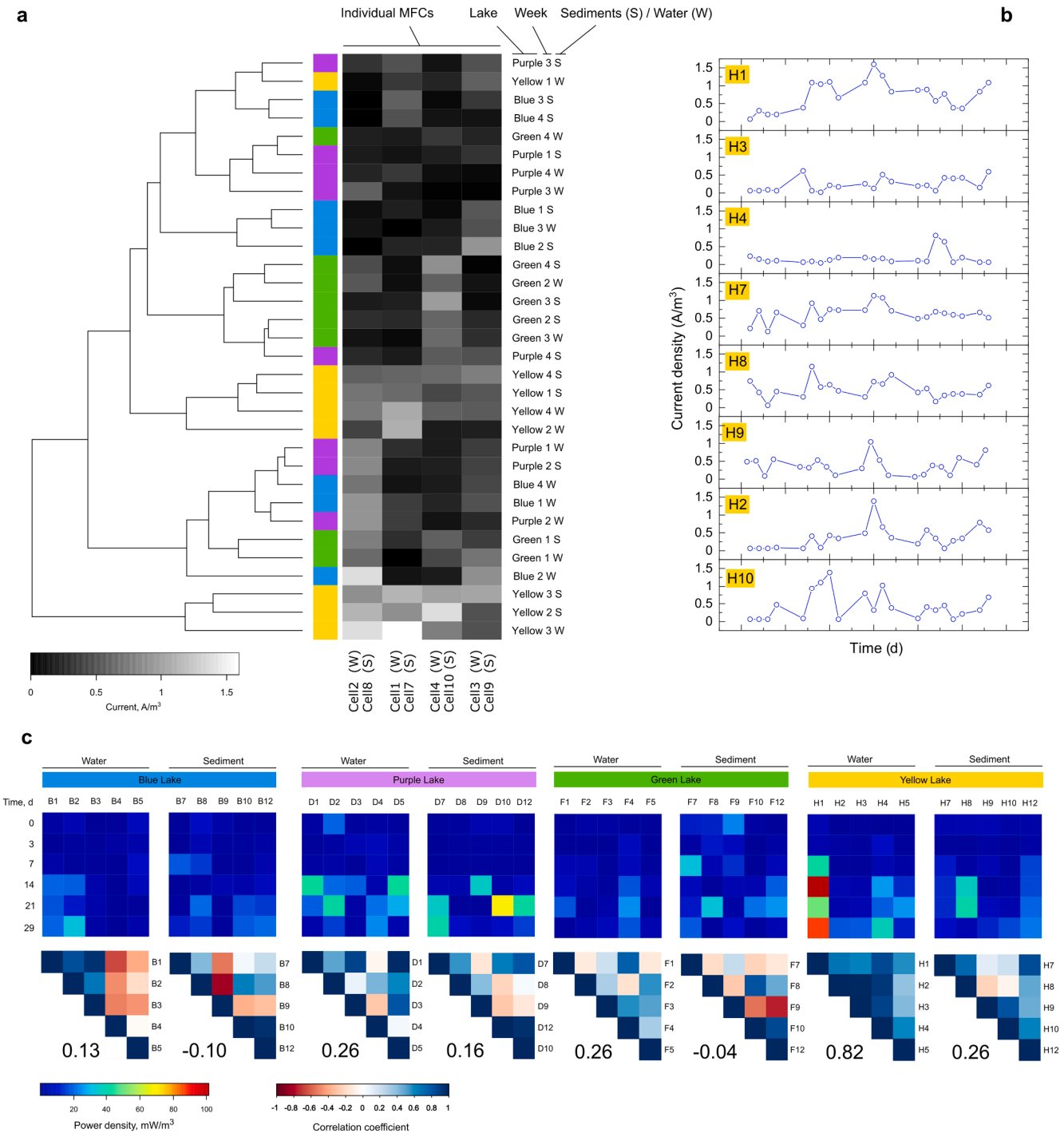

Fig. 2. a) Results of hierarchical clustering and heatmap of maximal weekly current densities observed for each inoculum and each individual replicate cell. Each row represents individual inoculum in 1 week, whereas each column represents individual MFC – corresponding either to rows designated as W (water) or S (sediment); b) current density (indicated on y-axis as A/m^3) from best-performing group (Yellow Lakelet); c) Maximum values of power density obtained from polarization experiments, observed in time for each individual MFC-well (square-shaped heatmaps), and analysis of correlation coefficients between each power profiles within individual inoculum (triangle-shaped correlograms). Numerical values represent average correlations observed within closed-circuit MFCs (cells 1–4 and 7–10). For the meanings of colors shown in this image, please refer to online version of manuscript.

taxonomic diversity, which is consistent with other studies [49,55], where the least diverse biofilms indicated strong selection toward electroactive bacteria. Although the pH in either the purple or Yellow Lake was acidic (3.11 and 3.36, respectively), these communities adapted to the near-neutral pH (6.8) of the MSM medium, indicating a broad range of living conditions.

The results of SEM and EDS analyses, as well as photographs of the biofilm, are shown in Fig. 5, which depict the workflow of biofilm transfer from the 96-well MFC to the larger MFCs. The SEM micrographs of the CV insets derived from miniature cells (community H1) confirmed the occurrence of an electroactive biofilm. The biofilm grown on these inserts was rich in lipopolysaccharides. Nanometer-scale filamentous and particle-shaped structures were identified (Fig. 5-1), which were similarly observed in larger MFCs. These filaments were

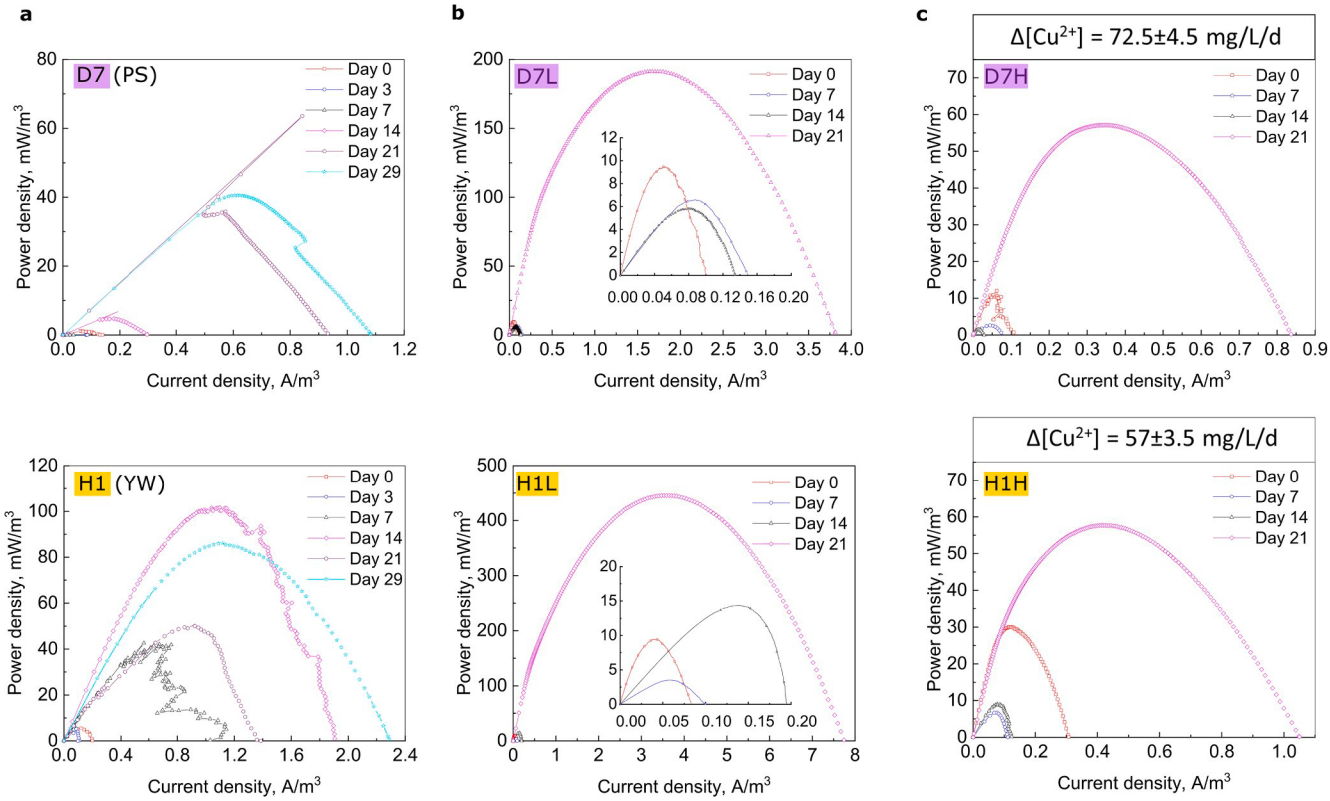

Fig. 3. Power curves for: a) best-performing well-plate cell reactors (D7 and H1); b) large reactors with 20 mg/L of Cu (D7L and H1L). c) Large reactors with 200 mg/L of Cu (D7H and H1H). Meanings of symbols: $\Delta[Cu^{2+}]$ - daily removal rate of soluble Cu calculated from anodic chamber; PS – Purple Lake (sediments); YW – Yellow Lake (water). Insets show magnified power curves within lower current and power ranges.

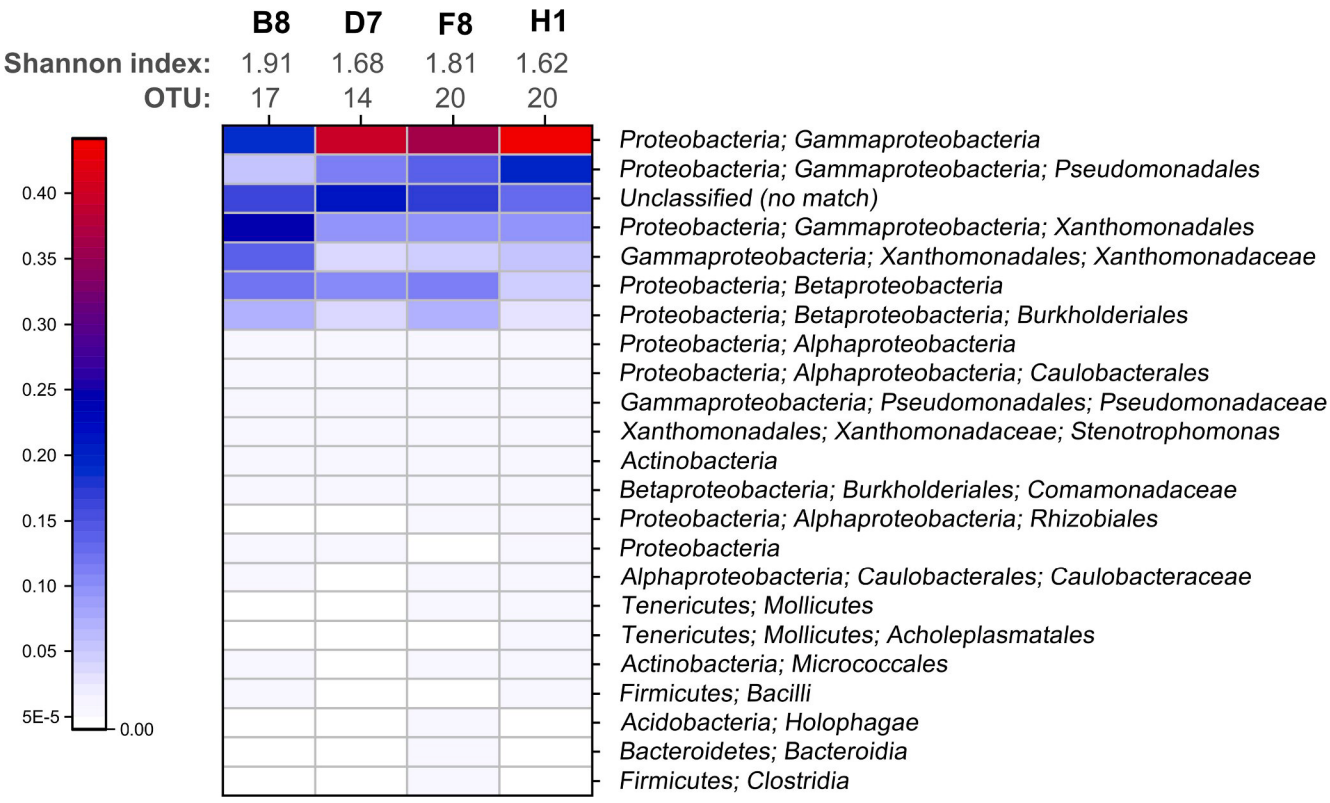

Fig. 4. Taxonomy analysis of well reactors selected from each lake. Colors represent proportions of reads in each metagenome (%) along with biodiversity (Shannon) index, and stotal number of OTUs in each metagenome.

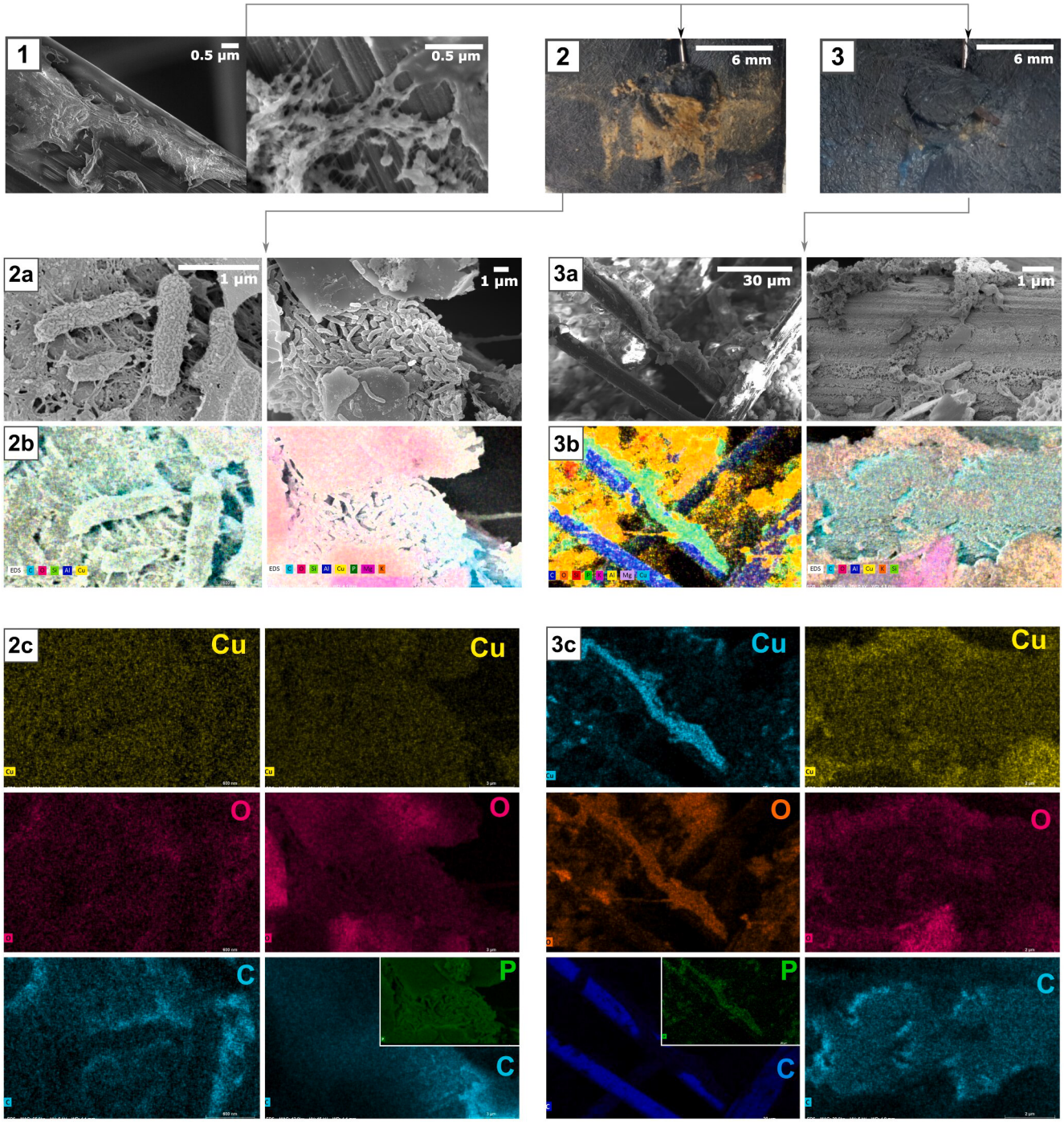

Fig. 5. Results of SEM and EDS analysis of biofilm present on electrode surface. 1–surface of electrode CV disks sampled from MFC-well D8; 2, 3–photographs showing biofilm colonization and electrode surface of large MFCs: H1L and H1H, respectively; 2a, 3a–surface of electrodes sampled from large MFCs: H1L and H1L, respectively; 2b, 3b–EDS mapping of electrodes sampled from large MFCs: H1L and H1H, respectively; 2c, 3c–individual elements detected by EDS mapping of electrodes H1L and H1H, respectively.

morphologically different from bacterial nanowires and their compositions were rich in Cu, as confirmed via EDS analysis. As shown in Figs. 5-3abc, these filaments were adjacent to bacterial cells; hence, their biofilm properties can be improved by improving their conductivity or limiting the access of bacterial cells to the electrodes. Apart from the toxicity of the Cu^{2+} ions, the presence of aforementioned filaments might have been a factor that inhibited the growth of the biofilm at the electrode surface (Fig. 5-3). By contrast, intensive biofilm colonization was observed in the H1L electrode (Fig. 5-2). The biofilm in these MFCs developed a rich network of conductive nanowires, which is characteristic of *Geobacter* sp. [56]. However, *Geobacter* typically appears in environments with near-neutral pH [57] therefore, it was not observed in the acidic communities of the yellow (H) and purple (D) lakes. Meanwhile, the appearance of *Pseudomonas* spp. was confirmed, and they formed conductive pili on anodic biofilms [31,58]. Moreover, the presence of *Pseudomonadaceae* and *Xanthomonadaceae* has been confirmed in electroactive communities adapted for Cu reduction [59] therefore, their presence in our reactors was consistent with our expectation.

The EDS analysis revealed that Cu^{2+} ions were uniformly distributed,

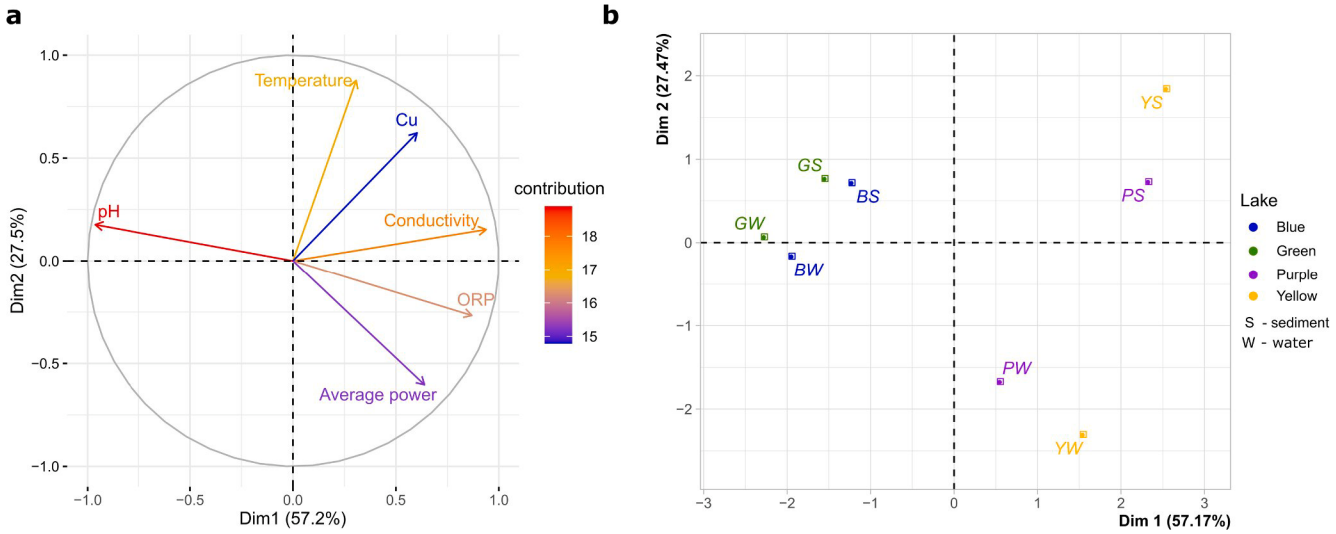

Fig. 6. Principal component analysis: a – variable, the correlation plot indicating correlation and contribution of each plot to dimensions (components) 1 and 2; b – plot of individuals indicating similarity between samples derived from each lake.

although their lower concentrations were present directly on the surface of the bacterial cells. In high-Cu MFCs, the carbon fibers were shielded by a thick layer of Cu-rich crystalline structures (Figs. 5-3abc). Therefore, the positively charged Cu^{2+} ions might be attracted to the negatively charged carbon fibers because of bacterial activity, which was further inhibited through the formation of these crystals. In some of the samples, Cu and oxygen or phosphate were detected, suggesting that either Cu oxides or Cu phosphates were formed—the latter are known as nanoflowers [60].The measurements of Cu ions in the anolyte indicated a 2.3- to 3.7-fold decrease in the H1H and D7H reactors, respectively (Fig. 3c). No change in Cu concentration was observed in the D7L and H1L reactors. In H1H, we observed Cu adsorption on the anodic CV in the form of $Cu_3(PO_4)_2$, as determined via the EDS (Fig. 5d). Adsorbed Cu was also found through Hach analysis of membrane and cathodic materials.

Although we expected the presence of Cu-tolerant microorganisms in acid mine drainage, a significant inhibition was observed at higher Cu concentrations. Cu concentrations of up to 20 mg/L are not considered toxic for microorganisms [38]; this may explain the absence of changes in Cu concentration in the D7L and H1L reactors. In D7H and H1H, Cu appeared as a precipitate on the anode (Fig. 5), as well as on the surface of the PEM and cathodes. Tao *et al.* [40] demonstrated that the reduction of Cu^{2+} in the MFC setup can result in the formation of either metallic Cu or cuprous oxide (Cu_2O), which depends on the initial Cu concentration (more initial Cu^{2+} yields more Cu^0), as well as the pH of the cathode (more Cu^0 is formed when pH is acidic). In membrane-free systems [41], the limiting factor for Cu reduction is the cathode. However, in our system, we investigated whether consortia resistant to elevated concentrations of Cu can be obtained. Alterations to the well-plate MFC, as well as larger-scale reactors with different cathodic materials, may provide a more comprehensive study pertaining to Cu reduction in the future.

As a result of the principal component analysis (Fig. 6), we have proven that the overall power performance of microbial communities was largely affected by the type and physical–chemical characteristics of the lakes. Two lakes (blue and green) had the most similar physical and chemical characteristics, as well as the lowest power output of their enriched cultures. Yellow and Purple Lakes reached the highest power output while having very similar characteristics, but a variation was observed between the samples taken from the sediment and water. Among all tested variables, pH and conductivity had the highest correlation with dimension 1 (component 1), while temperature was the main factor affecting component 2. Therefore, lower pH and temperature, accompanied by higher conductivity of the lake environment resulted in the enrichment of microbial communities with the highest power output observed in high-throughput system. Interestingly, Yellow Lake, which had the highest concentration of copper deposited in the sediments (Table 1), was the source of the best performing community, but from its water layer, where the Cu level was much lower (but still higher than for other water samples). Similarly, PCA revealed that Cu had only a moderate influence on the power output generated by microorganisms. These results suggest that Cu removal by microorganisms was not associated with generating power, but the most efficient consortia in generating power were also capable of conversion of copper.

4. Conclusions

Our findings indicate that high-throughput screening of various electroactive consortia may be realized through the presented 96-well-plate platform. Moreover, the subsequent transfer of electroactive biofilms into large-scale systems with selected traits (Cu tolerance) were proven to be successful. Alternatively, electrodes with electroactive communities, e.g., those enriched during fieldwork, may be preserved and revived for further analysis. By investigating various environmental samples in a high-throughput system, we were able to categorize different communities based on their electrochemical behavior, which correlated to the physicochemical parameters measured in each lake. This can further extend the use of the 96-well platform in environmental electromicrobiology, where multiple parameters may be studied in parallel to assess their effect on the growth and performance of electroactive communities.

Declaration of Competing Interest

The authors declare that they have no known competing financial interests or personal relationships that could have appeared to influence the work reported in this paper.

Acknowledgements

The project was performed under the Joint Research Agreement between Okinawa Institute of Science and Technology and Wroclaw University of Science and Technology (P/0180/609/2019) with the support of Faculty of Chemistry, and under the Polish National Agency for Academic Exchange–Polish Returns programme (PPN/PPO/2018/1/00038).

Appendix A. Supplementary material

Supplementary data to this article can be found online at https://doi.org/10.1016/j.cej.2021.131692.

References

[1] L. Zhuang, Y. Zheng, S. Zhou, Y. Yuan, H. Yuan, Y. Chen, Scalable microbial fuel cell (MFC) stack for continuous real wastewater treatment, Bioresour. Technol. 106 (2012) 82–88, https://doi.org/10.1016/j.biortech.2011.11.019.

[2] F.J. Hernández-Fernández, A. Pérez de los Ríos, M.J. Salar-García, V.M. Ortiz-Martínez, L.J. Lozano-Blanco, C. Godínez, F. Tomás-Alonso, J. Quesada-Medina, Recent progress and perspectives in microbial fuel cells for bioenergy generation and wastewater treatment, Fuel Process. Technol. 138 (2015) 284–297, https://doi.org/10.1016/j.fuproc.2015.05.022.

[3] I. Ieropoulos, J. Winfield, I. Gajda, A. Walter, G. Papaharalabos, I.M. Jimenez, G. Pasternak, J. You, A. Tremouli, A. Stinchcombe, S. Forbes, J. Greenman, The Practical Implementation of Microbial Fuel Cell Technology, 2015. https://doi.org/10.1016/B978-1-78242-375-1.00012-5.

[4] J. Dziegielowski, B. Metcalfe, P. Villegas-Guzman, C.A. Martínez-Huitle, A. Gorayeb, J. Wenk, M. Di Lorenzo, Development of a functional stack of soil microbial fuel cells to power a water treatment reactor: From the lab to field trials in North East Brazil, Appl. Energy. 278 (2020) 115680, https://doi.org/10.1016/j.apenergy.2020.115680.

[5] M. Di Lorenzo, A.R. Thomson, K. Schneider, P.J. Cameron, I. Ieropoulos, A small-scale air-cathode microbial fuel cell for on-line monitoring of water quality, Biosens. Bioelectron. 62 (2014) 182–188, https://doi.org/10.1016/j.bios.2014.06.050.

[6] G. Pasternak, J. Greenman, I. Ieropoulos, Self-powered, autonomous Biological Oxygen Demand biosensor for online water quality monitoring, Sensors Actuators, B Chem. 244 (2017) 815–822, https://doi.org/10.1016/j.snb.2017.01.019.

[7] A. Goglio, M. Tucci, B. Rizzi, A. Colombo, P. Cristiani, A. Schievano, Microbial recycling cells (MRCs): A new platform of microbial electrochemical technologies based on biocompatible materials, aimed at cycling carbon and nutrients in agro-food systems, Sci. Total Environ. 649 (2019) 1349–1361, https://doi.org/10.1016/j.scitotenv.2018.08.324.

[8] Y.-H. Wang, B.-S. Wang, B. Pan, Q.-Y. Chen, W. Yan, Electricity production from a bio-electrochemical cell for silver recovery in alkaline media, Appl. Energy. 112 (2013) 1337–1341, https://doi.org/10.1016/j.apenergy.2013.01.012.

[9] J.R. Kim, Y.E. Song, G. Munussami, C. Kim, B.-H. Jeon, Recent applications of bioelectrochemical system for useful resource recovery: retrieval of nutrient and metal from wastewater, Geosystem Eng. 18 (4) (2015) 173–180, https://doi.org/10.1080/12269328.2015.1037966.

[10] C.A. Ramírez-Vargas, C.A. Arias, P. Carvalho, L. Zhang, A. Esteve-Núñez, H. Brix, Electroactive biofilm-based constructed wetland (EABB-CW): A mesocosm-scale test of an innovative setup for wastewater treatment, Sci. Total Environ. 659 (2019) 796–806, https://doi.org/10.1016/j.scitotenv.2018.12.432.

[11] W.-W. Li, H.-Q. Yu, Stimulating sediment bioremediation with benthic microbial fuel cells, Biotechnol. Adv. 33 (1) (2015) 1–12, https://doi.org/10.1016/j.biotechadv.2014.12.011.

[12] G. Pasternak, T.D. Askitosari, M.A. Rosenbaum, Biosurfactants and Synthetic Surfactants in Bioelectrochemical Systems : A Mini-Review Influence on Electron Transfer, 11 (2020) 1–9. https://doi.org/10.3389/fmicb.2020.00358.

[13] J.C. Mayr, J.-H. Grosch, L. Hartmann, L.F.M. Rosa, A.C. Spiess, F. Harnisch, Resting Escherichia coli as Chassis for Microbial Electrosynthesis: Production of Chiral Alcohols, ChemSusChem 12 (8) (2019) 1631–1634, https://doi.org/10.1002/cssc.v12.810.1002/cssc.201900413.

[14] T.H.J.A. Sleutels, A. Ter Heijne, C.J.N. Buisman, H.V.M. Hamelers, Bioelectrochemical systems: An outlook for practical applications, ChemSusChem. 5 (6) (2012) 1012–1019, https://doi.org/10.1002/cssc.v5.610.1002/cssc.201100732.

[15] C. Santoro, C. Arbizzani, B. Erable, I. Ieropoulos, Microbial fuel cells: From fundamentals to applications. A review, J. Power Sources. 356 (2017) 225–244, https://doi.org/10.1016/j.jpowsour.2017.03.109.

[16] L. Koók, G. Dörgő, P. Bakonyi, T. Rózsenberszki, N. Nemestóthy, K. Bélafi-Bakó, J. Abonyi, Directions of membrane separator development for microbial fuel cells: A retrospective analysis using frequent itemset mining and descriptive statistical approach, J. Power Sources. 478 (2020) 229014, https://doi.org/10.1016/j.jpowsour.2020.229014.

[17] G. Pasternak, N. Ormeno-Cano, P. Rutkowski, Recycled waste polypropylene composite ceramic membranes for extended lifetime of microbial fuel cells, Chem. Eng. J. 425 (2021) 130707, https://doi.org/10.1016/j.cej.2021.130707.

[18] M.J. Salar-Garcia, F. Montilla, C. Quijada, E. Morallon, I. Ieropoulos, Improving the power performance of urine-fed microbial fuel cells using PEDOT-PSS modified anodes, Appl. Energy. 278 (2020) 115528, https://doi.org/10.1016/j.apenergy.2020.115528.

[19] S. Chen, S.A. Patil, R.K. Brown, U. Schröder, Strategies for optimizing the power output of microbial fuel cells: Transitioning from fundamental studies to practical implementation, Appl. Energy. 233–234 (2019) 15–28, https://doi.org/10.1016/J.APENERGY.2018.10.015.

[20] D.F. Call, B.E. Logan, A method for high throughput bioelectrochemical research based on small scale microbial electrolysis cells, Biosens. Bioelectron. 26 (11) (2011) 4526–4531, https://doi.org/10.1016/j.bios.2011.05.014.

[21] D.F. Call, B.E. Logan, Lactate oxidation coupled to iron or electrode reduction by Geobacter sulfurreducens PCA, Appl. Environ. Microbiol. 77 (24) (2011) 8791–8794, https://doi.org/10.1128/AEM.06434-11.

[22] H. Hou, L. Li, Y. Cho, P. de Figueiredo, A. Han, D. Fox, Microfabricated microbial fuel cell arrays reveal electrochemically active microbes, PLoS One. 4 (8) (2009) 1–8, https://doi.org/10.1371/journal.pone.0006570.

[23] H. Hou, L. Li, P. de Figueiredo, A. Han, Air-cathode microbial fuel cell array: A device for identifying and characterizing electrochemically active microbes, Biosens. Bioelectron. 26 (5) (2011) 2680–2684, https://doi.org/10.1016/j.bios.2010.06.037.

[24] H. Hou, L. Li, C.Ü. Ceylan, A. Haynes, J. Cope, H.H. Wilkinson, C. Erbay, P. de Figueiredo, A. Han, A microfluidic microbial fuel cell array that supports long-term multiplexed analyses of electricigens, Lab Chip. 12 (2012) 4151–4159, https://doi.org/10.1039/c2lc40405b.

[25] S.-J. Yuan, W.-W. Li, Y.-Y. Cheng, H. He, J.-J. Chen, Z.-H. Tong, Z.-Q. Lin, F. Zhang, G.-P. Sheng, H.-Q. Yu, A plate-based electrochromic approach for the high-throughput detection of electrochemically active bacteria, Nat. Protoc. 9 (1) (2014) 112–119, https://doi.org/10.1038/nprot.2013.173.

[26] T.R. Molderez, A. Prévoteau, F. Ceyssens, M. Verhelst, K. Rabaey, A chip-based 128-channel potentiostat for high-throughput studies of bioelectrochemical systems: Optimal electrode potentials for anodic biofilms, Biosens. Bioelectron. 174 (2021) 112813, https://doi.org/10.1016/j.bios.2020.112813.

[27] S. Zhou, J. Wen, J. Chen, Q. Lu, Rapid measurement of microbial extracellular respiration ability using a high-throughput colorimetric assay, Environ. Sci. Technol. Lett. 2 (2) (2015) 26–30, https://doi.org/10.1021/ez500405t.

[28] A. Fraiwan, S. Choi, Bacteria-powered battery on paper, Phys. Chem. Chem. Phys. 16 (47) (2014) 26288–26293, https://doi.org/10.1039/C4CP04804K.

[29] Y. Gao, D.J. Hassett, S. Choi, Rapid characterization of bacterial electrogenicity using a single-sheet paper-based electrofluidic array, Front. Bioeng. Biotechnol. 5 (2017) 1–12, https://doi.org/10.3389/fbioe.2017.00044.

[30] M. Tahernia, M. Mohammadifar, D.J. Hassett, S. Choi, A fully disposable 64-well papertronic sensing array for screening electroactive microorganisms, Nano Energy. 65 (2019) 104026, https://doi.org/10.1016/j.nanoen.2019.104026.

[31] M. Tahernia, M. Mohammadifar, Y. Gao, W. Panmanee, D.J. Hassett, S. Choi, A 96-well high-throughput, rapid-screening platform of extracellular electron transfer in microbial fuel cells, Biosens. Bioelectron. 162 (2020) 112259, https://doi.org/10.1016/j.bios.2020.112259.

[32] L. Szydlowski, J. Ehlich, N. Shibata, I. Goryanin, High-throughput screening and selection of PCB-bioelectrocholeaching, electrogenic microbial communities using single chamber microbial fuel cells based on 96-well plate array, BioRxiv. 447729 (2021).

[33] A. Mohamed, P.T. Ha, B.M. Peyton, R. Mueller, M. Meagher, H. Beyenal, In situ enrichment of microbial communities on polarized electrodes deployed in alkaline hot springs, J. Power Sources. 414 (2019) 547–556, https://doi.org/10.1016/j.jpowsour.2019.01.027.

[34] R. Toczyłowska-Mamińska, K. Pielech-Przybylska, A. Sekrecka-Belniak, U. Dziekońska-Kubczak, Stimulation of electricity production in microbial fuel cells via regulation of syntrophic consortium development, Appl. Energy. 271 (2020) 115184, https://doi.org/10.1016/j.apenergy.2020.115184.

[35] L.u. Lu, T. Huggins, S. Jin, Y.i. Zuo, Z.J. Ren, Microbial metabolism and community structure in response to bioelectrochemically enhanced remediation of petroleum hydrocarbon-contaminated soil, Environ. Sci. Technol. 48 (7) (2014) 4021–4029, https://doi.org/10.1021/es4057906.

[36] G. Pasternak, J. Greenman, I. Ieropoulos, Dynamic evolution of anodic biofilm when maturing under different external resistive loads in microbial fuel cells. Electrochemical perspective, J. Power Sources. 400 (2018) 392–401, https://doi.org/10.1016/j.jpowsour.2018.08.031.

[37] S. Riedl, R.K. Brown, D.Y. Alvarez Esquivel, H. Wichmann, K.J. Huber, B. Bunk, J. Overmann, U. Schröder, Cultivating Electrochemically Active Biofilms at Continuously Changing Electrode Potentials, ChemElectroChem 6 (8) (2019) 2238–2247, https://doi.org/10.1002/celc.v6.810.1002/celc.201900036.

[38] S.V. Avery, N.G. Howlett, S. Radice, Copper toxicity towards Saccharomyces cerevisiae: Dependence on plasma membrane fatty acid composition, Appl. Environ. Microbiol. 62 (11) (1996) 3960–3966, https://doi.org/10.1128/aem.62.11.3960-3966.1996.

[39] C.A. Flemming, J.T. Trevors, Copper toxicity and chemistry in the environment: a review, Water. Air. Soil Pollut. 44 (1-2) (1989) 143–158, https://doi.org/10.1007/BF00228784.

[40] H.-C. Tao, M. Liang, W. Li, L.-J. Zhang, J.-R. Ni, W.-M. Wu, Removal of copper from aqueous solution by electrodeposition in cathode chamber of microbial fuel cell, J. Hazard. Mater. 189 (1-2) (2011) 186–192, https://doi.org/10.1016/j.jhazmat.2011.02.018.

[41] H.-C. Tao, W. Li, M. Liang, N. Xu, J.-R. Ni, W.-M. Wu, A membrane-free baffled microbial fuel cell for cathodic reduction of Cu(II) with electricity generation, Bioresour. Technol. 102 (7) (2011) 4774–4778, https://doi.org/10.1016/j.biortech.2011.01.057.

[42] J. Ciesielczuk, Z. Bzowski, Secondary (Cu, Zn)-oxyminerals from the Miedzianka copper deposit in Rudawy Janowickie, Sudetes Mts, Preliminary Rep., Mineral. Soc. Pol. – Spec. Pap. 23 (2003) 54–56.

[43] R.C. Team, R: A language and environment for statistical computing, R Found. Stat. Comput. Vienna (2013).

[44] A. Santos, R. van Aerle, L. Barrientos, J. Martinez-Urtaza, Computational methods for 16S metabarcoding studies using Nanopore sequencing data, Comput. Struct. Biotechnol. J. 18 (2020) 296–305, https://doi.org/10.1016/j.csbj.2020.01.005.

[45] G. Pasternak, M.M. Hanczyc, Novel method for detecting and quantifying phenol with transient response of glycolytic oscillations of synchronised yeast cells, Sens. Bio-Sensing Res. 22 (2019) 100259, https://doi.org/10.1016/j.sbsr.2019.100259.
[46] S. Xin, J. Shen, G. Liu, Q. Chen, Z. Xiao, G. Zhang, Y. Xin, Electricity generation and microbial community of single-chamber microbial fuel cells in response to Cu2O nanoparticles/reduced graphene oxide as cathode catalyst, Chem. Eng. J. 380 (2020) 122446, https://doi.org/10.1016/j.cej.2019.122446.
[47] D.A. Finkelstein, L.M. Tender, J.G. Zeikus, Effect of electrode potential on electrode-reducing microbiota, Environ. Sci. Technol. 40 (22) (2006) 6990–6995, https://doi.org/10.1021/es061146m.
[48] D.E. Holmes, D.R. Bond, R.A. O?Neil, C.E. Reimers, L.R. Tender, D.R. Lovley, Microbial communities associated with electrodes harvesting electricity from a variety of aquatic sediments, Microb. Ecol. 48 (2) (2004) 178–190, https://doi.org/10.1007/s00248-003-0004-4.
[49] P.G. Dennis, B. Virdis, I. Vanwonterghem, A. Hassan, P. Hugenholtz, G.W. Tyson, K. Rabaey, Anode potential influences the structure and function of anodic electrode and electrolyte-associated microbiomes, Sci. Rep. 6 (1) (2016), https://doi.org/10.1038/srep39114.
[50] Y. Jangir, S. French, L.M. Momper, D.P. Moser, J.P. Amend, M.Y. El-Naggar, Isolation and Characterization of Electrochemically Active Subsurface Delftia and Azonexus Species, Front. Microbiol. 7 (2016) 1–11, https://doi.org/10.3389/fmicb.2016.00756.
[51] L. Szydlowski, A. Sorokin, O. Vasieva, S. Boerner, V. Fedorovich, I. Goryanin, Evolutionary dynamics of microbial communities in bioelectrochemical systems, J. Comput. Sci. Syst. Biol. 13 (2020), https://doi.org/10.1101/725580.
[52] S. Kato, R. Nakamura, F. Kai, K. Watanabe, K. Hashimoto, Respiratory interactions of soil bacteria with (semi)conductive iron-oxide minerals, Environ. Microbiol. 12 (2010) 3114–3123, https://doi.org/10.1111/j.1462-2920.2010.02284.x.
[53] N.S. Malvankar, G.M. King, D.R. Lovley, Centimeter-long electron transport in marine sediments via conductive minerals, ISME J. 9 (2) (2015) 527–531, https://doi.org/10.1038/ismej.2014.131.
[54] C. Méndez-García, A.I. Peláez, V. Mesa, J. Sánchez, O.V. Golyshina, M. Ferrer, Microbial diversity and metabolic networks in acid mine drainage habitats, Front. Microbiol. 6 (2015) 1–17, https://doi.org/10.3389/fmicb.2015.00475.
[55] C.I. Torres, R. Krajmalnik-Brown, P. Parameswaran, A.K. Marcus, G. Wanger, Y. A. Gorby, B.E. Rittmann, Selecting Anode-Respiring Bacteria Based on Anode Potential : Phylogenetic, Electrochemical, and Microscopic Characterization, Environ. Sci. Technol. 43 (2009) 9519–9524.
[56] D.R. Lovley, T. Ueki, T. Zhang, N.S. Malvankar, P.M. Shrestha, K.A. Flanagan, M. Aklujkar, J.E. Butler, L. Giloteaux, A.E. Rotaru, D.E. Holmes, A.E. Franks, R. Orellana, C. Risso, K.P. Nevin, Geobacter. The Microbe Electric's Physiology, Ecology, and Practical Applications, Adv. Microb. Physiol. (2011), https://doi.org/10.1016/B978-0-12-387661-4.00004-5.
[57] D.R. Bond, D.R. Lovley, Electricity Production by Geobacter sulfurreducens Attached to Electrodes, Appl. Environ. Microbiol. 69 (2003) 1548–1555, https://doi.org/10.1128/AEM.69.3.1548.
[58] G. Choi, D.J. Hassett, S. Choi, A paper-based microbial fuel cell array for rapid and high-throughput screening of electricity-producing bacteria, Analyst. 140 (12) (2015) 4277–4283, https://doi.org/10.1039/C5AN00492F.
[59] J. Shen, L. Huang, P. Zhou, X. Quan, G.L. Puma, Correlation between circuital current, Cu(II) reduction and cellular electron transfer in EAB isolated from Cu(II)-reduced biocathodes of microbial fuel cells, Bioelectrochemistry. 114 (2017) 1–7, https://doi.org/10.1016/j.bioelechem.2016.11.002.
[60] Yan-Kui Luo, Fei Song, Xiu-Li Wang, Yu-Zhong Wang, Pure copper phosphate nanostructures with controlled growth: A versatile support for enzyme immobilization, CrystEngComm. 19 (22) (2017) 2996–3002, https://doi.org/10.1039/C7CE00466D.

International Journal of
Molecular Sciences

MDPI

Article

Conductive Polymer PEDOT:PSS-Based Platform for Embryonic Stem-Cell Differentiation

Eva Šafaříková [1,2], Jiří Ehlich [3], Stanislav Stříteský [3], Martin Vala [3], Martin Weiter [3], Jiří Pacherník [2], Lukáš Kubala [1,2,4] and Jan Víteček [1,*]

[1] Institute of Biophysics of the Czech Academy of Sciences, Královopolská 135, 612 65 Brno, Czech Republic; safarikova.eva@ibp.cz (E.Š.); kubalal@ibp.cz (L.K.)
[2] Department of Experimental Biology, Faculty of Science, Masaryk University, Kamenice 5, 625 00 Brno, Czech Republic; jipa@sci.muni.cz
[3] Faculty of Chemistry, Brno University of Technology, Purkyňova 118, 612 00 Brno, Czech Republic; Jiri.Ehlich@vut.cz (J.E.); xcstritesky@fch.vut.cz (S.S.); vala@fch.vut.cz (M.V.); weiter@fch.vutbr.cz (M.W.)
[4] International Clinical Research Center, St. Anne's University Hospital Brno, Pekařská 53, 656 91 Brno, Czech Republic
* Correspondence: jan.vitecek@ibp.cz; Tel./Fax: +420-541-517104

Abstract: Organic semiconductors are constantly gaining interest in regenerative medicine. Their tunable physico-chemical properties, including electrical conductivity, are very promising for the control of stem-cell differentiation. However, their use for combined material-based and electrical stimulation remains largely underexplored. Therefore, we carried out a study on whether a platform based on the conductive polymer poly(3,4-ethylenedioxythiophene):polystyrene sulfonate (PEDOT:PSS) can be beneficial to the differentiation of mouse embryonic stem cells (mESCs). The platform was prepared using the layout of a standard 24-well cell-culture plate. Polyethylene naphthalate foil served as the substrate for the preparation of interdigitated gold electrodes by physical vapor deposition. The PEDOT:PSS pattern was fabricated by precise screen printing over the gold electrodes. The PEDOT:PSS platform was able to produce higher electrical current with the pulsed-direct-current (DC) electrostimulation mode (1 Hz, 200 mV/mm, 100 ms pulse duration) compared to plain gold electrodes. There was a dominant capacitive component. In proof-of-concept experiments, mESCs were able to respond to such electrostimulation by membrane depolarization and elevation of cytosolic calcium. Further, the PEDOT:PSS platform was able to upregulate cardiomyogenesis and potentially inhibit early neurogenesis per se with minor contribution of electrostimulation. Hence, the present work highlights the large potential of PEDOT:PSS in regenerative medicine.

Keywords: conductive polymer; PEDOT:PSS; screen print; embryonic stem cells; electrostimulation

Citation: Šafaříková, E.; Ehlich, J.; Stříteský, S.; Vala, M.; Weiter, M.; Pacherník, J.; Kubala, L.; Víteček, J. Conductive Polymer PEDOT:PSS-Based Platform for Embryonic Stem-Cell Differentiation. *Int. J. Mol. Sci.* **2022**, *23*, 1107. https://doi.org/10.3390/ijms23031107

Academic Editor: Yohei Okada

Received: 21 December 2021
Accepted: 17 January 2022
Published: 20 January 2022

Publisher's Note: MDPI stays neutral with regard to jurisdictional claims in published maps and institutional affiliations.

1. Introduction

Embryonic stem cells (ESCs) are pluripotent cells derived from the inner cell mass of blastocyst-stage embryos. Other types of stem cells (SCs) are isolated or induced from adult tissues. All SCs have unique regenerative abilities with a high potential for application in medicine [1,2]. A plethora of approaches to direct ESCs into a particular cell lineage has been developed for in vitro use. The differentiation protocol depends on the origin of the cells and the intended direction of SC differentiation. The methods to regulate differentiation could be divided into three groups: biological, chemical and physical [3]. Some growth factors and cytokines are able to stimulate ESCs and accelerate their differentiation. These are, for example, the TGF-beta family of proteins, insulin-like growth factor-1, leukemia inhibitory factor and cardiotrophin-1 [4]. Further, some chemicals can stimulate differentiation as well. These include dimethyl sulfoxide, 5-Azacytidin or ascorbic acid, as well as exogenous free radicals and reactive oxygen species [3,5]. The last group of stimulators is

physical stimuli. This group includes mechanical forces, heat treatment and electrostimulation [3]. The latter mentioned can affect endogenous electrical fields, which are essential for maintaining cellular homeostasis and are involved in many biological events [3]. With the development of new conductive materials, electrostimulation is entering into the focus of basic as well as applied research.

Indeed, electrostimulation can be beneficial in tissue formation, tissue regeneration and wound healing, directed cell migration and alignment [6]. There has been a special interest in myocardial regeneration after heart failure and cardiac-related diseases since the mammalian heart has a very limited self-regeneration capacity [7]. In particular, cardiac regenerative medicine requires mature and well-defined cells in order to treat pathologies such as ischemic heart disease, cardiomyopathy and congenital cardiac birth defects in children [8,9]. Electrical stimulation can potentially be one way to achieve this goal [10,11]. In addition to enhanced cardiomyocyte formation, electrostimulation can result in the functional improvement of phenotypes (contractility, synchrony of beating) of formed cardiomyocytes even if prepared ex vivo [6,11–13].

The electrostimulation of ESCs requires a platform to support the cells and to allow the application of external electrical fields. The vast majority of such platforms was constructed using inorganic materials. Indeed, the first systems for ESCs were made from platinum or stainless-steel electrodes in direct contact with the culture medium [10]. More sophisticated systems used salt bridges to separate electrode buffers from the culture medium. Such an arrangement eliminated any adverse effect of the electrolysis of the culture medium, which stressed the cells to a high extent [14–17].

The recent extensive development of organic semiconductors has rendered them to be used in biological applications as well. Among them, the conductive polymer poly(3,4-ethylenedioxythiophene):polystyrene sulfonate (PEDOT:PSS) has attracted a great deal of attention. Although the polymer chain of PEDOT shows conjugation of double bonds, the major contribution to electrical conductivity results from its nanocrystalline structure with extensive stacking. Hence, PEDOT:PSS requires post-deposition treatment to ensure favorable electrical properties [14]. Due to its stability and biocompatibility, it has been suggested for biological applications. Indeed, short (a few hours) and mid-term (a few days) proof-of-concept applications have been implemented [15]. Long-term applications have been rather scarce despite the fact that PEDOT:PSS can maintain its performance if processed appropriately [16,17]. In connection with SCs, nanostructured PEDOT:PSS has been shown to manipulate cell adhesion. However, there is no clear general relationship between SC fate and PEDOT:PSS structure [18]. Further, PEDOT:PSS-based composite materials have been introduced in order to provide 3D niches for SCs. In connection with electrostimulation, they appear to have great potential in regenerative medicine as shown by their support of the development of neurons from neural SCs [18–25]. Other applications include osteogenic differentiation [22,26]. Importantly, some works have indicated that PEDOT:PSS-based material could promote SC differentiation by itself [21,22,27]. PEDOT:PSS was specifically used to promote cardiomyogenesis. The electrostimulation of mESCs with PEDOT:PSS-based electrodes resulted in the synchronous beating of clusters of cardiomyocytes [28]. Further, recent work of Roshanbinfar et al., 2018 [27] indicated that PEDOT:PSS-based hydrogel can promote cardiomyogenesis per se. The authors determined electrical conductivity to be the key player in the observed phenomenon. However, the use of organic semiconductors, including PEDOT:PSS, for a combined material-based and electrical stimulation to control SC differentiation, such as in the work of Yoshida et al., 2019 [28], remains largely underexplored. By applying such an approach, the potential of organic conductive polymers and electrostimulation for regenerative medicine could be maximized.

This paper describes the construction of a PEDOT:PSS-based platform for the laboratory-scale electrostimulation of cells. The design took advantage of the precise screen printing of interdigitated PEDOT:PSS electrodes on a gold support. The platform was characterized in terms of biocompatibility and ability to produce electrical current at a pulsed-DC mode

of operation. The impact of electrostimulation as well as the platform itself on mESC differentiation was determined based on lineage-specific gene and protein expressions. To our knowledge it is the first time that such a PEDOT:PSS-based design was used in a device for the electrostimulation of SCs.

2. Results

2.1. Platforms for Differentiation of Mouse Embryonic Stem Cells

In order to determine the specific role of PEDOT:PSS during electrostimulation, two platform types were prepared in the 24-well-plate format. A platform containing only the gold electrodes (further referred to as the gold platform) served as a reference. The PEDOT:PSS platform was fabricated by screen-printing deposition of PEDOT:PSS paste onto the gold support. The procedure resulted in a 200 nm PEDOT:PSS layer that was stable for the entire cell-differentiation experiment.

The materials in direct contact with cells, i.e., the PEN foil, gold electrodes and PEDOT:PSS, showed wetting angles of 59.7 ± 1.5°, 79.4 ± 5.9° and 20.3 ± 3.5°, respectively.

Both platform types were coated with collagen IV to promote the adhesion of EBs (cell clusters prepared from mESCs). The biocompatibility was verified using mESCs. No adverse effects of the platforms were observed compared to the cell-culture plastics. Such an observation was supported by the occurrence of beating loci on both platforms at the end of the differentiation experiments, and the beating properties were comparable to the controls on the cell-culture plastics (Supplementary Figure S1).

For electrostimulation of EBs, square DC pulses (1 Hz, 200 mV/mm, pulse duration 100 ms) were chosen. In both platforms, these pulses resulted in capacitive current that reached about 2100 μA for the PEDOT:PSS platform and about 60 μA for the gold platform. The spike of capacitive current was followed by weak faradaic current that was about 5 μA for the PEDOT:PSS platform and 0.8 μA for the gold platform (Figure 1). Hence, the PEDOT:PSS platform showed about a one-order-of-magnitude-higher ratio of capacitive to faradaic current compared to the gold platform.

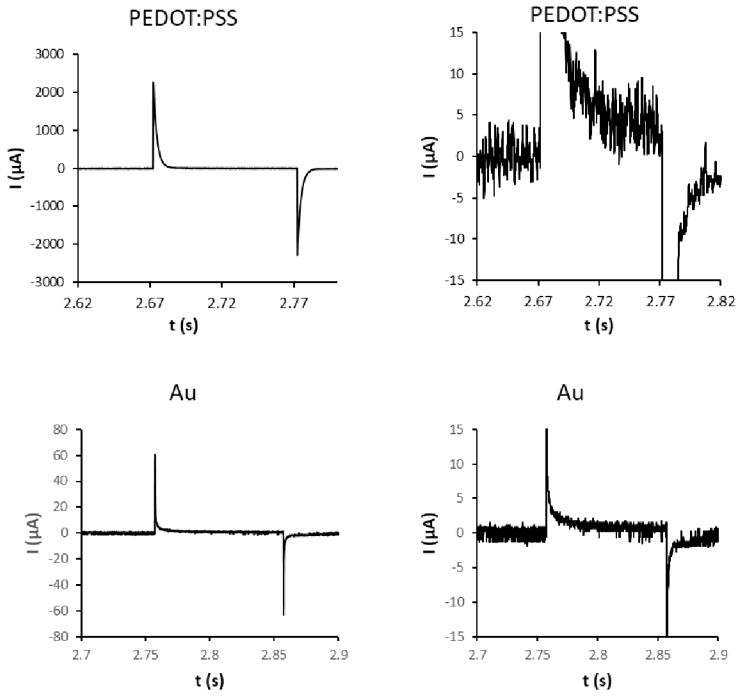

Figure 1. Chronoamperometric characteristics of PEDOT:PSS and gold platforms. Platform wells were loaded with PBS buffer. In two-electrode mode, the electric current was determined under pulses (1 Hz, 200 mV/mm, pulse duration 100 ms). Right column shows magnified views. Charts represent typical data.

2.2. Early Response of Embryonic Stem Cells

As the PEDOT:PSS platform showed much stronger electrical currents during the application of the 200 mV/mm square wave, its impact on early stem-cell response was estimated before the determination of changes in cell differentiation. Firstly, the membrane depolarization was checked. EBs that had adhered to PEDOT:PSS platform (6 d) were loaded with voltage probe and were electrostimulated (square DC pulses, 1 Hz, 200 mV/mm, pulse duration 100 ms). There was a rapid and sustained increase in fluorescence (Figure 2), indicating the membrane depolarization. Secondly, the possible downstream messenger of the depolarization event in cytosolic Ca^{2+} was checked by calcium-sensitive dye and a Fluo-4 AM probe. Ninety seconds of electrostimulation already showed elevated cytosolic calcium. However, the 15 min-long electrostimulation induced about three times more intense increase in cytosolic calcium (Figure 3).

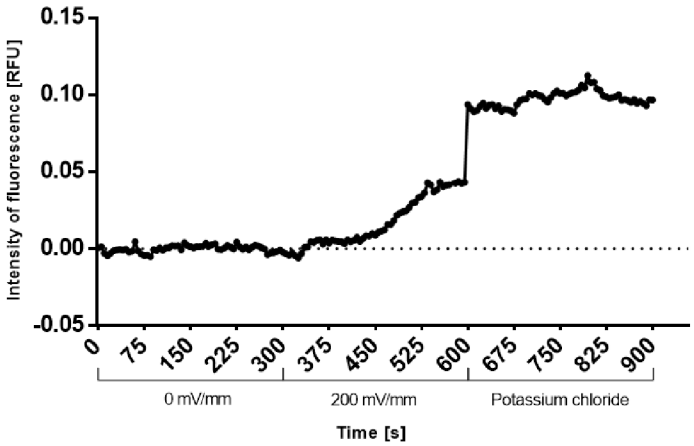

Figure 2. Depolarization of cytoplasmic membrane of mESCs under electrostimulation. EBs adhered to PEDOT:PSS platform wells (6 d) were loaded with voltage-sensitive probe DiBAC(4). The change in fluorescence upon stimulation with electric pulses (square wave, 1 Hz, 200 mV/mm, pulse duration 100 ms) recorded with a fluorescence microscope. Potassium chloride (40 mM) spike was used as a positive control. Records were processed in ImageJ software and normalized to the controls (0 mV/mm). The chart shows typical data from three replicates.

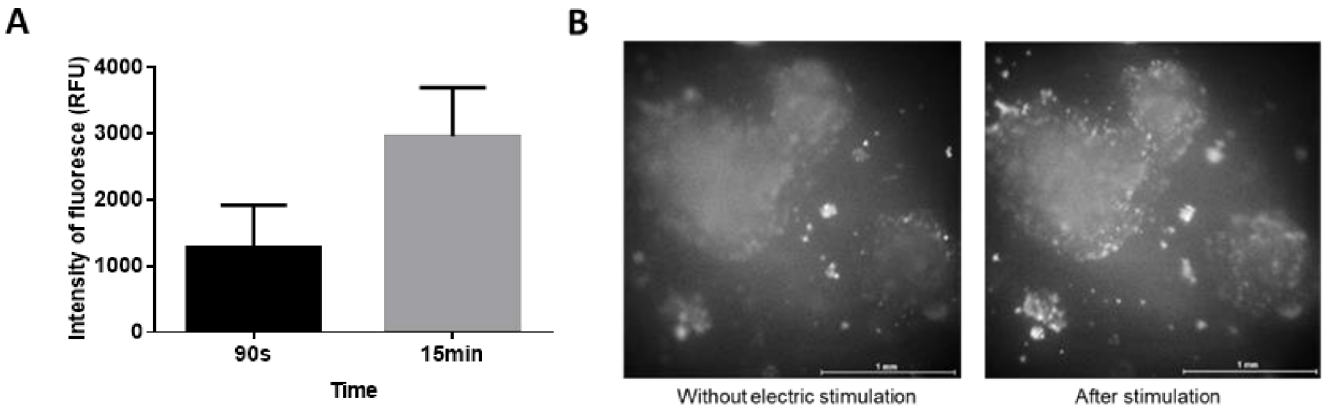

Figure 3. Elevation of cytosolic-calcium level under electrostimulation: EBs adhered to PEDOT:PSS platform wells (6 d) were loaded with calcium-sensitive probe Fluo-4 AM. The change in fluorescence upon stimulation with electric pulses (square wave, 1 Hz, 200 mV/mm, pulse duration 100 ms) recorded with a fluorescence microscope connected with camera. The record was processed in ImageJ software. (**A**) The chart shows typical data from three independent biological replicates. (**B**) Differences of fluorescence without electric stimulation and after stimulation for 15 min.

The 90 s electrostimulation resulted in no difference in beating onset compared to the controls (standard culture plastics, platform without electrostimulation). The 15 min-long electrostimulation induced the occurrence of beating loci 1–2 days earlier. Hence, the 15 min-long electrostimulation was used for further experiments.

2.3. Impact of Electrostimulation to Gene and Protein Expression

To see if the mESCs were undergoing complex changes because of the platform type and/or electrostimulation, the expressions of cardiomyogenesis- and neurogenesis-marker genes were chosen. Markers of cardiomyogenesis included the mRNA level of homeobox-containing gene Nkx2.5 and genes connected with the contractile apparatus (Myh6, Myh7, Myl2 and Myl7). Further, the level of cardiac heavy myosin chains was determined. The expression of markers was followed in pre-formed EBs.

The data suggest a marginal trend towards the higher expression of gene Nkx2.5 on both platform materials on day 15 after electrostimulation (Figure 4A). The expressions of Myh6, Myh7, Myl2 and Myl7 shared a similar pattern and were significantly or marginally upregulated on the PEDOT:PSS platform on day 5 + 15 of the experiment. The effect of electrostimulation was indistinguishable on this platform. The electrostimulation on the gold platform as well as the gold platform without electrostimulation did not change the expression of Myh6, Myh7 and Myl7 compared to the control (Figure 4B–E). The Myl2 gene showed marginally upregulated expression on the gold platform without electrostimulation on day 5 + 15 of the experiment (Figure 4D). The ratios of the expressions of Myh6, Myh7, Myl2 and Myl7 to Nkx2.5, as well as Myh6 to Myh7 and Myl2 to Myl7, showed inconsistent or insignificant differences in comparison to the control for both platforms regardless of electrostimulation (Supplementary Figures S2–S5). Clusters of beating cardiomyocytes occurred in all variants at the end of the experiment (Supplementary Figure S1). The expression of cardiac heavy myosin chains and the occurrence of myofibrils of the contractile apparatus did not provide conclusive data (Supplementary Figure S6).

As a marker of neurogenesis, the expression of the gene Sox1 at the mRNA level and the occurrence of LewisX antigen were chosen. Sox1 is a transcription factor specific to early neurogenesis. Compared with the control, the expression of Sox1 was marginally lowered due to the PEDOT:PSS platform regardless of electrostimulation on days 5 + 5 and 5 + 10 of the experiment. On day 5 + 15 there was statistically significant downregulation of Sox1 expression due to the PEDOT:PSS platform. The electrostimulation on this platform caused even more pronounced downregulation. Strikingly, gold did not affect the expression of Sox1 gene at early stages but induced dropdown on day 5 + 15 which was reverted by electrostimulation with this platform (Figure 5). Further, the expression of LewisX antigen (marker of neural precursor cells) was determined at the end of the experiment (day 5 + 15). LewisX antigen showed significant downregulation in cell differentiated on the PEDOT:PSS platform regardless of electrostimulation. In case of gold platform per se there was a significant decrease which was reverted by electrostimulation again (Figure 5B).

Additionally, the expression of neurogenesis markers Nestin, Pax6, Mash1 and TuJ1 was determined at the mRNA level. The expression pattern of Nestin on the gold platform followed a very similar trend to Sox1 in the late phase of the experiment (5 + 15 d). The Pax6 and TuJ1 expressions indicated no major difference among variants. The Mash1 expression showed no major difference among variants on the PEDOT:PSS platform but its expression was elevated on gold platform without electrostimulation at the end of the experiment (5 + 15 d) (Supplementary Figure S7).

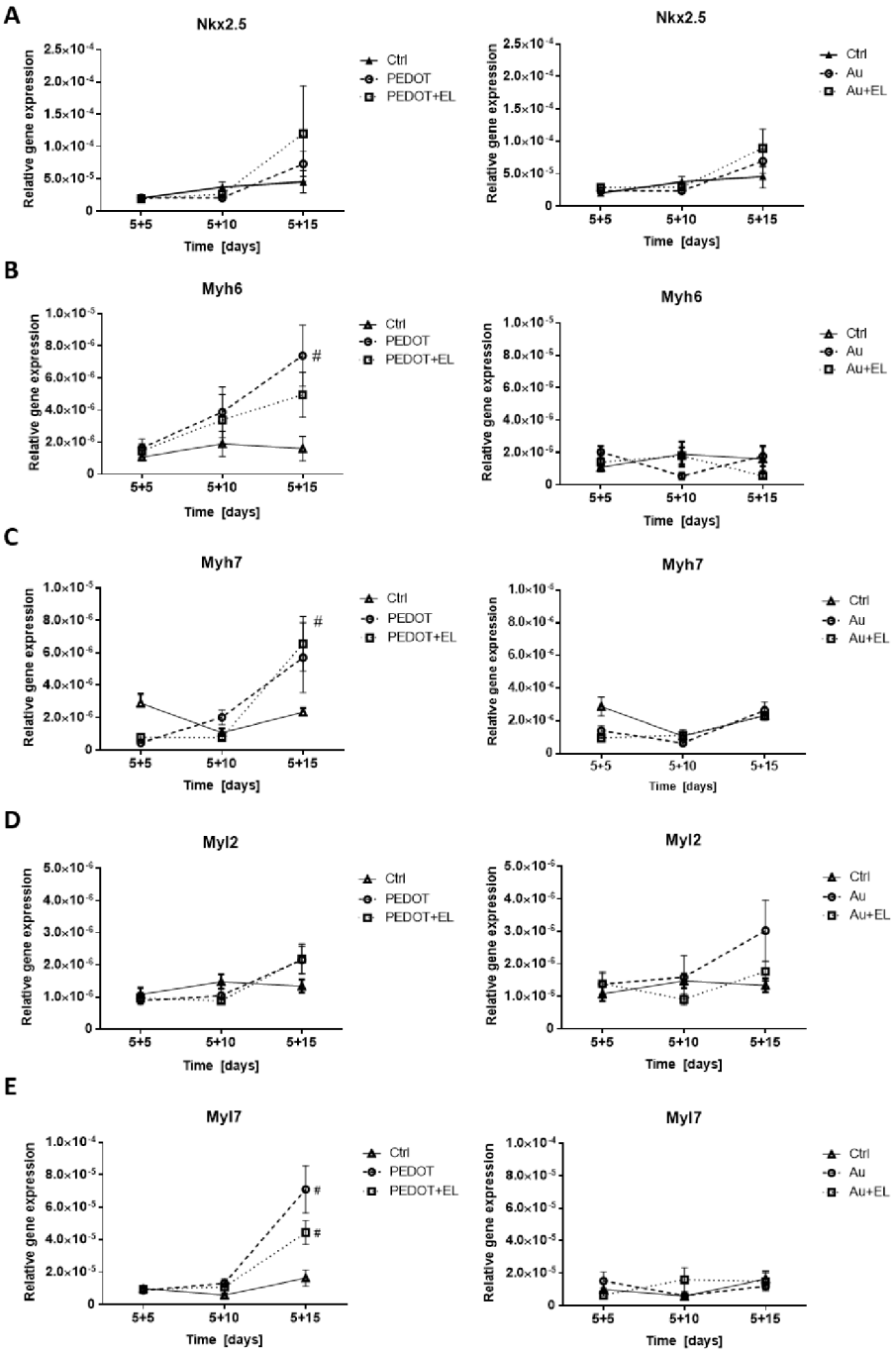

Figure 4. The effect of electrostimulation on expression cardiomyogenesis markers: Nkx2.5, Myh6, Myh7, Myl2, Myl7 on the PEDOT:PSS-based platform (left column) and the gold platform (right column). These genes represent markers of cardiomyocyte differentiation. The mRNA levels of NK2 transcription factor related locus 5 (Nkx2.5, (**A**)), myosin heavy chain 6 (Myh6, (**B**)), and myosin heavy chain 7 (Myh7, (**C**)), myosin light chain 2 (Myl2, (**D**)) and myosin light chain 7 (Myl7, (**E**)) were analyzed in mESC line R1 that was differentiated for 20 days. Different time points were studied (5 + 5, 5 + 10, 5 + 15 d). These time points represent individual phases of differentiation. EBs adhered to platforms were treated on day six with square electric pulses (1 Hz, 200 mV/mm, pulse duration 100 ms) for 15 min (PEDOT + EL, Au + EL). Culture plastics (Ctrl) served as the control, and a comparison to platforms without electrostimulation (PEDOT, Au) was drawn. Data are expressed as mean ± SEM ($n \geq 4$). Differences between samples were analyzed by paired *t*-test and considered statistically significant for $p < 0.05$; they are marked with hashtags (#) for statistical significance to the control.

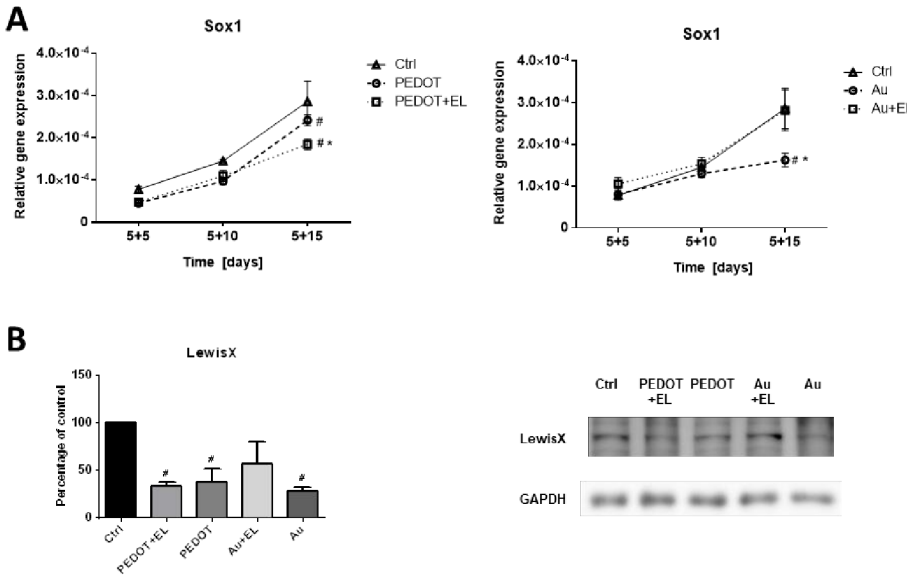

Figure 5. The effect of electrostimulation on expression of neural transcriptional factor Sox1 and LewisX antigen on PEDOT:PSS-based platform and platform with gold. These are markers of neural differentiation. The mRNA levels of transcription factor SOX-1 (**A**) were analyzed in mESCs line R1 which were differentiated for 20 days. Different time points were studied (5 + 5, 5 + 10, 5 + 15 d). These time points represent individual phases of differentiation. Level of antigen LewisX (**B**) was studied at the end-point (5 + 15 d). EBs adhered to platforms were treated on day 6 with square electric pulses (1 Hz, 200 mV/mm, pulse duration 100 ms) for 15 min (PEDOT + EL, Au + EL). Culture plastics (Ctrl) served as the control, and comparison to platforms without electrostimulation (PEDOT, Au) was drawn. Data are expressed as mean ± SEM ($n \geq 4$). Differences between samples were analyzed by paired *t*-test and considered statistically significant for $p < 0.05$; they are marked with asterisks (*) for material vs. material + electrical stimulation and with hashtags (#) for statistically significance to the control.

3. Discussion

The use of novel materials and electrostimulation to promote and control stem-cell differentiation is constantly gaining interest as a promising tool for regenerative medicine. The selective differentiation into a specific line is of special importance. [6,11–13]. Further, organic conductive materials appear to be an excellent alternative to commonly used inorganic materials (e.g., gold or platinum) [19]. Therefore, we determined if a PEDOT:PSS-based platform can be beneficial to the differentiation of mESCs compared to a gold-based platform.

The PEDOT:PSS platform was prepared using PEDOT:PSS paste deposited onto gold electrodes by screen printing. Such a method resulted in good quality and reasonably thin film, similar to the capabilities of spin coating. The major advantage was the precise deposition of PEDOT:PSS onto the supporting electrodes. Such a procedure in principle enables the production of cost-effective bio-electronic devices with submillimeter electrode size in a scalable manner. Though PEDOT:PSS in general reaches conductivity up to a few thousand Siemens, the thin layer (200 nm) in principle did not limit the overall conductivity of the platform. Importantly, the thin film was stabilized by ethylene-glycol treatment combined with heat annealing. This procedure improved the mechanical and electrical stability. Indeed, layers of PEDOT:PSS processed with ethylene glycol and thermal annealing were shown to be stable in terms of electrical conductivity for more than ten days [16]. More recent research in this field indicated that PEDOT:PSS-coated gold electrodes could be stable in physiological media for up to four months [17].

As demonstrated by the wetting angles, none of the materials in direct contact with cells (PEN foil, gold, PEDOT:PSS) showed excessively high hydrophobicity, which could prevent cell adhesion [29]. In order to yield the maximum performance from the platforms,

additional protein coating was carried out. Our previous work indicated that coating of PEDOT:PSS with collagen IV can provide excellent biocompatibility to cell cultures [16,30]. Indeed, the present work supported this idea. The differentiation of ESCs into functional cardiomyocytes is a sensitive process that is only successful in very good culture conditions [31,32]. In our work, the EBs resided on the platforms for 15 days. At the end of the differentiation, we regarded them as spread EBs (with clusters of cardiomyocytes). The ability of the PEDOT:PSS platform to enable the formation of beating loci with comparable beating frequency to the culture-plastics control proved the excellent biocompatibility of the PEDOT:PSS for long-term biological applications if coated appropriately.

Due to uncertainty about the possible combined effect of PEDOT:PSS and electrostimulation, the square DC electric pulses (1 Hz, 200 mV/mm, pulse duration 100 ms) based on the work of Hernandez et al. in 2016 [33] were applied in the two-electrode mode. In the literature, there is a range from 60 mV/mm to 750 mV/mm that is covered for various type of cells [33–38]. The voltage used in the present study corresponded to magnitude of endogenous physiological DC electrical fields that occur in animal tissues (10–200 mV/mm) [39]. Further, such electrostimulation produced a discernable biological effect, speeding up the cardiomyocyte-beating onset during the differentiation (see Section 2.2) The results clearly showed about 35 times higher capacitive current mediated by the PEDOT:PSS-covered electrodes compared with the gold electrodes. This generally corresponds with the ability of PEDOT:PSS to form high-electrical-capacity bio-interfaces [40]. The faradaic currents were about six times higher for PEDOT:PSS; hence, such material produced a one-order-of-magnitude-higher ratio of capacitive to faradaic current. The faradaic current can be described by the electrocatalytic properties of PEDOT [41,42] towards oxygen reduction [42]. The essential component of electrostimulation on both platforms was capacitive current compared to the relatively low faradaic one. However, it cannot be excluded that a minor electrocatalytic oxygen reduction could affect cells in further experiments. Additionally, a PEDOT:PSS-based platform can produce less reactive oxygen species due to the oxygen reduction per electrical current in a pulsed mode of electrostimulation.

First, a proof-of-concept experiment with the PEDOT:PSS platform was carried out in order to determine if ESCs can produce an early response to the selected mode of electrostimulation. Our data showed that these cells could sense the stimulation as they responded with changes in membrane potential and an increase in cytosolic calcium. Such a finding is in accordance with the fact that even very short electrostimulation can have an effect on cell differentiation [33], and we point to an early mechanism dependent on membrane depolarization behind such a response. Further, the data on the cytosolic-calcium level indicate that a longer electrostimulation has the potential to elicit a more pronounced response, which could be reflected in more intense late events. Indeed, the 15 min-long electrostimulation caused beating loci to occur about 1–2 days earlier compared to culture plastics and the platform without electrostimulation.

For differentiation, a general protocol was used. This approach did not induce any specific direction of stem-cell differentiation [43–45]. Hence, it provided a sensitive tool to observe if the electrostimulation of the PEDOT:PSS and gold platforms, or the platforms themselves, can modulate possible directions of differentiation. As a model system, we chose a fine balance between differentiation of ESCs to cardiomyocytes and neural cells [45]. Thus, for cardiomyogenesis the expression of transcription factor Nkx2.5 and the structural genes encoding the components of the contractile apparatus—Myh6, Myh7, Myl2, and Myl7—were chosen. The early neurogenesis was judged based on the expressions of Sox1 and Nestin in combination with the level of antigen LewisX. Additionally, expressions of Pax6, Mash1 and Tuj1 were determined to characterize later stages of neurogenesis [44].

There was a marginal trend towards elevated cardiomyogenesis due to electrostimulation regardless of the platform type, as demonstrated by the Nkx2.5 expression. This was in accordance with the earlier onset of beating after electrostimulation (see above). The expression of genes Myh6, Myh7 and Myl7 was elevated on the PEDOT:PSS platform regardless of electrostimulation. The absence of such an effect on the gold platforms strongly

indicated the predominant impact of the PEDOT:PSS material to boost cardiomyogenesis. Further, it implied no effect of the gold platform itself on cardiomyogenesis.

The expression of the contractile-apparatus genes was normalized to the level of the Nkx2.5 expression, which is relatively stable in cardiac precursor cells and cardiomyocytes. An increase in the ratio of contractile-apparatus-gene expression to the level of Nkx2.5 expression could point to a higher maturation of cells. The ratios of Myh6 to Myh7 and Myl2 to Myl7 expressions could provide information on the specific cardiomyocyte line (i.e., atrial or ventricular) [46]. The inconsistencies and absence of differences among the listed ratios indicated no enhancement in cardiomyocyte maturation and no specific direction towards a particular type of cardiomyocytes.

The early neurogenesis was potentially reduced on the PEDOT:PSS platform. This was even more pronounced by electrostimulation on this platform, as indicated by Sox1 and the LewisX antigen. There was a potential reduction of early neurogenesis by the gold platform, as indicated by Sox1, Nestin and LewisX expressions, which could be reverted by electrostimulation. Further, the gold platform without electrostimulation showed a potential enhancement of neural maturation, as deduced from the elevated expression of Mash1. Such surprising properties of the gold platform were not documented in the literature and deserve a more detailed study beyond the scope of the present work.

Compared to the work of Hernández and similar papers, which showed a clear shift to cardiomyogenesis, the electrostimulation using a gold-electrode system in the present study only induced a marginal shift to this direction of differentiation [10,33,36,47,48]. This was improved by the use of the PEDOT:PSS-based platform, but the effect of the material was more dominant. The combination of the improvement of cardiac differentiation by PEDOT:PSS with electrostimulation can be useful since the electrostimulation component can contribute to the functional improvement of the phenotype of formed cardiomyocytes, even if prepared ex vivo [6,11–13].

As demonstrated by recent works, almost all research using the PEDOT:PSS or PEDOT:PSS-based materials to electrostimulate SCs was focused on the differentiation of neural SCs or used conditions supporting neural differentiation [18–25]. In spite of this, fragments of the knowledge could be compared. Thus, a 10 min-long electrostimulation using a PEDOT:PSS-based scaffold was efficient in the upregulation of neural-cell maturation [24], confirming our finding that even a short electrostimulation of SCs can affect late events. Our findings of the effect of PEDOT:PSS per se corresponded to the literature, as PEDOT:PSS-based material has rather inhibited neurogenesis without electrostimulation [20].

The finding that PEDOT:PSS per se can significantly affect the ES differentiation could be hypothetically linked to the conductivity of the material or its surface properties. However, our data exclude the general electrical conductivity behind the effect of PEDOT:PSS, as it would behave in same manner as gold. In this regard, three recent works stating that PEDOT:PSS acts due to its electrical conductivity in the modulation of stem-cell differentiation should be interpreted conservatively [21,22,27]. Moyen et al. hypothesized that the effect of PEDOT:PSS could be related to its specific stiffness [18]. The coverage with collagen IV, which forms a relatively thick, 3D nonfibrillar network [49], is not supportive of the idea that stiffness is behind the action of PEDOT:PSS. On the other hand, the hydrophilicity and specific surface chemistry of PEDOT:PSS could affect the conformation of adhered proteins, which in turn could modulate the interaction with living cells [49].

4. Material and Methods

4.1. Electrostimulation Platform

The platform was prepared using the layout of a standard 24-well plate for cell cultures. Beneath the well plate was placed a 250 μm PEN foil (Goodlfellow Cambridge Ltd., Huntingdon, UK) as a substrate with patterned golden interdigitated electrodes. The electrodes were fabricated by physical vapor deposition, whereby the first 5 nm of NiCr alloy was evaporated as an adhesion layer that was subsequently covered by 100 nm of

gold. Patterning was achieved by evaporating through a stainless-steel shadow mask. The width and spacing of the interdigitated electrodes were 500 µm. This platform was further referred to as the gold platform.

The PEDOT:PSS (formula in Figure 6A) layer was printed onto the gold electrodes using commercially available Clevios™ S V3 screen-printing pastes (Heraeus GmbH & Co. KG, Hanau, Germany). The PEDOT:PSS pattern was printed using a screen mesh count of 140 threads/cm and then functional interdigitated electrodes were created with a good alignment of PEDOT:PSS layer with the gold support. The PEDOT:PSS layer was 195 ± 21 nm thick as determined by profilometer DetakXT (Bruker, Billerica, MA, USA). The final PEDOT:PSS layer was then annealed at 140 °C for 15 min, then soaked in ethylene glycol for 15 min and annealed again at 140 °C for 15 min in order to increase the conductivity and stability of the PEDOT:PSS layer. This platform was further referred to as the PEDOT:PSS platform. The substrate and the 24-well plate were glued together using the silicone elastomer Sylgard® 184 (Dow Europe GmbH, Praha, Czech Republic) and reinforced at the bottom by a 2 mm-thick acrylic sheet fixed to the well plate by screws (Figure 6B–D).

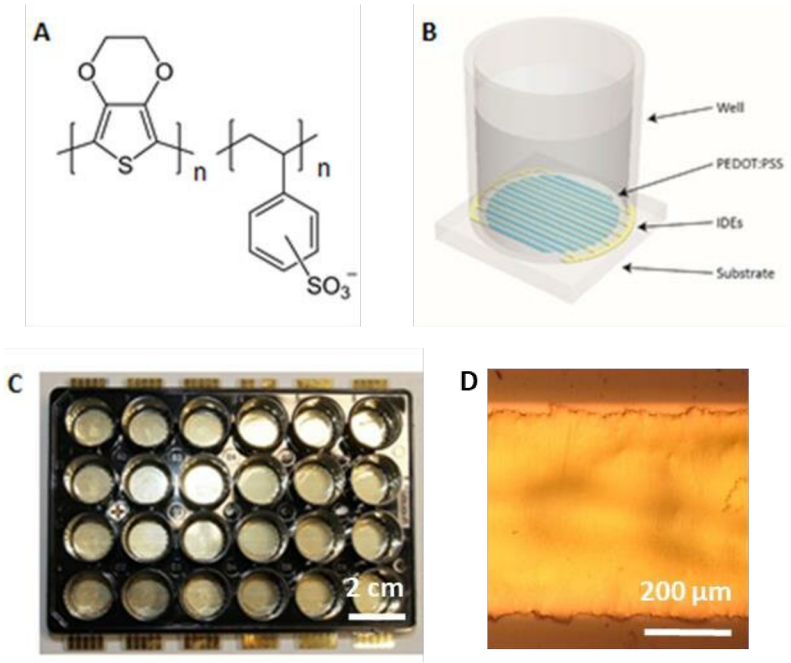

Figure 6. (**A**) chemical formula of PEDOT:PSS (source: https://en.wikipedia.org/wiki/PEDOT:PSS (accessed on 12 December 2021)). (**B**) Schematic view of one well in a platform used for electrostimulation. Interdigitated electrodes (IDEs) covered with PEDOT:PSS are highlighted (**C**) The electrostimulation platform in the format of 24-well plate. (**D**) Image of a section of gold IDE covered with PEDOT:PSS showing good alignment of PEDOT:PSS with gold support. Image was taken with Nikon Eclipse E200 microscope equipped with D5000 camera (Nikon Europe BV, Amsterdam, The Netherlands).

Immediately prior to any biological experiment, the platform wells were extensively washed with 70% (*v*/*v*) ethanol in order to remove contaminants and to sterilize surfaces. Further, the bottoms of wells were coated with murine collagen IV (cat No. 354233, BD Biosciences, Heidelberg, Germany) [30].

The chronoamperometric characterization of platforms was carried out using Potentiostat (Autolab PGSTAT 101, Metrohm Autolab B.V., Utrecht, The Netherlands).

4.2. Mouse Embryonic Stem-Cell Differentiation

A general protocol of spontaneous differentiation of mESCs line R1 was used as previously described [46,50]. The cells were cultivated on gelatin-coated dishes in Dulbecco's modified Eagle's medium (DMEM; HyClone; Logan, UT, USA) supplemented with 15% fetal bovine serum (Gibco; Carlsbad, CA, USA), 100 IU/mL penicillin and 0.1 mg/mL streptomycin (Sigma; St. Louis, MO, USA), 1× non-essential amino acid (Gibco; Carlsbad, CA, USA), 0.05 mM β-mercaptoethanol (Fluka; Buchs, Switzerland), and 1000 U/mL of leukemia inhibitory factor (Chemicon; Temecula, CA, USA). The cells were maintained at 37 °C in humidified air supplemented with 5% CO_2. A suspension of ES (2.5×10^6 cells/mL) was seeded on the top of agarose microwells. After 24 h of formation to embryoid bodies (EBs) of uniform size (day 0), EBs were transferred to agar plates and cultivated in medium without leukemia inhibitory factor [43,51]. On day 5 (5 d), the EBs were seeded onto the stimulation platform.

4.3. Stem-Cell Electrostimulation

Eight EBs on 5 d phase were transferred to each well of a platform filled with DMEM/F-12 (1:1) medium (HyClone; Logan, UT, USA) supplemented with insulin-transferrin selenium (Gibco; Carlsbad, CA, USA) and antibiotics (specification above). They were cultivated for a further 5 (5 + 5 d), 10 (5 + 10 d), 15 (5 + 15 d) days. These time points represent various stages of cardiomyocyte development. For electrostimulation it was necessary to have adherent bodies. After 24 h of adhesion, EBs were electrically stimulated. The DC electric field was 200 mV/mm at 1 Hz frequency and 100 ms pulse width. Control EBs were subjected to the same procedure but without electrical stimulation. Our stimulation protocol was inspired by Hernández et al. [33]. Cells were harvested at different time points (5 + 5 d, 5 + 10 d, 5 + 15 d), which represent various stages of cardiomyocyte development: cardiac progenitors (up to 5 days), early cardiomyocyte-like cells (up to 10 days) and beating cardiomyocyte-like cells (between 15 and 20 days) (Figure 7) [46].

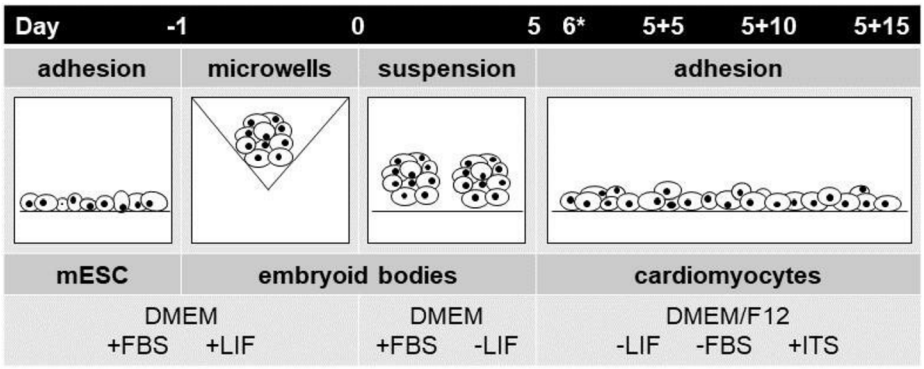

Figure 7. Schematic illustration of the protocol for differentiation of mESCs. For the preparation of EBs from mESCs, the silicone microwells were used. After 24 h of incubation (Day 0), the EBs were transferred onto an agar-coated dish. On day 5 (Day 5), the EBs were seeded to the 24-well stimulation platform. On day 6 (Day 6*) cells were electrostimulated.

4.4. Imaging of Intracellular Calcium

Intracellular free calcium (Ca^{2+}) was monitored using the fluorescent calcium indicator Fluo-4 AM (Invitrogen). Cells were incubated with Fluo-4 AM at a concentration of 5 µM for 30 min in serum-free media (DMEM/F12 1:1, HyClone; Logan, UT, USA) at 37 °C [33]. After the incubation, electrostimulation and time-lapse-image capturing (1 frame per 5 s) were started. Fluorescent images of EBs were obtained in each well using a fluorescent microscope (Axiobserver Z1, Zeiss, Germany). The fluorescence signal was visualized with a green-fluorescent-protein filter set. The image analysis was carried out using ImageJ software (version 1.47v) [52].

4.5. Depolarization Detection

To verify the sensitivity of cells to electrostimulation, the membrane-potential-sensitive probe DiBAC4(3) was used. A stock solution was prepared at a concentration of 5 mM. The stock solution was diluted in dimethyl sulfoxide to concentration 2 mM and aliquots were frozen at −20 °C. Aliquots with concentrations of 2 mM were diluted to 10 µM and cultivated in DMEM/F12 1:1 (HyClone; Logan, UT, USA) [53,54]. After 30 min of incubation, electrostimulation and time-lapse-image capturing (1 frame per 5 s) was started. Images were obtained of each well using a fluorescence microscope (Axiobserver Z1, Zeiss, Oberkochen, Germany). The fluorescence signal was visualized with a green-fluorescent-protein filter set. The image analysis was carried out using ImageJ software (version 1.47v) [52].

4.6. Gene Expression Analysis

Total RNA was extracted using the CatchGene Tissue DNA Kit (CatchGene; Taipei, Taiwan). Complementary DNA was synthesized according to the manufacturer's instructions for the Sensiscript RT Kit (Qiagen; Germantown, MD, USA) using TurboCycler Lite thermal cycler (BlueRay Biotech, Taipei, Taiwan). Real-time quantitative PCR (RT-qPCR) reactions were performed in a LightCycler480 instrument using LightCycler480 Probe Master solutions (Roche; Basel, Switzerland). The following program was used: initial denaturation step at 95 °C for 10 min, followed by 45 cycles (95 °C for 10 s, 60 °C for 30 s, and 72 °C for 1 s) and the final cooling step at 40 °C for 1 min. Ribosomal protein L13A (RPL13A) was used as a reference gene and the expression of genes of interest was presented as $2^{-\Delta cq}$. The sequences of primers and numbers of the Universal Probe Library probes are listed in Table 1.

Table 1. Sequence of primers used in quantitative RT-PCR.

Gene of Interest	Forward Primer 5′→3′	Reverse Primer 5′→3′	UPL Probe No.
Rpl13a	CATGAGGTCGGGTGGAAGTA	GCCTGTTTCCGTAACCTCAA	#25
Nkx2.5	GACGTAGCCTGGTGTCTCG	GTGTGGAATCCGTCGAAAGT	#53
Myh6	CGCATCAAGGAGCTCACC	CCTGCAGCCGCATTAAGT	#6
Myh7	CGCATCAAGGAGCTCACC	CTGCAGCCGCAGTAGGTT	#6
Myl2	CCCAGATCCAGGAGTTCAAG	CTGCAGCCGCAGTAGGTT	#95
Myl7	CCCATCAACTTCACCGTCTT	AACATGCGGAAGGCACTC	#7
Sox1	GTGACATCTGCCCCCATC	GAGGCCAGTCTGGTGTCAG	#60

4.7. Protein Expression Analysis

Total protein lysates were prepared from differentiated ESCs of day 5 + 15 d. Western-blot analysis, cell-sample harvesting, and preparation were performed by a standard procedure as previously presented [43]. Protein concentrations were determined using BCA Protein Assay (Pierce Biotechnology; Rockford, IL, USA) according to the manufacturer's instructions. The following primary antibodies were used to detect antigen LewisX, which is typical of neural precursor cells (mouse monoclonal anti-LewisX/Forse1, DSHB, University of Iowa, deposited by Patterson P.H., https://dshb.biology.uiowa.edu/FORSE-1, website accessed on 20 May 2021), GPDH in 5% non-fat milk/TBS-T at 4 °C overnight. The corresponding secondary HRP-conjugated anti-rabbit 1:3000 (Sera care, Milford, MA, USA) antibody in 5% non-fat milk for 1 h at RT was employed. The amount of 10 µg of protein was loaded onto a 10% SDS-PAGE gel, transferred onto a polyvinyl difluoride membrane (Merck Millipore; Darmstadt, Germany) and blocked in 5% low-fat milk. The immunoreactivity bands were detected using an ECL detection-reagent kit (Pierce, USA) and then exposed on Amersham 680 (GE Healthcare, North Richland Hills, TX, USA). Optical densities were quantified by scanning densitometry and expressed in arbitrary units determined by ImageJ software (version 1.47v) [52].

5. Conclusions

In the present work, we focused on a novel and largely underexplored combined material and electrical-based stimulation of SCs. Gold- as well as PEDOT:PSS-based platforms showed excellent biocompatibility. The PEDOT:PSS platform was able to produce a higher electrical current with the pulsed-DC electrostimulation mode (1 Hz, 200 mV/mm, 100 ms pulse duration) compared to the gold platform. In proof-of-concept experiments, ESCs were able to respond to such electrostimulation by membrane depolarization and elevation of cytosolic calcium. Electrical stimuli on both platforms induced a marginal trend towards cardiomyogenesis, as deduced from the expression of the Nkx2.5 gene, whereas on the gold platform it potentially attenuated the early neurogenesis, as demonstrated by the decrease in the expression of gene Sox1 and LewisX antigen. There was a boost of cardiomyogenesis on the PEDOT:PSS platform indicated by the elevated expression of the genes encoding the contractile apparatus. However, the effect of the PEDOT:PSS platform itself was dominant. The gold platform per se did not affect cardiomyogenesis because there was no change in expression of the contractile apparatus, but it potentially reduced early neurogenesis as demonstrated by the lowered expression of Sox1 and Nestin genes and the LewisX antigen. Taken together, an effect of PEDOT:PSS platform itself to upregulate cardiomyogenesis and potentially inhibit early neurogenesis with the minor contribution of electrostimulation could be concluded. Therefore, the present work further highlights the large potential of PEDOT:PSS in regenerative medicine.

Supplementary Materials: The following supporting information can be downloaded at: https://www.mdpi.com/article/10.3390/ijms23031107/s1.

Author Contributions: Conceptualization, E.Š. and J.V.; Data curation, J.E. and J.V.; Formal analysis, E.Š.; Funding acquisition, M.W. and J.V.; Investigation, E.Š., S.S. and J.E.; Methodology, E.Š., S.S., J.E., M.V., J.P. and J.V.; Project administration, M.W. and J.V.; Resources, M.W., L.K. and J.V.; Supervision, J.V.; Visualization, E.Š.; Writing–original draft, E.Š., J.E. and J.V.; Writing–review & editing, E.Š., J.E., M.V., M.W., J.P., L.K. and J.V. All authors have read and agreed to the published version of the manuscript.

Funding: This work was primarily supported by Czech Science Foundation grant No. 21-01057S. Jiri Pachernik gratefully acknowledges support from the Czech Science Foundation grant No. 18-18235S. Lukáš Kubala was supported by the Project INBIO No. CZ.02.1.01/0.0/0.0/16_026/0008451 from European Regional Development Fund.

Data Availability Statement: The data presented in this study are available on request from the corresponding author.

Acknowledgments: This work was primarily supported by Czech Science Foundation grant No. 21-01057S. Jiri Pachernik gratefully acknowledges support from the Czech Science Foundation grant No. 18-18235S. Lukáš Kubala was supported by the Project INBIO No. CZ.02.1.01/0.0/0.0/16_026/0008451 from European Regional Development Fund. The authors thank Jan Hrbáč for consultations on the electrical characterization of platforms. Further, the first author thanks the colleagues from Department of Biophysics of Immune System—Institute of Biophysics of the CAS, namely: Petra Dad'ová, Marek Černík, Svitlana Skoroplyas and Michaela Chorvátová.

Conflicts of Interest: The authors declare no conflict of interest. The funding bodies had no role in the design of the study; in the collection, analyses, or interpretation of data; in the writing of the manuscript, or in the decision to publish the results.

Abbreviations

embryoid bodies	(EBs)
stem cells	(SCs)
embryonic stem cells	(ESCs)
mouse embryonic stem cells	(mESCs)
poly(3:4-ethylenedioxythiophene):polystyrene sulfonate	(PEDOT:PSS)
direct current	(DC)

References

1. Sachinidis, A.; Fleischmann, B.K.; Kolossov, E.; Wartenberg, M.; Sauer, H.; Hescheler, J. Cardiac specific differentiation of mouse embryonic stem cells. *Cardiovasc. Res.* **2003**, *58*, 278–291. [CrossRef]
2. Keller, G. Embryonic stem cell differentiation: Emergence of a new era in biology and medicine. *Genes Dev.* **2005**, *19*, 1129–1155. [CrossRef]
3. Heng, B.C.; Cao, T.; Stanton, L.W.; Robson, P.; Olsen, B. Strategies for directing the differentiation of stem cells into the osteogenic lineage in vitro. *J. Bone Miner. Res.* **2004**, *19*, 1379–1394. [CrossRef]
4. Amin, M.; Kushida, Y.; Wakao, S.; Kitada, M.; Tatsumi, K.; Dezawa, M. Cardiotrophic growth factor-driven induction of human muse cells into cardiomyocyte-like phenotype. *Cell Transplant.* **2018**, *27*, 285–298. [CrossRef]
5. Tian, H.-C.; Liu, J.-Q.; Kang, X.-Y.; Wei, D.-X.; Zhang, C.; Du, J.-C.; Yang, B.; Chen, X.; Yang, C.-S. Biotic and abiotic molecule dopants determining the electrochemical performance, stability and fibroblast behavior of conducting polymer for tissue interface. *RSC Adv.* **2014**, *4*, 47461–47471. [CrossRef]
6. Chen, C.; Bai, X.; Ding, Y.; Lee, I.-S. Electrical stimulation as a novel tool for regulating cell behavior in tissue engineering. *Biomater. Res.* **2019**, *23*, 25. [CrossRef] [PubMed]
7. Broughton, K.M.; Wang, B.J.; Firouzi, F.; Khalafalla, F.; Dimmeler, S.; Fernandez-Aviles, F.; Sussman, M.A. Mechanisms of cardiac repair and regeneration. *Circ. Res.* **2018**, *122*, 1151–1163. [CrossRef]
8. Du Pré, B.C.; Doevendans, P.A.; van Laake, L.W. Stem cells for cardiac repair: An introduction. *J. Geriatr. Cardiol. JGC* **2013**, *10*, 186.
9. Parsa, H.; Ronaldson, K.; Vunjak-Novakovic, G. Bioengineering methods for myocardial regeneration. *Adv. Drug Deliv. Rev.* **2016**, *96*, 195–202. [CrossRef] [PubMed]
10. Thrivikraman, G.; Boda, S.K.; Basu, B. Unraveling the mechanistic effects of electric field stimulation towards directing stem cell fate and function: A tissue engineering perspective. *Biomaterials* **2018**, *150*, 60–86. [CrossRef]
11. Ma, R.; Liang, J.; Huang, W.; Guo, L.; Cai, W.; Wang, L.; Paul, C.; Yang, H.-T.; Kim, H.W.; Wang, Y. Electrical Stimulation Enhances Cardiac Differentiation of Human Induced Pluripotent Stem Cells for Myocardial Infarction Therapy. *Antioxid. Redox Signal.* **2018**, *28*, 371–384. [CrossRef]
12. Radisic, M.; Park, H.; Shing, H.; Consi, T.; Schoen, F.J.; Langer, R.; Freed, L.E.; Vunjak-Novakovic, G. Functional assembly of engineered myocardium by electrical stimulation of cardiac myocytes cultured on scaffolds. *Proc. Natl. Acad. Sci. USA* **2004**, *101*, 18129–18134. [CrossRef]
13. Cao, H.; Kang, B.J.; Lee, C.-A.; Shung, K.K.; Hsiai, T.K. Electrical and mechanical strategies to enable cardiac repair and regeneration. *IEEE Rev. Biomed. Eng.* **2015**, *8*, 114–124. [CrossRef] [PubMed]
14. Gueye, M.N.; Carella, A.; Faure-Vincent, J.; Demadrille, R.; Simonato, J.-P. Progress in understanding structure and transport properties of PEDOT-based materials: A critical review. *Prog. Mater. Sci.* **2020**, *108*, 100616. [CrossRef]
15. Rivnay, J.; Owens, R.M.; Malliaras, G.G. The rise of organic bioelectronics. *Chem. Mater.* **2013**, *26*, 679–685. [CrossRef]
16. Stritesky, S.; Markova, A.; Vitecek, J.; Safarikova, E.; Hrabal, M.; Kubac, L.; Kubala, L.; Weiter, M.; Vala, M. Printing inks of electroactive polymer PEDOT:PSS: The study of biocompatibility, stability, and electrical properties. *J. Biomed. Mater. Res. Part A* **2018**, *106*, 1121–1128. [CrossRef]
17. Dijk, G.; Rutz, A.L.; Malliaras, G.G. Stability of PEDOT:PSS-Coated Gold Electrodes in Cell Culture Conditions. *Adv. Mater. Technol.* **2020**, *5*, 1900662. [CrossRef]
18. Moyen, E.; Hama, A.; Ismailova, E.; Assaud, L.; Malliaras, G.; Hanbücken, M.; Owens, R.M. Nanostructured conducting polymers for stiffness controlled cell adhesion. *Nanotechnology* **2016**, *27*, 074001. [CrossRef]
19. Ritzau-Reid, K.I.; Spicer, C.D.; Gelmi, A.; Grigsby, C.L.; Ponder, J.F., Jr.; Bemmer, V.; Creamer, A.; Vilar, R.; Serio, A.; Stevens, M.M. An electroactive oligo-EDOT platform for neural tissue engineering. *Adv. Funct. Mater.* **2020**, *30*, 2003710. [CrossRef] [PubMed]
20. Heo, D.N.; Acquah, N.; Kim, J.; Lee, S.-J.; Castro, N.J.; Zhang, L.G. Directly induced neural differentiation of human adipose-derived stem cells using three-dimensional culture system of conductive microwell with electrical stimulation. *Tissue Eng. Part A* **2018**, *24*, 537–545. [CrossRef]
21. Aggas, J.R.; Abasi, S.; Phipps, J.F.; Podstawczyk, D.A.; Guiseppi-Elie, A. Microfabricated and 3-D printed electroconductive hydrogels of PEDOT:PSS and their application in bioelectronics. *Biosens. Bioelectron.* **2020**, *168*, 112568. [CrossRef] [PubMed]
22. Iandolo, D.; Sheard, J.; Levy, G.K.; Pitsalidis, C.; Tan, E.; Dennis, A.; Kim, J.-S.; Markaki, A.E.; Widera, D.; Owens, R.M. Biomimetic and electroactive 3D scaffolds for human neural crest-derived stem cell expansion and osteogenic differentiation. *MRS Commun.* **2020**, *10*, 179–187. [CrossRef]
23. Tomaskovic-Crook, E.; Zhang, P.; Ahtiainen, A.; Kaisvuo, H.; Lee, C.-Y.; Beirne, S.; Aqrawe, Z.; Svirskis, D.; Hyttinen, J.; Wallace, G.G.; et al. Human neural tissues from neural stem cells using conductive biogel and printed polymer microelectrode arrays for 3D electrical stimulation. *Adv. Healthc. Mater.* **2019**, *8*, 1900425. [CrossRef]
24. Tsai, N.-C.; She, J.-W.; Wu, J.-G.; Chen, P.; Hsiao, Y.-S.; Yu, J. Poly (3,4-ethylenedioxythiophene) polymer composite bioelectrodes with designed chemical and topographical cues to manipulate the behavior of pc12 neuronal cells. *Adv. Mater. Interfaces* **2019**, *6*, 1801576. [CrossRef]
25. Pires, F.; Ferreira, Q.; Rodrigues, C.A.; Morgado, J.; Ferreira, F.C. Neural stem cell differentiation by electrical stimulation using a cross-linked PEDOT substrate: Expanding the use of biocompatible conjugated conductive polymers for neural tissue engineering. *Biochim. Biophys. Acta Gen. Subj.* **2015**, *1850*, 1158–1168. [CrossRef] [PubMed]

26. Decataldo, F.; Druet, V.; Pappa, A.-M.; Tan, E.; Savva, A.; Pitsalidis, C.; Inal, S.; Kim, J.-S.; Fraboni, B.; Owens, R.M.; et al. BMP-2 functionalized PEDOT:PSS-based OECTs for stem cell osteogenic differentiation monitoring. *Flex. Print.* **2019**, *4*, 044006. [CrossRef]
27. Roshanbinfar, K.; Vogt, L.; Greber, B.; Diecke, S.; Boccaccini, A.R.; Scheibel, T.; Engel, F.B. Electroconductive biohybrid hydrogel for enhanced maturation and beating properties of engineered cardiac tissues. *Adv. Funct. Mater.* **2018**, *28*, 1803951. [CrossRef]
28. Yoshida, S.; Sumomozawa, K.; Nagamine, K.; Nishizawa, M. Hydrogel Microchambers Integrated with Organic Electrodes for Efficient Electrical Stimulation of Human iPSC-Derived Cardiomyocytes. *Macromol. Biosci.* **2019**, *19*, 1900060. [CrossRef]
29. Menzies, K.L.; Jones, L. The impact of contact angle on the biocompatibility of biomaterials. *Optom. Vis. Sci.* **2010**, *87*, 387–399. [CrossRef] [PubMed]
30. Safarikova, E.; Sindlerova, L.S.; Stritesky, S.; Kubala, L.; Vala, M.; Weiter, M.; Vitecek, J. Evaluation and improvement of organic semiconductors' biocompatibility towards fibroblasts and cardiomyocytes. *Sens. Actuators B Chem.* **2018**, *260*, 418–425. [CrossRef]
31. Radaszkiewicz, K.A.; Sykorova, D.; Bino, L.; Kudova, J.; Bebarova, M.; Prochazkova, J.; Kotasova, H.; Kubala, L.; Pachernik, J. The acceleration of cardiomyogenesis in embryonic stem cells in vitro by serum depletion does not increase the number of developed cardiomyocytes. *PLoS ONE* **2017**, *12*, e0173140. [CrossRef] [PubMed]
32. Lanza, R.; Gearhart, J.; Hogan, B.; Melton, D.; Pedersen, R.; Thomas, E.D.; Thomson, J.A.; West, M. *Essentials of Stem Cell Biology*; Elsevier: Amsterdam, The Netherlands, 2005.
33. Hernandez, D.; Millard, R.; Sivakumaran, P.; Wong, R.C.; Crombie, D.E.; Hewitt, A.W.; Liang, H.; Hung, S.S.; Pebay, A.; Shepherd, R.K.; et al. Electrical stimulation promotes cardiac differentiation of human induced pluripotent stem cells. *Stem Cells Int.* **2015**, *2016*, 1718041. [CrossRef] [PubMed]
34. Sauer, H.; Bekhite, M.M.; Hescheler, J.; Wartenberg, M. Redox control of angiogenic factors and CD31-positive vessel-like structures in mouse embryonic stem cells after direct current electrical field stimulation. *Exp. Cell Res.* **2005**, *304*, 380–390. [CrossRef]
35. Yamada, M.; Tanemura, K.; Okada, S.; Iwanami, A.; Nakamura, M.; Mizuno, H.; Ozawa, M.; Ohyama-Goto, R.; Kitamura, N.; Kawano, M.; et al. Electrical stimulation modulates fate determination of differentiating embryonic stem cells. *Stem Cells* **2007**, *25*, 562–570. [CrossRef]
36. Serena, E.; Figallo, E.; Tandon, N.; Cannizzaro, C.; Gerecht, S.; Elvassore, N.; Vunjak-Novakovic, G. Electrical stimulation of human embryonic stem cells: Cardiac differentiation and the generation of reactive oxygen species. *Exp. Cell Res.* **2009**, *315*, 3611–3619. [CrossRef] [PubMed]
37. Tandon, N.; Marsano, A.; Maidhof, R.; Numata, K.; Montouri-Sorrentino, C.; Cannizzaro, C.; Voldman, J.; Vunjak-Novakovic, G. Surface-patterned electrode bioreactor for electrical stimulation. *Lab Chip* **2010**, *10*, 692–700. [CrossRef] [PubMed]
38. Chan, Y.-C.; Ting, S.; Lee, Y.-K.; Ng, K.-M.; Zhang, J.; Chen, Z.; Siu, C.-W.; Oh, S.K.W.; Tse, H.-F. Electrical stimulation promotes maturation of cardiomyocytes derived from human embryonic stem cells. *J. Cardiovasc. Transl. Res.* **2013**, *6*, 989–999. [CrossRef]
39. Nuccitelli, R. Endogenous ionic currents and DC electric fields in multicellular animal tissues. *Bioelectromagnetics* **1992**, *13*, 147–157. [CrossRef] [PubMed]
40. Proctor, C.M.; Rivnay, J.; Malliaras, G.G. Understanding volumetric capacitance in conducting polymers. *J. Polym. Sci. B Polym. Phys.* **2016**, *54*, 1433–1436. [CrossRef]
41. Winther-Jensen, B.; Winther-Jensen, O.; Forsyth, M.; MacFarlane, D.R. High rates of oxygen reduction over a vapor phase-polymerized PEDOT electrode. *Science* **2008**, *321*, 671–674. [CrossRef]
42. Cottis, P.P.; Evans, D.; Fabretto, M.; Pering, S.; Murphy, P.; Hojati-Talemi, P. Metal-free oxygen reduction electrodes based on thin PEDOT films with high electrocatalytic activity. *RSC Adv.* **2014**, *4*, 9819–9824. [CrossRef]
43. Kudova, J.; Prochazkova, J.; Vasicek, O.; Perecko, T.; Sedlackova, M.; Pesl, M.; Pachernik, J.; Kubala, L. HIF-1alpha deficiency attenuates the cardiomyogenesis of mouse embryonic stem cells. *PLoS ONE* **2016**, *11*, e0158358. [CrossRef] [PubMed]
44. Vecera, J.; Kudova, J.; Kucera, J.; Kubala, L.; Pachernik, J. Neural Differentiation Is Inhibited through HIF1α/β-Catenin Signaling in Embryoid Bodies. *Stem Cells Int.* **2017**, *2017*, 8715798. [CrossRef]
45. Humpolicek, P.; Radaszkiewicz, K.A.; Kasparkova, V.; Stejskal, J.; Trchova, M.; Kucekova, Z.; Vicarova, H.; Pachernik, J.; Lehocky, M.; Minarik, A. Stem cell differentiation on conducting polyaniline. *RSC Adv.* **2015**, *5*, 68796–68805. [CrossRef]
46. Radaszkiewicz, K.A.; Beckerova, D.; Woloszczukova, L.; Radaszkiewicz, T.W.; Lesakova, P.; Blanarova, O.V.; Kubala, L.; Humpolicek, P.; Pachernik, J. 12-*O*-Tetradecanoylphorbol-13-acetate increases cardiomyogenesis through PKC/ERK signaling. *Sci. Rep.* **2020**, *10*, 15922. [CrossRef] [PubMed]
47. Tandon, N.; Cannizzaro, C.; Chao, P.-H.G.; Maidhof, R.; Marsano, A.; Au, H.T.H.; Radisic, M.; Vunjak-Novakovic, G. Electrical stimulation systems for cardiac tissue engineering. *Nat. Protoc.* **2009**, *4*, 155–173. [CrossRef]
48. Sauer, H.; Rahimi, G.; Hescheler, J.; Wartenberg, M. Effects of electrical fields on cardiomyocyte differentiation of embryonic stem cells. *J. Cell. Biochem.* **1999**, *75*, 710–723. [CrossRef]
49. Coelho, N.M.; González-Garcia, C.; Planell, J.; Salmerón-Sánchez, M.; Altankov, G. Different assembly of type IV collagen on hydrophilic and hydrophobic substrata alters endothelial cells interaction. *Eur. Cell. Mater.* **2010**, *19*, 262–272. [CrossRef]
50. Nagy, A.; Rossant, J.; Nagy, R.; Abramow-Newerly, W.; Roder, J.C. Derivation of completely cell culture-derived mice from early-passage embryonic stem cells. *Proc. Natl. Acad. Sci. USA* **1993**, *90*, 8424–8428. [CrossRef]

51. Dahlmann, J.; Kensah, G.; Kempf, H.; Skvorc, D.; Gawol, A.; Elliott, D.A.; Dräger, G.; Zweigerdt, R.; Martin, U.; Gruh, I. The use of agarose microwells for scalable embryoid body formation and cardiac differentiation of human and murine pluripotent stem cells. *Biomaterials* **2013**, *34*, 2463–2471. [CrossRef] [PubMed]
52. Schneider, C.A.; Rasband, W.S.; Eliceiri, K.W.; Schindelin, J.; Arganda-Carreras, I.; Frise, E.; Kaynig, V.; Longair, M.; Pietzsch, T.; Preibisch, S.; et al. NIH image to imageJ: 25 years of image analysis. *Nat. Methods* **2012**, *9*, 671–675. [CrossRef] [PubMed]
53. Adams, D.S.; Levin, M. Measuring resting membrane potential using the fluorescent voltage reporters DiBAC4 (3) and CC2-DMPE. *Cold Spring Harb. Protoc.* **2012**, *2012*, pdb-prot067702. [CrossRef] [PubMed]
54. Lan, J.-Y.; Williams, C.; Levin, M.; Black, L.D. Depolarization of cellular resting membrane potential promotes neonatal cardiomyocyte proliferation in vitro. *Cell. Mol. Bioeng.* **2014**, *7*, 432–445. [CrossRef] [PubMed]

Journal of Neural Engineering

PAPER

Direct measurement of oxygen reduction reactions at neurostimulation electrodes

Jiří Ehlich[1,4], Ludovico Migliaccio[1,4], Ihor Sahalianov[1], Marta Nikić[1,2], Jan Brodský[1], Imrich Gablech[1], Xuan Thang Vu[3], Sven Ingebrandt[3] and Eric Daniel Głowacki[1,*]

[1] Bioelectronics Materials and Devices Laboratory, Central European Institute of Technology CEITEC, Brno University of Technology, Purkyňova 123, 61200 Brno, Czech Republic
[2] Institute of Neuroelectronics, Technical University of Munich, Munich, Germany
[3] Institute of Materials in Electrical Engineering 1, RWTH Aachen University, 52074 Aachen, Germany
[4] These authors are contributed equally.
[*] Author to whom any correspondence should be addressed.

E-mail: eric.daniel.glowacki@ceitec.vutbr.cz

Keywords: bioelectronics, neurostimulation, faradaic reactions, hypoxia, reactive oxygen species

Supplementary material for this article is available online

OPEN ACCESS

RECEIVED
23 December 2021

REVISED
1 June 2022

ACCEPTED FOR PUBLICATION
10 June 2022

PUBLISHED
27 June 2022

Abstract

Objective. Electric stimulation delivered by implantable electrodes is a key component of neural engineering. While factors affecting long-term stability, safety, and biocompatibility are a topic of continuous investigation, a widely-accepted principle is that charge injection should be reversible, with no net electrochemical products forming. We want to evaluate oxygen reduction reactions (ORR) occurring at different electrode materials when using established materials and stimulation protocols. *Approach.* As stimulation electrodes, we have tested platinum, gold, tungsten, nichrome, iridium oxide, titanium, titanium nitride, and poly(3,4-ethylenedioxythiophene):poly(styrene sulfonate). We use cyclic voltammetry and voltage-step amperometry in oxygenated versus inert conditions to establish at which potentials ORR occurs, and the magnitudes of diffusion-limited ORR currents. We also benchmark the areal capacitance of each electrode material. We use amperometric probes (Clark-type electrodes) to quantify the O_2 and H_2O_2 concentrations in the vicinity of the electrode surface. O_2 and H_2O_2 concentrations are measured while applying DC current, or various biphasic charge-balanced pulses of amplitude in the range 10–30 μC cm^{-2}/phase. To corroborate experimental measurements, we employ finite element modelling to recreate 3D gradients of O_2 and H_2O_2. *Main results.* All electrode materials support ORR and can create hypoxic conditions near the electrode surface. We find that electrode materials differ significantly in their onset potentials for ORR, and in the extent to which they produce H_2O_2 as a by-product. A key result is that typical charge-balanced biphasic pulse protocols do lead to irreversible ORR. Some electrodes induce severely hypoxic conditions, others additionally produce an accumulation of hydrogen peroxide into the mM range. *Significance.* Our findings highlight faradaic ORR as a critical consideration for neural interface devices and show that the established biphasic/charge-balanced approach does not prevent irreversible changes in O_2 concentrations. Hypoxia and H_2O_2 can result in different (electro)physiological consequences.

1. Introduction

Electrical neurostimulation is an established part of numerous implantable bioelectronics devices like deep brain stimulators [1], peripheral nerve stimulation devices [2], spinal cord stimulators [3], and retinal prosthetics [4, 5]. Electrical stimulation involves charge injection from an electrode surface into physiological electrolyte. The safety and reliability of this process is a vital consideration. Mechanisms of charge exchange at the electrode/electrolyte interface are the subject of extensive research, and can be divided into capacitive, pseudo-capacitive, and faradaic [6–8]. Capacitive charge injection

involves the charging and discharging of electrolytic double-layers, and no charge is transferred to species in solution. The pseudo-capacitive mechanism, also known as pseudo-faradaic, features redox reactions of the electrode material itself. These reactions can result in high density of charge transfer, and this transfer can be highly reversible. The third category is faradaic, where charge is transferred to a species in solution via a redox process occurring at the electrode/electrolyte interface. This process may or may not be reversible, depending on kinetic factors like activation barriers (*aka* overpotentials) for a given reaction as well as diffusion of reactants/products. A stimulation electrode works by injecting current into a physiological medium and the resultant electric fields modulate the membrane potential of nearby excitable cells. For instance, a cathodic pulse will efficiently depolarize cell membranes and activate voltage-gated sodium channels, triggering action potentials. Cathodic, i.e. negative currents, have been long recognized as being most efficient at eliciting action potentials. However, it follows that charge artificially injected into a physiological environment should be subsequently removed, that is no net charging of the system should occur. This is because net charge remaining would correspond to polarization of the electrode, or to electrochemical changes in the biological surrounding itself. These changes could potentially be toxic or otherwise spurious. For this reason, virtually all neurostimulation protocols for both basic research and implanted biomedical devices rely on biphasic operation [6]. Charge-balanced, cathodic-leading pulses are the standard [9]. This way, the total injected cathodic charge in the first phase is equalized by an equal-charge anodic phase. In principle, any electrochemical reaction products formed on the electrode during the leading phase should be reoxidized during the second, anodic, phase [7, 10]. Determining safe limits for charge injection is the topic of debate and several empirical norms have been suggested for various *in vivo* applications. A number of studies have considered the reversibility of faradaic electrochemistry during biphasic pulsing [11]. Nearly all of these studies focus on testing corrosion of the metal electrode itself, or voltage excursions beyond the water-splitting window, and thus hydrogen evolution or oxygen evolution reactions [7, 11, 12]. The possibility of oxygen reduction, occurring during the cathodic stimulation phase, has received relatively little attention [13, 14], despite the fact that thermodynamically it is much more favoured than hydrogen evolution (by at least 1.23 V). Oxygen is present in all physiological fluids. While it is transported in heme-bound form in the vasculature, in excitable neural tissues, oxygen travels through the extracellular and intracellular space by passive diffusion. Neural tissue oxygenation levels vary depending on species, anaesthesia, location. The highest possible equilibrium concentration of dissolved O_2 is about 250 μM. This is the same level of oxygenation as what is expected for a container of water open to ambient 21% atmospheric oxygen. This condition also applies for most *in vitro* experiments. We therefore perform this study with this 21% reference point, since it applies to *in vitro* conditions and with respect to *in vivo* this assumption mirrors the 'best case' scenario.

To our knowledge, there are four published studies which consider oxygen reduction reactions (ORR) on neurostimulation electrodes, primarily on Pt and Au [13–16]. These all rely on some form of transient electrochemical measurement techniques to estimate irreversible charge transfer to O_2, and all these studies agree that a substantial fraction of cathodic current can be irreversibly transferred to oxygen (reported ranges between 5% and 80%). None of these studies quantified the generation of peroxide via two-electron reduction, or actual oxygen concentration changes. In contrast to these works, we have designed our study to probe both O_2 and H_2O_2 concentrations in the vicinity of the electrode surface to quantify the effects of ORR directly, and have used the same technique to compare eight different neurostimulation electrode materials we have prepared in thin-film from: Ti, TiN, Au, IrO_x, Pt, W, NiCr, and poly(3,4-ethylenedioxythiophene):poly(styrene sulfonate), shortened as PEDOT:PSS. This list is chosen it represents common electrode materials used in both neuroscience/electrophysiology research as well as biomedical devices. In addition, a sample of commercial high-surface area TiN was tested [17]. This way, we can establish to what extent irreversible ORR can occur at neurostimulation electrodes, and compare and contrast different electrode materials. To corroborate experimentally-measured O_2 and H_2O_2 concentrations, we have also established finite element simulations to understand the geometry of concentration gradients over time.

2. Materials and methods

2.1. Model stimulation electrode preparation

Microscope slides (3 × 1) inch^2 were cleaned according to established methods, treated with oxygen plasma, and then sputter coated with a 100 nm layer of Ti using a Kaufman ion-beam source (IBS). The Ti acts as the common conducting layer below all studied samples, as it has excellent adhesion on glass and is a suitable underlayer for all the studied materials. Platinum (60 nm) is deposited using DC magnetron sputtering. W (60 nm) was deposited using the same sputtering system. TiN (60 nm) is reactively sputtered from a Ti target using two Kaufman IBSs, and will be referred to in this article as IBS_TiN. The primary IBS is used for sputtering from Ti target employing Ar and N_2 plasma, while the secondary

IBS is used for substrate bombardment with ions from pure N_2 plasma. Au is also deposited using primary IBS, to a thickness of 60 nm. NiCr (60 nm) was prepared by the same primary IBS, using pure Ar. IrO_x was obtained via DC reactive magnetron sputtering in an Ar/O_2 plasma (100 nm) according to previous published methods [18]. PEDOT:PSS (PH1000 formulation from Clevios, plus 5 wt% ethylene glycol, 0.1 wt% 4-dodecylbenzenesulfonic acid and 1 wt% (3-glycidyloxypropyl)trimethoxysilane) was spin-coated at 3000 rpm and annealed for 1 h at 130 °C (giving roughly 100 nm thickness as measured by stylus profilometry). As a reference, we characterize commercial TiN used in multielectrode arrays (Multichannel Systems GmbH). These films are about 600 nm thick. To distinguish this TiN from our in-house prepared samples, we will refer to it as MCS_TiN.

2.2. Electrochemical cell

A homemade custom electrochemical cell allowed correct positioning and characterization of the electrodes under investigation. The cell was made from clear 5 mm thick acrylic sheets and a microscope glass slide as a front window. The internal volume of the cell was 9.3 ml. Microscope slides with deposited model stimulation electrodes were cut to (1×1) $inch^2$ pieces and horizontally inserted through a tight opening on the side of the cell. Polydimethylsiloxane was used to fix and seal the sample in position and to prevent any electrolyte leakage. The exposed area of each electrode was masked using a 70 μm thick polyvinylchloride foil (Minitronic elektronik GmbH). The circular opening in the foil had a diameter of 3 mm, defining the electrode under test area (active electrode area = 0.0706 cm^2). The cell was equipped with a Pt wire coil as counter (active area ~7 cm^2) and an Ag/AgCl as reference electrodes, two openings provided access for the O_2 or H_2O_2 sensor and a teflon tube for O_2/N_2 purging. The sensor was placed in vicinity of the exposed active electrode material (distance = 200 μm). The counter electrode is roughly 5 mm away from this area, at the top of the cell. Care should be taken that this distance is sufficient to ensure that any eventual products on the counter electrode do not affect the measurement. The cell was mounted on a submicrometer-precision XYZ stage (ThorLabs). Using a digital microscope (Q-SCOPE 20200-P), the sensor tip was positioned using XYZ stage to the point of light contact in the middle of the sample and then moved to the 200 μm distance in the Z direction (figures 1(b) and S1). The cyclic voltammetry (CV) electrochemical characterization was carried out in a larger cell (from Redox.me) using an electrochemical active area of 1 cm^2, in a three-electrode configuration having Ag/AgCl as reference electrode and Pt wire as counter electrode in a range of potentials using 0.1 M phosphate buffer saline (PBS) solution as electrolyte.

2.3. Electrochemical measurements—DC and AC conditions

CV and chronoamperometry (DC conditions) were applied using an Ivium PocketSTAT2 potentiostat. For biphasic pulsing, a Digitimer DS4 biphasic constant current isolated stimulator was used, waveform was driven by a PicoScope 3404D oscilloscope with a built-in function generator. Transient voltages were recorded during biphasic pulsing by measuring voltage using the oscilloscope input (1 MΩ input impedance) between the electrode under test and an Ag/AgCl reference electrode. Data were collected in oxygenated and deoxygenated conditions. The relatively low input impedance is selected in order to provide a shunt resistance to prevent potential ratcheting and thus prevent the introduction of a DC bias offset voltage during AC pulsing experiments.

2.4. Clark electrode O_2 and H_2O_2 quantification

Local oxygen and peroxide concentrations were measured *in situ* during electrochemical measurements described above in section 2.2 using a four-channel microamperometric amplifier system (TBR4100, World Scientific Instruments), with four-channel analog-digital converter board (LabTrax, World Scientific Instruments). The respective sensor probes used were ISO-HPO-2 and ISO-OXY-2. The O_2 sensor was kept constantly polarized at a bias of 700 mV, meanwhile the H_2O_2 specific sensor at 450 mV. The sensors were always calibrated before the measurement of an individual material following the procedure reported in the instruction manual. The drop in O_2 concentration or increase in H_2O_2 was tracked by LabScribe software (World Scientific Instruments). It should be noted that the O_2 sensor functions along the classic Clark-electrode mechanism where oxygen is reduced at the sensing electrode, and oxygen reaches the sensor via an oxygen-permeable membrane. The peroxide sensor, on the other hand, operates via the oxidation of H_2O_2, and is therefore also cross-sensitive to dissolved H_2 (via the H_2 oxidation reaction). For experiments where cathodic polarization of the electrode under test results in H_2 evolution, the sensor signal can register a false positive H_2O_2 signal. Caution should therefore be taken to test electrodes in deoxygenated electrolytes to establish the cathodic water-splitting onset. Peroxide sensor readings should only be accepted within the range before cathodic water splitting begins.

2.5. Finite element analysis of ORR at stimulation electrodes

Simulation of oxygen and peroxide diffusion was conducted with finite element method, implemented in COMSOL 5.5 software package and transport of diluted species module (www.comsol.com/product-download).

The experimental setup was reproduced within an axisymmetric 2D model. After the revolution, the

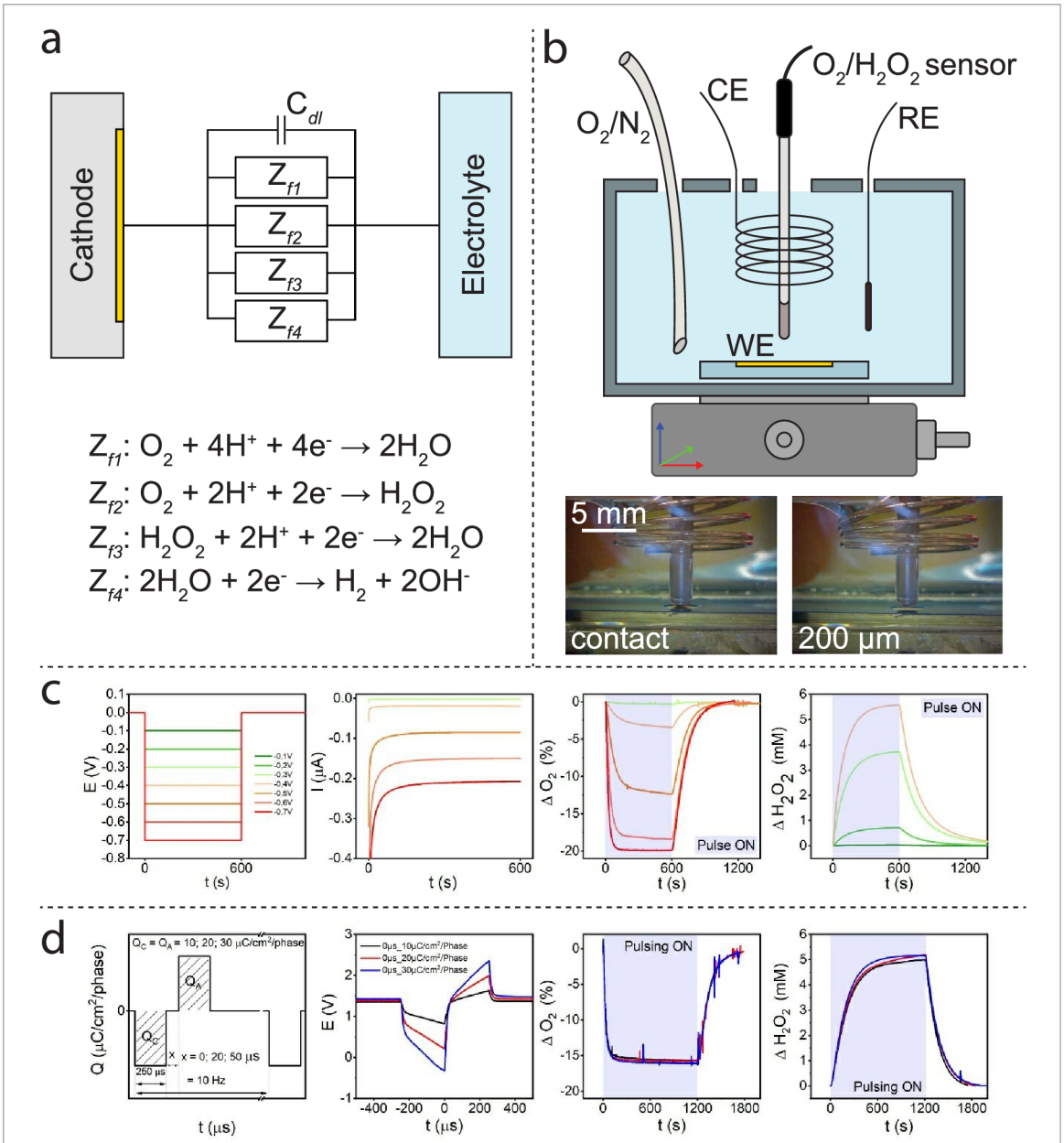

Figure 1. (a) Schematic of capacitive and faradaic charge transfer that can occur at an electrode interface during the cathodic phase. At a cathodically-polarized electrode, charge can accumulate in a capacitive double layer (C_{dl}), or can be transferred in a faradaic reaction to a species in solution (Z_{fx}). Oxygen reduction reactions (ORR), $Z_{f1} - Z_{f3}$, are thermodynamically favoured over the hydrogen evolution reaction Z_{f4}. Oxygen can undergo a four-electron, Z_{f1}, or $2 + 2$ electron reduction pathway ($Z_{f2} + Z_{f3}$) to yield water as a product. The two-electron pathway Z_{f2} produces hydrogen peroxide, while Z_{f3} consumes hydrogen peroxide. All ORR pathways $Z_{f1} - Z_{f3}$, lead to depletion of oxygen concentration near the electrode, and Z_{f2} can result in net accumulation of hydrogen peroxide. (b) Experimental setup for testing ORR occurring at an electrode interface. In this configuration, the voltage/current of the electrode under test is controlled in a three-electrode configuration with a potentiostat, or with a biphasic current stimulator. A Clark electrode sensor is used for probing the oxygen or peroxide concentration at a fixed position near the electrode under test (200 μm from the surface). The whole chamber is enclosed to allow experiments under air (21% O_2), 100% O_2, or 100% N_2. Photographs of the setup with the adjustable position between the electrode under test and sensor are shown below the schematic. (c) DC mode protocol used for testing electrodes involves steps of cathodic potentials from 0 to −0.7 V vs. Ag/AgCl. These example results are for an Au electrode. Potential is held for 600 s and current is registered. ORR currents start at highly cathodic values and decrease to diffusion-limited equilibrium values within tens of seconds. Over the course of 600 s, the sensor is used to register the local O_2 or H_2O_2 concentration. (d) AC mode involves charge-balanced cathodic-leading current pulses 250 μs per phase, 10 Hz modulation. Interpulse time is varied 0, 20, 50 μs; and three amplitudes are tested: 10, 20, 30 μC cm^{-2}/phase. These example traces are recorded for Au electrodes.

computational model obtained a cylindrical shape filled with water-based electrolytes (figure 5(a1)). Faradaic reactions occur on the area of a cathodic pixel located on the bottom. The diameter of pixel $d = 3$ mm was adopted from the experiment. The water electrolyte domain spreads on 5 mm from the stimulation electrode, thus making the diameter of the electrolyte cylinder 13 mm and its height 5 mm (figure 5(a1)). The model contained two variables: c_{O_2} and $c_{H_2O_2}$, which goes for a concentration of dissolved

oxygen and hydrogen peroxide. Initial values were assigned as $c_{O_2}^{saturated} = 300\,\mu M$ and $c_{H_2O_2} = 0\,\mu M$.

We simulated both two- and four-electron reaction pathways separately. In case of two-electron case, we considered the possibility of further reduction of peroxide into water, or so called 2 + 2 reaction pathway. ORR was modelled via the introduction [19] of the empirical faradaic efficiency function (1), which modifies fluxes of oxygen and peroxide:

$$f_{eff} = f_1 + f_2 \frac{C_{O_2}^{near\,pixel}}{C_{O_2}^{saturated}}, \quad (1)$$

where $C_{O_2}^{near\,pixel}$ is oxygen concentration, measured at 10 nm from the stimulation electrode. The values of constants f_1 and f_2 range between 0 and 1 ($f_1 + f_2 = 1$) and depend on the type of cathode. If the constant f_2 is bigger than zero, the resulting flux of hydrogen peroxide will decrease with oxygen depletion.

The diffusion equations governed the change of oxygen and peroxide concentration

$$\frac{dc_i}{dt} + \nabla \cdot J_i = 0, \quad (2)$$

$$J_i = -D_i \nabla c_i, \quad (3)$$

where i goes for O_2 and H_2O_2 and J_i are fluxes of oxygen and peroxide. Diffusion coefficients at 23 °C are: $D_{H_2O_2} = 1.8 \times 10^{-9}\ m^2\ s^{-1}$; $D_{O_2} = 2.5 \times 10^{-9}\ m^2\ s^{-1}$ [20, 21].

Production and consumption of diluted O_2 and H_2O_2 molecules were carried out through boundary fluxes and can be found with all other boundary conditions in figure 5(a2). The model considered oxygen reduction into hydrogen peroxide in ratio 1:1 with a possible correction by faradaic efficiency function. Boundary fluxes R_{O_2} and $R_{H_2O_2}$ were defined as in the recent work of Abdullaeva *et al* [19]:

$$R_{H_2O_2} = \frac{FI}{2A} \times f_{eff}, \quad (4)$$

$$R_{O_2} = -\frac{FI}{2A} \times \left(f_{eff} + \frac{1 - f_{eff}}{2} \right), \quad (5)$$

where I is applied current (different in case of DC or AC simulations), F is Faraday constant, $A = 3.14 \times 1.5^2\ mm^2$ is the stimulation electrode area, f_{eff} is dimensionless faradaic efficiency function, defined by constants f_1 and f_2 and measured O_2 concentration $C_{O_2}^{near\,pixel}$ on the 10 nm distance from a production pixel.

In the case of the four-electron ORR reaction pathway, H_2O_2 does not participate in the process, and diffusion equations (2) and (3) is solved only for a concentration of oxygen with fluxes of O_2 molecules. Assuming the absence of the reversed reaction, oxygen consumption is defined by

$$R_{O_2} = -\frac{FI}{4A}. \quad (6)$$

More details on the model construction can be found in the supplementary information appendix 1.

3. Results

3.1. CV characterization of electrodes

CV was used to characterize both capacitive charging and faradaic process occurring at each electrode material in PBS solution (figure 2). The system has been oxygenated and de-oxygenated (N_2 gas flow) to monitor the electrochemical behaviour of the materials under three different conditions (21% O_2 (atmospheric pressure), 100% N_2 and 100% O_2). Comparing CV curves from de-oxygenated conditions versus oxygenated ones can reveal which peaks are originating from ORR. The faradaic/capacitive charging behaviour differs markedly depending on the electrode material, nevertheless in all cases it is possible to observe an increase in cathodic current corresponding to oxygenation. ORR is apparent in CVs for voltages lower than +100 mV. For each material, we chose a smaller voltage window to measure in a region where capacitive charging dominates, allowing estimation of the double-layer capacitance of each electrode material (table 1; supplementary figure S2). CV scans for capacitance determination were obtained using a 1 mV step and current averaging according to methods described by Weltin and Kieninger [22].

3.2. DC chronoamperometry and direct measurements of ORR processes

While CV is useful to screen for possible ORR and other faradaic reactions, it does not reveal the magnitude of diffusion-limited oxygen reduction currents, or quantify the concentration of ORR products. To accomplish this, we combine DC chronoamperometry experiments with simultaneous recording of oxygen and hydrogen peroxide concentrations at a fixed point near the stimulation electrode surface (at a height of 200 μm). In these experiments, we measure current over time during the application of a constant potential (from +0.1 V to −0.9 V, by 0.1 V steps, depending on the material investigated) over a defined time (600 s) on each different stimulation electrode. The protocol and example results are plotted in figure 1(C). At potentials which are too anodic to reduce oxygen at a given electrode material, no sustained chronoamperometric currents are measurable. Once the onset potential is reached, sustained cathodic ORR current is clear. Onset potentials for ORR processes can be found in table 1. For reference,

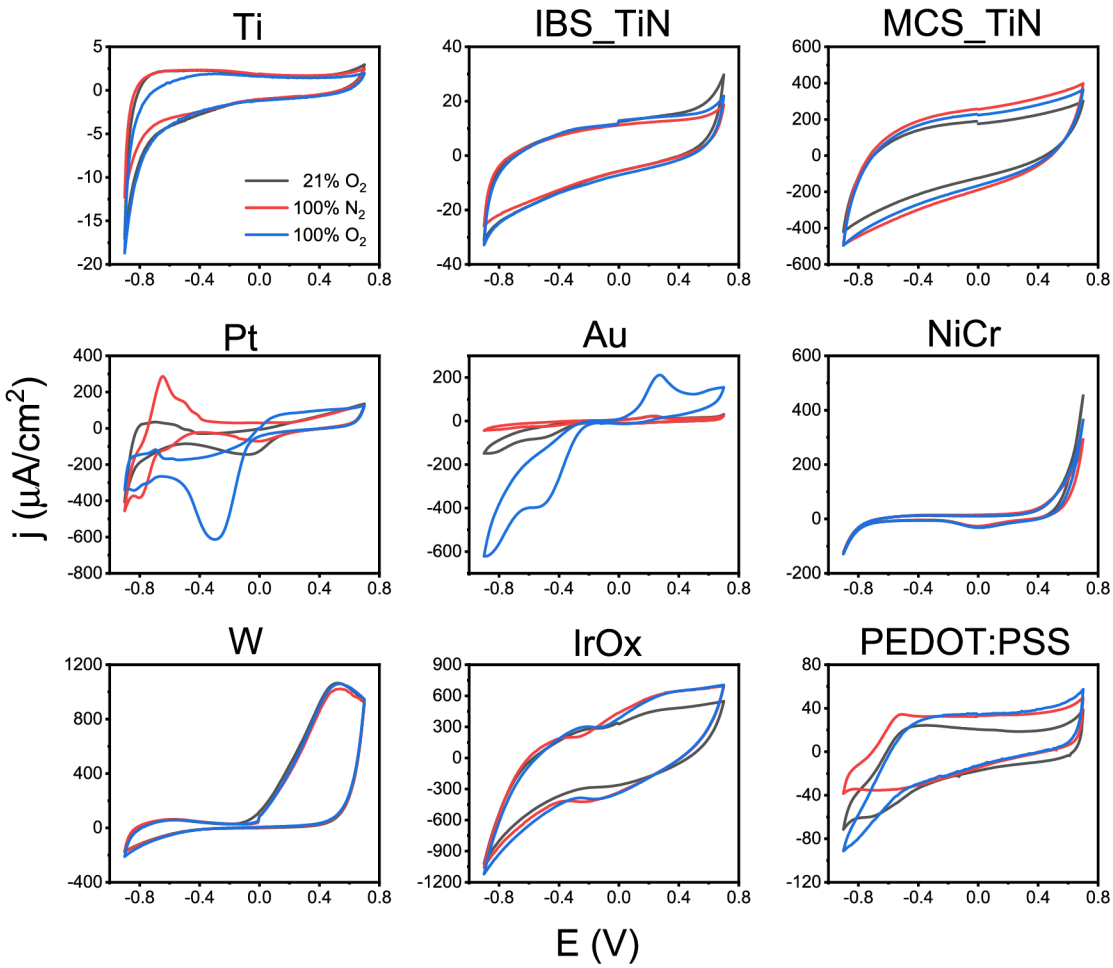

Figure 2. Cyclic voltammetry of neurostimulation electrodes in PBS solution. CVs of Ti, IBS_TiN, MCS_TiN, Pt, Au, NiCr, W, IrO_x and PEDOT:PSS in 100% oxygenated (blue), 21% oxygenated (ambient air, black), and 0% oxygenated (100% N_2 purged, red) conditions. Scan rate = 100 mV s^{-1}; Potential, *E*, range +0.7 V to −0.9 V versus Ag/AgCl. Due to large differences between materials in terms of their capacitive and faradaic currents, the respective plots have different current density *y*-axes.

Table 1. ORR process onset potentials for each electrode materials in PBS solution, and electrochemical double-layer capacitance estimated for CVs measured in a nonfaradaic potential window (CVs shown in figure S2). Onset potentials for ORR and cathodic water-splitting are estimated from the chronoamperometry voltage-step profile and corresponding amperometric confirmation of oxygen reduction/peroxide generation. Potentials are given versus Ag/AgCl, [Cl^-] = 0.12 M.

Material	Oxygen reduction onset (mV vs. Ag/AgCl)	Hydrogen peroxide evolution onset (mV vs. Ag/AgCl)	Hydrogen evolution reaction onset (mV vs. Ag/AgCl)	Double-layer capacitance (μF cm^{-2})
Ti	−700	−700	−900	21
IBS_TiN	−500	−600	−1400	22
MCS_TiN	−500	−500	−1400	669
Pt	+100	0[a]	−700	97
Au	−300	−300	−700	56
NiCr	−400	−400	−1000	24
W	−500	−600	−1000	69
IrO_x	0	0	−700	530
PEDOT:PSS	−600	−600	−1600	197

[a] Only trace amounts of peroxide detected.

each sample is measured also in deoxygenated electrolyte to establish the cathodic onset potential for water splitting/H_2 evolution. These H_2 evolution onsets, also given in table 1, are always more negative than measured ORR potentials. Chronoamperometry reveals a peak cathodic ORR current which then decays to a steady-state cathodic current. We define the steady-state current value as the current measured at the t = 600 s timepoint. The steady-state current as a function of applied potential for each material

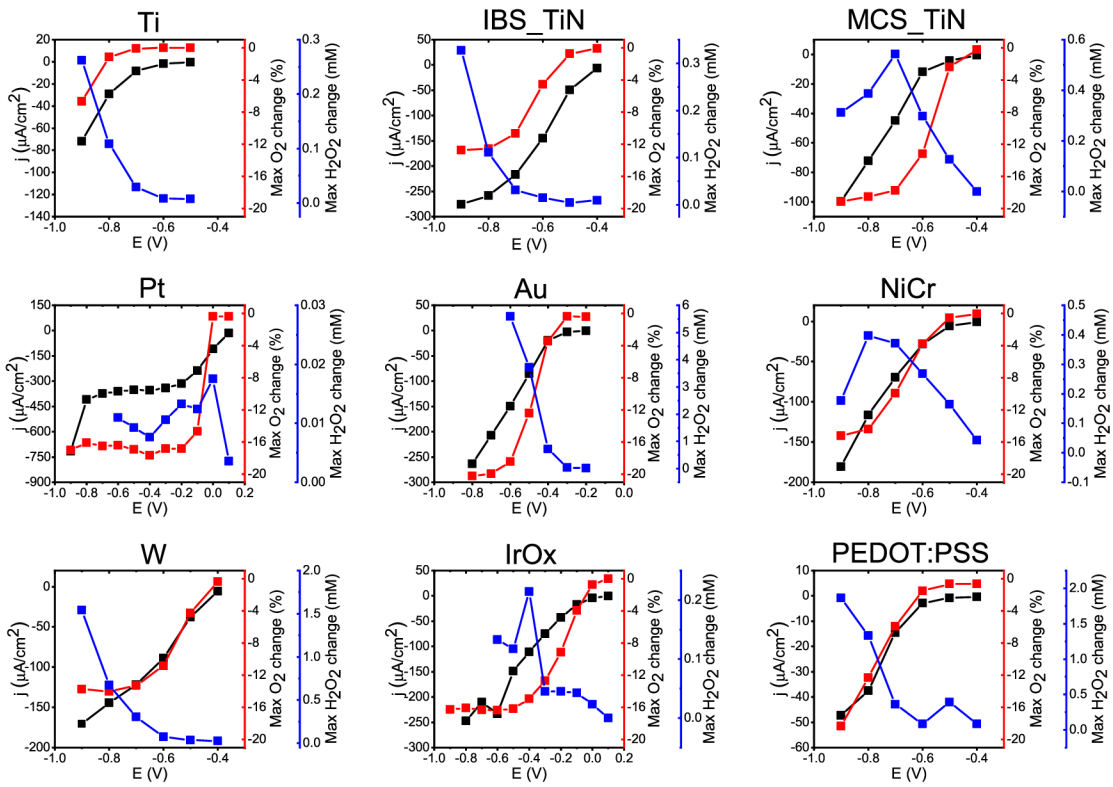

Figure 3. DC chronoamperometry with voltage-step protocol and resultant O_2 drop and H_2O_2 increase for each electrode material. All potentials are versus Ag/AgCl. Each point along the $J(V)$ trace (black) is the equilibrium current at $t = 600$ s. The red trace is the lowest measured $\%O_2$ at a position 200 μm above the electrode surface over the 600 s period. A drop of -21% is complete deoxygenation, while 0% corresponds to a normal 21% oxygen saturation. The blue traces mark the $[H_2O_2]$ in mM measured at each potential after 600 s, at a position 200 μm above the electrode surface. Peroxide recordings at voltages where cathodic H_2 evolution occurs on a given material are not plotted, since H_2 evolution interferes with the peroxide sensor.

is plotted in the black traces shown in figure 3. Simultaneously to recording chronoamperometry, the O_2/H_2O_2 amperometric sensor is active and recording the respective O_2 or H_2O_2 concentration value at a point in the electrolyte directly above the electrode-under-test. The measured values of O_2 or H_2O_2 concentration at the $t = 600$ s timepoint are shown in figure 3 as the red and blue traces, respectively. A change of -21% O_2 corresponds to a situation where the sensor records 0% oxygen, i.e. the calibrated lowest limit of a fully-deoxygenated solution. In between each voltage-step, the electrolyte in the cell is replaced with fresh, oxygenated electrolyte. It is noteworthy that all electrode materials can produce quite hypoxic conditions, with some such as Pt, Au, and PEDOT:PSS reaching nearly complete deoxygenation at higher cathodic potentials. The materials differ in their ability to produce peroxide from ORR. Au and PEDOT:PSS, for instance, produce concentrations into the millimolar range, while Pt generates barely-detectable trace amounts of peroxide. The recorded chronoamperometric currents and accompanying oxygen and peroxide measurements used to construct the plots in figure 3 can be found in supplementary figures S3–S11.

3.3. Direct measurements of ORR processes during AC stimulation protocols

Using the same configuration for amperometric sensing of oxygen and peroxide, we next applied charge balanced cathodic-leading pulses to the electrodes under test. The pulse duration per phase of charge balanced cathodic leading pulses used during experiments is kept constant (250 μs) and the interpulse spacing is changed to have three different durations (0, 20, or 50 μs). We use a period of 100 ms ($f = 10$ Hz). We tested three charge density values: 10, 20, or 30 μC cm^{-2}/phase. The total time for each AC experiment is 1200 s, compared with the DC chronoamperometry which was 600 s. This AC stimulation protocol and accompanying examples of measured amperometric transients are given in figure 1(d). The raw data of the amperometric traces of oxygen and peroxide over the course of AC pulsing are shown in figures S3–S11. In all cases, charge-balanced biphasic pulses led to drops in oxygen concentration comparable in magnitude to those found under the most cathodic DC conditions. The generation of peroxide as a byproduct varied based on material, with IrO_x and Pt producing only trace quantities, and Au and PEDOT:PSS producing the most. Surprisingly,

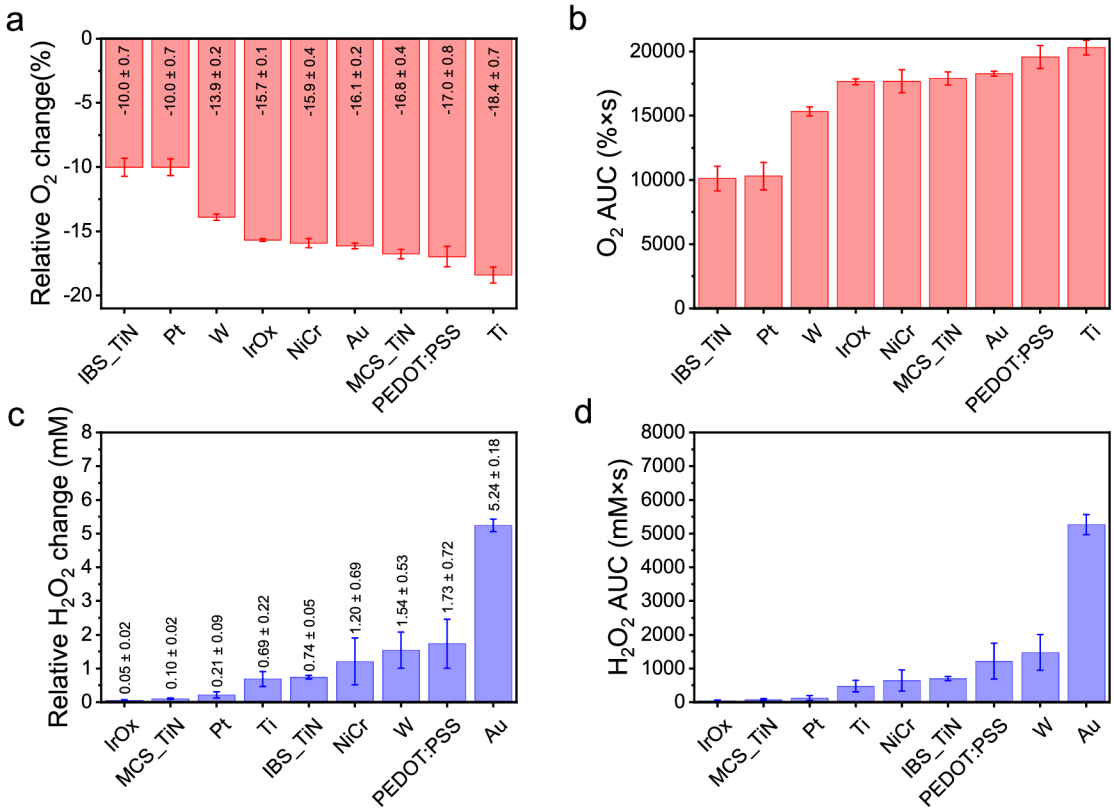

Figure 4. Charge-balanced cathodic-leading biphasic pulses 250/*x*/250, at 10, 20, or 30 μC cm^{-2} result in net oxygen reduction, and in the case of some materials, appreciable H_2O_2 generation. The interpulse spacing, *x*, of 0, 20, or 50 μs has little effect on the outcome. The charge density also has minimal impact. The error bars represent one standard deviation after taking the mean of all conditions (three different charge densities × three different interpulse spacings). (a) Peak O_2 change during the 1200 s period; (b) Total integrated area-under-curve of consumed O_2 over the course of the 1200 s period; (c) Peak peroxide concentration recording over the 1200 s period; (d) Total produced peroxide area-under-curve over 1200 s. While O_2 concentration values (a), (b) should be considered an accurate, quantitative result, the peroxide values in (c), (d) should be considered semi-quantitative, due to peroxide sensor cross-sensitivity to H_2. Materials like Au do produce some amount of H_2 during the cathodic phase.

the magnitude of the charge density applied in the pulse had little effect on the peak and total amounts of ORR observed. The interpulse spacing has a minimal contribution on the overall change in %O_2 or H_2O_2 concentration. Since both pulse amplitude and interpulse have no definitive impact on ORR levels, the data presented in figure 4 feature the nine different AC conditions all pooled to give a mean for a given material, with the standard deviation between conditions expressed by the error bar. Oxygen depletion and peroxide generation are expressed by both peak values, as well as the area-under-curve (AUC), the integral of the measured amperometric signal over time (1200 s) signifying the total amount of oxygen reduced/peroxide generated. During biphasic current pulses, voltage transients were collected (figure S12).

4. Discussion

4.1. ORR on electrode materials during CV and DC measurements

In this study, we have decided to investigate ORRs on commonly-used neurostimulation electrode materials, aiming to find out to what extent these reactions affect concentrations of dissolved oxygen and hydrogen peroxide near the electrode. We selected eight representative electrode materials which we fabricated in thin-film form. Additionally, as a ninth material we studied a commercial TiN sample with high charge-injection capacity. The logic behind this study was to first measure CV in oxygenated versus deoxygenated electrolytes. This kind of characterization unambiguously reveals the presence of ORR. Next, we performed step-voltage chronoamperometric measurements to establish the magnitude of equilibrium ORR current density that is possible at a given electrode material. During the chronoamperometric measurements, O_2 or H_2O_2 concentration is registered in real time in the solution above the electrode surface. The magnitude of ORR currents, as well as the onset potentials, varied greatly between the samples, which is why the current density *y*-axes plotted in figures 2 and 3 are all different. These differences originate because of the electrocatalytic properties of each material with respect to ORR. Measured peroxide concentrations in this study varied over four orders of magnitude, from 1 μM to 10 mM. The use of a Clark-type chronoamperometric detection system is, to the best of our knowledge, the only method to measure peroxide concentrations over such a large

range. Optical methods based on photo- or fluorometric detection of dyes can be highly sensitive at low concentrations <1 μM but these methods do not have a high dynamic range.

Firstly, we can turn our attention to results for platinum. Aside from being commonly used in many stimulation devices, Pt is a well-known textbook example of a good ORR catalyst [23]. In the CV measurements (figure 2), onset of ORR current is clearly observable around +100 mV. Under 100% and 21% oxygen conditions, a pronounced ORR peak is visible at negative potentials. In N_2-purged conditions, these ORR peaks are absent, and the reduction peaks can be assigned to proton absorption and then, by potentials more negative than −700 mV, clear hydrogen evolution reaction. The hydrogen evolution at potentials of −700 mV or more is present in both oxygenated and deoxygenated conditions, though oxygenation removes the peaks from Pt–H formation due to competitive adsorption of oxygen on the Pt surface. From chronoamperometry measurements of Pt electrodes, the steady-state ORR current densities in the range from +100 to −700 mV are higher on platinum than any of the other studied materials. Between −300 and −700 mV, there is a constant current density of −400 μA cm^{-2} which can be assigned as the equilibrium ORR level. Based on what is known about the electrocatalytic properties of Pt, this ORR current is almost exclusively four-electron reduction of oxygen to water. This is confirmed via the O_2/H_2O_2 sensor measurements. All applied potentials between −100 mV and −900 mV yield the same pronounced oxygen depletion of −17% (−21% corresponds to complete deoxygenation). In parallel, the peroxide sensor reveals relatively low concentrations of peroxide close to the detection limit, around 5 μM. This corroborates Pt as an efficient four-electron catalyst, moreover, Pt is well-known to decompose peroxide by either further two-electron reduction to water, or catalysed disproportionation to oxygen and water. Therefore, it is not surprising that our measurement of net peroxide production at Pt electrodes is minimal (though not completely absent). Taken together, these results for DC chronoamperometry show that Pt is an efficient oxygen reduction catalyst, and produces little peroxide as a by-product.

Following along by ordering materials with respect to their ORR onset potential, the next to consider is IrO_x. ORR is apparent from both CV and chronoamperometry. ORR is obscured in CV measurements due to the very high capacitive charging currents, which exceed in magnitude the maximum faradaic ORR currents. We calculate a capacitance of 530 μF cm^{-2} for our IrO_x samples. This material is well-known as a pseudofaradaic material with high capacitance. However, in chronoamperometry, the onsets and magnitudes of ORR currents are clearly resolved. Sustained ORR current (between 50 and 250 μA cm^{-2}) is apparent from potentials <0 V. ORR current densities are not as high as on Pt, and oxygen depletion does not reach −16% until −0.5 V is applied. The ORR process produces minimal amounts of peroxide, which is detectable from potentials <0 V.

The next 'classic' material we considered was gold. While gold is rarely used as a stimulation electrode material directly, it is frequently used as an interconnect, or as an electrode material in biosensor devices. ORR onset is visible in CV and chronoamperometry at around −300 mV, and faradaic currents are similar in magnitude to IrO_x. Au is recognized as an electrocatalyst which, unlike Pt, favours the two-electron pathway to generate peroxide [13]. Our results confirm that ORR current on Au is primarily via the peroxide pathway. Already by −500 mV, 5 mM of peroxide are detectable. Au overall is the most efficient peroxide-producing electrode among those we have tested. The two-electron pathway also corresponds to efficient oxygen depletion. Voltages more negative than −600 mV led to −21% oxygen level, that is, oxygen concentration reaches the lowest measurable value. In total, Au can be described as the material leading to the most deoxygenation and highest generation of peroxide.

PEDOT:PSS is a conducting polymer formulation which has attracted great attention as a promising low-impedance, high charge injection capacity electrode coating [24]. The CV of PEDOT:PSS shows a characteristic large capacitive background, nevertheless comparison of oxygenated and deoxygenated electrolytes clearly resolves the presence of ORR currents at potentials lower than −600 mV. PEDOT:PSS is known to be a highly-selective two-electron oxygen reduction catalyst [25]. The course of chronoamperometric currents for PEDOT:PSS resembles gold, though total equilibrium ORR currents are over four times lower than gold. Peroxide is generated from −600 mV onwards, reaching values into the mM range. A recent study by Dijk *et al* compared reactive oxygen species (ROS) generation and possible long-term safety of PEDOT:PSS versus Au, and found that thick PEDOT:PSS coatings can account for larger capacitive charge injection and less overall ROS generation [16]. The results of our DC measurements appear to be consistent with those findings as well.

NiCr and W are both materials which are not used in biomedical applications but are popular in basic neuroscience research. They both have relatively low double-layer capacitance and afford ORR with an onset potential of −400 mV. Equilibrium ORR currents are moderate (50–200 μA cm^{-2}), thus between the values of Au and PEDOT:PSS. W results in the production of peroxide with concentrations up to 2 mM, while NiCr generates about an order of magnitude less peroxide than W. These two materials

therefore are less active ORR catalysts than Pt or Au, yet more faradaic than PEDOT:PSS.

The final category of electrode materials are Ti and TiN, relevant in both basic research and biomedical stimulation devices. These materials are relatively the least faradaic. ORR currents on these materials are lower than on the other electrodes, and onset potentials are more negative. In CV and DC experiments, Ti is the most inert in terms of ORR current magnitude. Two types of TiN were studied, our own in-house thin film IBS_TiN and the MCS_TiN. The IBS_TiN is overall more faradaic than MCS_TiN or Ti, however the faradaic potential onsets are more cathodic than other studied materials, and currents remain relatively low. These findings correspond with what has been reported for titanium-based materials [26], in that they are regarded as being relatively inert and capacitive in terms of charge injection mechanism.

4.2. ORR during AC biphasic charge injection

While ORR is evident on all materials during CV measurements and during voltage-step chronoamperometric protocols, it can be postulated that rapid charge-balanced biphasic pulses will minimize ORR in terms of net oxygen consumption or peroxide generation. Lack of net ORR would be expected based on the logic of charge-balanced biphasic pulses minimizing any irreversible charge transfer into physiological solution [6, 8]. Nevertheless, the findings shown in figure 4 with biphasic pulses of 10, 20, and 30 μC cm^{-2} amplitude show that ORR occurs to an extent similar to DC conditions. Surprisingly, charge amplitude and interpulse spacing have little effect on ORR. The traces for oxygen and peroxide changes over the AC pulsing experiment follow different time courses on different materials (figures S3–S11). For this reason, in figure 4 we plot both peak values of O_2 and H_2O_2 concentration differences (figures 4(a) and (c), respectively), as well as the total area-under-curve (AUC), shown in figures 4(b) and (d). The AUC corresponds to the integral value of O_2 consumed or H_2O_2 generated over 1200 s (at the given point 200 μm away from the centre of the stimulation electrode), and therefore may be a more relevant metric than peak value when comparing different materials. This is particularly evident for materials like NiCr, where a rapid peak of peroxide concentration is followed by a decline, as the resultant peroxide is further decomposed to water.

From these biphasic experiments, the materials resulting in the least irreversible ORR are IBS_TiN, and Pt. The oxygen concentration drops as well as peroxide evolution magnitudes presented in figure 4 do not completely correlate with expectations from CV and DC measurements for different electrode materials. In the case of Au and PEDOT:PSS, the results from biphasic pulses do correspond to expectations from DC measurements in that these two materials generate the most hydrogen peroxide and also result in electrochemical deoxygenation to a high extent. IrO_x and Pt generate only trace amounts of peroxide. A material showing significant divergence from DC measurements is Ti: under biphasic pulsing, Ti leads to more deoxygenation than any other material. We do not have a clear mechanistic explanation for this result, and can speculate that this must have to do with oxygen consumption occurring during the anodic phase, likely during the anodization of the Ti surface and the reversible formation of an oxide layer which results in decrease of dissolved oxygen near the electrode. Another interesting comparison is between the two TiN samples. The porous MCS_TiN has 30 times higher double-layer capacitance than our in-house planar IBS_TiN sample. The MCS_TiN sample is known to have high capacitance due to a porous structure [17]. In both DC and AC conditions, the MCS_TiN sample is more active in ORR, consuming more oxygen. This indicates that the higher surface area affords also more active surface for faradaic reactions. As a point of reference to typical stimulation electrode characterization, we have recorded voltage transients for all AC conditions (figure S12). Such voltage transient data does not reveal ORR effects directly. The contributions of ORR can be interrogated by comparing transients for oxygenated versus deoxygenated electrolyte (figure S13). For most materials, the contribution of ORR as a charge-injection pathway is hinted by the apparent shift of the open circuit potential. Interpreting voltage transient data alone may give only limited information about the extent of ORR, which only becomes fully clear with the direct amperometric methods we have demonstrated. What can be emphasized from our findings is that electrochemical ORR during biphasic pulses is not as fully reversible as often assumed in the literature. Moreover, we have tried anodic-leading pulses, and found this also has little impact on total ORR. The overall characterization shows that all the electrode materials reduce O_2 in both AC and DC conditions. It should be noted that some of the peroxide data from AC pulsing may not be accurate due to sensor cross-sensitivity to H_2. For most of the materials studied this is apparently not an issue, but Au electrodes do produce some H_2 during cathodic pulsing and therefore the resulting sensor signal is mixed, and not quantitative. The possibility for over-estimation also becomes apparent in the upcoming theoretical calculation section, where it is possible to calculate the range of concentrations which can be expected based on the amount of available oxygen.

5. Theoretical modelling

As we have shown experimentally, when ORR occurs at a neurostimulation electrode surface, oxygen is consumed and often peroxide accumulates. It is evident that gradients of [O_2] and [H_2O_2] form and evolve over time. To visualize these gradients, we have

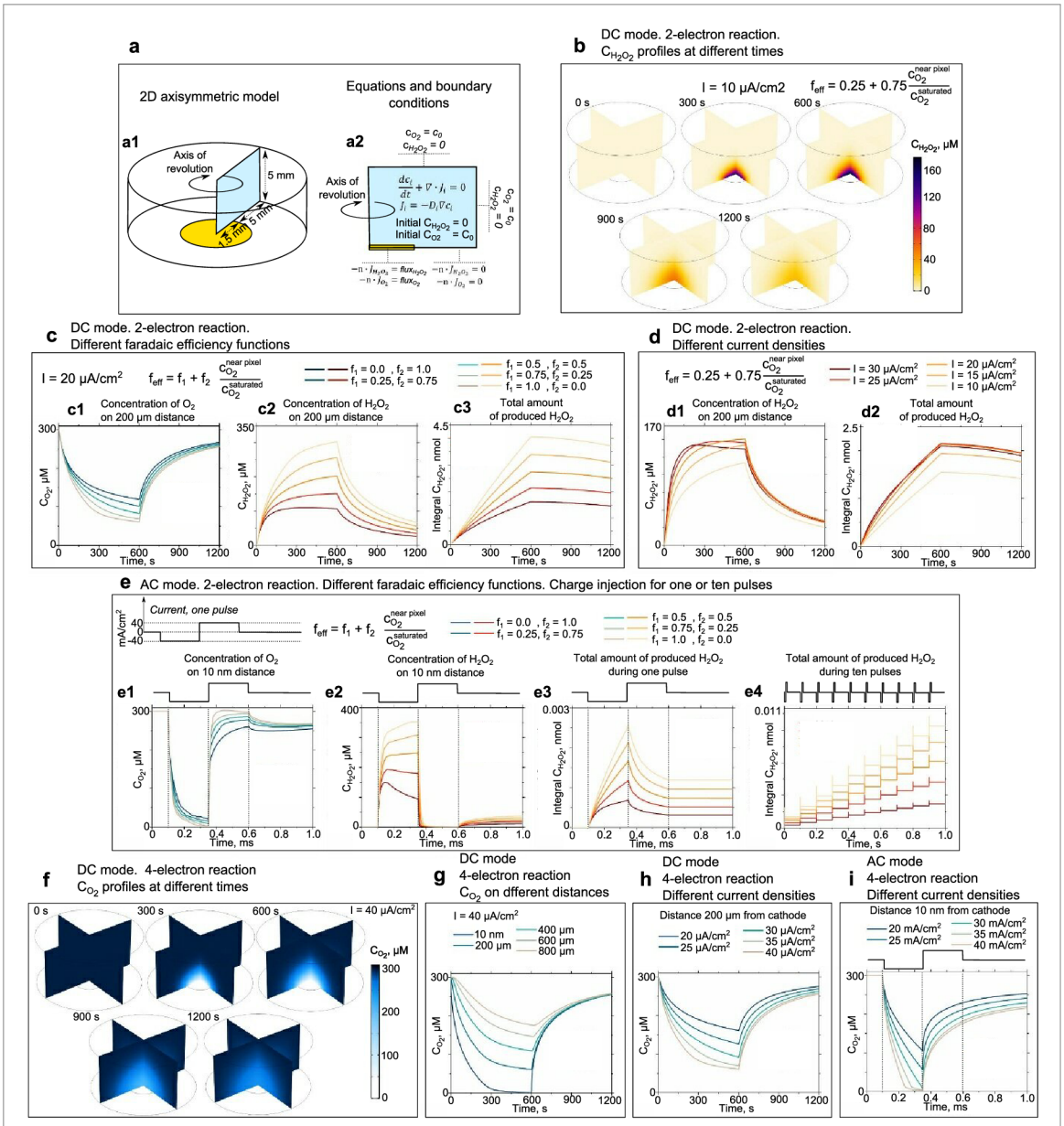

Figure 5. Finite element simulation of ORR and resulting O_2/H_2O_2 gradients at stimulation electrodes. (a) The model geometry, differential equations, and boundary conditions. (b) Example peroxide concentration profile during two-electron ORR under DC conditions. (c) O_2/H_2O_2 concentrations over time during DC operation considering different faradaic efficiency values. (d) Effect of current density on the O_2/H_2O_2 concentrations. (e) O_2/H_2O_2 concentrations during AC biphasic pulsing on an electrode favouring the two-electron ORR pathway. (f) O_2 concentration profiles during DC operation of a four-electron ORR electrode, showing the substantial region of hypoxia created by such an electrode. (g), (h) O_2 concentration as a function of distance and current density, respectively. (i) O_2 concentration at the electrode surface during different current densities applied during a 500 μs biphasic pulse.

performed a finite element simulation conducted in the COMSOL 5.5 software package. The finite element method is a good choice for this task because of its ability to reproduce the experimental setup in its actual sizes and flexibility in choosing the governing differential equation. We choose a two-dimensional axisymmetric model. After the revolution, it obtained a shape of a cylinder filled with electrolyte and the stimulation electrode at its bottom (figure 5(a1)). Concentrations of dissolved oxygen and hydrogen peroxide were simulated with diffusion equations and production/consumption fluxes on the stimulation electrode area (figure 5(a2)).

Faradaic ORR depends mainly on applied current and oxygen availability in the vicinity of a stimulation electrode. At the beginning of the process, we can assume that there is no hydrogen peroxide in the system and the concentration of dissolved oxygen is uniform across the electrolyte and equal to $c_{O_2}^{saturated} = 300\,\mu$M. The stationary concentration of dissolved oxygen in the electrolyte depends on many factors, such as salinity or temperature. It can vary in the range between 250 and 450 μM. The value of $c_{O_2}^{saturated}$ affects simulation results quantitatively but does not change them qualitatively. While ORR happen, oxygen near the cathodically-polarized surface

is rapidly consumed while the reaction products diffuse away from the electrode. As was shown experimentally, preferable reaction pathways can be chosen by varying cathode material. For instance, platinum is known to be an efficient four-electron oxygen reduction electrocatalyst, meanwhile PEDOT:PSS or Au catalyse two-electron peroxide production. Simulations were carried out for two- and four-electron reaction pathways separately. In the case of two-electron reaction pathway, there was a possibility of an additional two-electron reduction of produced peroxide into water (2 + 2 reaction). The amount of current that goes to H_2O_2 reduction in 2 + 2-electrode reaction, was defined with a faradaic efficiency according to equation (1) and fluxes according to equations (4) and (5).

Applying these calculations allows one to input realistic conditions used in a given neurostimulation experiment. Likewise, we wanted to use the model to understand the main differences between DC and AC faradaic production. An example of DC two-electron ORR with hydrogen peroxide as product can be found in figure 5(b), where $c_{H_2O_2}$ is depicted on two slices at different times up to 1200 s. A concentration gradient of H_2O_2 increases during the first 600 s. Because of the circular shape of the cathodic electrode, most of the produced peroxide is diffusing in a direction perpendicular to the stimulation electrode in a semispherical shape. The local $c_{H_2O_2}$ in front of the electrode centre will be higher than on its sides. Dissipation of produced H_2O_2 happens through the fixed concentration $c_{H_2O_2} = 0$ on the borders of electrolyte domain during the following 600 s, when no current is applied. In figures 5(c1) and (c2) one can find concentration profiles of c_{O_2}, $c_{H_2O_2}$ on the distance of 200 μm (as is in the experimental measurements) and in figure 5(c3) $\int c_{H_2O_2} dV$, which corresponds to the total amount of peroxide in nmoles, available in the system at a given time. Different values f_1 and f_2 define how efficiently the cathode can reduce O_2 into H_2O_2. The shape of concentration profiles recorded on 200 μm can be significantly altered by changing f_1 and f_2 in a range from 0 to 1. If peroxide production is not efficient at low oxygen content ($f_1 = 0$, $f_2 = 1$), a sensor will record a clear 'plateau' in H_2O_2 concentration accompanied by lower deoxygenation. In the opposite case, if production efficiency of H_2O_2 is maximum ($f_1 = 1, f_2 = 0$) regardless of $C_{O_2}^{\text{near pixel}}$, H_2O_2 concentration, recorded by the sensor will have a steady increase in the form of 'hill' until the end of 600 s with strong deoxygenation. Despite the sublinear behaviour of H_2O_2 concentration profile in figure 5(c2), the total amount of produced H_2O_2 increases linearly with time and slowly dissipates through the boundaries in the following 600 s. This means that concentration data measured by the sensor cannot quantify the total amount of produced H_2O_2 in the system.

Faradaic efficiency is not the only factor affecting the shape of H_2O_2 concentration recorded by the sensor. An increase of the current density, applied to cathodic electrode from 10 to 30 μA cm^{-2} leads to the transition from the 'hill' shape towards 'plateau' and even further into 'reversed hill' at 30 μA cm^{-2} when recorded $c_{H_2O_2}$ decreases with time (figure 5(d1)). Considering the total amount of produced H_2O_2, the system reaches its production limit at some current density, when additional increase of current density to the production pixel cannot increase peroxide content (figure 5(d2)). Production limit means that diffusional inflow of oxygen into the production zone is insufficient to support more ORR flux. This production limit can be surpassed in two cases: the temperature of electrolyte must be significantly increased (affecting the O_2 diffusion coefficient), or $C_{O_2}^{\text{saturated}}$ would have to be higher (oxygen-enriched electrolytes). All three simulated archetypes of H_2O_2 concentration profiles ('hill', 'plateau', 'reversed hill') and transition between them were indeed observed experimentally and can be found in figures S3–S9.

AC peroxide production is based on different processes compared to DC production. According to the traditional expectations of charge-balanced biphasic pulsing, one can anticipate an absence of H_2O_2, because of compensation of all produced peroxide by the reversed reaction. Experiments show net H_2O_2 efflux from the cathodic electrode surface. To explain this effect, we performed calculations of ORR during one and ten AC pulses, summarized in figure 5(e). One AC pulse consists of three phases: forward 250 μs pulse, reversed 250 μs pulse, and 99 ms relaxation phase. It is essential to underline that current density, applied to the cathodic stimulation electrode in AC case ($\geqslant$40 mA cm^{-2}) is orders of magnitude larger than in the DC case ($\geqslant$10 μA cm^{-2}). This means that the process which takes seconds in the DC case and occurs in milliseconds in the AC case. It is apparent in figures 5(e1) and (e2), where almost all oxygen near the production zone is consumed during the first 250 μs forward pulse, regardless of the faradaic efficiency. The concentration of H_2O_2 near the production zone also reaches large numbers. In case of maximized production (assuming all O_2 is reduced into H_2O_2), the recorded $c_{H_2O_2} \approx 350$ μM can even surpass $C_{O_2}^{\text{saturated}} = 300$ μM. This fact is explained by the difference in diffusion coefficients of O_2 and H_2O_2—oxygen inflow occurs faster than outflow of peroxide. After the forward pulse, the reverse pulse starts. It is reasonable to assume that the faradaic yield for H_2O_2 oxidation back to O_2 is close to unity. Therefore, H_2O_2 located near the cathode zone is oxidized into oxygen. $c_{H_2O_2}$ immediately drops to zero and c_{O_2} regains its initial value. While in figures 5(e1) and (e2) it may look as if all H_2O_2 is consumed during the reverse pulse, approximately half of

the total H_2O_2 produced during the AC pulse remains in the system (figure 5(e3)). This is due to diffusion. During the forward pulse, there is a flux of peroxide from the production zone. An additional gradient direction opens during the reversed pulse: towards the production zone with further consumption, while the gradient from the production zone remains. At this moment, there is a wave of peroxide near the stimulation electrode, which diffuses in two opposite directions, where the concentration of peroxide is zero. The duration of the reversed pulse is too low to reoxidize all the produced peroxide. At the same time, O_2 concentration is recovered not only by the consumption of peroxide but also by the diffusion of O_2 from the deeper electrolyte medium. After the reversed pulse, a relaxation stage occurs, where for more than 99 ms there is no current in the system. During this phase, H_2O_2 diffuses uniformly around all available space (resulting in a minor increase of $c_{H_2O_2}$ near production zone) and c_{O_2} decreases to compensate losses in electrolyte medium. At the end of the relaxation phase, the system almost recovers into its initial stage. Simulation of the sequential ten AC pulses shows a linear step-like increase of total H_2O_2 amount with each pulse figure 5(e4). The simulation shows that while DC conditions operate at small current values and thus a relatively slow reaction at the cathode goes for minutes, AC biphasic conditions result in rapid consumption of all available O_2 near the production zone at each current pulse and net oxygen depletion and, dependent on faradaic efficiency, peroxide accumulation.

The 2-electron reaction pathway implies the production of peroxide, and is to a lesser or greater degree present on all electrode materials tested in our work. However, some materials like Pt and IrO_x produce only trace amounts of peroxide, consistent with the expectation that they catalyse four-electron oxygen reduction to water. Four-electron reaction leads only to deoxygenation of electrolyte around the stimulation electrode. The electron multiplicity of the reaction translates to larger current requirements for the reaction, meaning twice slower consumption of dissolved oxygen at the same current density than during two-electron reaction. Oxygen concentration slices formed during DC faradaic production at a different time from 0 s to 1200 s can be found in figure 5(f). Oxygen is reduced with the formation of an apparent reversed gradient from the cathode zone. An oxygen-free region is formed at some distance from it, where all of the dissolved oxygen is consumed. A depletion of oxygen is observed at up to several mm from the pixel. Precise values of O_2 concentrations at a distance from 10 nm to 800 μm from the cathode are in plotted in figure 5(g). While four-electron reaction takes place, full deoxygenation is observed at 10 nm. However, at the distance of 200 μm, the simulation shows noticeable c_{O_2} presence. This effect is a manifestation of gradient formation because of the diffusion of O_2 from the electrolyte medium towards the production zone and explains the impossibility of detecting full deoxygenation at 200 μm experimentally. Gradual increase of current density from 20 to 40 μA cm^{-2} allows recording of slow saturation of c_{O_2} towards its minimal value at the distance of 200 μm with the formation of a clear plateau (figure 5(h)). As for the AC case, similarly to the hydrogen peroxide production, the forward pulse almost immediately deoxygenates the whole cathodic zone on tens of nm deep (figure 5(i)). Assuming the absence of the reversed reaction, slow redistribution of oxygen starts after the cathodic phase, similar to the AC hydrogen peroxide production (figure 5(e1)).

6. Conclusions

Thermodynamically, oxygen is the most favourable electron acceptor present in physiological environments [22]. The formal potential of four-electron ORR to water as the product is 1.23 V more positive than the hydrogen evolution reaction. The formal potential of two-electron ORR to H_2O_2 is 0.7 V more positive than hydrogen evolution. However, this value is often cited misleadingly, as it is important to remember that formal potential assumes standard conditions, i.e. $[H_2O_2] = 1$ M. Under physiological conditions, peroxide evolution is even more favourable since starting equilibrium concentrations of hydrogen peroxide are orders of magnitude lower than 1 M. By applying the Nernst equation, the actual thermodynamic potential for peroxide evolution is approx. 1.2 V, therefore as favourable as four-electron reduction [27]. Despite this likelihood of ORR happening at neurostimulation electrodes, the effects of ORR have not been extensively studied. The work we have done was aimed at introducing a set of methods for directly probing oxygen and peroxide concentrations at different neurostimulation electrodes. Using amperometric sensor measurements of oxygen and hydrogen peroxide concentration in the vicinity of electrodes we can unambiguously conclude that ORR occurs at all the studied materials, and that charge-balanced biphasic pulsing still leads to irreversible ORR. The method we present can in principle be applied *in vivo* by using appropriate microelectrodes which are commercially available.

Our results imply that during certain neuromodulation procedures, ORR may have consequences. Conditions near the electrode surface become hypoxic, which may significantly affect neuronal viability. Just a few minutes of hypoxia can trigger irreversible neuronal cell death [28, 29]. Many electrode materials additionally foster the accumulation of hydrogen peroxide. Hydrogen peroxide can be toxic at higher concentrations, and at lower concentrations functions as a signalling molecule in numerous pathways [30]. From the point of view of disturbing the balance of physiological oxygen the least, we can conclude

that IrO_x, Pt, and TiN appear to be the most promising. This applies to our in-house fabricated samples and depending on morphology and surface catalytic properties, results may vary significantly. An interesting observation is that the porous commercial TiN appears to be more active with respect to ORR than our planar thin film TiN. Therefore, just increasing double-layer capacitance of a sample does not necessarily minimize irreversible faradaic charge injection. Several of the other studied materials emerge as possibly problematic in neurostimulation applications due to relatively large hydrogen peroxide production: Au, W, and PEDOT:PSS can yield local peroxide concentrations in the mM range. All three materials are well-known to be active electrocatalysts for two-electron ORR, therefore our findings are not surprising. Extracellular peroxide concentrations in the range of 0.1–1 mM are toxic to cells [31]. More moderate concentrations in the range of tens of micromolar [H_2O_2] can have distinct electrophysiologic effects. Concentrations in this range cause oxidative modification of certain $K_v7.x$ channels, which result in significantly higher outward potassium currents (the so-called M-current) and by this mechanism peroxide downregulates cellular excitability [19, 32]. On the other hand, cells expressing transient receptor vanilloid voltage-gated channels can be depolarized by the presence of such peroxide concentrations, therefore peroxide may cause action potential firing [33]. Our results for the different ORR behaviours occurring on different electrode materials can serve as a guide to eliminating problematic variables from electrophysiology experiments. Our findings of hypoxia being produced by DC currents, on the other hand, may be useful for electrically-addressable on-demand hypoxia or ROS delivery, which can be a useful experimental technique.

Data availability statement

All data that support the findings of this study are included within the article (and any supplementary files).

Acknowledgments

This project has been supported by funding from the European Research Council (ERC) under the European Union's Horizon 2020 research and innovation program (E D G Grant Agreement No. 949191), and a contribution from the city council of Brno, Czech Republic. The work was also supported by the Grant Agency of the Czech Republic under Contract 20-30129Y. Sample fabrication was supported by *CzechNanoLab Research Infrastructure* financed by MEYS CR (LM2018110). The computations were performed on resources provided by the Swedish National Infrastructure for Computing (SNIC) at NSC and HPC2N.

Author contributions

E D G conceived the project. J E designed and built the measurement setup. J E; L M; and M N performed all electrochemical experiments. I S developed the finite element model and did all calculations. M N set up the AC pulsing experiments and wrote software for data collection. J E and L M performed all data analysis. J B and I G fabricated all electrodes, except for IrO_x, which was fabricated by X T V and S I. E D G supervised the project. The paper was written by all co-authors.

Conflict of interest

The authors declare no competing financial interests.

ORCID iDs

Jiří Ehlich https://orcid.org/0000-0003-0478-6875
Ihor Sahalianov https://orcid.org/0000-0002-0609-471X
Imrich Gablech https://orcid.org/0000-0003-4218-1287
Xuan Thang Vu https://orcid.org/0000-0001-6797-2443
Sven Ingebrandt https://orcid.org/0000-0002-0405-2727
Eric Daniel Głowacki https://orcid.org/0000-0002-0280-8017

References

[1] Lozano A M *et al* 2019 Deep brain stimulation: current challenges and future directions *Nat. Rev. Neurol.* **15** 148–60
[2] Kwan H, Garzoni L, Liu H L, Cao M, Desrochers A, Fecteau G, Burns P and Frasch M G 2016 Vagus nerve stimulation for treatment of inflammation: systematic review of animal models and clinical studies *Bioelectron. Med.* **3** 1–6
[3] Cameron T 2004 Safety and efficacy of spinal cord stimulation for the treatment of chronic pain: a 20-year literature review *J. Neurosurg.* **100** 254–67
[4] Krames E S, Peckham P H and Rezai A R 2009 *Neuromodulation* (London: Academic)
[5] Grill W M and Kirsch R F 2000 Neuroprosthetic applications of electrical stimulation *Assist. Technol.* **12** 6–20
[6] Cogan S F 2008 Neural stimulation and recording electrodes *Annu. Rev. Biomed. Eng.* **10** 275–309
[7] Merrill D R, Bikson M and Jefferys J G R 2005 Electrical stimulation of excitable tissue: design of efficacious and safe protocols *J. Neurosci. Methods* **141** 171–98
[8] Merrill D R 2010 The electrochemistry of charge injection at the electrode/tissue interface *Implantable Neural Prostheses 2* eds D D Zhou and E Greenbaum (New York: Springer) pp 85–138
[9] Günter C, Delbeke J and Ortiz-Catalan M 2019 Safety of long-term electrical peripheral nerve stimulation: review of the state of the art *J. Neuroeng. Rehabil.* **16** 13
[10] Leung R T, Shivdasani M N, Nayagam D A X and Shepherd R K 2015 *In vivo* and *in vitro* comparison of the charge injection capacity of platinum macroelectrodes *IEEE Trans. Biomed. Eng.* **62** 849–57
[11] Boehler C, Carli S, Fadiga L, Stieglitz T and Asplund M 2020 Tutorial: guidelines for standardized performance tests for electrodes intended for neural interfaces and bioelectronics *Nat. Protocols* **15** 3557–78

[12] Shepherd R K, Carter P, Dalrymple A, Enke Y L, Wise A K, Nguyen T, Firth J, Thompson A and Fallon J B 2021 Platinum dissolution and tissue response following long-term electrical stimulation at high charge densities *J. Neural Eng.* **18** 036021
[13] Morton S L, Daroux M and Mortimer J T 1991 The role of oxygen reduction in electrical stimulation of nervous tissue *Proc. Annual Conf. Engineering in Medicine and Biology Society* vol 13 pp 552–3
[14] Cogan S F, Ehrlich J, Plante T D, Gingerich M D and Shire D B 2010 Contribution of oxygen reduction to charge injection on platinum and sputtered iridium oxide neural stimulation electrodes *IEEE Trans. Biomed. Eng.* **57** 2313–21
[15] Musa S, Rand D R, Bartic C, Eberle W, Nuttin B and Borghs G 2011 Coulometric detection of irreversible electrochemical reactions occurring at Pt microelectrodes used for neural stimulation *Anal. Chem.* **83** 4012–22
[16] Dijk G, Ruigrok H J and Connor R P O 2021 PEDOT:PSS-coated stimulation electrodes attenuate irreversible electrochemical events and reduce cell electropermeabilization *Adv. Mater. Interfaces* **8** 2100214
[17] Egert U, Schlosshauer B, Fennrich S, Nisch W, Fejtl M, Knott T, Müller T and Hämmerle H 1998 A novel organotypic long-term culture of the rat hippocampus on substrate-integrated multielectrode arrays *Brain Res. Protocols* **2** 229–42
[18] van Ooyen A, Topalov G, Ganske G, Mokwa W and Schnakenberg U 2009 Iridium oxide deposited by pulsed dc-sputtering for stimulation electrodes *J. Micromech. Microeng.* **19** 074009
[19] Abdullaeva O S, Sahalianov I, Ejneby M S, Jakešová M, Zozoulenko I, Liin S I and Głowacki E D 2022 Faradaic pixels for precise hydrogen peroxide delivery to control M-type voltage-gated potassium channels *Adv. Sci.* **9** 2103132
[20] Wise D L and Houghton G 1966 The diffusion coefficients of ten slightly soluble gases in water at 10–60 °C *Chem. Eng. Sci.* **21** 999–1010
[21] van Stroe-biezen S A M M, Everaerts F M, Janssen L J J J and Tacken R A 1993 Diffusion coefficients of oxygen, hydrogen peroxide and glucose in a hydrogel *Anal. Chim. Acta* **273** 553–60
[22] Weltin A and Kieninger J 2021 Electrochemical methods for neural interface electrodes *J. Neural Eng.* **18** 052001
[23] Song C and Zhang J 2008 Electrocatalytic Oxygen Reduction Reaction *PEM Fuel Cell Electrocatalysts and Catalyst Layers: Fundamentals and Applications* ed J Zhang (London: Springer) pp 89–134
[24] Donahue M J, Sanchez-Sanchez A, Inal S, Qu J, Owens R M, Mecerreyes D, Malliaras G G and Martin D C 2020 Tailoring PEDOT properties for applications in bioelectronics *Mater. Sci. Eng.* R **140** 100546
[25] Mitraka E *et al* 2019 Electrocatalytic production of hydrogen peroxide with Poly(3,4-ethylenedioxythiophene) electrodes *Adv. Sustain. Syst.* **3** 1800110
[26] Schaldach M, Hubmann M, Weikl A and Hardt R 1990 Sputter-deposited TiN electrode coatings for superior sensing and pacing performance *Pacing Clin. Electrophysiol.* **13** 1891–5
[27] Katsounaros I, Schneider W B, Meier J C, Benedikt U, Biedermann P U, Auer A A and Mayrhofer K J J 2012 Hydrogen peroxide electrochemistry on platinum: towards understanding the oxygen reduction reaction mechanism *Phys. Chem. Chem. Phys.* **14** 7384
[28] Kirino T 2000 Delayed neuronal death *Neuropathology* **20** 95–7
[29] Lipton P 1999 Ischemic cell death in brain neurons *Physiol. Rev.* **79** 1431–568
[30] Sies H and Jones D P 2020 Reactive oxygen species (ROS) as pleiotropic physiological signalling agents *Nat. Rev. Mol. Cell Biol.* **21** 363–83
[31] Sies H 2017 Hydrogen peroxide as a central redox signaling molecule in physiological oxidative stress: oxidative eustress *Redox Biol.* **11** 613–9
[32] Gamper N, Zaika O, Li Y, Martin P, Hernandez C C, Perez M R, Wang A Y C, Jaffe D B and Shapiro M S 2006 Oxidative modification of M-type K + channels as a mechanism of cytoprotective neuronal silencing *EMBO J.* **25** 4996–5004
[33] Lodola F, Rosti V, Tullii G, Desii A, Tapella L, Catarsi P, Lim D, Moccia F and Antognazza M R 2019 Conjugated polymers optically regulate the fate of endothelial colony-forming cells *Sci. Adv.* **5** eaav4620